agriculture

Special Issue Reprint

Intelligent Equipment and Automation Technology in Farmland Production

Edited by
Jiale Zhao and Mingzhuo Guo

mdpi.com/journal/agriculture

MDPI

Intelligent Equipment and Automation Technology in Farmland Production

Intelligent Equipment and Automation Technology in Farmland Production

Guest Editors

Jiale Zhao
Mingzhuo Guo

MDPI

Basel • Beijing • Wuhan • Barcelona • Belgrade • Novi Sad • Cluj • Manchester

Guest Editors

Jiale Zhao
Key Laboratory of Bionics Engineering
Jilin University
Changchun
China

Mingzhuo Guo
College of Biological and Agricultural Engineering
Jilin University
Changchun
China

Editorial Office
MDPI AG
Grosspeteranlage 5
4052 Basel, Switzerland

This is a reprint of the Special Issue, published open access by the journal *Agriculture* (ISSN 2077-0472), freely accessible at: https://www.mdpi.com/journal/agriculture/special_issues/X4B0L7348E.

For citation purposes, cite each article independently as indicated on the article page online and as indicated below:

Lastname, A.A.; Lastname, B.B. Article Title. *Journal Name* **Year**, *Volume Number*, Page Range.

ISBN 978-3-7258-8987-7 (Hbk)
ISBN 978-3-7258-8988-4 (PDF)
https://doi.org/10.3390/books978-3-7258-8988-4

© 2026 by the authors. Articles in this reprint are Open Access and distributed under the Creative Commons Attribution (CC BY) license. The reprint as a whole is distributed by MDPI under the terms and conditions of the Creative Commons Attribution-NonCommercial-NoDerivs (CC BY-NC-ND) license (https://creativecommons.org/licenses/by-nc-nd/4.0/).

Contents

About the Editors . . . . . **vii**

Preface . . . . . **ix**

Mingzhuo Guo and Jiale Zhao
Intelligent Equipment and Automation Technology in Farmland Production
Reprinted from: *Agriculture* **2026**, *16*, 1143, https://doi.org/10.3390/agriculture16111143 . . . . **1**

He Li, Zhan He, Changchang Yu, Changle Guo, Qiming Ding, Shuaishan Cao, et al.
Optimization and Experimental Evaluation of a Deep Learning-Based Target Spraying Device for Weed Control in Soybean Fields
Reprinted from: *Agriculture* **2026**, *16*, 395, https://doi.org/10.3390/agriculture16040395 . . . . . **5**

Li Ding, Feiyang Wu, Yuanyuan Li, Kaixuan Wang, Yechao Yuan, Bingjie Liu and Yufei Dou
Design and Experimentation of High-Throughput Granular Fertilizer Detection and Real-Time Precision Regulation System
Reprinted from: *Agriculture* **2026**, *16*, 290, https://doi.org/10.3390/agriculture16030290 . . . . . **31**

Xuanting Liu, Zhanhong Guo, Zhenwei Tong, Miao He, Peng Gao, Yunhai Ma and Zihe Xu
A Study on the Interaction Mechanism Between Disc Coulters and Maize Root-Soil Composites Based on DEM-MBD Coupling Simulation
Reprinted from: *Agriculture* **2026**, *16*, 270, https://doi.org/10.3390/agriculture16020270 . . . . . **57**

Tuanpeng Tu, Xiwen Luo, Lian Hu, Jie He, Pei Wang, Peikui Huang, et al.
Analysis Method and Experiment on the Influence of Hard Bottom Layer Contour on Agricultural Machinery Motion Position and Posture Changes
Reprinted from: *Agriculture* **2026**, *16*, 170, https://doi.org/10.3390/agriculture16020170 . . . . . **77**

Henry O. Velesaca, Francisca Ruano, Alice Gomez-Cantos and Juan A. Holgado-Terriza
Image Segmentation of Cottony Mass Produced by *Euphyllura olivina* (Hemiptera: Psyllidae) in Olive Trees Using Deep Learning
Reprinted from: *Agriculture* **2025**, *15*, 2485, https://doi.org/10.3390/agriculture15232485 . . . . **105**

Dezhi Ren, Ruiqiang Wang, Zefei Zhang, Guolong Li, Wanyuan Huang and Wei Wang
Design and Application of a Portable Chestnut-Harvesting Device
Reprinted from: *Agriculture* **2025**, *15*, 2382, https://doi.org/10.3390/agriculture15222382 . . . . **121**

Peng Gao, Xuanting Liu, Zihe Xu, Shuo Wang, Mingzi Qu and Yunhai Ma
DEM Simulation and Experimental Investigation of Draft-Reducing Performance of Up-Cutting Subsoiling Method Inspired by Animal Digging
Reprinted from: *Agriculture* **2025**, *15*, 2046, https://doi.org/10.3390/agriculture15192046 . . . . **146**

Tengyuan Hou, Xinxin Chen, Jianping Hu, Wei Liu, Junpeng Lv, Youheng Tan and Fengpeng Li
Design and Experimental Research on an Automated Force-Measuring Device for Plug Seedling Extraction
Reprinted from: *Agriculture* **2025**, *15*, 1939, https://doi.org/10.3390/agriculture15181939 . . . . **171**

Xiaodong Zhang, Xiangyu Han, Yixue Zhang, Lian Hu and Tiezhu Li
Multi-Trait Phenotypic Extraction and Fresh Weight Estimation of Greenhouse Lettuce Based on Inspection Robot
Reprinted from: *Agriculture* **2025**, *15*, 1929, https://doi.org/10.3390/agriculture15181929 . . . . **195**

Kui Zhang, Yong-Ying Zhang, Xinliang Zhao, Yun Zhao, Xin Feng, Qi Wang and Jinwu Wang
Design and Test of a Bionic Auxiliary Soil-Crushing Device for Strip-Tillage Machines
Reprinted from: *Agriculture* **2025**, *15*, 944, https://doi.org/10.3390/agriculture15090944 . . . . . **211**

About the Editors

Jiale Zhao

Jiale Zhao is a Tang Aoqing Distinguished Professor and doctoral supervisor at Jilin University, China. He is the Director of the Scientist Studio for Intelligent Agricultural Machinery and Equipment at the National Key Laboratory of Smart Farm Technology and Systems. His research focuses on high-speed electric-drive precision maize-seeding equipment for large-scale smart farms in Northeast China, in addition to dedicated sensors, embedded systems and intelligent control technologies for agricultural machinery. His work is closely related to precision seeding, smart farm equipment, agricultural machinery automation, and the integration of sensing and control systems for modern crop production.

Mingzhuo Guo

Mingzhuo Guo is an associate professor and doctoral supervisor at the College of Biological and Agricultural Engineering, Jilin University, China. His research interests include intelligent agricultural machinery, bionic design of agricultural equipment, soil–machine interaction, precision agriculture, agricultural sensing and control, and simulation-based design methods for agricultural engineering. He serves on academic committees related to agricultural machinery and agricultural engineering. His work focuses on the integration of mechanical design, bionic principles, intelligent sensing, and control methods to improve the efficiency, adaptability and reliability of agricultural equipment used in farmland production.

Preface

The modernization of farmland production increasingly depends on the deep integration of agricultural machinery, sensing technology, automation control and artificial intelligence. This Reprint was prepared to present representative progress in this interdisciplinary field and to highlight how intelligent equipment can support more accurate, efficient and reliable field operations. The collected articles address key links in agricultural production, from perception and monitoring to mechanism design, simulation analysis, control optimization and practical validation. We hope that this Reprint will serve as a useful reference for researchers, engineers, graduate students and practitioners who are interested in smart agricultural machinery, digital farmland systems and the future development of automated crop production.

Jiale Zhao and Mingzhuo Guo
Guest Editors

agriculture

MDPI

Editorial

Intelligent Equipment and Automation Technology in Farmland Production

Mingzhuo Guo and Jiale Zhao *

College of Biological and Agricultural Engineering, Jilin University, Changchun 130022, China; gmz@jlu.edu.cn
* Correspondence: zhaojl@jlu.edu.cn

Agricultural production is undergoing a rapid transition from mechanized field operations to data-informed, perception-supported, and adaptive equipment systems. This transition is driven by several practical pressures, including soil heterogeneity, variable crop growth, uneven terrain, biological material diversity, labor shortages, and increasingly strict requirements for input reduction and sustainable production. As a result, agricultural machinery is no longer judged only by whether it can complete a field operation with sufficient power and acceptable efficiency. A more important question is whether a machine can perceive changing field conditions, interpret them in time, and adjust its working process accordingly. Mechanical improvement remains the foundation of agricultural equipment, but it is now being combined more closely with sensing, modeling, artificial intelligence, and automatic control [1–4].

This Special Issue, "Intelligent Equipment and Automation Technology in Farmland Production", was organized to reflect and promote this shift. The papers collected here address bionic design of tillage and soil-engaging components, soil–tool and root–soil–tool simulation, agricultural robotics, crop phenotyping, transplanting force measurement, precision fertilization, target spraying, pest symptom segmentation, terrain-related posture analysis, and portable harvesting devices. Although these topics cover different operating objects and technical routes, they share a central purpose: to connect mechanical structure, field perception, computational modeling, and agronomic performance in equipment that can operate reliably under real farmland conditions.

Several papers in this Special Issue return attention to the working component itself. This is important because intelligent agricultural equipment should not be understood simply as conventional machinery with sensors or algorithms attached to it. In many cases, intelligence begins with the structure that directly interacts with soil, crop, seedling, fertilizer, weed, or harvested material. The geometry, motion mode, contact behavior, and biological or soil-adaptive characteristics of the working part determine whether later sensing and control can be effective. This view is consistent with recent developments in field robots and agricultural robotic arms, where mechanical execution, perception, decision-making, and adaptability are increasingly designed as coupled problems rather than separate modules [5,6]. In this Special Issue, studies on bionic soil-engaging components and subsoiling mechanisms show how a better understanding of soil deformation, fracture, and tool–soil interaction can be converted into low-resistance and high-quality field operations [7].

Simulation-assisted design is another clear feature of the collected papers. Soil, roots, seedling substrates, granular fertilizers, and harvested biological materials cannot be fully described by simple rigid-body assumptions. Their behavior is affected by contact, adhesion, cohesion, fragmentation, accumulation, and local failure. Recent reviews have

shown that the discrete element method and DEM-coupled approaches are becoming important tools for analyzing agricultural processes that are difficult to observe directly [8]. For equipment design, the value of simulation lies not only in producing visualized particle movement but also in explaining why a tool reduces draft, why a material accumulates or separates, and why a working component fails under particular contact conditions. At the same time, simulation should not be treated as a replacement for experiments. Its credibility still depends on material calibration, parameter validation, bench testing, soil bin testing, and field verification.

This Special Issue also reflects the rapid expansion of agricultural sensing. Modern sensing in farmland production is moving from single-point measurement toward multi-trait, multi-source, and task-specific perception. In greenhouse and field environments, robotic and imaging systems are being used to acquire plant traits, identify biological targets, and support management decisions. Recent studies on image-based high-throughput plant phenotyping emphasize that the practical value of sensing depends on the integration of sensors, platforms, algorithms, and deployment scenarios [9]. Similarly, deep learning has advanced crop monitoring, but field application still depends on generalization ability, processing speed, robustness, and compatibility with the physical operation being performed [10].

Many failures in field equipment are not caused by a single weak component but by a mismatch between sensing results and mechanical action. A transplanting end-effector may fail when the seedling substrate differs from the assumed state; a tillage tool may experience excessive resistance when root–soil reinforcement is ignored; a spraying system may miss weeds because recognition and actuation are not synchronized; and a field vehicle may deviate when terrain-induced posture changes are not properly considered. For this reason, agricultural sensing should be designed together with the machinery task it serves. Sensor layout, signal processing, control logic, and mechanical response need to be considered as parts of one equipment system.

Closed-loop and real-time control represent another important direction. Precision fertilization and target spraying are typical examples. In such systems, the critical issue is not only whether fertilizer flow, crop state, or weed targets can be detected but also whether detection, decision-making, actuation, and machine motion can remain synchronized at operating speed. Recent studies on site-specific weed management, variable-rate spraying, and agricultural spray robots have shown the potential of robotics, machine vision, and variable-rate technology, while also exposing persistent challenges in navigation, target identification, sensing–actuation delay, and system integration [11–13]. One paper in this Special Issue illustrates this engineering problem by combining a lightweight deep-learning model, grid-based target matching, and delay compensation for soybean-field weed control [14]. This type of work is valuable because it moves beyond model accuracy alone and emphasizes whether perception results can be converted into timely and reliable actuation under field conditions.

The papers in this Special Issue also point to several unresolved issues. First, many intelligent equipment systems are still tested under limited conditions. Soil type, crop variety, lighting, field roughness, residue distribution, and travel speed can all change system performance. Multi-site validation and environmental robustness, therefore, need more attention. Second, simulation calibration remains a bottleneck. DEM and coupled simulation methods are useful, but their reliability depends on contact parameters, material properties, and validation procedures that are often not yet standardized for cohesive soil, root–soil composites, seedling substrates, fertilizers, and biological materials. Third, perception modules and mechanical systems are still too often developed separately. Future

https://doi.org/10.3390/agriculture16111143

equipment should be designed from the beginning as an integrated architecture in which sensing, mechanics, control, and agronomic objectives constrain and support one another.

Digital twins and data-driven system modeling may provide one route for this integration. Agricultural digital twins are increasingly discussed as tools for linking field data, simulation models, equipment behavior, and management decisions in smart farming systems [15]. For intelligent equipment, the concept is useful only when it serves engineering decisions. A practical equipment-level digital twin does not need to reproduce every detail of the field. Its value lies in diagnosis, prediction, parameter optimization, and adaptive control under realistic operating constraints.

Evaluation criteria also need to change. Traditional machinery evaluation often focuses on draft, operation quality, damage rate, productivity, or fuel consumption. Intelligent equipment requires additional indices, including detection accuracy, response time, latency, control stability, energy consumption, adaptability, input reduction, maintainability, and serviceability. For field-deployable systems, robustness and ease of maintenance are not secondary indicators; they often determine whether a technology can leave the laboratory. The contribution of modern agricultural technologies to productivity and land-use efficiency ultimately depends on whether they can overcome barriers in cost, scalability, usability, and field adaptation [16].

Overall, this Special Issue shows that intelligent farmland equipment is moving from mechanized execution toward perception-supported, model-guided, and decision-oriented operation. Three take-home messages can be drawn from the collected papers. First, intelligence in agricultural equipment should begin with the working component itself, where mechanical structure, contact behavior, and biological or soil-adaptive design determine the effectiveness of later sensing and control. Second, simulation, sensing, robotics, and control algorithms should be integrated as an equipment-level system rather than developed as separate technical modules. Third, future intelligent equipment must be evaluated not only by traditional machinery indices but also by robustness, latency, adaptability, maintainability, input reduction, and field deployability. Continued progress along these directions will be essential for improving production efficiency, reducing labor demand, lowering input use, and supporting sustainable farmland management.

Acknowledgments: We sincerely thank all authors who contributed to this Special Issue of Agriculture, titled "Intelligent Equipment and Automation Technology in Farmland Production", as well as the reviewers for their careful evaluations and constructive suggestions. We also gratefully acknowledge the support of the editorial team of Agriculture. Special thanks are extended to Siyang Wu for his valuable assistance with the coordination of this Special Issue.

Conflicts of Interest: The authors declare no conflicts of interest.

References

1. Chandra, V.S.S.; Hareendran, A.S.; Albaaji, G.F. Precision farming for sustainability: An agricultural intelligence model. *Comput. Electron. Agric.* **2024**, *226*, 109386. [CrossRef]
2. Dusadeerungsikul, P.O.; Nof, S.Y. Precision agriculture with AI-based responsive monitoring algorithm. *Int. J. Prod. Econ.* **2024**, *271*, 109204. [CrossRef]
3. Kumar, V.; Sharma, K.V.; Kedam, N.; Patel, A.; Kate, T.R.; Rathnayake, U. A comprehensive review on smart and sustainable agriculture using IoT technologies. *Smart Agric. Technol.* **2024**, *8*, 100487. [CrossRef]
4. Jiang, L.; Xu, B.; Husnain, N.; Wang, Q. Overview of agricultural machinery automation technology for sustainable agriculture. *Agronomy* **2025**, *15*, 1471. [CrossRef]
5. Liu, L.; Yang, F.; Liu, X.; Du, Y.; Li, X.; Li, G.; Chen, D.; Zhu, Z.; Song, Z. A review of the current status and common key technologies for agricultural field robots. *Comput. Electron. Agric.* **2024**, *227*, 109630. [CrossRef]
6. Jin, T.; Han, X. Robotic arms in precision agriculture: A comprehensive review of the technologies, applications, challenges, and future prospects. *Comput. Electron. Agric.* **2024**, *221*, 108938. [CrossRef]

7. Gao, P.; Liu, X.; Xu, Z.; Wang, S.; Qu, M.; Ma, Y. DEM simulation and experimental investigation of draft-reducing performance of up-cutting subsoiling method inspired by animal digging. *Agriculture* **2025**, *15*, 2046. [CrossRef]
8. Maraveas, C.; Tsigkas, N.; Bartzanas, T. Agricultural processes simulation using discrete element method: A review. *Comput. Electron. Agric.* **2025**, *237*, 110733. [CrossRef]
9. Wang, R.; Qu, H.; Su, W. From sensors to insights: Technological trends in image-based high-throughput plant phenotyping. *Smart Agric. Technol.* **2025**, *12*, 101257. [CrossRef]
10. Zhang, R.; Wu, X.; Li, J.; Zhao, P.; Zhang, Q.; Wuri, L.; Zhang, D.; Zhang, Z.; Yang, L. A bibliometric review of deep learning in crop monitoring: Trends, challenges, and future perspectives. *Front. Artif. Intell.* **2025**, *8*, 1636898. [CrossRef] [PubMed]
11. Upadhyay, A.; Zhang, Y.; Koparan, C.; Rai, N.; Howatt, K.; Bajwa, S.; Sun, X. Advances in ground robotic technologies for site-specific weed management in precision agriculture: A review. *Comput. Electron. Agric.* **2024**, *225*, 109363. [CrossRef]
12. Lochan, K.; Khan, A.; Elsayed, I.; Suthar, B.; Seneviratne, L.D.; Hussain, I. Advancements in precision spraying of agricultural robots: A comprehensive review. *IEEE Access* **2024**, *12*, 129447–129483. [CrossRef]
13. Taseer, A.; Han, X. Advancements in variable rate spraying for precise spray requirements in precision agriculture using unmanned aerial spraying systems: A review. *Comput. Electron. Agric.* **2024**, *219*, 108841. [CrossRef]
14. Li, H.; He, Z.; Yu, C.; Guo, C.; Ding, Q.; Cao, S.; Yang, Z.; Wang, W. Optimization and experimental evaluation of a deep learning-based target spraying device for weed control in soybean fields. *Agriculture* **2026**, *16*, 395. [CrossRef]
15. Subeesh, A.; Chauhan, N. Agricultural digital twin for smart farming: A review. *Green Technol. Sustain.* **2026**, *4*, 100299. [CrossRef]
16. Chen, X. The role of modern agricultural technologies in improving agricultural productivity and land use efficiency. *Front. Plant Sci.* **2025**, *16*, 1675657. [CrossRef] [PubMed]

Disclaimer/Publisher's Note: The statements, opinions and data contained in all publications are solely those of the individual author(s) and contributor(s) and not of MDPI and/or the editor(s). MDPI and/or the editor(s) disclaim responsibility for any injury to people or property resulting from any ideas, methods, instructions or products referred to in the content.

agriculture

MDPI

Article

Optimization and Experimental Evaluation of a Deep Learning-Based Target Spraying Device for Weed Control in Soybean Fields

He Li, Zhan He, Changchang Yu *, Changle Guo, Qiming Ding, Shuaishan Cao, Zishang Yang and Wanzhang Wang

College of Mechanical and Electrical Engineering, Henan Agricultural University, Zhengzhou 450002, China
* Correspondence: yuchang@henau.edu.cn

Abstract

Weed management during the seedling stage is a critical component of soybean production. Efficient weed control can significantly improve crop yield and crop quality. However, conventional spraying techniques exhibit low pesticide utilization and contribute to environmental pollution. To address these challenges, this study proposes a deep learning-based precision target spraying method. A lightweight YOLOv5-MobileNetv3-SE model was developed by replacing the backbone feature extraction network and incorporating an attention mechanism. Field images of weeds were collected to construct a dedicated dataset, and the detection performance of the model was evaluated. Furthermore, a grid-based matching spraying algorithm was developed to synchronize target detection with spray actuation. The system time delay, including image processing delay, communication and control delay, and spray deposition delay, was analyzed and measured, and a time-delay compensation strategy was implemented to ensure accurate spraying. Experimental results demonstrated that the improved model achieved an mAP@0.5 of 86.9%, a model size of 7.5 MB, and a frame rate of 38.17 frames per second. The weed detection accuracy exceeded 92.94%, and spraying accuracy exceeded 85.88% at forward speeds of 1–4 km·h^{-1}. Compared with conventional continuous spraying, the proposed method achieved pesticide reduction rates of 79.0%, 72.5%, 55.8%, and 48.6% at weed coverage rates of 5%, 10%, 15%, and 20%, respectively. The proposed method provides a practical approach for precise herbicide application, effectively reducing chemical usage and minimizing environmental impact.

Keywords: weed management; weed detection; target spraying device; YOLOv5-MobileNetv3-SE; grid-based matching spraying algorithm

1. Introduction

Soybean is rich in high-quality plant protein and various essential nutrients, making it a major source of dietary protein. It is widely used in edible oil processing, feed production, and the food industry and plays a crucial role in ensuring global food security and promoting sustainable agricultural development [1,2]. Consequently, soybeans are widely cultivated worldwide. Weed management during the seedling stage is a crucial component of soybean production, as weeds directly compete with crops for essential resources such as nutrients, water, and light, thereby adversely affecting crop growth and yield [3,4]. Currently, weed control in soybean fields is predominantly achieved through the application of herbicides. Conventional herbicide application in farmland mainly relies on

continuous full-coverage spraying. However, a large proportion of the applied chemicals either evaporates or infiltrates into the soil, and only a small fraction is effectively deposited on the target weeds. This practice leads to excessive herbicide use, chemical residues, and environmental pollution, thereby hindering sustainable agricultural development [5–7]. In China, the effective utilization rate of pesticides for major grain crops is only 41.8%. Target spraying technology enables real-time identification of weeds and other targets through object detection, allowing pesticides to be applied precisely according to their spatial distribution and size. Compared with conventional continuous full-coverage spraying, this approach significantly reduces pesticide consumption, improves application efficiency, and mitigates environmental pollution [8].

Accurate target detection is a fundamental prerequisite for the effective implementation of target spraying. According to the type of sensors employed, existing systems can be broadly classified into ultrasonic-based, LiDAR-based, and vision-based approaches. LiDAR measures distances by emitting laser pulses and recording the time of flight of the reflected signals. When combined with the rotational angle of the scanning unit, LiDAR enables the acquisition of three-dimensional (3D) point cloud data of plant structures. Owing to its high spatial resolution, strong robustness to illumination variations, and large sensing range, LiDAR has been widely applied in orchard environments for 3D reconstruction and for estimating canopy characteristics such as volume, height, and density, thereby providing a basis for variable-rate spraying decisions [9–12]. According to measurement configuration, LiDAR systems can be classified into single-line and multi-line scanners. Single-line LiDAR utilizes a single laser channel to perform point-by-point scanning and is typically used for reconstructing local or partial structures [13], whereas multi-line LiDAR employs multiple laser beams to capture high-density point cloud data and is more suitable for reconstructing entire orchard scenes [14]. Ultrasonic sensors measure distances by emitting sound waves and measuring the time required for the echoes to return. However, their response speed is relatively slow due to the limited propagation velocity of sound in air and the constraints of analog signal processing. Ultrasonic sensors have been used in agricultural applications, including the estimation of canopy volume and density [15,16], leaf area density in Osmanthus trees [17], and the height of blueberries and weeds [18]. In recent years, machine vision technology has been extensively applied in crop and weed detection research [19]. Visual sensors are used to capture images, which are subsequently analyzed using traditional machine learning methods or deep learning algorithms to achieve accurate crop and weed recognition. Commonly used visual sensors include monocular cameras, stereo cameras, and RGB cameras [20]. Monocular RGB cameras operate based on the pinhole imaging principle, projecting three-dimensional spatial information onto a two-dimensional image plane. Owing to their simple structure, low cost, and the availability of well-established algorithms, these sensors have been widely used in agricultural applications such as canopy analysis, pest and disease detection [21], fruit detection [22,23], and weed identification [24,25]. In contrast, RGB-D cameras are capable of actively acquiring depth information, primarily through infrared structured light projection or time-of-flight (TOF) techniques. As a result, they are particularly suitable for tasks requiring three-dimensional perception and have been widely employed in fruit detection and localization applications [26,27].

Conventional weed detection algorithms predominantly rely on machine learning approaches to distinguish crops from weeds, such as k-nearest neighbors (k-NN) clustering [28], support vector machines (SVMs) [29,30], random forests [31], and artificial neural networks (ANNs) [32] to classify crops and weeds. However, these traditional approaches typically rely on manually designed features, such as color, texture, and shape. Consequently, their robustness is limited under real field conditions, including variable

https://doi.org/10.3390/agriculture16040395

illumination, high morphological similarity between crops and weeds, leaf occlusion, and complex backgrounds [33,34]. Moreover, due to constraints in sample size and variations in data distribution, these methods often demonstrate poor generalization across different weed species and operational scenarios, making it difficult to satisfy the accuracy and stability requirements of target spraying applications. Recent advances in deep learning have significantly improved weed detection in agricultural fields. Representative object detection algorithms include R-CNN, Faster R-CNN, SSD, Mask R-CNN, and the YOLO series [35–37]. Among them, YOLO is an end-to-end, single-stage object detector that performs target localization and classification within a single forward pass. Owing to its high detection speed, strong real-time capability, and relatively simple network architecture, YOLO has been widely applied in real-time recognition of weeds, crops, and pests in agricultural scenarios. Several improved YOLO-based models have been proposed to enhance detection accuracy and efficiency. Wang et al. [38] proposed a YOLOv5-SGS model for multi-species weed recognition in wheat fields, achieving a mean average precision (mAP) of 91.4% and an F1 score of 85.3%. Xu et al. [39] proposed W-YOLOv5 algorithm for crop seedling detection, reporting an overall mAP of 87.6%, demonstrating its capability in recognizing multiple weed species. Rahman et al. [40] evaluated thirteen one-stage and two-stage detectors, including YOLOv5n and Fast R-CNN, for weed detection in cotton fields. RetinaNet (R101-FPN) achieved the highest detection performance with an mAP@0.50 of 79.98%, although its inference time was relatively long. Rai et al. [41] proposed YOLO-Spot model based on YOLOv7-tiny, reducing parameters by over 75% and GFLOPs by 86%, while improving mAP@0.50 by 2.7% compared with YOLOv7-Base. Sunil [42] trained six YOLOv8 and eight YOLOv9 variants on datasets comprising eight crop species and five weed species, achieving an overall mAP@50 of 86.2%. Li et al. [43] developed an improved YOLOv10n-FCDS model for weed detection in UAV-acquired rice field images. By integrating a FasterNet backbone with a CGBlock module, the model effectively enhanced the detection accuracy of small and occluded weeds, achieving an mAP@50 of 87.4%. To address computational efficiency, lightweight models have also been developed. Fan et al. [44] proposed YOLO-WDNet for weed detection in cotton fields, reducing parameters by 82.3%, and model size by 91.6%, compared with contemporary models. He et al. [45] developed EDS-YOLOv8 weed detection algorithm, employing EfficientViT as the backbone, optimizing key modules, and integrating the SimAM attention mechanism, resulting in significant performance improvement. Liu et al. [46] proposed an improved lightweight weed detection model based on YOLOv9s, achieving an mAP of 81.7% by optimizing anchor boxes and introducing the SPPELAN-ECA and AGSConv modules. Overall, YOLO-based models demonstrate strong capabilities in weed detection; nevertheless, their high computational requirements often limit real-time performance and operational efficiency. Therefore, achieving a balance between model lightweighting and recognition accuracy is essential to enhance practical applicability in field operations.

In precision target spraying systems and devices, Wang et al. [38] developed a lightweight and improved YOLOv5s model and designed a target spraying decision and hysteresis algorithm. The experiments indicated that, at operational speeds of 0.3–0.6 m/s, the system achieved a spraying accuracy of 95.7%, demonstrating its effectiveness in real-time field applications. Zhao et al. [30] developed a cabbage identification and pesticide spraying control system based on an artificial light source, in which weeds were detected using SVM. The results demonstrated that the fitted curve coefficient achieved a maximum identification accuracy of 95.7%. However, as the vehicle speed increased, target displacement also increased, with a maximum centroid deviation of 28.6 mm observed at 0.93 m/s. Xu et al. [39] proposed a hierarchical detection algorithm for multi-species weed identification and developed a variable-rate spraying system based on the severity of weed

https://doi.org/10.3390/agriculture16040395

infestation, categorized into five levels. Field trials demonstrated that the system could achieve a spraying accuracy of 90.32% at an operational speed of 4 km·h^{-1}. Jiang et al. [47] developed a weeding method in which herbicides were applied following mechanical injury to weed tissues. Field tests on Chinese cabbage demonstrated a weed removal rate of 94.5% while using only 15.3% of the herbicide required by conventional chemical methods. Sunil et al. [48] proposed a grid map creation algorithm using the YOLOv4 model to control the nozzles of a robotic platform. Based on the grid map algorithm, herbicide application was reduced by 79%. Although existing research on target spraying systems has made significant progress in weed detection algorithms, few studies have addressed the challenge of maintaining accurate herbicide application at varying operational speeds using advanced control strategies, which remains a critical issue for practical field applications.

In this study, weed control is investigated during the seedling stage of non-GMO cultivars of soybean, specifically at the V1–V2 growth stage (one- to two-trifoliate leaf stage). To address the challenges of accurate and efficient weed management at this stage, a deep learning-based targeted spraying method for soybean fields is proposed, along with a grid-based matching spraying algorithm for precise weed elimination. Field weed images are first acquired using a camera, and weeds are detected using an improved YOLOv5 model. Based on the detection results, the proposed algorithm controls the opening and closing of solenoid valves in real time to ensure accurate herbicide application to target weeds. The performance of the developed system is subsequently evaluated through both laboratory and field experiments. Overall, this study provides a practical solution for integrating weed detection with precision target spraying, enabling reliable spraying accuracy under variable field conditions.

2. Materials and Methods

2.1. Design of the Target Spraying Device

The target spraying device was integrated into a 3WPZ-200 self-propelled electric boom sprayer and comprised four main subsystems, i.e., an image acquisition unit, a pesticide supply unit, a spray execution unit, and a traveling system, as shown in Figure 1. The image acquisition unit was responsible for real-time field image collection, while the pesticide supply and spray execution units cooperatively enabled precise pesticide delivery. The traveling system provided stable forward motion during field operations.

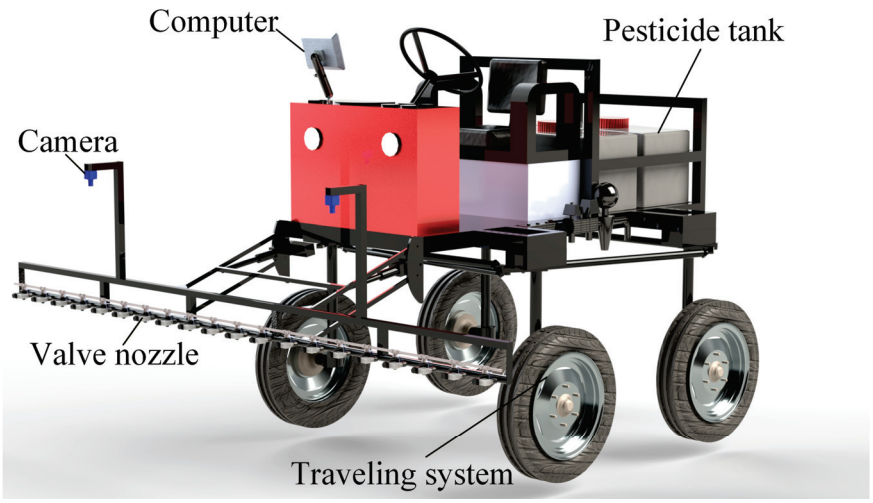

Figure 1. Overall structure of the target spraying device.

The image acquisition unit consisted of two cameras (MV-CA016, Hangzhou Hikvision Digital Technology Co., Ltd., Hangzhou, China) and an onboard computer (Intel NUC, Intel

Corporation, Santa Clara, CA, USA) equipped with an Intel i7-1165G7 CPU, an NVIDIA GTX 2060 GPU with 6 GB memory, and 16 GB RAM. The cameras, each with a resolution of 1440 × 1080 pixels and equipped with a 4 mm focal-length lens, were used to acquire field images. To ensure full coverage of the spray boom, the two cameras were mounted symmetrically at one-quarter and three-quarters of the boom length on the left and right sides, respectively, with each camera responsible for monitoring half of the operating area. The cameras were installed at a height of 0.5 m above the spray boom. The onboard computer received the video streams captured by the cameras, executed deep learning-based target detection and precision target spraying strategy in real time, and transmitted control commands to the controller via serial communication.

The pesticide supply unit mainly consisted of a pesticide tank, a filter (Kaiping WOEN Sanitary Ware Co., Ltd., Kaiping, China), a pump (Dafengda 5G-210, Chaozhou, China), a buffer tank (TY-11-0.5G-5, Taizhou Tianyang Electrical Co., Ltd., Taizhou, China), a flow sensor (Shanghai Weill Instrument Co., Ltd., Shanghai, China), and a pressure sensor (MIK-P300, Hangzhou MEACON Automation Technology Co., Ltd., Hangzhou, China). The filter was installed upstream of the pump to remove impurities from the pesticide solution. The pump was used to pressurize the spray liquid and deliver it to the nozzles for atomization. The buffer tank was used to attenuate pressure fluctuations in the liquid flow, thereby ensuring stable spray pressure. The flow sensor was used to measure the real-time flow rate in the pipeline. The pressure sensor was used to monitor the pressure of the spraying system in the range of 0–1.0 MPa, with a measurement accuracy of 0.005 MPa.

The spray execution unit consisted of a controller, solenoid valves (2V025, AirTAC International Group, Ningbo, China), MOSFET-based valve driver circuits, an incremental encoder (E6B2-CWZ3E, VEHA Corporation, Shenzhen, China), and nozzles (model 2501, Dongguan Wuyuan Spraying and Purification Technology Co., Ltd., Dongguan, China). The controller was based on an STM32F103ZET6 microcontroller (Guangzhou Xingyi Electronic Technology Co., Ltd., Guangzhou, China). The solenoid valve controlled the opening and closing of the nozzle at a voltage of DC 24 V and a pressure range of 0–1.0 MPa, with a maximum switching frequency of 10 Hz. In the de-energized state, the solenoid valve remained closed under the action of the spring. When the solenoid coil was energized, the valve core was rapidly attracted, switching the valve to the open state and enabling spray on/off operation. The MOSFET-based valve driver circuits converted the control signals from the controller into driving signals for the solenoid valves. The incremental encoder was used to measure the forward speed of the sprayer. Flat-fan stainless-steel nozzles with a spray angle of 25° were used, with a nozzle spacing of 15 cm. When the solenoid valves were activated, the pesticide solution flowed through the nozzle, enabling precision target spraying.

The traveling unit consisted of a liftable spray boom, chassis, steering system, battery (60 V), and drive motors. A four-wheel steering mode was adopted to enhance maneuverability under field conditions. The spray boom had a working width of 3 m. Detailed technical parameters of the sprayer are summarized in Table 1.

During operation, the cameras capture field images and transmit them to the onboard computer. The computer preprocesses the images and performs target detection using a pre-trained deep learning model. Based on the detection results, decisions are made regarding the opening and closing of the solenoid valve assembly. These control signals are transmitted in real time to the spray execution unit via serial communication as data frames. The controller of the spray execution unit parses the data frames, sets the corresponding control pins to the low or high level, and, after processing by the valve driver circuit, actuates the solenoid valves. Consequently, the pesticide solution is sprayed from the nozzles, enabling precision target spraying. Meanwhile, the buffer tank of the pesticide

https://doi.org/10.3390/agriculture16040395

supply unit mitigates pressure fluctuations in the pipeline caused by intermittent spraying, maintaining a constant supply pressure and ensuring stable nozzle atomization quality. The schematic diagram of the main components of the target spraying system is shown in Figure 2.

Table 1. Technical parameters of the self-propelled boom sprayer.

Parameter	Value
Overall dimensions (mm)	2000 × 3000 × 1500
Maximum operating speed (km·h^{-1})	8
Total weight (kg)	450
Pesticide tank capacity (L)	200
Spray boom width (mm)	3000
Ground clearance (mm)	800
Drive motor power (W)	1600
Battery pack voltage (V)	60

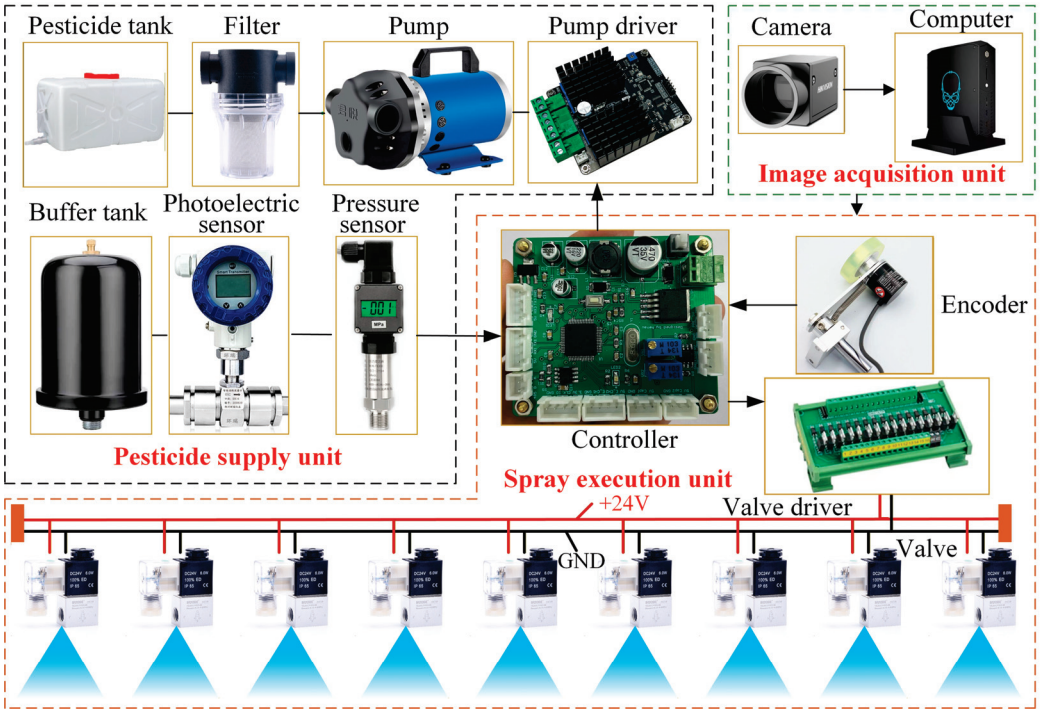

Figure 2. Schematic diagram of the main components of the target spraying system.

2.2. Weed Detection Method

2.2.1. Image Acquisition

Field image data were collected at three locations in Henan Province in July 2022: Yuan Zhuang Village, Suixian County (34.136° N, 115.343° E); Zhou Zhuang Village, Linying County (33.774° N, 113.837° E); and the experimental field at the Changyuan Branch of the Henan Academy of Agricultural Sciences (35.428° N, 114.289° E). All experiments were carried out in non-GMO soybean fields at the early post-emergence stage (V1–V2, one- to two-trifoliate leaf stage). Weed samples in soybean fields are shown in Figure 3. The images were captured using a smartphone (Redmi K30 Pro, Xiaomi Corporation, Beijing, China) in JPEG format with a resolution of 1440 × 1080 pixels. The weed species collected was *Cirsium setosum* (also known as *Cirsium arvense* var. *integrifolium*). The dataset included images taken under various weather conditions, such as sunny, cloudy, and post-rain, as well as different land backgrounds, including bare soil and wheat stubble fields. These

images exhibit diversity in environmental lighting and background conditions, which enhances the generalization ability of the trained model.

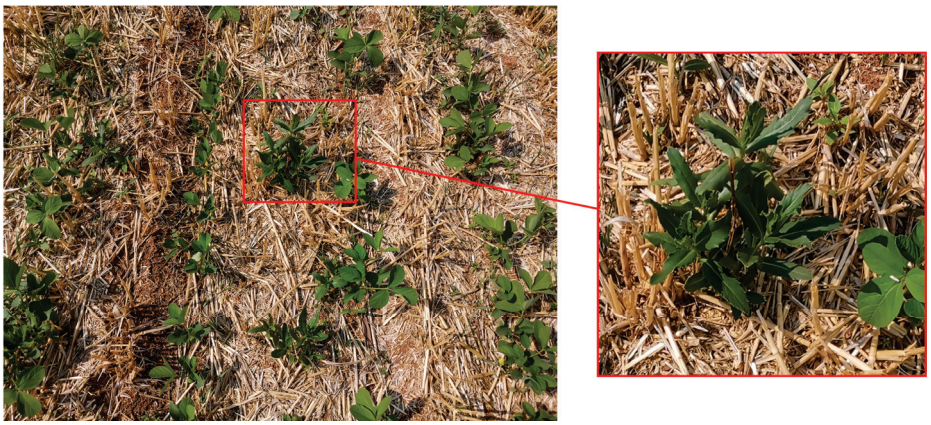

Figure 3. Weed samples in Soybean Fields.

2.2.2. Data Augmentation

To improve the generalization ability of the model, data augmentation was applied to increase the diversity and size of the original dataset [49]. Mosaic online data augmentation was employed during model training. This technique involves randomly cropping and concatenating multiple images to create a new training sample, referred to as a mosaic sample, which contains multiple objects and backgrounds. During training, the model learns to detect and classify these different targets while distinguishing their relationships with the background. Mosaic augmentation also reduces dependence on the training data, mitigates the risk of overfitting, and improves model performance. Weed-labeled images after mosaic augmentation are shown in Figure 4.

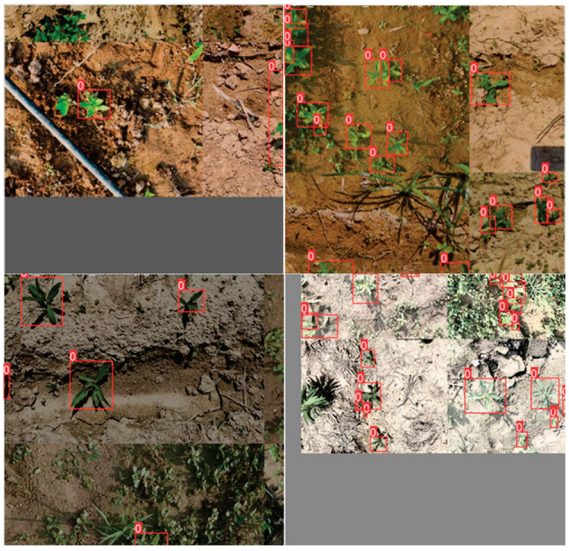

Figure 4. Images after mosaic augmentation.

In this study, a total of 3200 images were annotated using the CVAT image annotation tool. The annotated dataset was then randomly divided into training, validation, and test sets at a ratio of 7:1:2, resulting in 2240 images for the training set, 320 images for the validation set, and 640 images for the test set. These subsets were subsequently used for model training and evaluation.

2.2.3. Weed Detection Model Based on YOLOv5-MobileNetv3-SE

This study is based on the YOLOv5 object detection algorithm. The extensive convolutional operations in the CSPDarknet backbone of YOLOv5 require substantial computational resources and time, which makes it unsuitable for deployment on resource-constrained edge devices [50]. To improve efficiency, the model was lightened by replacing the CSPDarknet backbone with the more lightweight MobileNetV3 model, reducing computational load and model size. MobileNetV3 is constructed using depthwise separable convolutions and inverted residual blocks with linear bottlenecks, which significantly reduce the number of parameters and floating-point operations while preserving feature extraction capability. Additionally, given the complexity of field images and the small size of some weed targets, which may lead to misdetections or missed detections, an SE (Squeeze-and-Excitation) attention module was added after each of the three output layers of the backbone network. The attention mechanism, similar to human visual selective attention, selects the most relevant information for the task, suppresses irrelevant data, and increases the weight of useful features. This enables the network to automatically learn and improve computational efficiency, enhance the weight of effective feature channels, and focus on important features, ultimately improving the accuracy of small-target weed detection. Specifically, the SE module first performs a squeeze operation using global average pooling to capture global channel-wise contextual information. This is followed by an excitation operation implemented through fully connected layers to generate channel-wise weighting coefficients. These weights are then applied to the original feature maps to adaptively enhance important feature channels while attenuating irrelevant ones, ultimately improving the detection accuracy of small weed targets in complex field environments. The network takes 640 × 640 RGB images as input, and its output consists of three tensors of different sizes: 80 × 80 × 255, 40 × 40 × 255, and 20 × 20 × 255, corresponding to detection layers with strides of 8, 16, and 32, respectively. In each feature map, the dimension "255" represents the prediction vector at each spatial location, which is generated based on five preset anchors and consists of 4 bounding box coordinates, 1 objectness confidence score, and 50 class probabilities (i.e., 5 × (4 + 1 + 50)). The Architecture of the improved model is shown in Figure 5.

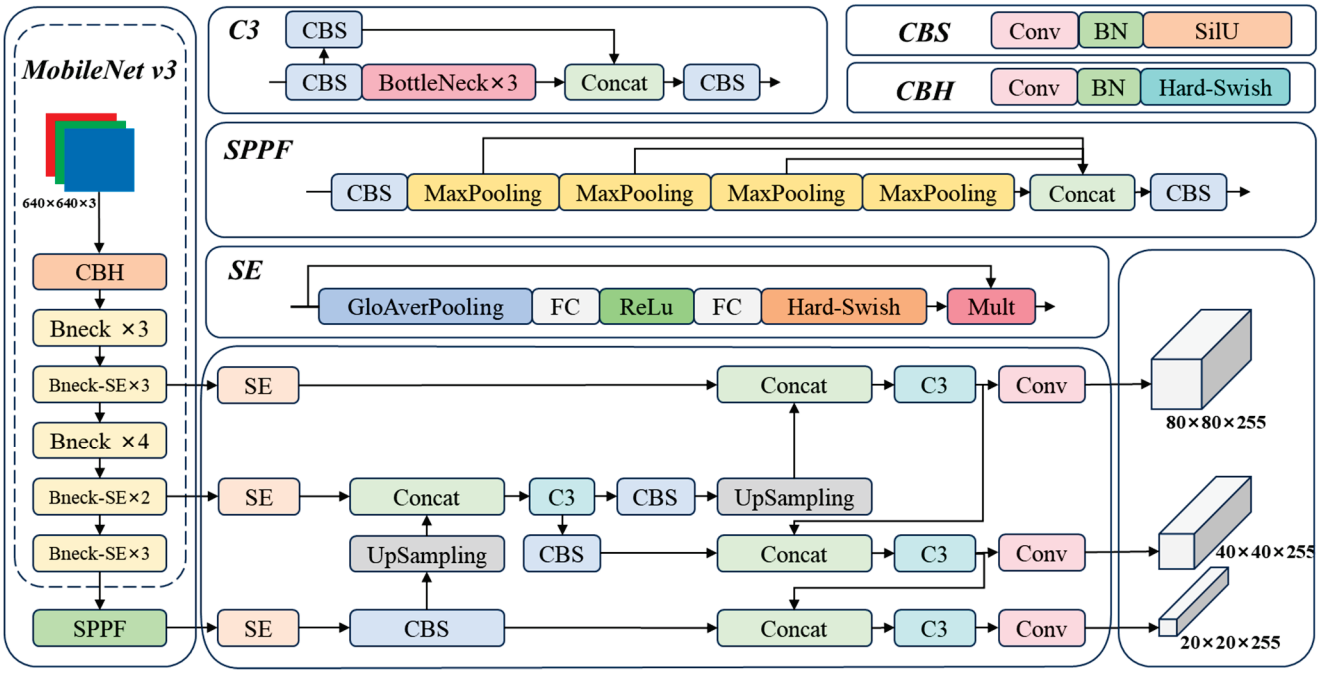

Figure 5. Architecture of the weed detection model based on YOLOv5-MobileNetv3-SE.

2.2.4. Model Training and Parameter Settings

The hardware environment used for model training in this study consists of an NVIDIA GeForce RTX 3090 GPU with 24 GB of VRAM, an Intel® Core™ i9-12900K processor, and 64 GB of RAM. The software environment includes the Windows 10 operating system, Python 3.7, PyTorch 11.7.1, CUDA 11.5, and PyCharm 2020. The input image size was set to 640 × 640, with padding applied to maintain the original aspect ratio. The initial learning rate was set to 0.1, and a cosine annealing schedule was used during training. The Adam optimizer was employed for model optimization, and the model was trained for 300 epochs. Model convergence was assessed by monitoring the loss value during training and the variation in mAP curves on the validation set. Once convergence was achieved, the weights corresponding to the lowest loss in the final training epochs were selected as the trained model.

2.3. Precision Target Spraying Strategy

Based on the weed detection results obtained by the proposed YOLOv5-MobileNetv3-SE model, a precision target spraying strategy was developed to achieve accurate synchronization between target position and spray actuation. The overall strategy consisted of a grid-based matching spraying algorithm, system time delay analysis, and a time-delay compensation method.

2.3.1. Grid-Based Matching Spraying Algorithm

Line-crossing detection algorithms have been widely used in applications such as video surveillance and traffic safety, where targets are identified by determining whether they cross predefined virtual lines, enabling effective monitoring and management of designated regions [51,52]. Based on this concept, an improved grid-based matching spraying algorithm was proposed in this study. The algorithm established a correspondence between the targets detected by the image acquisition unit and the spray nozzles mounted on the boom, thereby determining which nozzles should be activated and when they should be triggered. Based on this matching relationship, control data frames for the solenoid valve array were generated and transmitted to implement an on–off control strategy, whereby each solenoid valve was switched on or off according to the algorithm decision results. This enabled precise regulation of solenoid valve opening and closing, ultimately achieving accurate target spraying.

The specific implementation of the proposed algorithm is illustrated in Figure 6. A series of grids is overlaid on the image plane, where each grid corresponds one-to-one with a solenoid valve on the spray boom. The width of each grid is set equal to the average spray width of a single nozzle, while the grid height is fixed at 60 pixels. During forward operation of the boom sprayer, images move downward in the image frame. The deep learning-based target detection algorithm continuously detects weed targets and generates regions of interest (ROIs), which are represented by red bounding boxes. When an ROI overlaps with a grid, it indicates that the target has entered the spraying area of the corresponding nozzle. The intersection area between each grid and the ROI is calculated. If the intersection area exceeds a predefined threshold, the corresponding grid is assigned a value of 1, indicating that the solenoid valve should be activated for spraying; otherwise, it is assigned a value of 0, indicating that the valve remains closed. In this study, the threshold is set to 20% of the grid area.

https://doi.org/10.3390/agriculture16040395

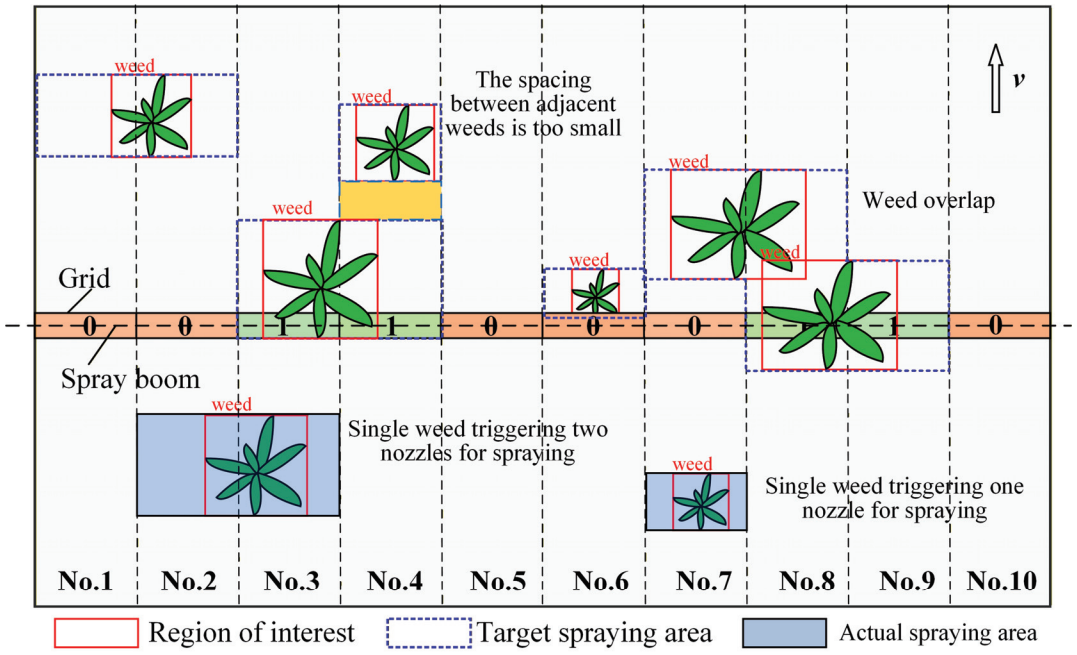

Figure 6. Schematic diagram of the grid-based matching spraying algorithm.

Several spatial relationships between ROIs and grids may occur during operation. When the ROI of a single weed intersects with only one grid, a single nozzle is activated. When the ROI intersects with two or more grids, multiple nozzles are activated simultaneously. In cases where multiple weeds overlap spatially, the resulting ROIs intersect multiple grids, and the corresponding solenoid valves are activated accordingly. Furthermore, due to the inherent opening and closing response time of the solenoid valves during practical operation, a continuous spraying strategy is adopted when adjacent weeds are closely spaced along the forward travel direction. Specifically, if the longitudinal spacing between adjacent weeds is shorter than the effective spraying distance corresponding to the valve response time, the grid control signal is maintained at 1 (as indicated by the yellow region in Figure 6), ensuring uninterrupted spraying and preventing missed targets. This effective spraying distance is determined by the product of the sprayer's forward speed and the measured solenoid valve response time, thereby defining a clear distance threshold for continuous spraying. In this study, each camera is responsible for controlling ten nozzles. Data exchange between the onboard computer and the controller is performed via serial communication.

2.3.2. System Time Delay Analysis

In the above analysis, it is assumed that the grid positions coincide with the locations of the spray boom within the camera field of view. Accordingly, when the intersection area between the ROI and a grid exceeds a predefined threshold, the onboard computer sends an opening signal to the corresponding solenoid valve. However, during actual operation, a certain amount of time is required from the moment the control command is issued by the computer to the moment when pesticide droplets are deposited on the weeds. This time delay causes a longitudinal offset between the actual spraying region and the target spraying region, resulting in the missed spraying region in precision target spraying applications, as illustrated in Figure 7.

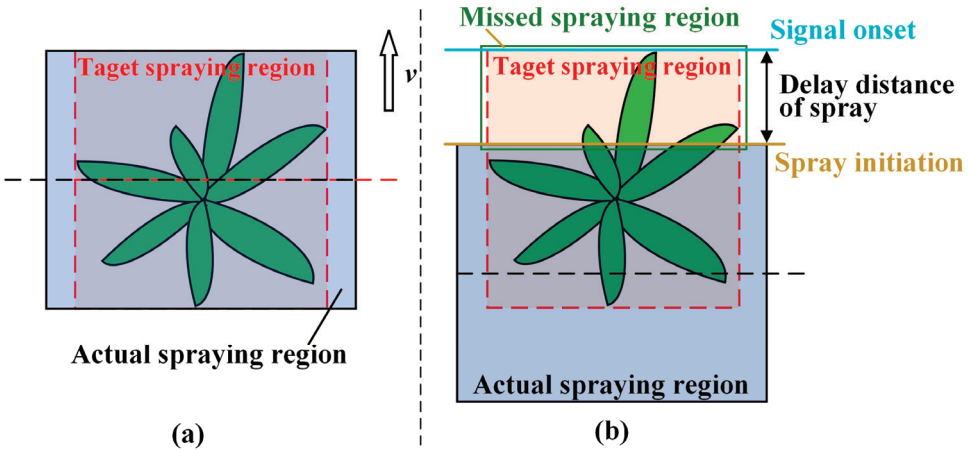

Figure 7. Spray lag caused by system time delay. (**a**) Ideal spraying condition, where the actual spraying region coincides with the target spraying region. (**b**) Spray lag induced by system time delay, resulting in missed spraying region.

Further analysis indicates that the total system time delay in the target spraying process mainly consists of three components: image processing delay, communication and control delay, and spray deposition delay. Therefore, it is necessary to quantitatively measure each delay component through dedicated experiments to determine the overall system latency. The resulting total delay can then be used to compensate for the spraying lag by adjusting the spatial offset distance, thereby reducing spray omission and improving target spraying accuracy.

1. Image processing delay

The image processing delay mainly originated from the inference time required by the deep learning-based weed detection model. Although the target detection model was lightweighted in this study to reduce computational complexity, the delay introduced by image processing remained non-negligible. To quantify the image processing delay, the trained detection model was deployed on the onboard computer. A total of 200 field-acquired images were processed using a weed detection model based on YOLOv5-MobileNetv3-SE. The total inference time was measured as 5.58 s, corresponding to an average processing time of 27.9 ms per image.

2. Communication and control delay

The communication and control delay referred to the time consumed from the moment when the onboard computer transmitted a control command to the moment when the microcontroller decoded the data frame, set the corresponding control pins, and output the driving voltage through the solenoid valve driver circuit to actuate the solenoid valve. To measure the communication and control delay, a single-channel solenoid valve control setup was constructed, consisting of a microcontroller, a solenoid valve driver board, and a solenoid valve, as shown in Figure 8. A valve-opening command was transmitted from the onboard computer using serial communication debugging software to trigger the opening of the solenoid valve. Meanwhile, a digital oscilloscope (TBS1102C, Tektronix, Inc., Beaverton, OR, USA) was used to monitor the signals. One channel of the oscilloscope was connected to the serial input pin of the microcontroller, while the other channel was connected to the output terminal of the solenoid valve driver board. By capturing and comparing the waveforms from the two channels, the time difference between the input control signal and the output driving voltage was determined. The results showed that the time interval from the reception of the first pulse signal at the microcontroller serial port to the output of the 24 V driving voltage by the solenoid valve driver board was 6.37 ms.

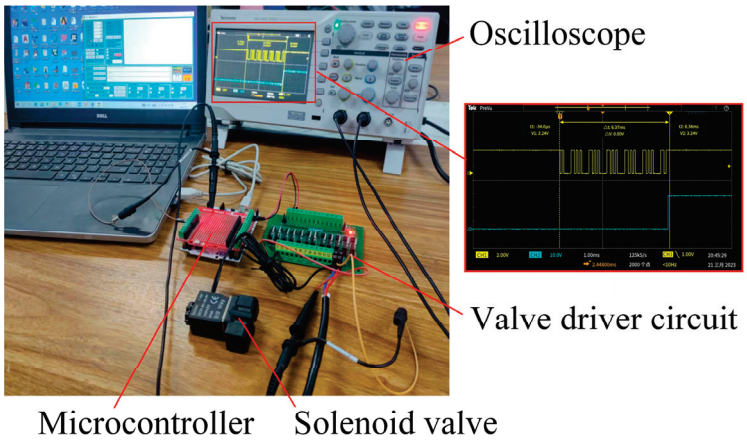

Figure 8. Measurement of the communication and control delay.

3. Spray deposition delay

The spray deposition delay referred to the time interval from the moment when the solenoid valve received the driving signal from the driver board and initiated opening to the moment when the pressurized pesticide was atomized through the nozzle, traveled through the air, and finally deposited onto the weed. In this study, the spray process was captured using a high-speed camera, and the deposition delay was determined through frame-by-frame image analysis, as shown in Figure 9. The high-speed camera operated at a frame rate of 960 frames per second, corresponding to a temporal resolution of 1.04 ms per frame. To accurately determine the initial moment when the solenoid valve was energized, a green indicator light was installed above the solenoid valve. The indicator illuminated simultaneously with valve energization and turned off when the power was cut, thereby serving as a reference for the timing of valve coil energization and de-energization. A container filled with water dyed with carmine was placed beneath the nozzle. When spray droplets reached the water surface, visible surface disturbances were generated, which were used to identify the moment when the droplets arrived at the target surface.

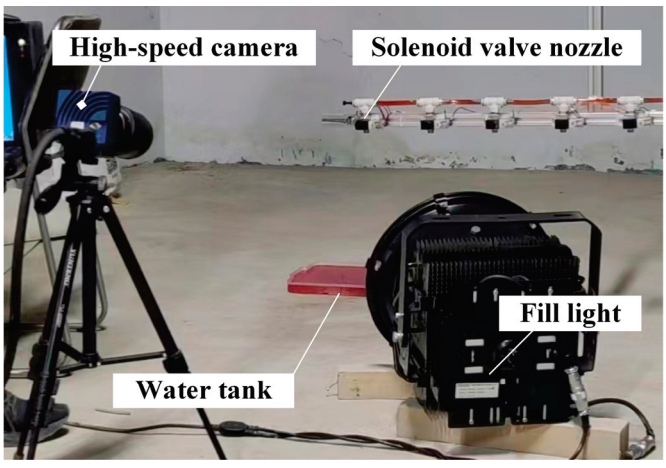

Figure 9. Measurement of the spray deposition delay.

During the experiment, the spray pressure was set to 0.3 MPa, and the nozzle height above the ground was 50 cm. The solenoid valve was briefly energized to generate a single intermittent spraying event. The spraying process was recorded using a high-speed camera, and the corresponding image frames are shown in Figure 10. The spraying sequence was divided into six key stages: signal onset, spray initiation, droplet arrival at the ground, continuous spraying, signal termination, and spray termination. The frame in

which the indicator light switched from off to on was defined as frame 0. Spray droplets were first observed emerging from the nozzle at frame 6. At frame 35, visible ripples appeared on the water surface in the collection tray placed on the ground, indicating that the droplets had reached the ground surface. Continuous spraying was maintained until frame 43, when the indicator light began to turn off. Subsequently, the ripples on the water surface gradually weakened and nearly disappeared by frame 90, marking the end of the intermittent spraying event. Based on the frame intervals, the elapsed time from the indicator light turning on to the initial droplet ejection was approximately 6.24 ms, while the droplet travel time from the nozzle to the ground was approximately 36.40 ms. After the control signal was terminated at 44.72 ms, spraying continued until 93.60 ms, resulting in a solenoid valve closing delay of 48.88 ms from the open to the closed state. Therefore, the spray deposition delay was determined to be 36.40 ms.

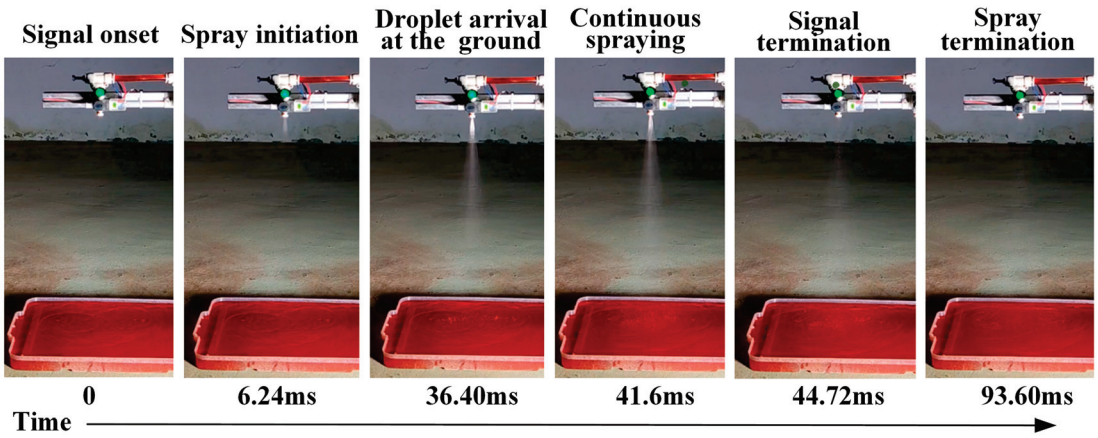

Figure 10. High-speed camera image sequence of the spraying process.

Based on the above experimental measurements, the total system time delay of the precision target spraying system was determined to be 70.67 ms.

2.3.3. Time-Delay Compensation Method

In the camera field of view, the grid position determines the triggering timing of the solenoid valves. As discussed above, when the grid position coincides with the actual spray boom position, an overlap between the grid and the ROI leads to mistimed spraying due to system time delay, resulting in spray misalignment or missed spraying. Therefore, advancing the grid position relative to the spray boom to trigger the solenoid valve earlier effectively compensates for the system time delay, thereby reducing spray omission and improving the precision of target spraying. A schematic illustration of the time-delay compensation method is shown in Figure 11. A planar coordinate system XOY is established, in which the center of the camera field of view is defined as the X-axis and the forward traveling direction of the sprayer is defined as the Y-axis. The distance between the nozzle and the camera along the forward direction is denoted as e. When the target spraying system is stationary, the grid centerline L_2 coincides with the spray centerline L_1, ensuring that the pesticide droplets accurately deposit onto the target. During forward operation, the grid is shifted upward in the image by a certain distance, allowing the predicted bounding box to intersect the grid earlier and thereby compensating for the system delay. Consequently, the relative distance g between the matching grid centerline L_2 and the Y-axis in the world coordinate system can be expressed as:

$$g = d - e \tag{1}$$

where d is the distance between the grid centerline and the spray centerline (m). The distance e represents the separation between the nozzle and the camera along the forward traveling direction (m), which was set to 0.1 m in this study.

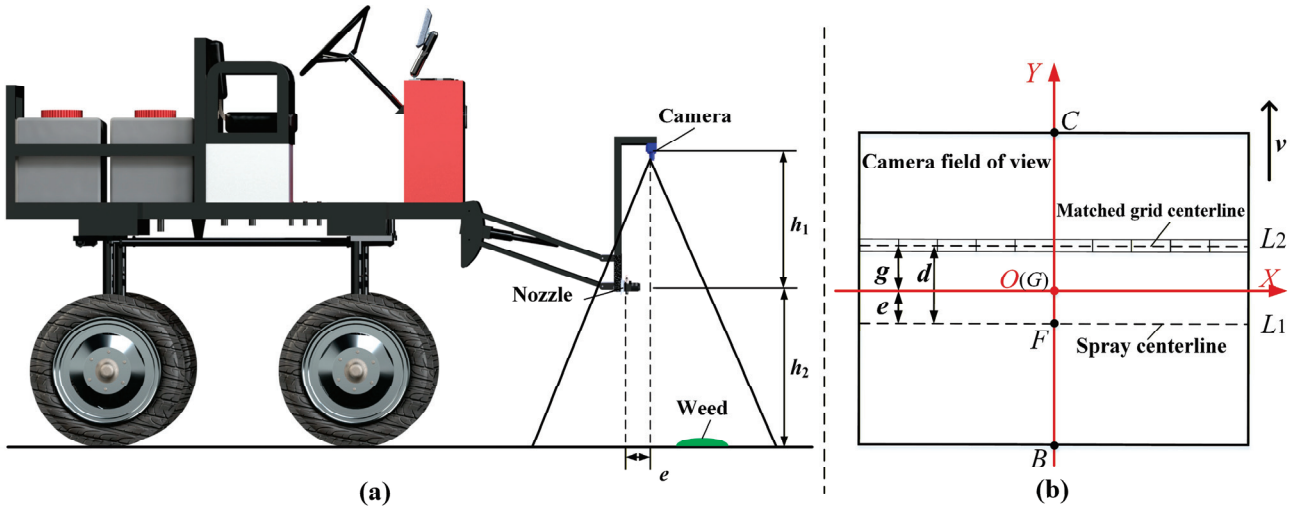

Figure 11. Schematic illustration of the delay compensation method: (**a**) main view; (**b**) relative positions of the grid centerline and the spray centerline in the camera field of view.

The value of d is determined by the system delay time and the forward speed of the sprayer.

$$d = v \cdot t \tag{2}$$

where v is the real-time forward speed of the sprayer (m·s^{-1}), and t represents the total delay time (s). Based on the above experimental measurements, t was determined to be 70.67 ms. The real-time forward speed of the sprayer was obtained using an incremental encoder.

The incremental encoder is coaxially mounted on the sprayer wheel. Given the known wheel diameter and the encoder resolution of 1000 pulses per revolution, the real-time forward velocity v of the sprayer is calculated by counting the number of encoder pulses within a fixed sampling interval. The sprayer velocity is computed as

$$v = \frac{n}{N} \cdot \frac{\pi D}{\Delta t} \tag{3}$$

where n is the number of pulses detected during the sampling interval Δt, N is the encoder resolution (1000 pulses per revolution), and D is the wheel diameter (m).

Accordingly, the grid position in the image is dynamically adjusted according to the sprayer speed to advance the opening timing of the solenoid valves, thereby achieving accurate alignment between the spray deposition area and the target region.

To implement the grid-based matching algorithm, the compensated grid position is first transformed from the world coordinate system to the pixel coordinate system. Subsequently, an intersection calculation is performed between the transformed grid and the pixel coordinates of the ROI obtained from target detection. The grid state (1 or 0) is then determined to control the opening and closing of the corresponding solenoid valves. Through this dynamic grid adjustment strategy, accurate alignment between the spray deposition area and the target spraying region is achieved. The world coordinate system is a three-dimensional Cartesian coordinate system used to describe the spatial relationship between the camera and observed objects, whereas the pixel coordinate system is defined on the image plane output by the camera and is used to represent pixel locations in the

https://doi.org/10.3390/agriculture16040395

image. In this study, the world coordinate system is denoted as *OXYZ*, where the *Z*-axis points toward the camera viewing direction, the *X*-axis points to the right side of the image, and the *Y*-axis points downward, as shown in Figure 12. A spatial point *P* in the world coordinate system is represented as $[X, Y, Z]^{\mathrm{T}}$. The pixel coordinate system corresponding to the camera imaging process is denoted as *ouv*, with the origin *o* located at the upper-left corner of the image. The *u*-axis is parallel to the *X*-axis, and the *v*-axis is parallel to the *Y*-axis. Accordingly, the pixel coordinates of point *P* on the image plane can be expressed as $p[u, v]^{\mathrm{T}}$.

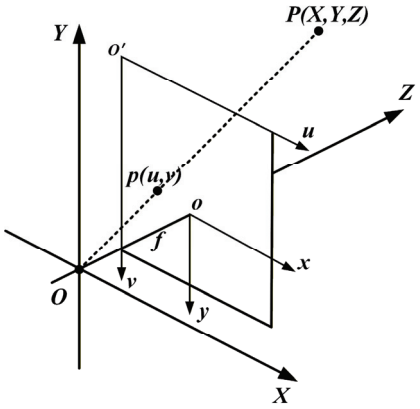

Figure 12. Schematic diagram of the transformation between the world coordinate system and the pixel coordinate system.

According to the pinhole camera model, the relationship between the world coordinate system and the pixel coordinate system can be expressed as follows:

$$Z\begin{pmatrix} u \\ v \\ 1 \end{pmatrix} = \begin{pmatrix} f_x & 0 & c_x \\ 0 & f_y & c_y \\ 0 & 0 & 1 \end{pmatrix}\begin{pmatrix} X \\ Y \\ Z \end{pmatrix} = K \cdot P \tag{4}$$

Here, the matrix composed of the intermediate parameters represents the intrinsic parameter matrix *K* of the camera. In this study, the camera was calibrated using Zhang's calibration method. The calibration results indicate that the focal lengths in the horizontal and vertical directions are approximately 1205.5 pixels, and the principal point is located near (759.8, 558.7) in the image plane. The camera is mounted above and slightly ahead of the spray nozzle. The width of the field of view on the ground is related to the lens viewing angle and the installation height, as described below.

$$Z = h_1 + h_2 \tag{5}$$

where h_1 is the installation height of the spray nozzle (m) and h_2 is the installation height of the camera relative to the nozzle (m). In this study, the nozzle installation height was set to 0.5 m, and the camera was mounted 0.5 m above the nozzle. Consequently, the pixel coordinates of point *p* in the image plane can be obtained.

The above analysis mainly aims to ensure that the onset of the actual spraying region coincides with that of the target spraying region. High-speed camera observations of the spraying process indicate that, after the stop signal is issued, spray droplets continue to be discharged for a short duration before completely ceasing, resulting in overspray at the end of the spraying operation, as illustrated in Figure 13. Therefore, to ensure that the termination of spraying accurately coincides with the target area, the stop signal must be issued in advance during the fitting of the weed prediction bounding box, as

https://doi.org/10.3390/agriculture16040395

shown in Figure 7a. Accordingly, the length L of the actual target spraying region can be expressed as:

$$L = L_{ROI} - v \cdot t_0 \tag{6}$$

where L_{ROI} is the length of the ROI fitted by the deep learning-based detection algorithm after target recognition, and t_0 is the time interval from the issuance of the stop signal to the complete cessation of spraying, measured as 48.88 ms (Figure 10). With this advance stopping strategy, the termination position of the actual spraying precisely coincides with the target spraying region.

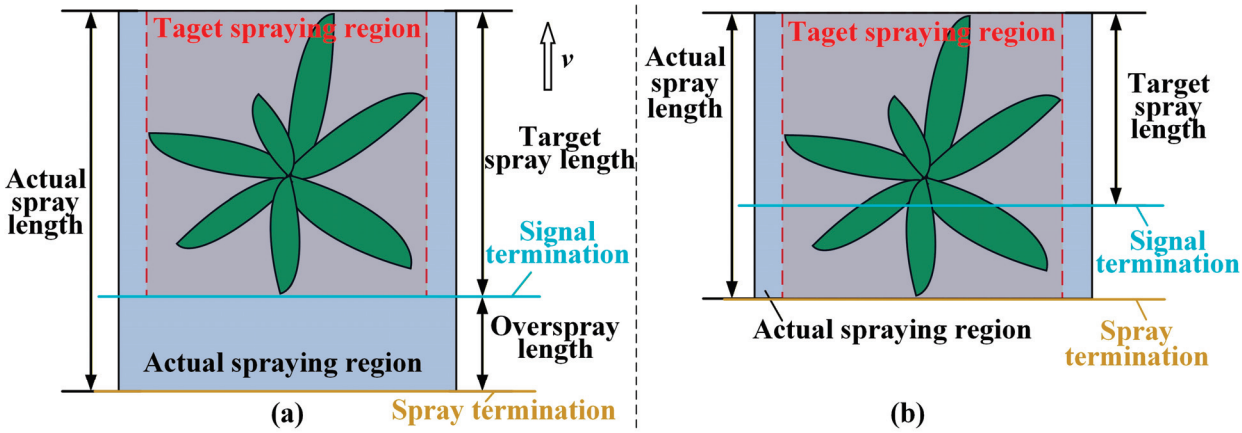

Figure 13. Schematic diagram of overspray compensation: (**a**) Overspray occurring after the stop signal; (**b**) Compensation achieved by advancing the stop signal.

The overall control flow chart of the target spraying system is illustrated in Figure 14.

2.4. Evaluation Experiments

An experimental evaluation of the target spraying system was conducted using both laboratory and field experiments. The laboratory experiments primarily assessed model recognition performance, target spraying accuracy, pesticide reduction rate, and spray distribution uniformity. The laboratory test platform, shown in Figure 15, consisted of a rail system, a power supply module, an electric rail vehicle, and the target spraying system. The platform had a maximum load capacity of 150 kg, a maximum forward speed of 8 km·h^{-1}, and an adjustable spray boom height ranging from 0 to 120 cm.

2.4.1. Model Detection Performance

An experimental evaluation was conducted to assess the weed recognition performance of the trained YOLOv5-MobileNetv3-SE model. The evaluation metrics included precision (P), recall (R), and mean average precision at 0.5 intersection over union (mAP@0.5), model size, and frames per second (FPS).

$$P = \frac{TP}{TP + FP} \tag{7}$$

$$R = \frac{TP}{TP + FN} \tag{8}$$

$$AP = \int_0^1 P_{\text{thresh}}(r)dr \tag{9}$$

$$mAP@0.5 = \frac{1}{N}\sum_{i=1}^{N} AP_i(IoU_{thresh} = 0.5) \tag{10}$$

where TP is true positive, FP is false positive, TN is true negative, and FN is false negative.

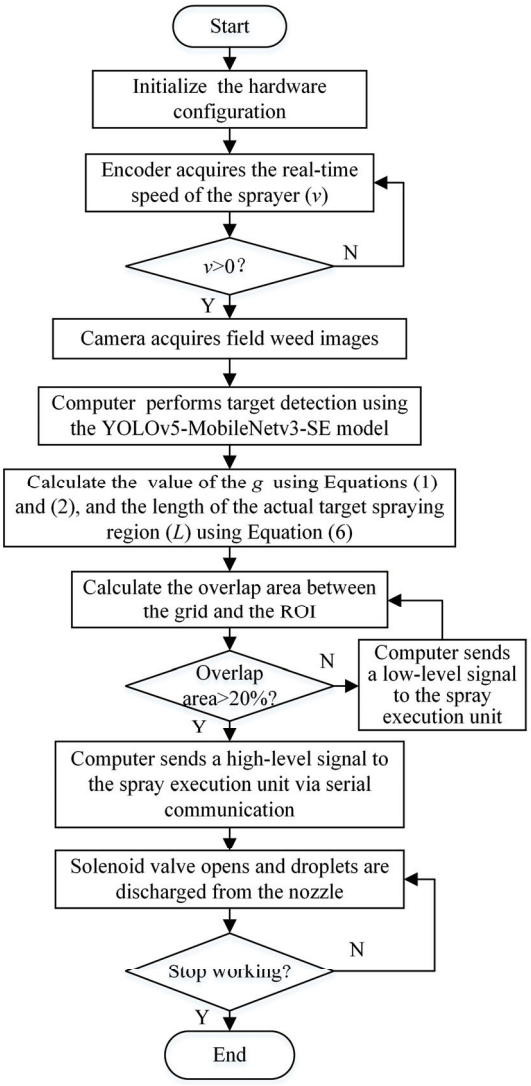

Figure 14. Control flow chart the target spraying system.

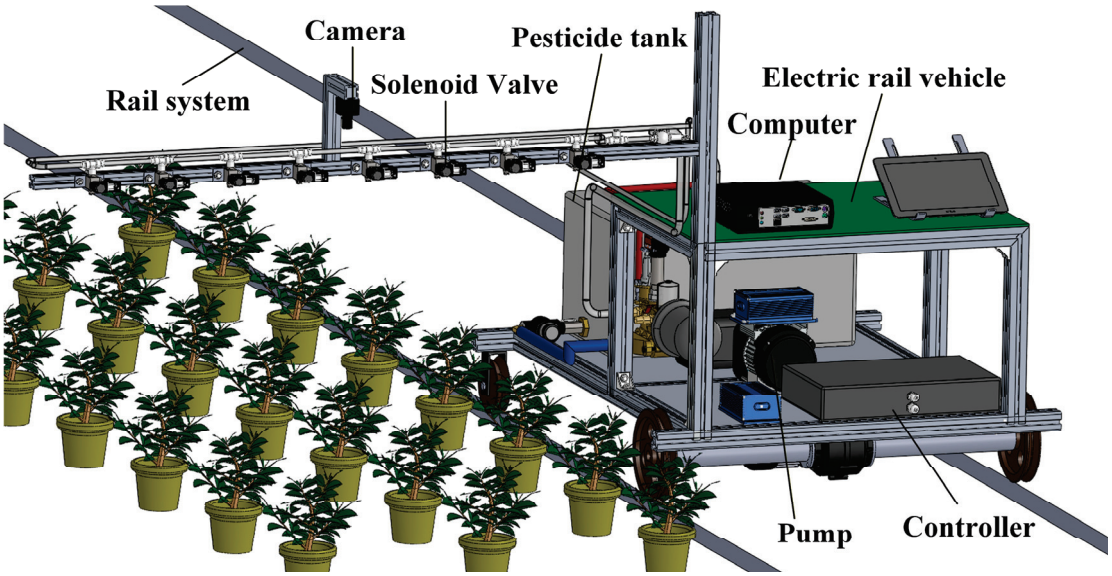

Figure 15. Laboratory test platform for precision target spraying.

To further evaluate the performance of the proposed model, comparative experiments were conducted with several classical deep learning-based detection models, including

Faster R-CNN, YOLOv3, YOLOv5s, and YOLOv5x. All models were trained using identical training strategies, data augmentation methods, and parameter settings, and were evaluated on the same experimental platform using the same dataset.

2.4.2. Target Spraying Accuracy

The laboratory test for target spraying accuracy is illustrated in Figure 16. Considering the acceleration and deceleration phases of the electric rail vehicle, the first and last 2 m of the track were excluded, and only the central 8 m section with constant speed was used for testing. The width of the test area was 1.2 m. To facilitate the experiments, plastic weed models were used to replace real weeds. Each plastic weed model was approximated as a circular projection on the ground with a diameter of 0.12 m, corresponding to a single-weed coverage area of 0.0113 m^2. With a weed coverage rate of 10%, a total of 85 plastic weed models were randomly distributed within the test area. Additionally, three rows of plastic soybean models (60 plants in total) were uniformly arranged as interference objects, with both row spacing and plant spacing set to 0.5 m. To determine whether spray droplets reached the weeds, a 2 cm × 2 cm water-sensitive paper was attached to the leaf of each plastic weed model. During the experiment, the forward speed of the electric rail vehicle was set to 1, 2, 3, and 4 $km \cdot h^{-1}$. The experimental metrics include weed detection accuracy rate (WDAR) and spraying accuracy rate (SAR).

$$WDAR = \frac{W_t}{W_a} \times 100\% \tag{11}$$

$$SAR = \frac{W_s}{W_a} \times 100\% \tag{12}$$

where W_a is the total number of weeds in the test area, W_t is the actual number of detected weeds, W_s the number of weeds effectively sprayed. Detection accuracy was determined by the appearance of a purple bounding box around the weed (Figure 16). For spraying accuracy, if the actual spray length covered at least 60% of the target spray length, the weed was considered successfully sprayed (Figure 13b).

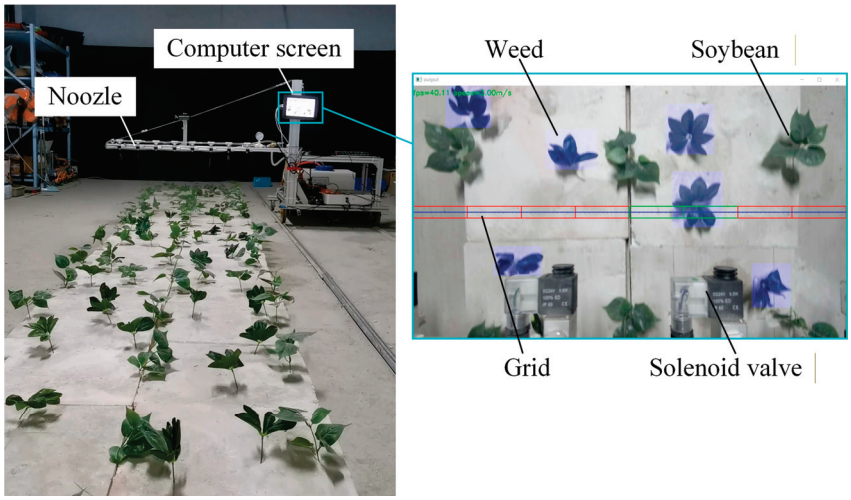

Figure 16. Laboratory test setup for evaluating target spraying accuracy.

2.4.3. Pesticide Reduction Rate

Precision target spraying can effectively reduce pesticide consumption compared to conventional full-coverage spraying. In this study, the pesticide reduction rate of target spraying under different weed coverage levels was evaluated by comparing it with conventional continuous spraying. Weed coverage is an important factor influencing the

pesticide reduction rate. To simulate different weed coverage scenarios, plastic weed models were used instead of real weeds. Each plastic weed model had an approximately circular ground projection with a diameter of 0.12 m, corresponding to an area of approximately 0.0113 m^2. Four simulated field environments with weed coverage rates of 5%, 10%, 15%, and 20% were established within a test area of 1.2 m × 5 m, corresponding to 13, 27, 53, and 106 weed models, respectively. The plastic weed models were randomly distributed within the experimental area. Water was used in the pesticide tank instead of actual pesticide, and target spraying experiments were conducted on the precision spraying test platform at a forward speed of 2 $km \cdot h^{-1}$. For each weed coverage level, 30 experimental runs were performed. Additionally, a control group was tested using conventional continuous spraying, in which all solenoid valves remained fully open, also repeated 30 times. After each test, the remaining liquid volume in the pesticide tank was recorded. The pesticide reduction rate S was calculated as the percentage reduction in liquid consumption achieved by precision target spraying compared with conventional continuous spraying:

$$S = \frac{Q_c - Q_t}{Q_c} \times 100\% \tag{13}$$

where Q_c and Q_t are the pesticide consumption under conventional continuous spraying and precision target spraying, respectively.

2.4.4. Spray Distribution Uniformity

The uniformity of pesticide droplet distribution directly affects the efficacy of pesticide application. The target spraying system is an upgraded version of traditional sprayers, retaining compatibility with conventional full-coverage spraying. In target spraying mode, ensuring even droplet distribution is crucial for optimal application effectiveness. Therefore, a droplet distribution scanner (SALVARANI, AAMS Co., Ltd., Maldegem, Belgium), as shown in Figure 17, was used to measure spray distribution uniformity. Each collecting channel of the scanner had a width of 10 cm, and a standard graduated cylinder equipped with a liquid level sensor was installed beneath each channel. The filling time of each cylinder was automatically recorded, enabling determination of the spray flow rate for each channel. The scanner was mounted on a motor-driven rail, allowing lateral movement beneath the spray boom to measure the overall transverse distribution of the spray volume.

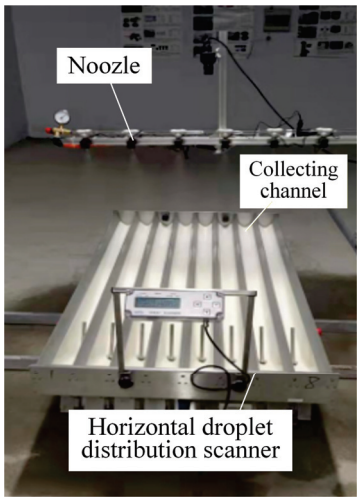

Figure 17. Horizontal droplet distribution scanner used to measure spray distribution uniformity.

The experiment was conducted in accordance with the requirements of the national standard GB/T 24677.1–2009 [53], China. Water was used as the test medium, and the

measurements were performed at a pressure of 0.3 MPa, a nozzle spacing of 15 cm, and a nozzle height of 50 cm above the ground. The coefficient of variation (CV) was employed to evaluate the spray distribution uniformity. A lower CV value indicates a more uniform distribution of spray volume along the boom.

$$\overline{q} = \frac{q_1 + q_2 + \cdots\cdots + q_n}{n} = \frac{\sum q}{n} \tag{14}$$

$$S = \sqrt{\frac{\sum q^2 - \frac{(\sum q)^2}{n}}{n-1}} \tag{15}$$

$$CV = \frac{S}{\overline{q}} \times 100\% \tag{16}$$

where q_i is the spray flow rate of the ith nozzle (L/min); n is the number of nozzles; $\overline{q}$ is the average spray flow rate (L/min); $\sum q$ is the total spray flow rate of the sprayer (L/min); S is the standard deviation (L/min). After three repeated tests, the CV of the nozzles was 5.9%. This value satisfies the requirement specified in GB/T 24677.1–2009 [53], which stipulates that the CV of spray volume distribution should be less than 20%.

2.4.5. Field Performance of Precision Target Spraying

To verify the field performance of the precision target spraying system, field experiments were conducted in Suixian City, Henan Province, China (34.136° N, 115.343° E). The experiment employed commonly used selective herbicides appropriate for the soybean seedling stage, with application rates strictly following pesticide registration safety regulations to ensure that the herbicides would not harm the soybean crops while evaluating system performance. Non-genetically modified soybeans at the seedling stage were used, planted using a conventional row spacing of 40 cm. All field tests were conducted under clear weather conditions with wind speeds below 2 m/s to minimize environmental interference and ensure accurate assessment of the system's performance. Within the experimental field, three rectangular plots, each measuring 20 m × 3 m, were delineated within the experimental field as sampling areas. The number of weeds and the dimensions of their bounding rectangles within each plot were recorded. Precision target spraying trials were conducted at forward speeds of 2, 3, and 4 km·h^{-1}. The field experimental setup and spraying process are illustrated in Figure 18.

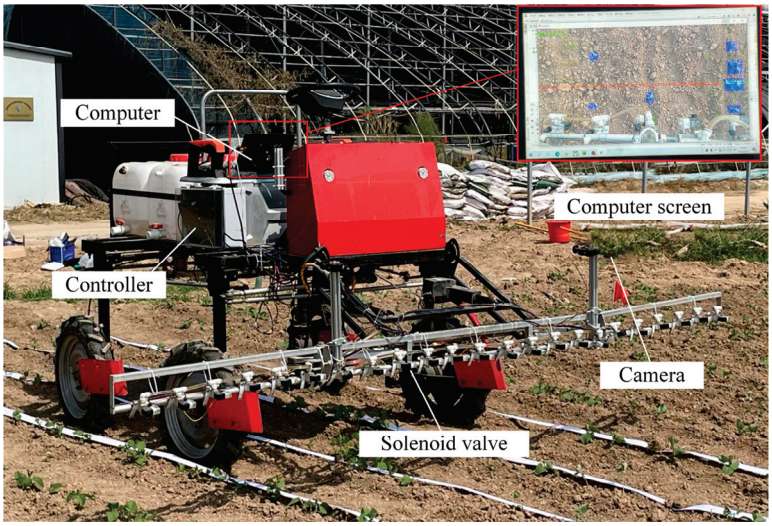

Figure 18. Field experiment setup of the target spraying device prototype.

A 2 cm × 2 cm water-sensitive paper was affixed to the leaves of each weed. The paper changed color to red upon contact with spray droplets, allowing verification of whether the pesticide effectively reached the target, as shown in Figure 19. The weed detection accuracy rate and spraying accuracy rate were then calculated using Equations (11) and (12), respectively.



Figure 19. Method for assessing spray coverage on weeds: (**a**) no droplet deposition; (**b**) droplet deposition indicating successful spraying.

3. Results and Discussion

3.1. Model Detection Performance

The detection results of different models are summarized in Table 2. The mAP@0.5 of YOLOv5-MobileNetv3-SE was 86.9%, which is slightly lower than YOLOv3, YOLOv5s, and YOLOv5x by 0.9%, 0.7%, and 1.3%, respectively, while outperforming Faster R-CNN by 6.0%. The model size of YOLOv5-MobileNetv3-SE was 7.5 MB, which is 46.4%, 95.6%, 93.8%, and 93.2% smaller than YOLOv5s, YOLOv5x, YOLOv3, and Faster R-CNN, respectively. The FPS of YOLOv5-MobileNetv3-SE was 38.17, which is 1355.2%, 46.5%, 27.7%, and 68.6% higher than YOLOv5s, YOLOv5x, YOLOv3, and Faster R-CNN, respectively. These results indicate that the proposed YOLOv5-MobileNetv3-SE model significantly reduces model complexity and improves real-time performance while incurring only a marginal loss in detection accuracy [54,55]. The superior performance can be attributed to the combination of the lightweight MobileNetv3 backbone, which reduces computational load, and the SE attention mechanism, which enhances feature representation for small or densely distributed weeds. Compared with standard YOLOv5 models, YOLOv5-MobileNetv3-SE achieves a better trade-off between detection accuracy, model size, and inference speed, which is particularly important for deployment on embedded or mobile platforms in precision agriculture.

Table 2. Comparison of different models.

Model	mAP0.5/%	Model Size/MB	FPS
Faster R-CNN	80.9	110.7	2.61
YOLOv3	87.8	120.6	26.04
YOLOv5s	87.6	14.0	29.85
YOLOv5x	88.2	169.0	22.67
YOLOv5-MobileNetv3-SE	86.9	7.5	38.17

There are several deployment strategies for deep learning models, including local deployment, cloud-based deployment, and hybrid deployment approaches [56]. In this

https://doi.org/10.3390/agriculture16040395

study, the trained model was deployed on the local onboard computer of the sprayer using TensorRT. TensorRT is a high-performance inference engine developed by NVIDIA that exploits GPU parallel computing to automatically optimize deep learning models through techniques such as layer fusion, weight compression, and quantization, thereby significantly accelerating the inference process. The improved YOLOv5-MobileNetv3-SE model was first converted into the ONNX format using the conversion scripts provided by the YOLOv5 framework. Subsequently, the ONNX model was converted into a TensorRT engine file, enabling efficient inference on the onboard computer.

3.2. Target Spraying Accuracy

The target spraying accuracy results are shown in Table 3. The weed detection accuracy rates were 98.88%, 97.64%, 94.11%, and 92.94% at forward speeds of 1, 2, 3, and 4 km·h^{-1}, respectively. At higher speeds, the time available for the model to detect and classify weeds was reduced, resulting in lower recognition accuracy because the model had less time to process each frame and make precise predictions. Additionally, higher speeds could introduce motion blur or reduced image resolution, further impairing the model's ability to accurately identify weeds. The target spraying accuracy rates were 97.64%, 95.29%, 90.58%, and 85.88% at forward speeds of 1, 2, 3, and 4 km·h^{-1}, respectively, showing a clear downward trend as speed increased. This reduction is consistent with previous studies on precision spraying, where higher forward speeds negatively affected both detection and spraying performance [30,38]. The decrease in spraying accuracy can be attributed to two main factors: first, reduced weed detection accuracy at higher speeds led to fewer weeds being correctly identified and sprayed; second, the increased forward speed negatively affected the precision target spraying strategy, causing deviations in droplet deposition and occasional off-target spraying.

Table 3. Target spraying accuracy test results at forward speeds of 1, 2, 3 and 4 km·h^{-1}.

Forward Speed (km·h^{-1})	Total Number of Weeds	Number of Detected Weeds	Number of Weeds Effectively Sprayed	Weed Detection Accuracy Rate (%)	Spraying Accuracy Rate (%)
1	85	84	83	98.88	97.64
2	85	83	81	97.64	95.29
3	85	80	77	94.11	90.58
4	85	79	73	92.94	85.88

3.3. Pesticide Reduction Rate

The pesticide reduction rates for precision target spraying and conventional continuous spraying under different weed coverage levels are presented in Table 4. The results indicate that precision target spraying achieved pesticide savings of 79.0%, 72.5%, 55.8%, and 48.6% at weed coverage rates of 5%, 10%, 15%, and 20%, respectively. As the weed coverage rate decreased, the pesticide-saving effect of precision target spraying became more pronounced, which aligns with the intended design of the system. The corresponding relative pesticide application rates of target spraying compared with continuous spraying were reduced to 21.0%, 27.5%, 44.2%, and 51.4% at weed coverage rates of 5%, 10%, 15%, and 20%, respectively. In all cases, the relative pesticide application rates exceeded the corresponding weed coverage rates. This is attributable to the system design, in which the spray coverage area was deliberately set larger than the ground-projected area of individual weeds to ensure complete droplet deposition on the targets (Figure 6). Overall, the experimental results demonstrate that precision target spraying can substantially reduce pesticide usage compared with conventional continuous spraying, particularly under conditions of low weed coverage.

https://doi.org/10.3390/agriculture16040395

Table 4. Pesticide reduction rates of precision target spraying under different weed coverage levels.

Weed Coverage Rate (%)	Pesticide Application Rate of Conventional Continuous Spraying (L)	Pesticide Application Rate of Precision Target Spraying (L)	Pesticide Reduction Rate (%)
5	13.8	2.9	79.0
10	13.8	3.8	72.5
15	13.8	6.1	55.8
20	13.8	7.1	48.6

3.4. Field Performance of Precision Target Spraying

The field test results of the precision target spraying system are summarized in Table 5. The weed detection accuracy rates were 95.40%, 92.41%, and 86.40% at forward speeds of 2, 3, and 4 km·h^{-1}, respectively, which decreases with increasing speed. As the forward speed increased from 2 km·h^{-1} to 4 km·h^{-1}, the weed detection accuracy rate decreased by 9%. The field test results showed a reduction in weed detection accuracy rate compared to the laboratory tests, with decreases of 2.29%, 1.81%, and 7.04%, respectively. The spraying accuracy rates were 90.80%, 86.20%, and 79.61% at forward speeds of 2, 3, and 4 km·h^{-1}, respectively, corresponding to decreases of 4.95%, 5.08%, and 7.87% relative to the laboratory experiments. These reductions in both detection and spraying accuracy can be attributed to several factors. Uneven field terrain combined with increased forward speed resulted in enhanced vibrations of the sprayer, which degraded image capture quality and reduced effective detection rates. The vibrations also amplified nozzle movements on the spray boom, causing misalignment between the nozzle and the target, thereby lowering spraying accuracy [30,38,55]. Additionally, environmental factors such as variations in lighting, background interference, and differences in weed appearance, along with motion blur and reduced image resolution at higher speeds, further affected the model's detection performance [39].

Table 5. Field test results of the precision target spraying system at forward speeds of 2, 3, and 4 km·h^{-1}.

Forward Speed (km·h^{-1})	Total Number of Weeds	Number of Detected Weeds	Number of Weeds Effectively Sprayed	Weed Detection Accuracy Rate (%)	Spraying Accuracy Rate (%)
2	87	83	79	95.40	90.80
3	145	134	125	92.41	86.20
4	103	89	82	86.40	79.61

4. Conclusions

This paper proposes a deep learning-based precision target spraying method for weed control in soybean fields at the seedling stage, and develops a grid-based matching spraying algorithm to synchronize target detection with spray actuation. Based on the detection model YOLOv5, a lightweight YOLOv5-MobileNetv3-SE model was designed by replacing the backbone feature extraction network and adding an attention mechanism. The improved model achieves an mAP@0.5 of 86.9%, a model size of 7.5 MB, and a frame rate of 38.17 frames per second. Compared to the original YOLOv5s model, the improved model reduced the size to 53.5% of the original while increasing the frame rate by 27.8%, with only minimal loss in detection accuracy. The laboratory test platform and prototype of the target spraying device were employed to evaluate the model detection performance, target spraying accuracy, pesticide reduction rate, and spray distribution uniformity. Laboratory results indicated that, within a forward speed range of 1–4 km·h^{-1}, the weed detection accuracy exceeded 92.94%, and the spraying accuracy exceeded 85.88%, meeting the precision target requirements. Pesticide reduction tests demonstrated that

https://doi.org/10.3390/agriculture16040395

target spraying achieved pesticide saving rates of 79.0%, 72.5%, 55.8%, and 48.6% at weed coverage rates of 5%, 10%, 15%, and 20%, respectively, with greater savings observed under lower weed coverage, consistent with the design expectations of the system. Spray distribution uniformity tests showed a coefficient of variation of 5.9%, satisfying the national standard GB/T 24677.1–2009 [53]. Field experiments further validated the system's performance, with weed detection accuracy and spraying accuracy exceeding 86.4% and 79.61%, respectively, at forward speeds of 2, 3, and 4 km·h^{-1}. Overall, these results demonstrate that the proposed method effectively balances model efficiency and detection accuracy, achieving precise spraying while significantly reducing pesticide usage. It should be noted that the experimental validation in this study was conducted using a single dominant weed species (*Cirsium arvense*), and therefore the conclusions are primarily applicable to scenarios involving this species under the tested field conditions. Future work will extend the proposed framework to multiple weed species and more complex field environments, further exploring its potential for practical and sustainable crop protection applications.

Author Contributions: Conceptualization, C.Y., C.G. and Z.H.; methodology, C.Y., Z.Y. and H.L.; formal analysis, C.Y., Q.D. and Z.H.; data curation, C.Y., S.C. and Z.H.; writing—original draft preparation, C.Y. and Z.H.; writing—review and editing, W.W. and H.L. All authors have read and agreed to the published version of the manuscript.

Funding: This research was funded by China Agriculture Research System of MOF and MARA, grant number CARS-04; the Postdoctoral Research Funding Program of Henan, grant number 24XM0495; the Science and Technology Project of Henan, grant number 242102111176; and the High-Level Talents Support Fund Program of Henan Agricultural University, grant number 30501404.

Institutional Review Board Statement: Not applicable.

Data Availability Statement: The original contributions presented in this study are included in the article. For further inquiries, please contact the corresponding author.

Acknowledgments: The authors would like to thank their schools and colleagues as well as those who funded the project. All support and assistance are sincerely appreciated.

Conflicts of Interest: The authors declare no conflicts of interest.

References

1. Rotundo, J.L.; Marshall, R.; McCormick, R.; Truong, S.K.; Styles, D.; Gerde, J.A.; Gonzalez-Escobar, E.; Carmo-Silva, E.; Janes-Bassett, V.; Logue, J.; et al. European soybean to benefit people and the environment. *Sci. Rep.* **2024**, *14*, 7612. [CrossRef]
2. Messina, M. Perspective: Soybeans Can Help Address the Caloric and Protein Needs of a Growing Global Population. *Front. Nutr.* **2022**, *9*, 909464. [CrossRef]
3. Majidi, M.; Salehian, H.; Rezvani, M.; Dorbeiki, M. Weed flora and wheat yield comparison in conventional (small grain cereals) and organic (soybean-wheat rotation) systems. *J. Agric. Food Res.* **2025**, *24*, 102324. [CrossRef]
4. Schatke, M.; Bensch, J.; Ulber, L.; Gerowitt, B.; Redwitz, C.v. Trait-based weed control decisions compared to economic thresholds for site-specific weed management. *Eur. J. Agron.* **2026**, *174*, 127946. [CrossRef]
5. Zhou, J.; Yang, Y.; Fang, Z.; Liang, J.; Tan, Y.; Liao, C.; Gong, D.; Liu, W.; Liu, G. Trends of pesticide residues in agricultural products in the Chinese market from 2011 to 2020. *J. Food Compos. Anal.* **2023**, *122*, 105482. [CrossRef]
6. Faraj, T.K.; EL-Saeid, M.H.; Najim, M.M.M.; Chieb, M.; Faraj, T.K.; EL-Saeid, M.H.; Najim, M.M.M.; Chieb, M. The Impact of Pesticide Residues on Soil Health for Sustainable Vegetable Production in Arid Areas. *Separations* **2024**, *11*, 46. [CrossRef]
7. He, X.; Bonds, J.; Herbst, A.; Langenakens, J. Recent development of unmanned aerial vehicle for plant protection in East Asia. *Int. J. Agric. Biol. Eng.* **2017**, *10*, 18–30. [CrossRef]
8. Ye, K.; Hu, G.; Tong, Z.; Xu, Y.; Zheng, J.; Ye, K.; Hu, G.; Tong, Z.; Xu, Y.; Zheng, J. Key Intelligent Pesticide Prescription Spraying Technologies for the Control of Pests, Diseases, and Weeds: A Review. *Agriculture* **2025**, *15*, 81. [CrossRef]
9. Teng, H.; Wang, Y.; Chatziparaschis, D.; Karydis, K. Adaptive LiDAR odometry and mapping for autonomous agricultural mobile robots in unmanned farms. *Comput. Electron. Agric.* **2025**, *232*, 110023. [CrossRef]

10. Wang, H.; Lin, Y.; Wang, Z.; Yao, Y.; Zhang, Y.; Wu, L. Validation of a low-cost 2D laser scanner in development of a more-affordable mobile terrestrial proximal sensing system for 3D plant structure phenotyping in indoor environment. *Comput. Electron. Agric.* **2017**, *140*, 180–189. [CrossRef]
11. Berk, P.; Stajnko, D.; Belsak, A.; Hocevar, M. Digital evaluation of leaf area of an individual tree canopy in the apple orchard using the LIDAR measurement system. *Comput. Electron. Agric.* **2020**, *169*, 105158. [CrossRef]
12. Mahmud, M.S.; Zahid, A.; He, L.; Choi, D.; Krawczyk, G.; Zhu, H.; Heinemann, P. Development of a LiDAR-guided section-based tree canopy density measurement system for precision spray applications. *Comput. Electron. Agric.* **2021**, *182*, 106053. [CrossRef]
13. Cao, H.L.S.X.S. SGTBN: Generating Dense Depth Maps From Single-Line LiDAR. *IEEE Sens. J.* **2021**, *21*, 19091–19100. [CrossRef]
14. Zeng, L.; Feng, J.; He, L. Semantic segmentation of sparse 3D point cloud based on geometrical features for trellis-structured apple orchard. *Biosyst. Eng.* **2020**, *196*, 46–55. [CrossRef]
15. Palleja, T.; Landers, A.J. Real time canopy density validation using ultrasonic envelope signals and point quadrat analysis. *Comput. Electron. Agric.* **2017**, *134*, 43–50. [CrossRef]
16. Zhou, H.; Jia, W.; Li, Y.; Ou, M.; Zhou, H.; Jia, W.; Li, Y.; Ou, M. Method for Estimating Canopy Thickness Using Ultrasonic Sensor Technology. *Agriculture* **2021**, *11*, 1011. [CrossRef]
17. Nan, Y.; Zhang, H.; Zheng, J.; Bian, L.; Li, Y.; Yang, Y.; Zhang, M.; Ge, Y. Estimating leaf area density of Osmanthus trees using ultrasonic sensing. *Biosyst. Eng.* **2019**, *186*, 60–70. [CrossRef]
18. Zaman, Q.U.; Esau, T.J.; Schumann, A.W.; Percival, D.C.; Chang, Y.K.; Read, S.M.; Farooque, A.A. Development of prototype automated variable rate sprayer for real-time spot-application of agrochemicals in wild blueberry fields. *Comput. Electron. Agric.* **2011**, *76*, 175–182. [CrossRef]
19. Wang, A.; Zhang, W.; Wei, X. A review on weed detection using ground-based machine vision and image processing techniques. *Comput. Electron. Agric.* **2019**, *158*, 226–240. [CrossRef]
20. Wang, Y.; Zhang, Z.; Jia, W.; Ou, M.; Dong, X.; Dai, S.; Wang, Y.; Zhang, Z.; Jia, W.; Ou, M.; et al. A Review of Environmental Sensing Technologies for Targeted Spraying in Orchards. *Horticulturae* **2025**, *11*, 551. [CrossRef]
21. Duan, Y.; Han, W.; Guo, P.; Wei, X.; Duan, Y.; Han, W.; Guo, P.; Wei, X. YOLOv8-GDCI: Research on the Phytophthora Blight Detection Method of Different Parts of Chili Based on Improved YOLOv8 Model. *Agronomy* **2024**, *14*, 2734. [CrossRef]
22. Ji, W.; Pan, Y.; Xu, B.; Wang, J.; Ji, W.; Pan, Y.; Xu, B.; Wang, J. A Real-Time Apple Targets Detection Method for Picking Robot Based on ShufflenetV2-YOLOX. *Agriculture* **2022**, *12*, 856. [CrossRef]
23. Zhang, F.; Chen, Z.; Ali, S.; Yang, N.; Fu, S.; Zhang, Y. Multi-class detection of cherry tomatoes using improved Yolov4-tiny model. *Int. J. Agric. Biol. Eng.* **2023**, *16*, 225–231. [CrossRef]
24. Pei, H.; Sun, Y.; Huang, H.; Zhang, W.; Sheng, J.; Zhang, Z.; Pei, H.; Sun, Y.; Huang, H.; Zhang, W.; et al. Weed Detection in Maize Fields by UAV Images Based on Crop Row Preprocessing and Improved YOLOv4. *Agriculture* **2022**, *12*, 975. [CrossRef]
25. Deng, L.; Miao, Z.; Zhao, X.; Yang, S.; Gao, Y.; Zhai, C.; Zhao, C.; Deng, L.; Miao, Z.; Zhao, X.; et al. HAD-YOLO: An Accurate and Effective Weed Detection Model Based on Improved YOLOV5 Network. *Agronomy* **2024**, *15*, 57. [CrossRef]
26. Zhang, J.; He, L.; Karkee, M.; Zhang, Q.; Zhang, X.; Gao, Z. Branch detection for apple trees trained in fruiting wall architecture using depth features and Regions-Convolutional Neural Network (R-CNN). *Comput. Electron. Agric.* **2018**, *155*, 386–393. [CrossRef]
27. Yu, C.; Shi, X.; Luo, W.; Feng, J.; Zheng, Z.; Yorozu, A.; Hu, Y.; Guo, J. MLG-YOLO: A Model for Real-Time Accurate Detection and Localization of Winter Jujube in Complex Structured Orchard Environments. *Plant Phenomics* **2024**, *6*, 258. [CrossRef] [PubMed]
28. Kazmi, W.; Garcia-Ruiz, F.; Nielsen, J.; Rasmussen, J.; Andersen, H.J. Exploiting affine invariant regions and leaf edge shapes for weed detection. *Comput. Electron. Agric.* **2015**, *118*, 290–299. [CrossRef]
29. Ahmed, F.; Al-Mamun, H.A.; Bari, A.S.M.H.; Hossain, E.; Kwan, P. Classification of crops and weeds from digital images: A support vector machine approach. *Crop Prot.* **2012**, *40*, 98–104. [CrossRef]
30. Zhao, X.; Wang, X.; Li, C.; Fu, H.; Yang, S.; Zhai, C. Cabbage and Weed Identification Based on Machine Learning and Target Spraying System Design. *Front. Plant Sci.* **2022**, *13*, 924973. [CrossRef]
31. Lottes, P.; Hoeferlin, M.; Sander, S.; Müter, M.; Schulze, P.; Stachniss, L.C. An effective classification system for separating sugar beets and weeds for precision farming applications. In Proceedings of the IEEE International Conference on Robotics and Automation (ICRA), Stockholm, Sweden, 16–21 May 2016; pp. 5157–5163. [CrossRef]
32. Bakhshipour, A.; Jafari, A.; Nassiri, S.M.; Zare, D. Weed segmentation using texture features extracted from wavelet sub-images. *Biosyst. Eng.* **2017**, *157*, 1–12. [CrossRef]
33. Min, W.; Wang, Z.; Yang, J.; Liu, C.; Jiang, S. Vision-based fruit recognition via multi-scale attention CNN. *Comput. Electron. Agric.* **2023**, *210*, 107911. [CrossRef]
34. Zhang, X.; Wang, Q.; Wang, C.; Wang, X.; Xu, Z.; Lu, C. Guidelines for mechanical weeding: Developing weed control lines through point extraction at maize root zones. *Biosyst. Eng.* **2024**, *248*, 321–336. [CrossRef]

35. Chen, J.; Zheng, Y.; Zhang, L.; Wang, M.; Gai, F.; Li, C. The design and implementation of the kernel level mobile storage medium data protection system. In Proceedings of the IEEE International Conference on Granular Computing (GrC), Beijing, China, 13–15 December 2013; pp. 53–57. [CrossRef]
36. Sun, S.R.K.H.R.G.J. Faster R-CNN: Towards Real-Time Object Detection with Region Proposal Networks. *IEEE Trans. Pattern Anal. Mach. Intell.* **2017**, *39*, 1137–1149. [CrossRef]
37. Girshick, R.; Donahue, J.; Darrell, T.; Malik, J. Rich Feature Hierarchies for Accurate Object Detection and Semantic Segmentation. In Proceedings of the IEEE Conference on Computer Vision and Pattern Recognition, Columbus, OH, USA, 23–28 June 2014; pp. 580–587. [CrossRef]
38. Wang, H.; Chen, Y.; Zhang, S.; Guo, P.; Chen, Y.; Hu, G.; Ma, Y. Deep learning-based target spraying control of weeds in wheat fields at tillering stage. *Front. Plant Sci.* **2025**, *16*, 1540722. [CrossRef]
39. Xu, Y.; Bai, Y.; Fu, D.; Cong, X.; Jing, H.; Liu, Z.; Zhou, Y. Multi-species weed detection and variable spraying system for farmland based on W-YOLOv5. *Crop Prot.* **2024**, *182*, 106720. [CrossRef]
40. Rahman, A.; Lu, Y.; Wang, H. Performance evaluation of deep learning object detectors for weed detection for cotton. *Smart Agric. Technol.* **2023**, *3*, 100126. [CrossRef]
41. Rai, N.; Zhang, Y.; Villamil, M.; Howatt, K.; Ostlie, M.; Sun, X. Agricultural weed identification in images and videos by integrating optimized deep learning architecture on an edge computing technology. *Comput. Electron. Agric.* **2024**, *216*, 108442. [CrossRef]
42. Sunil, G.C.; Upadhyay, A.; Zhang, Y.; Howatt, K.; Peters, T.; Ostlie, M.; Aderholdt, W.; Sun, X. Field-based multispecies weed and crop detection using ground robots and advanced YOLO models: A data and model-centric approach. *Smart Agric. Technol.* **2024**, *9*, 100538. [CrossRef]
43. Li, Y.; Guo, Z.; Sun, Y.; Chen, X.; Cao, Y.; Li, Y.; Guo, Z.; Sun, Y.; Chen, X.; Cao, Y. Weed Detection Algorithms in Rice Fields Based on Improved YOLOv10n. *Agriculture* **2024**, *14*, 2066. [CrossRef]
44. Fan, X.; Sun, T.; Chai, X.; Zhou, J. YOLO-WDNet: A lightweight and accurate model for weeds detection in cotton field. *Comput. Electron. Agric.* **2024**, *225*, 109317. [CrossRef]
45. He, C.; Wan, F.; Ma, G.; Mou, X.; Zhang, K.; Wu, X.; Huang, X.; He, C.; Wan, F.; Ma, G.; et al. Analysis of the Impact of Different Improvement Methods Based on YOLOV8 for Weed Detection. *Agriculture* **2024**, *14*, 674. [CrossRef]
46. Liu, L.; Zhang, M.; Zhou, X.; Zhai, R.; Wang, D.; Zhu, S. A lightweight weed detection algorithm designed based on YOLOv9. *Appl. Soft Comput.* **2026**, *186*, 114183. [CrossRef]
47. Jiang, W.; Quan, L.; Wei, G.; Chang, C.; Geng, T. A conceptual evaluation of a weed control method with post-damage application of herbicides: A composite intelligent intra-row weeding robot. *Soil Tillage Res.* **2023**, *234*, 105837. [CrossRef]
48. Sunil, G.C.; Upadhyay, A.; Sun, X. Development of software interface for AI-driven weed control in robotic vehicles, with time-based evaluation in indoor and field settings. *Smart Agric. Technol.* **2024**, *9*, 100678. [CrossRef]
49. Shorten, C.; Khoshgoftaar, T.M.; Shorten, C.; Khoshgoftaar, T.M. A survey on Image Data Augmentation for Deep Learning. *J. Big Data* **2019**, *6*, 1–48. [CrossRef]
50. Wang, L.; Zhao, Y.; Xiong, Z.; Wang, S.; Li, Y.; Lan, Y. Fast and precise detection of litchi fruits for yield estimation based on the improved YOLOv5 model. *Front. Plant Sci.* **2022**, *13*, 965425. [CrossRef] [PubMed]
51. Han, Y.; Zhang, R.; Lu, C.; Wang, G.; Han, X.; Xu, D. Design and Test of Control System for Intelligent Kitchen Waste Treatment Equipment. *Trans. Chin. Soc. Agric. Mach.* **2022**, *53*, 161–169. [CrossRef]
52. Azimjonov, J.; Özmen, A.; Varan, M.; Azimjonov, J.; Özmen, A.; Varan, M. A vision-based real-time traffic flow monitoring system for road intersections. *Multimed. Tools Appl.* **2023**, *82*, 25155–25174. [CrossRef] [PubMed]
53. *GB/T 24677.1–2009*; Boom Sprayer—Technical Requirements. Standards Press of China: Beijing, China, 2009.
54. Si, H.; Wang, Y.; Zhao, W.; Wang, M.; Song, J.; Wan, L.; Song, Z.; Li, Y.; Fernando, B.; Sun, C.; et al. Apple Surface Defect Detection Method Based on Weight Comparison Transfer Learning with MobileNetV3. *Agriculture* **2023**, *13*, 824. [CrossRef]
55. Li, H.; Guo, C.; Yang, Z.; Chai, J.; Shi, Y.; Liu, J.; Zhang, K.; Liu, D.; Xu, Y. Design of field real-time target spraying system based on improved YOLOv5. *Front. Plant Sci.* **2022**, *13*, 1072631. [CrossRef] [PubMed]
56. Li, J.; Liu, C.; Lu, X.; Wu, B. Fish passage monitoring based on improved YOLO v5s and TensorRT deployment. *Trans. Chin. Soc. Agric. Mach.* **2022**, *53*, 3–14. [CrossRef]

Disclaimer/Publisher's Note: The statements, opinions and data contained in all publications are solely those of the individual author(s) and contributor(s) and not of MDPI and/or the editor(s). MDPI and/or the editor(s) disclaim responsibility for any injury to people or property resulting from any ideas, methods, instructions or products referred to in the content.

agriculture

MDPI

Article

Design and Experimentation of High-Throughput Granular Fertilizer Detection and Real-Time Precision Regulation System

Li Ding [1], Feiyang Wu [1], Yuanyuan Li [1], Kaixuan Wang [1], Yechao Yuan [1], Bingjie Liu [2,*] and Yufei Dou [3]

[1] College of Mechanical and Electrical Engineering, Henan Agricultural University, Zhengzhou 450003, China; dingli@henau.edu.cn (L.D.); w255063585@163.com (F.W.); lyy18749019024@163.com (Y.L.); 18211941739@163.com (K.W.); y95625048@163.com (Y.Y.)
[2] College of Information and Management Science, Henan Agricultural University, Zhengzhou 450003, China
[3] College of Mechanical and Electronic Engineering, Northwest Agriculture and Forestry University, Yangling 712100, China; douyufei1010@163.com
* Correspondence: liubingjie@henau.edu.cn

Abstract

To address the challenge of imprecise detection and control of fertilizer application rates caused by high granular flow during fertilization operations, a parallel diversion detection method with real-time application rate regulation is proposed. The mechanism of uniform distribution of discrete particles formed by high-throughput aggregated granular fertilizer was elucidated. Key components including the uniform fertilizer tube, sensor detection structure, six-channel diversion cone disc, and fertilizer convergence tube underwent parametric design, culminating in the innovative development of a six-channel parallel diversion detection device. A multi-channel parallel signal detection method was studied, and a synchronous multi-channel signal acquisition system was designed. Through calibration tests, relationship models were established between the measured flow rate of granular fertilizer and voltage, as well as between the actual flow rate and the rotational speed of the fertilizer discharge shaft. A fuzzy PID control model was constructed in MATLAB2023/Simulink. Using overshoot, response time, and stability as evaluation metrics, the control performance of traditional PID and fuzzy PID was compared and analyzed. To validate the control system's precision, device performance tests were conducted. Results demonstrated that fuzzy PID control reduced the time required to reach steady state by 66.87% compared to traditional PID, while overshoot decreased from 7.38 $g \cdot s^{-1}$ to 1.49 $g \cdot s^{-1}$. Divergence uniformity tests revealed that at particle generation rates of 10, 20, 30, and 40 $g \cdot s^{-1}$, the coefficient of variation for channel divergence consistency gradually increased with rising tilt angles. During field operations at 0–5.0° tilt, the coefficient of variation for channel divergence consistency remained below 7.72%. Bench tests revealed that the fuzzy PID control system achieved an average accuracy improvement of 3.64% compared to traditional PID control, with a maximum response time of 0.9 s. Field trials demonstrated detection accuracy no less than 92.64% at normal field operation speeds of 3.0–6.0 $km \cdot h^{-1}$. This system enables real-time, precise detection of fertilizer application rates and closed-loop regulation.

Keywords: fuzzy PID control; traditional PID control; fertilizer quantity detection; flow consistency; real-time regulation of fertilizer application

1. Introduction

Precision fertilization technology, which applies fertilizer according to the type and amount required by the target crop, is one of the effective ways to address the issues of unreasonable fertilizer input, low average fertilizer utilization rate, and agricultural ecological environmental pollution. Therefore, the urgent technical bottleneck in precision fertilization is how to accurately detect the flow rate of granular fertilizer in real time and apply it precisely as needed, ultimately achieving a uniform and consistent flow of fertilizer granules. Numerous scholars have conducted extensive research on this topic. In terms of fertility detection, the existing methods mainly include efficient point cloud volume conversion algorithm detection, dielectric sensor detection, variable light distance fertilization amount detection, etc., but they have the following limitations: the overall volume of fertilizer is easily affected by field environment interference, leading to a decrease in volume detection accuracy; sensors are prone to failure under extreme vibration conditions; and the mutual obstruction between granular fertilizers affects the accuracy of light detection. Zhao et al. [1] designed a fertilizer application detection system based on point cloud data and volume conversion algorithms; however, there is a certain delay in fat content detection. Ku mahala et al. [2] developed a parallel plate capacitor, which can deduce the mass flow rate variation law by fitting the relationship between material mass and sensor signal output. However, the measurement results are influenced by two factors: the material compaction force between the plates and the moisture content. Yongqian Ding et al. [3] based on the dynamic weighing principle, by detecting changes in the amount of fertilizer in the fertilizer tank can calculate the discharge volume of granular fertilizer. However, the applicability of this method in addressing uneven surfaces in conservation tillage still needs further improvement. Liwei Yang et al. [4] proposed a preprocessing algorithm based on microwave sensors to collect the flow rate signal of granular fertilizers in precision agriculture, which is difficult to accurately measure.

Zegang Shen et al. [5] proposed a collaborative adaptive fish swarm particle filtering algorithm to address the issues of signal interference and errors in the collection process of fertilizer discharge signals in the granular fertilizer mass flow measurement system. This algorithm effectively solves the problems of signal interference and errors in granular fertilizer mass flow measurement, but its adaptability to environmental temperature changes needs to be improved. Lixin Zhao et al. [6] designed a variable light-distance fertilizer application detection system, but the problem of mutual obstruction between particles affects the detection accuracy. Chunbao Xu et al. [7] designed a thin-film light refraction type particle flow multi-channel parallel detection device based on the principles of convex lens refraction and non-contact photoelectric sensing and conducted experiments on it.

In terms of real-time and precise regulation of fertilizer application rates, Jiqin Zhang et al. [8] proposed centrifugal variable spraying technology and strip sowing variable spraying technology to address the issue of incomplete dosage control technology for granular fertilizer application. John Deere has developed the RELATIVE FLOW^{TM} blockage monitoring system, which enables full-process blockage monitoring from the fertilizer tank to the opener, intelligently adjusting the fertilization rate [9]. Two scholars, Umeda and Lina from Japan [10], have developed a variable-rate fertilization machine for rice based on fertilization prescription maps. Maleki et al. [11] from Belgium determined the response time measurement of soil sensors, thereby enhancing the fertilization accuracy of variable-rate fertilizers. JiCheng Zhang et al. [12] adopted an incremental PID closed-loop control algorithm for regulating the fertilization motor, which improved the rapid automatic proportioning and real-time mixing accuracy of three fertilizers: nitrogen, phosphorus, and potassium. Xu Ma et al. [13] designed an online detection system and intelligent regulation system for fertilizer application based on piezoelectric sensors, which is suitable for slow

https://doi.org/10.3390/agriculture16030290

and low-flux fertilization operations. Hui Wang et al. [14] proposed a segmented PID control method based on fertilizer flow feedback to achieve accurate control of fertilizer flow. Man Chen et al. [15] studied a real-time variable topdressing amount adjustment algorithm based on fuzzy PID control, which regulates the dual variables of the fertilizer feeder's speed and opening.

Research on fertilizer discharge detection and regulation technology, both domestically and internationally, primarily focuses on aspects such as emptying of fertilizer bins, blockages in fertilizer pipes, and the inversion of fertilizer discharge rate based on the rotational speed of the fertilizer discharge device, which indirectly reflects the field operation status of fertilization machinery. However, there is a relative lack of research on real-time detection of high-throughput granular fertilizer and how to precisely regulate and control the amount of fertilizer discharged in a closed-loop manner.

In response to the problems of insufficient real-time detection accuracy, poor uniformity of fertilizer discharge, and imperfect closed-loop control systems in existing variable fertilization technologies, this paper proposes a parallel detection method for high-throughput granular fertilizers based on the two core objectives of "high-throughput granular fertilizer detection" and "real-time precision regulation", explores the impact of the shunt structure of the fertilizer quantity detection device on the shunting effect, and develops a multi-channel signal synchronous acquisition system based on PVDF sensors. We explore the relationship between the height of fertilizer application and the intensity of piezoelectric signals and complete the development of a high-frequency fertilizer application detection system. A fuzzy PID closed-loop control method based on fertilizer quantity information feedback is proposed, integrating machine operation speed, operation parameters, and fertilizer flow information. This method clarifies the precise intelligent regulation strategy for fertilizer quantity under complex spatiotemporal pattern data integration, achieving real-time precise detection and closed-loop regulation of fertilizer quantity. We also provide theoretical support and innovative practical technologies for precision variable-rate fertilization and granular fertilizer detection.

2. Materials and Methods

2.1. Overall Structural Design and Working Principle

2.1.1. Overall Structure

The structure of the granular fertilizer shunt parallel diversion device is shown in Figure 1, which mainly consists of a fertilizer homogenizing device, a shunt device, and a detection device. The precise control system for granular fertilizer mainly consists of a human–computer interaction module, a stepper motor, a stepper motor driver, a 24 V lithium battery, a fertilizer amount detection device, an amplification module, STM32F103cet6, an LM2596S step-down module, an encoder, a PVDF sensor, and a data acquisition module. The human–machine interaction module can display the flow rate and operating speed of granular fertilizer and enable the setting of parameters such as fertilizer application rate per acre and operating width. The encoder output shaft is connected to the ground wheel drive shaft, allowing real-time acquisition of the implement operating speed and transmission to the controller. The AD7606 data acquisition module collects the voltage signals collected by the PVDF sensor and transmits them to the controller. The controller processes the signals and displays them through the human–computer interaction module.

https://doi.org/10.3390/agriculture16030290

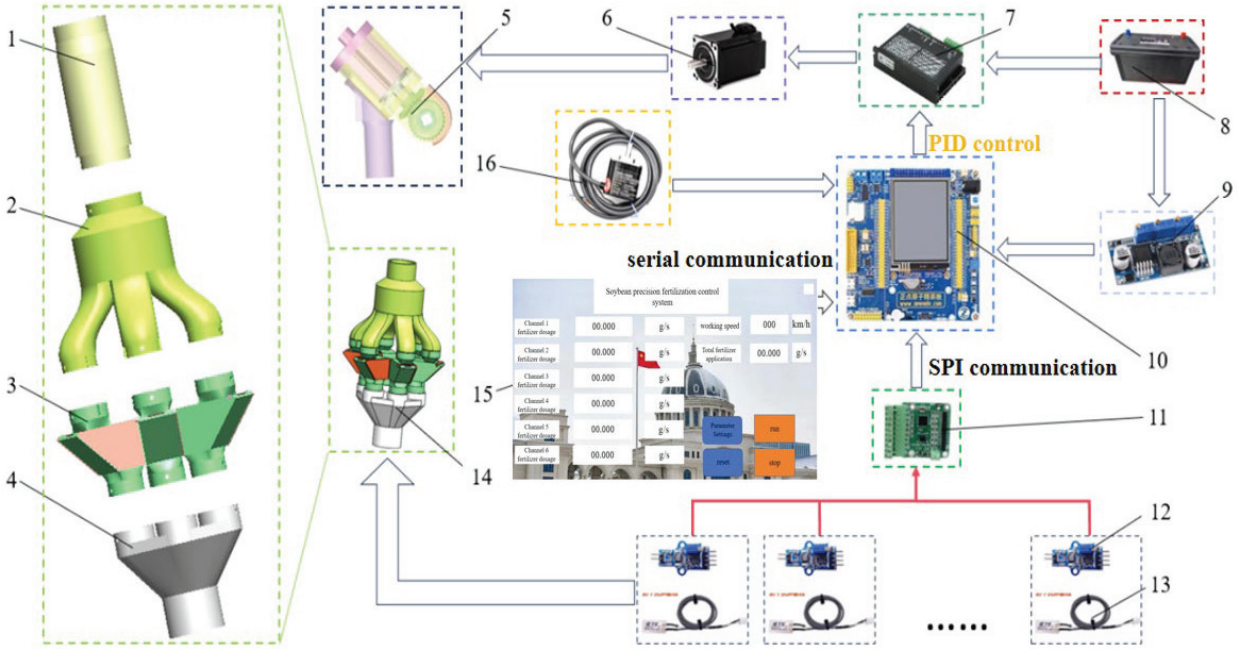

Figure 1. Schematic diagram of the parallel detection structure for granular fertilizer diversion. 1. Uniform fertilizer distribution device; 2. diversion structure; 3. sensing device; 4. manifold; 5. fertilizer distributor; 6. stepper motor; 7. motor driver; 8. 24 V power supply; 9. step-down module; 10. STM32 controller; 11. data acquisition module; 12. amplification module; 13. PVDF piezoelectric sensor; 14. fertilizer amount detection device; 15. human–computer interaction module; 16. encoder. Note: The ellipsis in the figure indicates that there are three identical devices at this location.

2.1.2. Working Principle

First, input the target fertilization amount, working width, and number of working rows for the plot in the human–machine interaction module. Then, the encoder speed measurement module installed on the transmission shaft of the implement's ground wheel acquires the real-time traveling speed of the implement. During operation, the high-throughput fertilizer particles discharged from the fertilizer distributor flow through the uniform fertilizer device and fall into the diversion structure; under the action of the diversion structure, the flow is evenly divided into six low-pass fertilizer granule streams; the streams of fertilizer particles after being diverted are independent of each other, the fertilizer particles falling from the diverging port land on the piezoelectric film that is tilted downward, and after colliding with it, it flows out from the sensor device's manifold. Meanwhile, the data acquisition module transmits the six-channel signals it has collected to the controller. The controller sets the target fertilization amount forward speed of machinery and tools, information such as the number of rows of homework and the flow rate of real-time granular fertilizer are used as input variables for the control system; based on the control strategy of the control system, the control quantity of the current fertilizer discharge motor speed is derived. And utilize the fuzzy PID algorithm to enable the fertilizer control system to output corresponding PWM signals; the PWM signal controls the motor through the motor driver to adjust its speed in real time, achieving precise control over fertilization operations.

2.2. Key Component Design

2.2.1. Uniform Fertilizer Distribution Device

To ensure uniformity of flow distribution [16], a fertilizer distribution device was designed, as shown in Figure 2. It mainly consists of a fertilizer management interface, a

double-helix uniform fertilizer baffle ring, a uniform fertilizer baffle rod, and connecting holes. To ensure the continuous and stable descent of granular fertilizer along the flow direction, the inlet of the uniform fertilizer pipe is connected to the end of the fertilizer discharge pipe and is coaxial with the latter. At the same time, the inner wall of the uniform fertilization tube is designed with a double-helix uniform fertilization baffle ring with an equal height and length of spiral lines, and the starting and ending positions of the double-helix baffle ring are 180° apart. On each layer, set up uniform fertilizer distribution rods with equal length and shaft diameter, and no crossing in the middle. According to the preliminary experimental results, the number of uniform fertilizer distribution rods on each layer is 4. During operation, the granular fertilizer is evenly distributed to the pipe orifice of the diverging structure under the influence of gravity, baffle rings, and baffle bars within the uniform fertilization pipe.

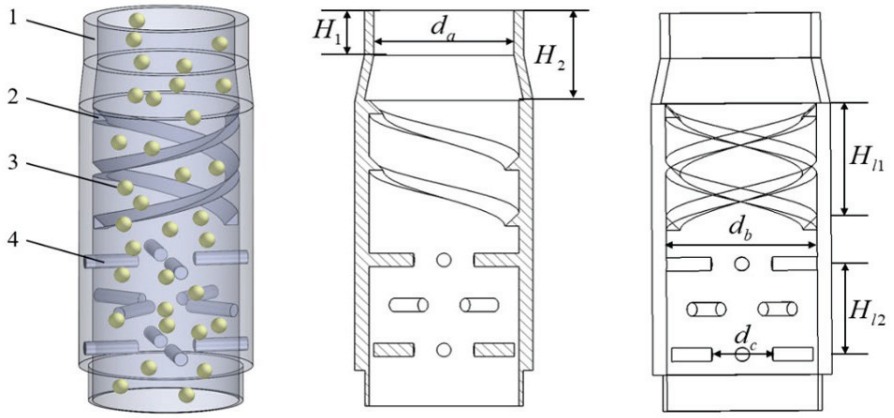

Figure 2. Uniform fertilization device structure. (**a**) Working diagram. (**b**) Internal cross-sectional view. (**c**) Internal perspective. 1. Fertilizer pipe interface; 2. double helix uniform fertilization retaining ring; 3. uniform fertilizer gear lever; 4. connection hole. Note: The light-yellow spheres in the picture represent granular fertilizer.

Based on the size of the fertilizer discharge pipe, the outer diameter of the fertilizer receiving pipe of the uniform fertilization device is determined to be 34 mm, the wall thickness is 2 mm (with an inner diameter d_a of 30 mm), and the height of the fertilizer pipe connection H_1 is 10 mm. In practical operations, most of the granular fertilizer falls along the axis, thus determining an outer diameter d_a of 36 mm and a wall thickness of 2 mm (with an inner diameter of 32 mm). To ensure that granular fertilizer gathers towards the center without affecting its circulation, the cross-section of the double-helix retaining ring is an isosceles right triangle with a side length of 2 mm, and the pitch of the helical line H_{l1} is 25 mm, and the number of spiral coils is one. To ensure the smooth flow of granular fertilizer through the uniform fertilizer pipe, according to the principle of circulation, the relationship between the inner diameter of the uniform fertilizer pipe and the diameter of the inscribed circle of the uniform fertilizer rod is as follows:

$$\pi\left(\frac{d_b}{2}\right)^2 - 4 \times \frac{d_b - d_c}{2} \times d_g \geq \pi\left(\frac{d_a}{2}\right)^2 \quad (1)$$

In Formula (1), d_g is the diameter of the gear lever, mm.

The diameter of the baffle rod affects the circulation of granular fertilizer and the collision effect of particles. The larger the diameter of the baffle rod for uniform fertilization, the better the fertilization effect and the higher the structural strength, but an excessively large diameter of the baffle rod affects the passage ability. Set the maximum diameter d_g

https://doi.org/10.3390/agriculture16030290

of the uniform fertilizer gear lever to 3 mm, and substitute it into Formula (1) to calculate d_c = 13.74 mm. If the diameter of the inscribed circle of the uniform fertilizer rod is too small, it will increase the friction between the granular fertilizers inside the tube, affecting the circulation and uniform distribution of the granular fertilizers. Considering factors such as processing errors, the diameter of the inscribed circle of the uniform fertilizer rod is determined to be d_c = 15 mm.

2.2.2. Design of Diversion Structure

To facilitate detection and improve detection accuracy, it is required that the granular fertilizer can quickly pass through each shunt tube, and the number of granular fertilizers passing through each tube should not vary significantly. With the goal of uniform shunting and rapid passage, the shunting structure parameters are designed as shown in Figure 3. The granular fertilizer shunting structure mainly consists of fertilizer inlet a, a conical shunting disk, shunt tubes, a limiting structure, and fertilizer outlet a. During operation, the granular fertilizer enters the shunting structure through fertilizer inlet a, falls onto the surface of the conical shunting disk, and falls along its surface, being uniformly shunted into the shunt tubes. The random dispersion and uniform shunting of granular fertilizer can reduce the impact of the machine's tilting condition in the field on the shunting uniformity of the detection device.

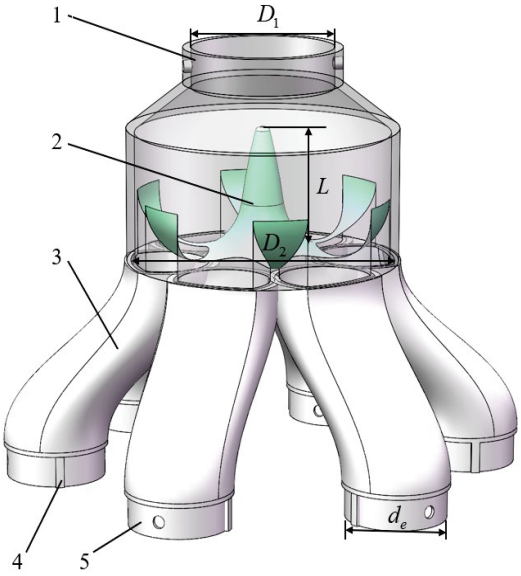

Figure 3. Schematic diagram of shunt structure. 1. Fertilizer inlet a; 2. conical flow divider disk; 3. diversion tube; 4. limit stop structure; 5. fertilizer outlet a.

The main parameter of the diverging structure includes the inlet of fertilizer a, diameter D_1, number of shunt tubes N_s, inner diameter of the diversion tubes d_e, cone disk height L, and cone disk diameter D_2 of the conical disk. To ensure the stability of the flow divider, diameter D_1 of the inlet pipe should be consistent with that of the even fertilizer device, set at 32 mm. The fertilizer demand of crops and the operating speed of machinery directly affect the fertilizer discharge frequency, which in turn determines the structural form and size of the flow divider. During the fertilization process, the relationship between the fertilizer discharge rate of the fertilizer distributor and the number of flow divider channels is as follows:

$$q_{ut} = \frac{vBQ}{36n_r} \tag{2}$$

$$f = \frac{1000q_{ut}}{m_g} \tag{3}$$

https://doi.org/10.3390/agriculture16030290

$$N_s \leq \frac{f}{f_{max}} \tag{4}$$

In formula, q_{ut} is the fertilizer discharge rate per unit time, g·s^{-1}; v is the operating speed of the seeder, km·h^{-1}; B is the operating width, m; Q is the agronomy required fertilizer application rate, kg·hm^{-2}; n_r is the number of rows operated by the seeder; m_g is the mass of 1000 granular fertilizer grains, g; N is the number of diverging channels; f is the total fertilizer discharge frequency, Hz; f_{max} is the effective detection frequency of the detection device, Hz.

According to the agronomic requirements for soybean fertilization in the Huang-Huai-Hai region, the fertilization rate for soybeans is 225 kg·hm^{-2}; based on the calculation using the fertilization and seeding machine with a working width of 1.2 m, a total of 3 fertilization rows, and a machine operating speed of 2.0~5.0 km·h^{-1}, the soybean fertilizer discharge rate can be calculated as 5.0~12.5 g·s^{-1} according to the formula, with the maximum value taken as 12.5 g·s^{-1}. After measurement, the weight of 1000 grains of Stanley compound fertilizer are 48.7 g. Substituting this value into the formula, we obtain the total fertilizer discharge frequency f of 257 Hz. Considering the detection performance of the selected piezoelectric sensor [17], taking f_{max} as 45 Hz, substituting the formula, we can obtain the number of branch pipes, *Ns*, as 5.7, the diversion device is determined to be in the form of six diversion branches.

In accordance with the design requirements for the diverging structure, considering factors such as the characteristics and movement patterns of granular fertilizer materials, the sum of the areas of the six diverging tube orifices should be equal to the inlet cross-sectional area. Therefore, inner diameter *d*e of the diverging tube should satisfy the following conditions:

$$\left(\frac{D_1}{2}\right)^2 \pi = 6\left(\frac{d_e}{2}\right)^2 \pi \tag{5}$$

In Formula (5), d_e is the inner diameter of the shunt tube, mm.

Substitute the known parameters into Equation (5) to calculate the inner diameter of the shunt tube as 13.1 mm. Considering the overall structure of the shunt cone disk and its threaded connection with the spiral tube, the inner diameter of the shunt tube is determined as d_e = 15 mm.

2.2.3. Sensing Device

After preliminary experiments comparing and analyzing the signals from collisions between granular fertilizer and various piezoelectric films, the LDTO-028K piezoelectric film from MEAS Corporation was ultimately selected as the piezoelectric sensing element. This component is manufactured by Precision Electronics, a company headquarters in Hampton, VA, USA. It has a thickness of 0.2 mm and a minimum sensing force of 0.01 N. During operation, the sensing device is installed below fertilizer outlet a of the diverging structure. The granular fertilizer sensing device mainly consists of fertilizer inlet b, a limit slot, a collision chamber, fertilizer outlet b, and a connecting hole, as shown in Figure 4.

To reduce the free oscillation of the piezoelectric film caused by the collision of granular fertilizer with the film, a sinking groove substrate–piezoelectric film structure was designed. A rectangular sinking groove, consistent with the effective sensing area of the piezoelectric film (11 mm × 16 mm), was cut below the sensor, with a depth of 0.5 mm. Considering the thickness of the piezoelectric sensor, the sensor card slot was designed to be 0.8 mm deep. To avoid blockage of granular fertilizer in the collision chamber, the depth of the collision chamber was set to 0.5 mm. To ensure that the falling granular fertilizer can effectively collide with the piezoelectric film, the inclination angle α of the piezoelectric film is constrained by the requirement that the granular fertilizer must collide within the

https://doi.org/10.3390/agriculture16030290

effective sensing area of the piezoelectric film, α should not be too large; to avoid secondary or even multiple collisions between granular fertilizer and piezoelectric film, theoretically, α is within the range of 0–90.0°. When inclination angle α of the piezoelectric sensor is too small, it may cause secondary or multiple collisions between the granular fertilizer and the piezoelectric sensor and even lead to the accumulation and blockage of granular fertilizer in the sensing device. When inclination angle α of the piezoelectric sensor is too large, the projection area of the effective sensing area of the piezoelectric sensor on the horizontal plane decreases. Considering the selected size of the piezoelectric sensor, inclination angle α of the piezoelectric sensor should be taken as the minimum value within a reasonable range; therefore, select α is 45°.

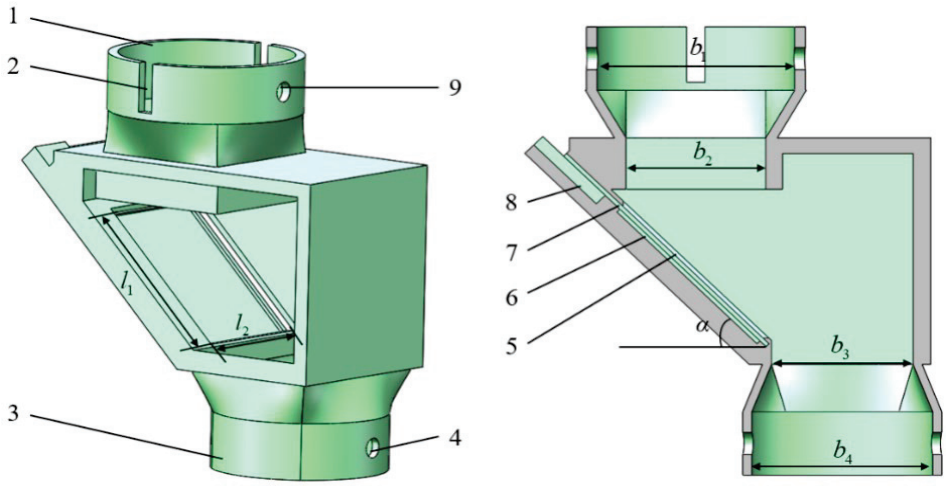

Figure 4. Schematic diagram of shunt structure. 1. Fertilizer inlet b; 2. limit stop slot; 3. fertilizer outlet b; 4. connection hole; 5. collision chamber; 6. rectangular recess; 7. sensor slot; 8. cable duct. 9. connection hole.

2.2.4. Flow Detection Calibration Test

According to Section 2.2, when the operating speed of the machinery is between 2 and 5 km·h^{-1}, the maximum fertilizer discharge rate is 12.5 g·s^{-1}. Stanley compound fertilizer was selected as the material for this experiment. Under 10 different rotational speeds of the fertilizer discharge device, the fertilizer discharge time was timed using the timer of the STM32, with each discharge lasting for 20 s. After each test, the actual fertilizer discharge mass was measured using an electronic scale. Each set of experiments was conducted three times. The calibration test data were processed using Origin 2023 software, and the model of the relationship between the actual fertilizer flow rate and the rotational speed of the fertilizer discharge device was obtained as follows:

$$q_p = 49.193 n_p + 0.177 \quad (6)$$

In Formula (6), n_p is the rotational speed of the fertilizer dispenser, r·s^{-1}; and q_p is the actual flow rate of fertilizer, g·s^{-1}.

As can be seen from Figure 5, the actual flow rate of fertilizer increases with the increase in the rotational speed of the fertilizer discharge device, and there is a linear relationship between the fertilizer flow rate and the rotational speed of the fertilizer discharge device. Upon inspection, the coefficient of determination R^2 of the fitted equation is 0.994, indicating a significant linear relationship. Therefore, the system can utilize the relationship model for regulating the actual flow rate of fertilizer.

https://doi.org/10.3390/agriculture16030290

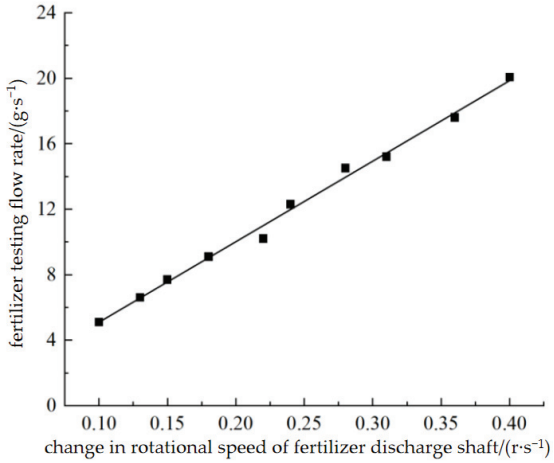

Figure 5. Change curve between the actual flow rate of fertilizer and the speed of fertilizer dispenser.

2.2.5. Testing Process

The control process of the precision fertilization control system is shown in Figure 6. Before operation, the precision fertilization control system is initialized first. When fertilizer particles collide with the PVDF piezoelectric sensor, voltage signals are generated. The original signals are processed through filtering, amplification, comparison, and other methods to be converted into digital interrupt signals. The timer TIM4 is used to achieve timing acquisition of operation speed and fertilizer quantity information, with a timing time of 1 s. The timer TIM3 uses encoder mode to convert the rotation speed of the ground wheel into electrical signals. The STM32 converts the collected digital fertilizer quantity signals into fertilizer flow rates for each channel, and converts the electrical signals collected in encoder mode of the timer TIM3 into implement speed information, which is displayed on the LCD screen. The STM32 converts the input parameter information and implements operation speed into real-time flow rate information and combines it with the collected fertilizer flow rate information as the input for the fuzzy PID algorithm. The fuzzy PID algorithm is used to perform real-time self-tuning of the fertilizer discharge motor speed.

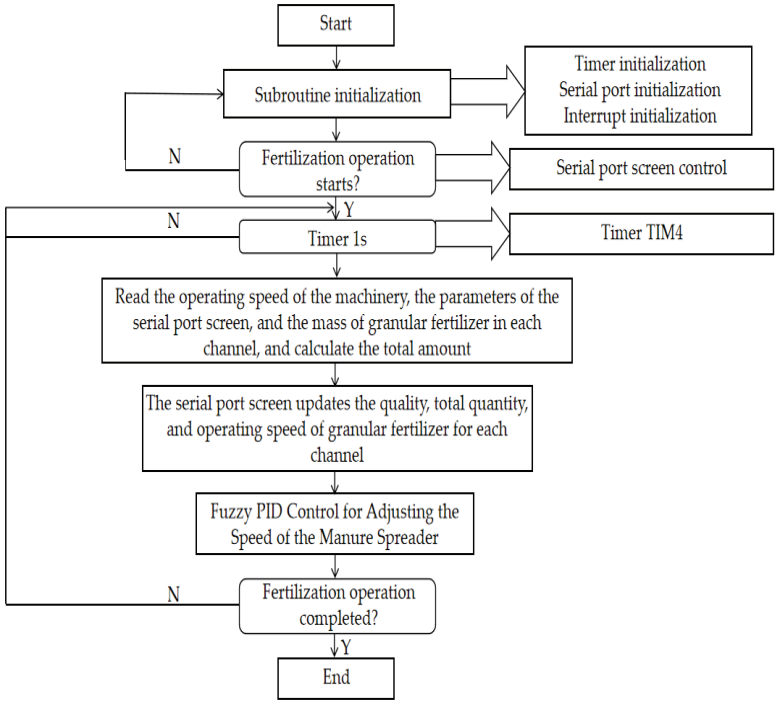

Figure 6. Detection flowchart.

2.3. Fuzzy PID Control

Addressing the issue of insufficient system adaptability caused by fixed parameters in traditional PID controllers, a fuzzy inference mechanism is adopted to implement a real-time online optimization strategy for PID parameters [18], as shown in Figure 7. When the system is operating, the fertilizer flow detection unit inputs the real-time fertilizer discharge rate as a feedback signal c to the controller. Based on the externally input operational parameters (number of rows, fertilizer application rate, operational width) and the real-time detected operational speed, calculate the real-time target fertilization rate r. By constructing a dual-parameter feedback mechanism for the error quantity e ($e = r - c$) and its rate of change ec ($ec = \mathrm{d}e/\mathrm{d}t$), a closed-loop control system is formed, where the error characteristics are pattern recognized through a fuzzy rule base, and the PID parameter combination is dynamically adjusted, thereby achieving precise control over nonlinear time-varying systems.

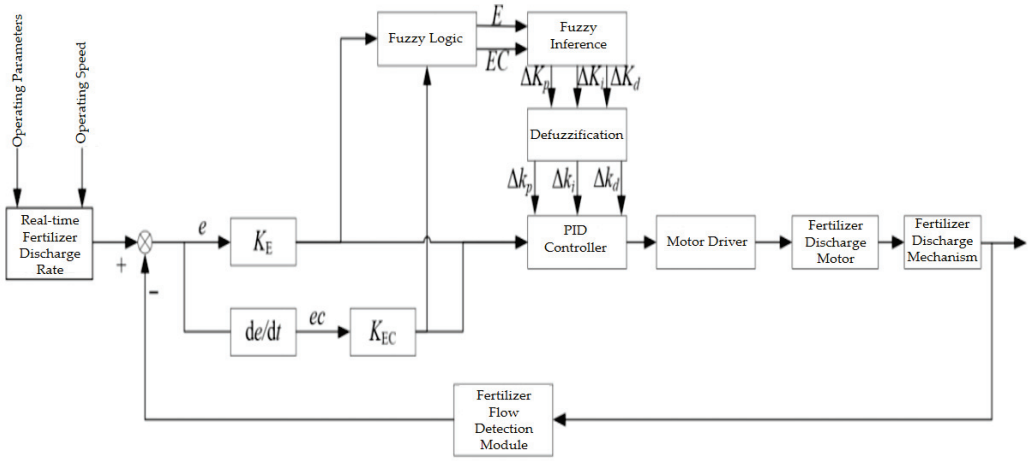

Figure 7. Block diagram of fuzzy PID control system. Note: e is the deviation between the targeted fertilization amount and the real-time fertilization amount, $g \cdot s^{-1}$; ec is the rate of change in the deviation value, $g \cdot s^{-1} \cdot s^{-1}$; K_E and K_{EC} are the quantization factors for e and ec; E and EC are linguistic variables of e and ec in the fuzzy universal; ΔK_p, ΔK_i and ΔK_d represent the linguistic variable values of the gain correction parameters obtained through fuzzy inference ; Δk_p, Δk_i and Δk_d represent the actual values of the gain correction parameters obtained after blur removal.

Fuzzy controller is a control system based on fuzzy logic theory, mainly composed of three core modules: fuzzification, fuzzy inference, and deblurring. The fuzzification module converts actual measurement values into fuzzy language variable values and generates fuzzy sets through methods such as input point membership degree 1 method, graded fuzzy set method, or membership degree value method to achieve fuzzy mapping of accurate values. The fuzzy reasoning module performs logical reasoning based on a preset fuzzy rule library, using NB (Negative Big), NM (Negative Medium), NS (Negative Small), ZO (Zero), PS (Positive Small), PM (Positive Medium), PB (Positive Big) Seven level fuzzy word sets to describe input–output relationships. The selection of the number of word sets directly affects the control accuracy. More words can refine the control rules and improve the system's response precision, while fewer words can simplify the model but reduce the control accuracy. The deblurring module converts the fuzzy inference results in precise control output, completing closed-loop control.

2.3.1. Modeling of Precision Fertilization Control System

The control model of the fertilizer precision control system takes the fertilization parameters inputted by the human–computer interaction module and the real-time machine

https://doi.org/10.3390/agriculture16030290

operation speed collected by the encoder as inputs. The controller transmits the processed signals to the fertilizer discharge stepper motor, which changes its speed to control the fertilizer discharge amount. The fertilizer flow rate is the final output of the control system. The fertilizer flow detection module consists of a shunt parallel detection device, a piezoelectric sensor, and a data acquisition module, detects the real-time flow of fertilizer and transmits the fertilizer flow information to the controller. The controller performs closed-loop negative feedback control, as shown in Figure 8.

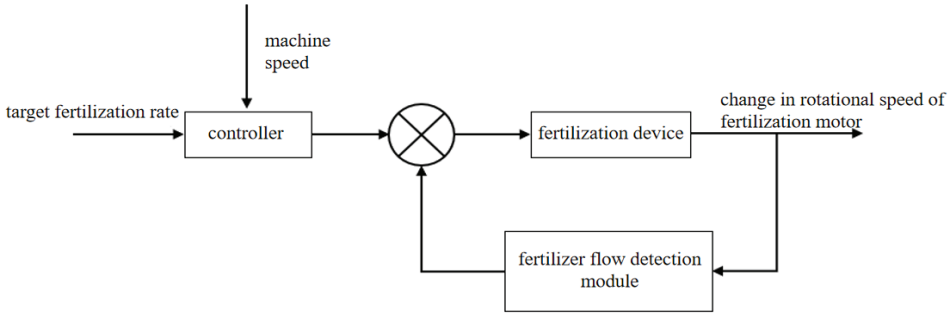

Figure 8. Fertilizer flow control system block diagram. Notes: In the figure, the circle symbol represents the fertilizer feeding stepper motor.

Based on the input–output relationship of the control system block diagram, the input–output relationship of the system is obtained as follows:

$$q_0 = \frac{vAQ}{36N_1} \tag{7}$$

In Formula (7), A is the operating width, m; and N_1 is the number of rows operated by the seeder.

As can be seen from Figure 8, the real-time flow rate of granular fertilizer collected by the fertilizer flow detection module serves as the input signal for the control system's feedback mechanism. The feedback signal received by the controller is an analog signal. The controller compares the real-time target fertilization amount with the feedback signal, ultimately achieving negative feedback control of the control system. The feedback function in the control model can be expressed as

$$H(s) = \frac{v(s)}{q_0(s)} = \frac{36N_1}{AQ} \tag{8}$$

In Formula (8), s is the complex variable after the Laplace transform of the transfer function; and H is the negative feedback loop of the transfer function.

The fertilization motor adopts an 86BYG250-150 two-phase hybrid stepping motor. The motor is manufactured by NiMotion Company, whose headquarters is located in Beijing, China. The mathematical modeling of the stepping motor requires the construction of voltage balance equations, motor torque balance equations, and motor rotation equations [19]; after operational transformation, the transfer function of the stepper motor is

$$G_1(s) = \frac{\frac{LN_rI^2}{2J}}{s^2 + \frac{B}{J}s + \frac{LN_rI^2}{2J}} \tag{9}$$

In Formula (9), $G_1(s)$ is the transfer function of the stepper motor; L is the self-inductance of the phase winding of a stepper motor, H; N_r is the number of teeth; I represents the rated current, A; J is rotational inertia of the rotating shaft of a stepper motor, kg·cm^{-2}; and B is the motor viscous damping coefficient, 0.08.

https://doi.org/10.3390/agriculture16030290

The transmission of parameters such as stepper motor drivers and transmission mechanisms is less affected by electrical interference during the operation of the action mechanism, and the operating characteristics remain stable and unchanged, thus they can all be regarded as proportional elements. Calculations show that the stepper motor driver transmits a constant value $G_2(s) = 10$. Through the calibration experiment of actual fertilizer flow rate in Section 2.4, a linear relationship was observed between the rotational speed of the system's fertilizer discharge shaft and the fertilizer flow rate, with the relationship expressed as

$$G_3(s) = \frac{q_0(s)}{\theta(s)} = K_q \tag{10}$$

In Formula (10), $G_3(s)$ is the fertilizer discharge axis transfer function; $\theta(s)$ is the Laplace transform function of the rotational speed of the fertilizer discharge shaft; $q_0(s)$ is the Laplace transform function of the fertilizer flow rate; and K_q is the conversion coefficient between the rotational speed of the fertilizer discharge shaft and the fertilizer flow rate. The transfer function $G(s)$ of the fertilization mechanism is

$$G(s) = G_1(s)G_2(s)G_3(s) \tag{11}$$

In Formula (7), N_1 is 3; A is 1.2 m; and Q is taken as 225 kg·hm^{-2}. In Formula (10), K_q is taken as 49.19.

According to Figure 9 and Formulas (7)–(11), the closed-loop feedback control transfer function $G_z(s)$ of the precision fertilization control system is expressed as

$$G_z(s) = \frac{G(s)}{1 + G(s)H(s)} = \frac{510.13}{s^2 + 0.03s + 205.09} \tag{12}$$

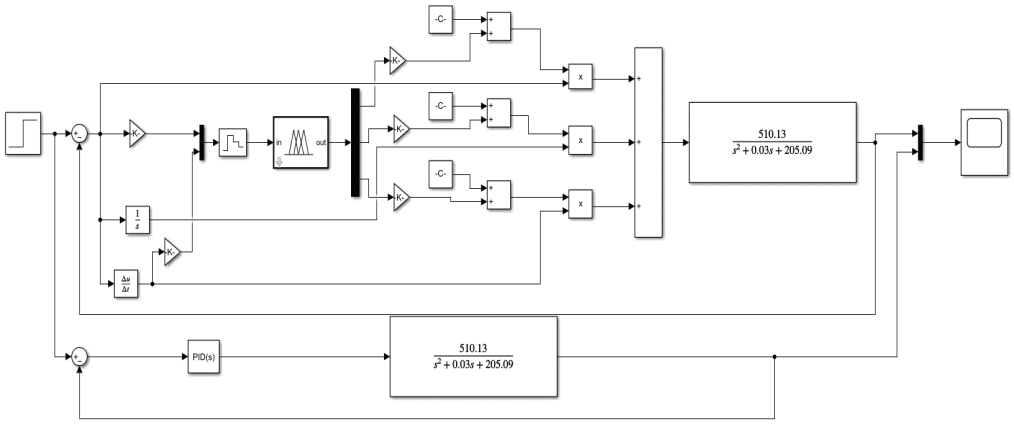

Figure 9. Traditional PID and fuzzy PID simulation models.

2.3.2. Fuzzy Controller Design

To facilitate engineering implementation, triangular membership functions are commonly adopted in practical applications [20]. Based on the characteristics of fertilization rate required by agronomy and actual operating conditions, the feasible ranges for fertilizer application rate errors e and ec are set to [−30 g·s^{-1}, 30 g·s^{-1}] and [−15 g·s^{-1}, 15 g·s^{-1}], respectively. Other defined variables and their values are shown in Table 1. According to the PID parameter adjustment principles and the actual adjustment process and experience of the fertilizer discharge device, fuzzy control rules are established, as shown in Table 2.

https://doi.org/10.3390/agriculture16030290

Table 1. Fuzzy PID algorithm parameter setting.

Input and Output Variables	e	ec	Δk_P	Δk_i	Δk_d
language variable	E	EC	ΔK_P	ΔK_i	ΔK_d
Basic Domain	$[-30, 30]$	$[-15, 15]$	$[-1, 1]$	$[-0.5, 0.5]$	$[-2, 2]$
fuzzy subset	[NB NM NS ZE PS PM PB]				
fuzzy universe	$[-3, 3]$	$[-1.5, 1.5]$	$[-3, 3]$	$[-1.5, 1.5]$	$[-6, 6]$
quantitative factor	0.1	0.1	3	3	3

Table 2. Fuzzy rule table.

Parameter	ec	e						
		NB	**NM**	**NS**	**ZO**	**PS**	**PM**	**PB**
ΔK_P	NB	PB	PB	PM	PM	PS	ZO	Z0
	NM	PB	PB	PM	PS	PS	ZO	NS
	NS	PM	PM	PM	PS	ZO	NS	NS
	ZO	PM	PM	PS	ZO	NS	NM	NM
	PS	PS	PS	ZO	NS	NM	NM	NM
	PM	PS	ZO	NS	NM	NM	NM	NB
	PB	ZO	ZO	NM	NM	NB	NB	NB
ΔK_i	NB	NB	NB	NM	NM	NS	ZO	ZO
	NM	NB	NB	NM	NS	NS	ZO	ZO
	NS	NB	NM	NS	NS	Z0	PS	PS
	ZO	NM	NM	NS	Z0	PS	PM	PM
	PS	NM	NS	ZO	PS	PS	PM	PB
	PM	ZO	ZO	PS	PS	PM	PB	PB
	PB	ZO	ZO	PS	PM	PM	PB	PB
ΔK_d	NB	PS	NS	NB	NB	NB	NM	PS
	NM	PS	NS	NB	NM	NM	NS	ZO
	NS	ZO	NS	NM	NM	NS	NS	ZO
	ZO	ZO	NS	NS	NS	NS	NM	ZO
	PS	ZO	ZO	ZO	ZO	Z	ZO	ZO
	PM	PB	NS	PS	PS	PS	PS	PB
	PB	PB	PM	PM	PM	PS	PS	PB

Sensitivity analysis of fuzzy PID parameters:

1. When the system exhibits significant deviation, prioritize the application of a reinforced proportional-derivative control strategy. At this stage, increase the proportional gain ΔK_p to accelerate error elimination while reducing the derivative gain ΔK_d to prevent overshoot. Typically, set the integral gain ΔK_i to zero to avoid integral saturation. This configuration balances response speed and stability requirements.
2. When the deviation converges to a smaller range, the proportional gain ΔK_p and integral gain ΔK_i should be increased simultaneously. This strategy maintains the system's ability to adjust for deviations while enhancing steady-state accuracy through integral action. Care must be taken to avoid oscillations or reduced stability caused by excessively large parameters.
3. If the deviation and its rate of change share the same sign, particularly when approaching the target value, the proportional control component and integral action exhibit an inverse relationship. By suppressing the integral accumulation effect, overshoot and accompanying periodic oscillations can be effectively avoided, thereby achieving a smooth convergence process.

https://doi.org/10.3390/agriculture16030290

4. When the absolute value of deviation change rate is large, ΔK_p should be appropriately reduced to minimize sudden increases in control output, while simultaneously increasing ΔK_i to enhance cumulative compensation for dynamic error. This balances system disturbance rejection with control robustness.

2.3.3. Fuzzy PID Control Simulation

To verify the effectiveness of the control system, a numerical simulation model of the control system was constructed using the MATLAB/Simulink platform to compare and analyze the control performance of fuzzy PID and traditional PID. A fuzzy inference system with two inputs and three outputs was created in the MATLAB Fuzzy Logic Toolbox, defining the domain range and membership functions of the input and output variables. Forty-nine fuzzy conditional statements based on expert experience were imported through the rule editor to complete the construction of the fuzzy rule base. The fuzzy PID controller module and the mathematical model of the control system were integrated into Simulink, with a step signal as the system input. A traditional PID control comparison model was also established simultaneously to ensure that both had the same initial conditions, as shown in Figure 9. Through simulation analysis, the PID parameters of the controlled object were tuned, and the system response speed and overshoot were observed.

The system simulation duration is 10 s. When the fertilizer discharge rate is adjusted from 0 to 10 g·s^{-1}, the simulation curve is shown in Figure 10. The traditional PID control reaches steady state at 3.86 s, with a maximum overshoot of 2.1 g·s^{-1}. The fuzzy PID control reaches steady state at 1.15 s, with a system overshoot of 0.5 g·s^{-1}. Compared with traditional PID control, the system's rise time is reduced by 68.75%, the time required for the system to reach steady state is reduced by 70.21%, and the system has a shorter response time and stronger stability.

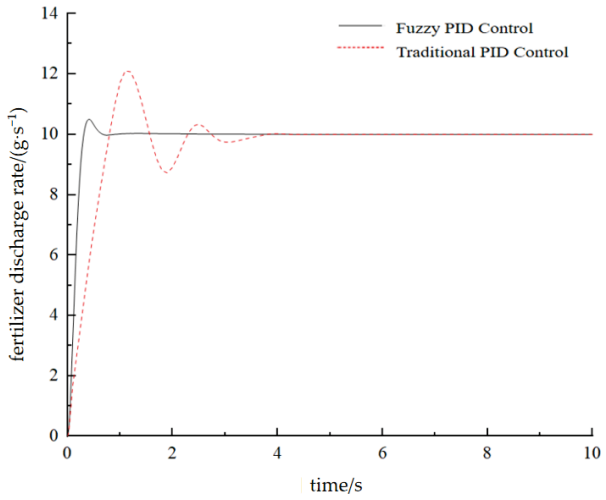

Figure 10. Simulation results of conventional PID and fuzzy PID applied fertilizer control.

The advantage of fuzzy PID in maintaining consistency under high-throughput operating conditions lies in its adaptive physical mechanism. Fuzzy PID fuzzifiers input variables (such as *e*, *ec*) through a fuzzy rule library, and dynamically adjusts PID parameters (such as ΔKp, ΔKd, ΔKi) based on expert experience or adaptive algorithms to achieve nonlinear mapping; the fuzzy inference mechanism of fuzzy PID smooths the error signal through the membership function, reducing the impact of measurement noise on the control output.

https://doi.org/10.3390/agriculture16030290

2.3.4. System Control Principle

During operation, the system is first initialized, which involves initializing the timer, serial port, external interruption and SPI bus. Then set the target plot fertilization rate, number of working rows, and working width. The target fertilization amount, number of working rows, and working width of the plot are set on the human–computer interaction interface. Timer TIM3 uses encoder mode to convert the rotation speed of the ground wheel into an electrical signal, and the STM32 converts the electrical signal into implement speed information. Encoder speed measurement is acquired via ports PA6 and PA7 from channels CH1 and CH2 of timer TIM3; channel CH1 of TIM1 transmits PWM waves to drive the stepper motor. Timer TIM4 is used to achieve timed acquisition of working speed and fertilization amount information. The STM32 converts the digital signals collected by the data acquisition module into actual flow values, calculates the real-time target fertilization amount based on the working parameters set on the human–computer interaction interface and the implement traveling speed, calculates the fertilization amount error by comparing the target value with the actual value, obtains the error change rate through differential operation, and forms a dual-input fuzzy PID. Based on fuzzy control rules, the PID parameters are tuned online, and the fertilization motor speed is dynamically adjusted through outputting PWM signals, achieving closed-loop control of fertilizer flow.

2.4. Simulation Analysis of Shunt Distribution Uniformity

2.4.1. Shunt Distribution Uniformity Simulation Test

In the simulation, the granular fertilizer is simplified as a hard sphere model, with a diameter of 2 mm, Poisson's ratio of 0.25, shear modulus of 1.1×10^8 Pa and density of 845.61 kg·m^{-3}. The contact model is set to the Hertz–Mindlin non-sliding contact model. To facilitate the simulation analysis, the diverted granular fertilizer is collected in six rectangular empty slots. Figure 11 shows the simulation model of the diverting structure.

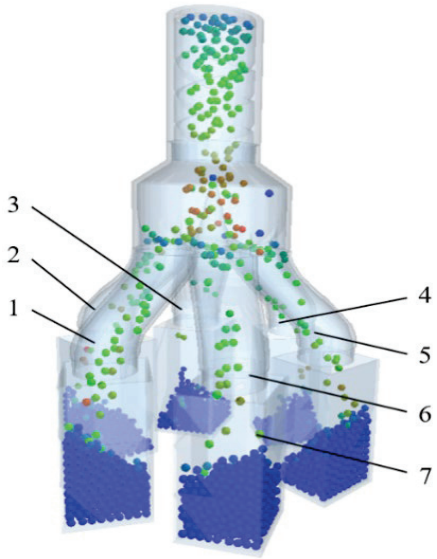

Figure 11. Shunt structure simulation model. 1–6. Diversion tube; 7. granular fertilizer hard ball model. Notes: All colored balls are uniformly labeled as granular fertilizer, solely for the convenience of observation.

2.4.2. Test Method

According to Section 2.2, the maximum fertilizer discharge frequency is approximately 257 Hz. Since the inclination angle of the fertilizer applicator during field operations generally does not exceed 5°, EDEM simulation tests were conducted for the particle

https://doi.org/10.3390/agriculture16030290

factory to generate particles at speeds of 100, 200, 300, and 400 particles per second under inclined conditions of 1°, 3°, and 5°. Each simulation was performed three times, and the average value was taken. During the simulation tests, the particle generation time was set to 10 s, and the total simulation time was 15 s. The initial velocity of the granular fertilizer generated in the particle factory was set to v_x = 0.5 m·s^{-1}, v_y = 0.5 m·s^{-1}, and vz = 0.5 m·s^{-1}, so that the granular fertilizer falls along the inner wall of the fertilizer distributor device. The number of granular fertilizers in the fertilizer receiving box was counted through the EDEM post-processing module. By processing the simulation data, the consistency variation coefficient of the fertilizer discharge amount from the shunt branch pipe under different inclination angles was obtained. The smaller the variation coefficient, the better the shunt uniformity. A radar chart was drawn using Origin 2023 software, as shown in Figure 12.

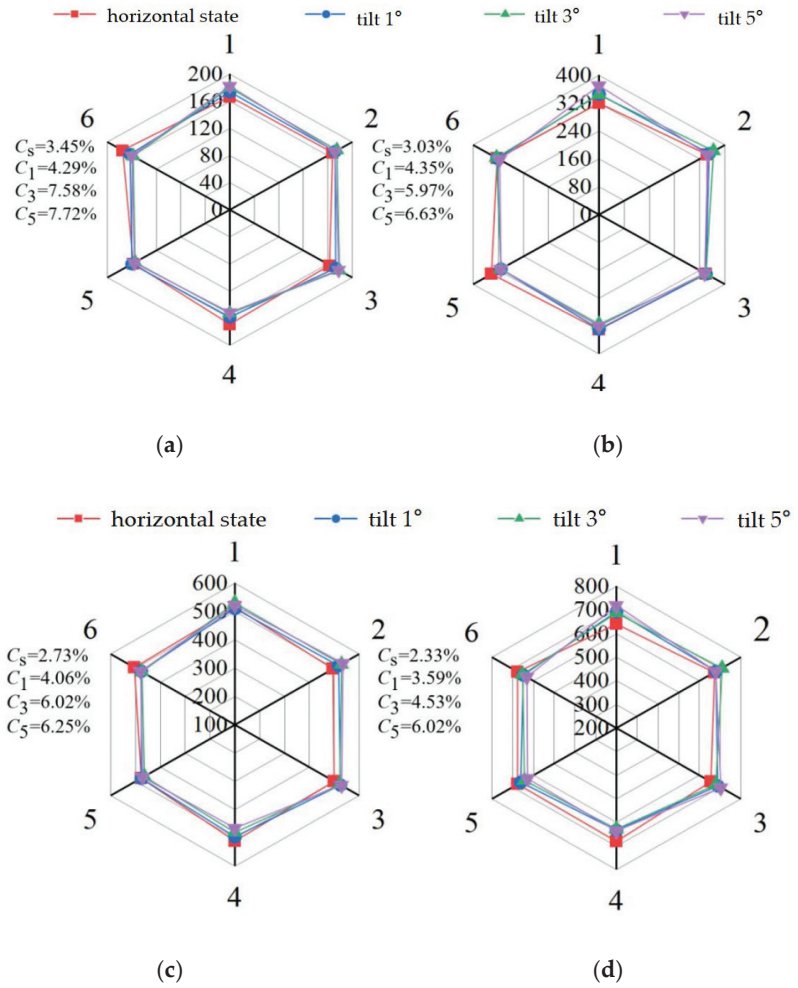

Figure 12. Results of diversion uniformity test. (**a**) 100 grains·s^{-1}. (**b**) 200 grains·s^{-1}. (**c**) 300 grains·s^{-1}. (**d**) 400 grains·s^{-1}. Note: The six corner markers represent six diverging branch pipes. C_S denotes the consistency variation coefficient of each channel in the horizontal state, C_1 is the consistency variation coefficient of each channel at a tilt of 1°, C_3 signifies the consistency variation coefficient of each channel at a tilt of 3°, and C_5 indicates the consistency variation coefficient of each channel at a tilt of 5°. Among them, channels 1, 2, and 3 are channels below the original horizontal plane, while channels 4, 5, and 6 are channels above the original horizontal plane. The tilt angle refers to the angle between the lower end surface of the detection device and the horizontal plane. The numerical values in each circle represent the actual mass of granular fertilizer in each channel.

https://doi.org/10.3390/agriculture16030290

3. Results

3.1. Simulation Analysis of Flow Distribution Uniformity Test

According to Figure 12, when the fertilizer flow rate is the same, the coefficient of variation in the flow consistency among the branch pipes of the flow divider gradually increases with the increase in the inclination angle of the flow divider; at the same inclination angle, the coefficient of variation in the flow consistency among the branch pipes of the flow divider gradually decreases with the increase in the fertilizer flow rate; when the fertilizer flow rate is relatively low, the quantity of granular fertilizer in the branch pipes above the horizontal plane is significantly greater than that in the branch pipes below the horizontal plane, and the difference in the quantity of granular fertilizer between the two gradually decreases with the increase in the fertilizer flow rate. When the granular fertilizer generation rate is 100 grains·s^{-1} and the inclination angle is 5°, the coefficient of variation in the flow consistency among the branch pipes of the flow divider is 7.72%, indicating that the flow divider can maintain good flow distribution performance even when the fertilizer flow rate is low and the inclination angle is large.

3.2. Rack and Field Tests

3.2.1. Shunt Distribution Uniformity Bench Test

To verify the feasibility of the uniform fertilizer device and the shunt divider design, a bench test for flow uniformity was conducted. The main equipment used in the test included an inclined staggered fertilizer feeder, a uniform fertilizer device, a shunt divider, a fertilizer receiving bucket, an electronic scale, an angle measuring instrument, a stepper motor, a control box, etc. The test bench is shown in Figure 13.

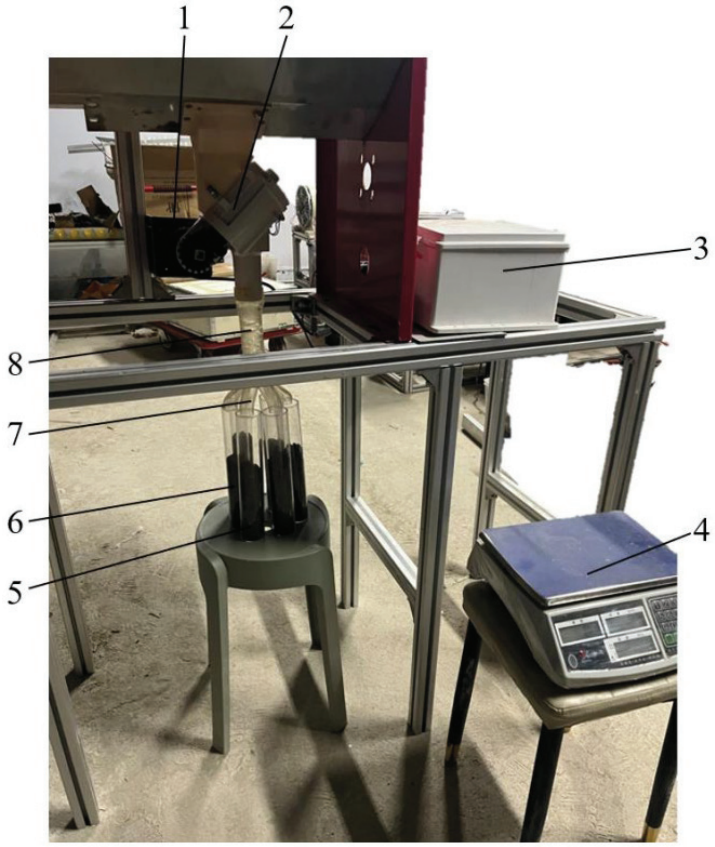

Figure 13. Shunt uniformity test bench. 1. Stepper motor; 2. oblique-type staggered tooth fertilizer distributor; 3. control box; 4. electronic scale; 5. fertilizer bucket; 6. granular fertilizer; 7. diversion device; 8. uniform fertilizer distribution device.

https://doi.org/10.3390/agriculture16030290

Stanley compound fertilizer was selected as the material for this bench test, and the fertilizer particles were dry and non-caking. Its average diameter is 2 mm, with a bulk density of 1000 kg·m^{-3}, low moisture content, and low hygroscopicity. Before the test, an angle measuring instrument was used to measure whether the flow divider was horizontal. The uniformity test of the fertilizer discharge was conducted at fertilizer discharge speeds of 5, 15, and 25 r·min^{-1} for the uniform fertilizer device and flow divider. The test was divided into three scenarios: without a uniform fertilizer device, without a uniform fertilizer retaining ring, and with a uniform fertilizer retaining ring. When there was no uniform fertilizer retaining ring, the uniform fertilizer device only had a uniform fertilizer retaining rod; when there was a uniform fertilizer retaining ring, the uniform fertilizer device included both the uniform fertilizer retaining ring and the retaining rod. During the test, when there was a uniform fertilizer device, the upper end of the uniform fertilizer device was connected to the fertilizer outlet of the fertilizer discharge device, and the lower end was connected to the fertilizer inlet a of the flow divider; when there was no uniform fertilizer device, the upper end of the flow divider was directly connected to the fertilizer outlet of the fertilizer discharge device. Each test was conducted three times, and the results were averaged. Each test lasted for 30 s, and after each test, the granular fertilizer in six receiving buckets was weighed. The test results are shown in Figure 14.

Granular fertilizer quality/g branch pipe

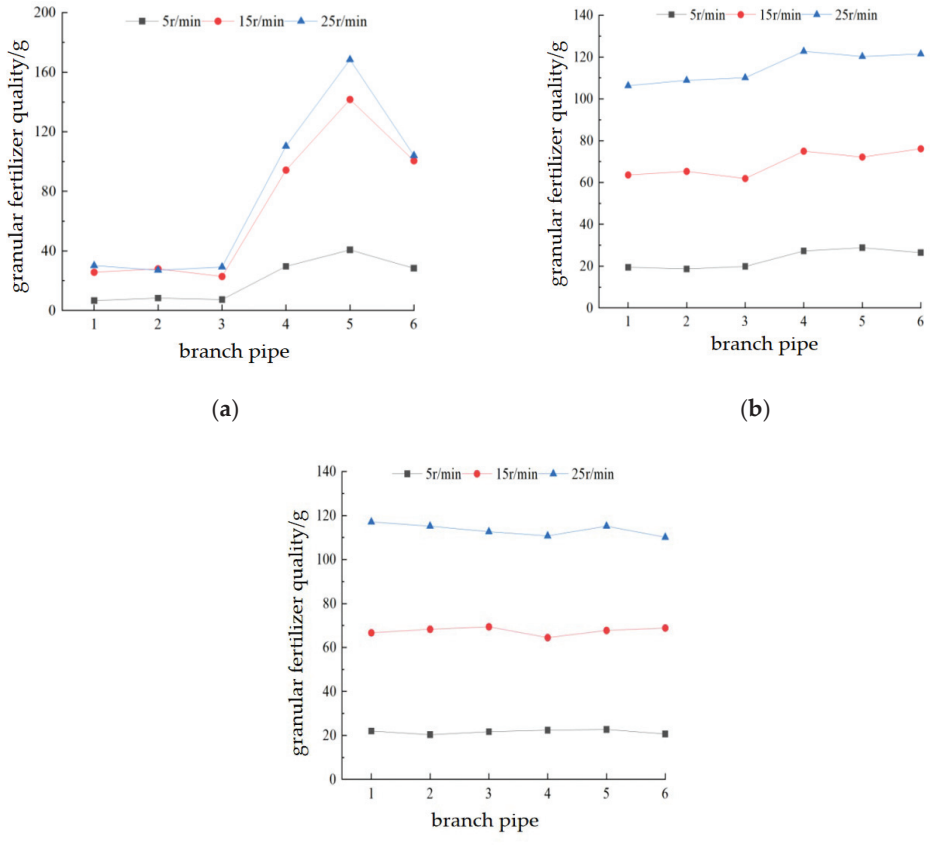

Figure 14. Results of shunt uniformity test. (**a**) Non-uniform fertilizer application device; (**b**) non-uniform fertilizer distribution ring; (**c**) equipped with a uniform fertilizer distribution ring.

From Figure 14, when there is no fertilizer uniform device, there is a significant difference in the mass of granular fertilizer among the six diverging branch pipes. Among them, the mass of granular fertilizer in branch pipes 1, 2, and 3 is relatively small, while that

https://doi.org/10.3390/agriculture16030290

in branch pipes 4, 5, and 6 is relatively large. When there is no fertilizer uniform retaining ring, the uniformity of flow is improved, but there is still a certain difference in the mass of granular fertilizer among the six diverging branch pipes. When there is a fertilizer uniform retaining ring, the uniformity of flow in each diverging branch pipe is better; at the same time, the coefficient of variation in flow consistency at different rotational speeds is calculated. The coefficients of variation in flow uniformity from low to high rotational speeds of the fertilizer feeder are 4.37%, 2.64%, and 2.43%, respectively, indicating that the flow uniformity gradually increases with the increase in rotational speed. The fertilizer uniform device and the diverging device meet the operational requirements of the system.

3.2.2. Performance Test of Response Time to Changes in Fertilizer Discharge Quantity

The response time to changes in fertilizer discharge quantity is a key factor affecting the effectiveness of variable-rate fertilization operations. Due to the difficulty of measuring this indicator in field experiments, a simulated process was conducted on a test bench as shown in Figure 15. The test bench was constructed from a fertilizer box, conveyor belt, etc. The surface of the conveyor belt was made of hard rubber to prevent fertilizer particles from bouncing and shifting. The height of the fertilizer box frame was adjusted so that the fertilizer discharge opening was 0.1 mm away from the conveyor belt. The STM32 controller adjusted the speed of the conveyor belt motor, the human–machine interface set the fertilizer amount, and the encoder and friction wheel measured the conveyor belt speed. Conveyor belt parameters are as follows: width 0.4 m and total length 3.0 m.

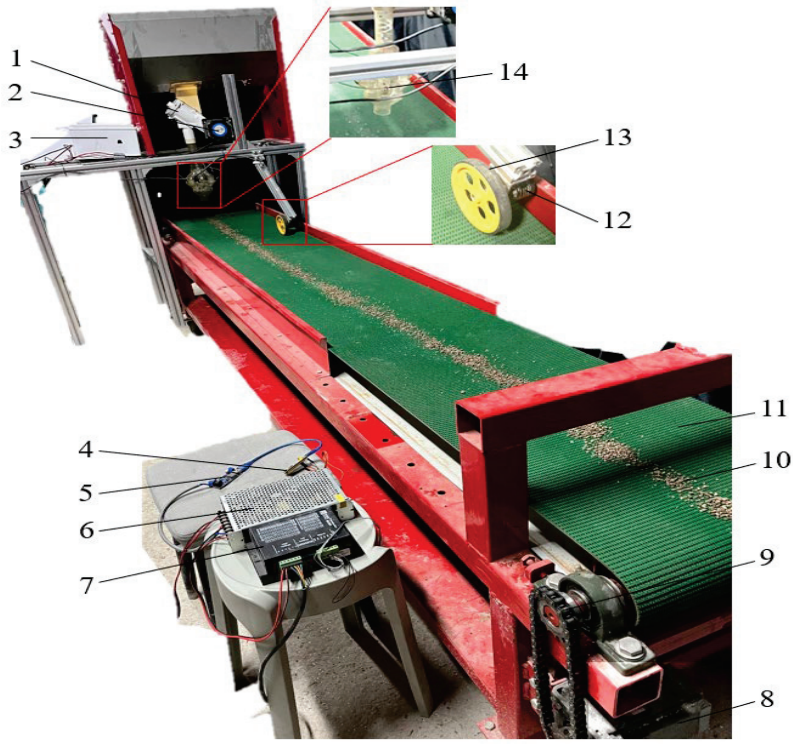

Figure 15. Response time performance test bench for fertilizer discharge variation. 1. Oblique-type staggered tooth fertilizer distributor; 2. fertilizer discharge motor; 3. control box; 4. STM32controller; 5. step-down module; 6. switching power supply; 7. motor driver; 8. conveyor belt motor; 9. chain; 10. granular fertilizer; 11. conveyor belt; 12. speed measuring encoder; 13. friction wheel; 14. shunt parallel detection device.

Using the fertilizer discharge response time test platform, the response times of traditional PID and fuzzy PID control to changes in fertilizer discharge were tested separately. The human–computer interaction interface was set with the same operational parameters

https://doi.org/10.3390/agriculture16030290

as in the field experiment, including three rows of operations, a width of 1.2 m, and a target fertilizer application rate of 225 kg·hm^{-2}. Considering the operational performance of the conveyor belt, tests were conducted on the response time to changes in fertilizer discharge at operating speeds ranging from 1.8 km·h^{-1} to 2.88, 3.6, and 4.32 km·h^{-1}. To eliminate errors caused by manual adjustment of the conveyor belt stepper motor speed, the STM32 program algorithm was set to maintain a conveyor belt speed of 1.8 km·h^{-1} for the first 8 s and then we changed the speed to 8 s. The granular fertilizer after 7 s was used as the test data. After the fertilization was completed, the fertilizer discharge amount within a range of 3.0 m on the conveyor belt at intervals of 0.2 m was recorded, and the respective fertilizer amounts and time points were noted to obtain the results of fertilizer discharge variation with response time, as shown in Figure 16.

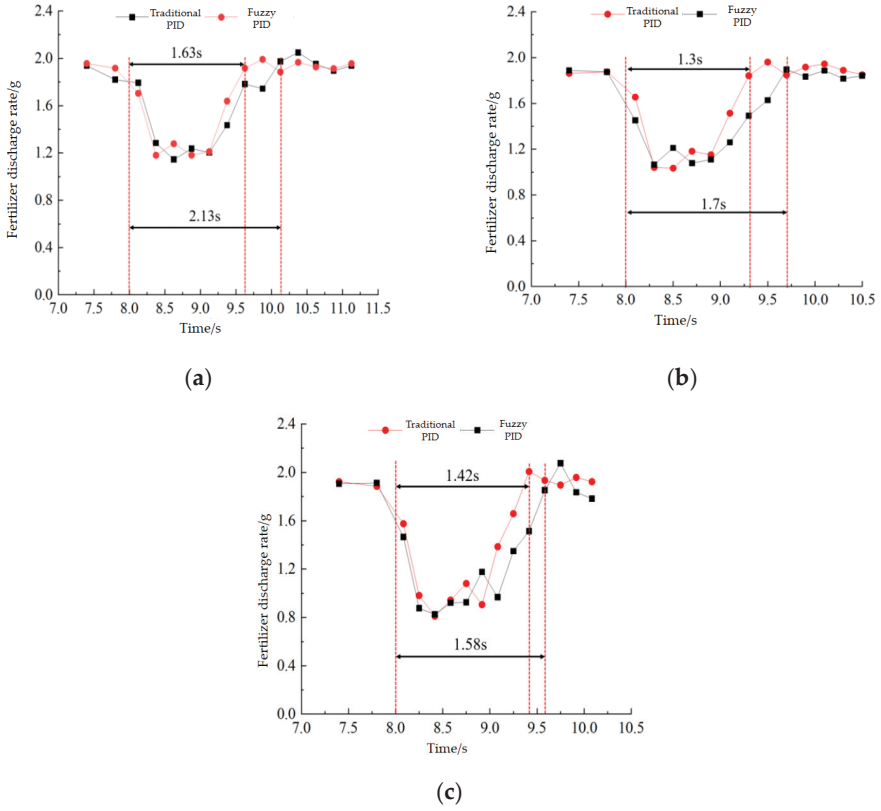

Figure 16. Results of response time test for fertilizer discharge variation. (**a**) 2.88 km·h^{-1}; (**b**) 3.6 km·h^{-1}; (**c**) 4.32 km·h^{-1}. Notes: In the figure, the seconds are marked between the two dashed lines, representing the response time.

The experimental results indicate that when the operating speed varies from 1.8 km·h^{-1} to 2.88, 3.6, and 4.32 km·h^{-1}, the maximum response time of fuzzy PID control is 1.63 s, and the average response time is 1.45 s; the maximum response time of traditional PID control is 2.13 s, and the average response time is 1.80 s. The fuzzy PID control has an average reduction of 19.44% in response time compared to traditional PID control, indicating that the fuzzy PID control has a shorter response time for fertilizer dispensing.

3.2.3. Fertilizer Discharge Quantity Control Accuracy Test

To verify the control accuracy of the system's fertilizer discharge volume, a test was conducted on the fertilization test bench. The main equipment used in the test included a fertilizer discharge device, flow divider, fertilizer uniform device, sensing device, fertilizer collection pipe, fertilizer receiving bucket, fertilizer discharge stepper motor, electronic scale, STM32, etc. The test bench is shown in Figure 17. Before the test, the same operating

https://doi.org/10.3390/agriculture16030290

parameters as those used in the field test were set on the human–computer interaction interface, with three operating rows, a width of 1.2 m, and a target fertilization amount of 225 kg·hm^{-2} for the plot. Since this test was a stationary bench test, it was not possible to obtain the operating speed in real time. Therefore, four operating speeds were set in the control program, namely 2, 3, 4, and 5 km·h^{-1}. Traditional PID and fuzzy PID control were tested three times at each operating speed, with a total fertilizer discharge time of 20 s.

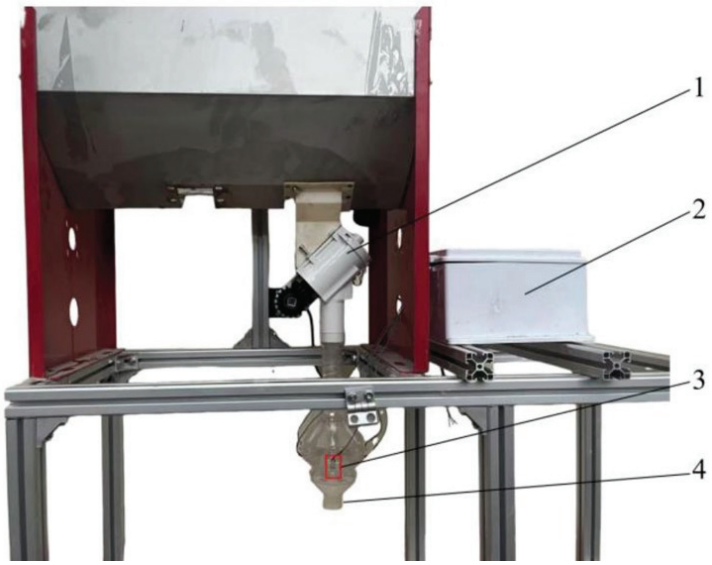

Figure 17. Fertilizer control precision test bench. 1. Fertilizer distributor; 2. control box; 3. PVDF piezoelectric sensor; 4. fertilizer quantity detection device.

After each experiment, the granular fertilizer in the fertilizer bucket was weighed using an electronic scale. The average of the weighing values from the three experiments was recorded as the actual fertilizer discharge amount. The fertilizer discharge rate per unit time, q_{ut}, can be calculated using Formula (2), and the target fertilizer discharge amount is

$$M_1 = 20q_{ut} \tag{13}$$

In Formula (13), M_1 is the target fertilizer application rate, g.

The formula for calculating the control accuracy of fertilizer dispensing quantity is

$$W_1 = \left(1 - \frac{|M_1 - M_2|}{M_1}\right) \times 100\% \tag{14}$$

In Formula (14), M_2 is actual fertilizer discharge, g; and W_1 is the dispensing control accuracy, %.

As can be seen from Figure 18, under different operating speeds, the fertilizer discharge amount controlled by fuzzy PID control is closer to the target fertilizer discharge amount than that controlled by traditional PID control. According to Formula (12), the maximum control accuracy of the fertilizer discharge amount controlled by traditional PID control is 91.60%, with an average of 90.44%. The minimum control accuracy of the fertilizer discharge amount controlled by fuzzy PID control is 95.50%, with an average of 95.94%. Compared to traditional PID control, fuzzy PID control improves the control accuracy of the fertilizer discharge amount by an average of 5.50%. Therefore, the control accuracy of the fertilizer discharge amount controlled by fuzzy PID is better.

https://doi.org/10.3390/agriculture16030290

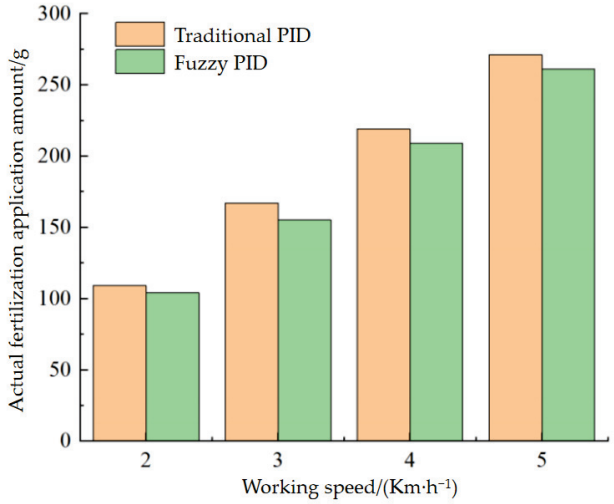

Figure 18. Test result of control precision of fertilizer amount.

3.2.4. Field Experiment

Field experiments were conducted on 25–26 July 2024, in the experimental field of the Changyuan Branch of the Henan Academy of Agricultural Sciences. The experimental plot measured 120 m in length and 20 m in width. The experimental equipment utilized was a fertilization and seeding machine jointly developed by Henan Agricultural University and Henan Nongyouwang Agricultural Equipment Technology limited company (Henan, China), as depicted in Figure 19. Prior to the experiment, a fertilizer receiving bag was placed beneath the fertilizer outlet of the fertilizer collection pipe to facilitate the measurement of fertilizer discharge volume.



Figure 19. Field fertilizer rate precision control system experiment. 1. MASCHIO fertilizer distributor; 2. stepper motor; 3. fertilizer quantity detection device;4. control box; 5. encoder.

Stanley compound fertilizer was selected as the material for field experiments. Before the experiment, the fertilizer was loaded into a fertilizer box. The target fertilization amount for the plot was set at 225 kg·hm^{-1}, the width of the machinery was set at 1.2 m, and the number of working rows was set at 3. The fertilization and seeding machine were driven at speeds of 2, 3, 4, and 5 km·h^{-1} for 60 s, respectively. After each experiment, the mass of fertilizer in the receiving bag was weighed using an electronic scale to obtain

https://doi.org/10.3390/agriculture16030290

the actual fertilizer discharge amount. Three experiments were conducted at each speed, and the control accuracy of the fertilizer discharge amount was calculated according to Formula (12).

3.2.5. Test Results and Analysis

The test results are presented in Table 3. The minimum and average control accuracy of the fuzzy PID control for fertilizer applications is 95.04% and 95.53%, respectively. For the traditional PID control, the maximum and average control accuracy for fertilizer applications is 91.66% and 89.70%, respectively. When the operating speed is 2, 3, 4, and 5 km·h^{-1}, the average control accuracy of the fuzzy PID control is 96.22%, 95.13%, 95.42%, and 95.36%, respectively, meeting the requirements of GB/T 35487-2017. When the operating speed is 2, 3, 4, and 5 km·h^{-1}, the average control accuracy of the traditional PID control is 90.31%, 89.30%, 88.94%, and 90.24%, respectively. When the homework speed is 2 km·h^{-1}, the average control accuracy of fuzzy PID control is 5.91% higher than that of traditional PID control.; when the homework speed is 3 km·h^{-1}, the average control accuracy of fuzzy PID control is 5.83% higher than that of traditional PID control; when the homework speed is 4 km·h^{-1}, the average control accuracy of fuzzy PID control is 6.48% higher than that of traditional PID control; when the homework speed is 5 km·h^{-1}, the average control accuracy of fuzzy PID control is 5.12% higher than that of traditional PID control. The control accuracy of the fuzzy PID control for fertilizer application at each vehicle speed is higher than that of the traditional PID control, indicating that the system can achieve precise variable fertilization. Due to the influence of vibration and other working conditions in the field on piezoelectric sensors, the control accuracy of the system for fertilizer application under field conditions is slightly lower than that under the conditions of the fertilization test bench.

Table 3. Field experiment of the precision fertilizer control system.

Working Speed/(km·h^{-1})	Target Fertilizer Discharge Rate/(g)	System Type	Actual Fertilizer Discharge/(g)	Fertilizer Application Rate Control Accuracy/(%)
2	300	Traditional PID	266.29	88.76%
			328.43	90.52%
			274.97	91.66%
		Fuzzy PID	312.81	95.73%
			310.03	96.66%
			288.85	96.28%
3	450	Traditional PID	496.57	89.65%
			411.65	91.48%
			509.48	86.78%
		Fuzzy PID	472.30	95.04%
			471.52	95.22%
			428.09	95.13%
4	600	Traditional PID	658.30	90.28%
			652.46	91.26%
			688.36	85.27%
		Fuzzy PID	571.89	95.32%
			625.74	95.71%
			628.66	95.22%

https://doi.org/10.3390/agriculture16030290

Table 3. *Cont.*

Working Speed/(km·h^{-1})	Target Fertilizer Discharge Rate/(g)	System Type	Actual Fertilizer Discharge/(g)	Fertilizer Application Rate Control Accuracy/(%)
5	750	Traditional PID	834.34	88.75%
			818.25	90.90%
			683.04	91.07%
		Fuzzy PID	785.65	95.25%
			781.73	95.77%
			786.95	95.07%

4. Current System Restrictions and Latest Developments

4.1. Current System Restrictions

1. The current system has been optimized for specific fertilizer particle characteristics. In the future, it is necessary to establish a more universal particle physical parameter database, develop adaptive detection algorithms and control models, and improve the compatibility of the system with different shapes, densities, and humidity of granular fertilizers.
2. Under extreme high humidity conditions close to 100% RH, PVDF sensors may experience performance degradation due to excessive adsorption of water vapor. Water vapor may condense on the surface or inside of the sensor, affecting its piezoelectric effect or conductivity, resulting in inaccurate or ineffective measurements; under extreme low humidity conditions close to 0% RH, PVDF sensors may not generate sufficient electrical signals due to a lack of sufficient interaction between water vapor molecules and sensitive materials. This may result in weak or unstable sensor output signals, thereby affecting their measurement accuracy. Try to avoid these two situations as much as possible when working.
3. Mechanical vibration during high-speed field operations can easily cause sensor signal fluctuations and component fatigue. In the future, a multi-level damping structure can be designed to optimize the mechanical stability of the device, while exploring real-time filtering algorithms for vibration noise to further improve detection accuracy and control robustness.

4.2. Latest Developments

1. Multi-channel parallel detection: Blue Rainbow Optoelectronics uses a rotating matrix design with 12 independent optical detection channels to shorten the detection time of N, P, and K for eight soil samples to within 1 h, with a sensitivity of red light $\geq 4.5 \times 10^{-5}$. Compared to reference [1], the delay is smaller.
2. Precision Rotating Colorimetric Cell: Yuntang Technology employs a precision rotating multi-channel colorimetric cell structure integrated with a constant-temperature control module. This design eliminates variations in light source intensity and thermal drift effects between channels, achieving absorbance measurement drift of <0.003 over one hour with error stability maintained at $\leq$1%. Compared to reference [6], it offers higher detection accuracy.

5. Conclusions

1. A high-throughput parallel detection method for granular fertilizer diversion has been proposed. Parametric designs have been carried out for key components such as the uniform fertilizer tube, sensing detection structure, six-channel diversion cone disk, and converging fertilizer tube, and an innovative six-channel parallel detection device

https://doi.org/10.3390/agriculture16030290

has been designed. Research has been conducted on the performance of diversion uniformity. When the generation speed of granular fertilizer is between 100 and 400 particles per second, the coefficient of variation in the diversion consistency in each diversion branch tube of the tilted diversion device gradually decreases with increasing generation speed. Under normal field operation at a tilt angle of 0° to 5°, the coefficient of variation in the diversion consistency in each diversion branch tube does not exceed 7.72%. A multi-channel signal synchronous acquisition system has been designed, and relationship models between the detection flow rate and voltage of granular fertilizer, as well as between the actual flow rate of granular fertilizer and the rotational speed of the fertilizer discharge shaft, have been established through calibration experiments.

2. A real-time precision regulation system control model for fertilizer quantity was established, utilizing fuzzy rules to dynamically adjust the parameters of the PID controller. A fuzzy PID control simulation model was created using MATLAB's Simulink simulation module to analyze the PID parameters of the controlled object and study the system's response speed and overshoot. The control effects of fuzzy PID and traditional PID algorithms were compared. The results showed that fuzzy PID control reduced the time required to reach steady state by 66.87% compared to traditional PID, and the overshoot decreased from 7.38 $g \cdot s^{-1}$ to 1.49 $g \cdot s^{-1}$.
3. Bench tests and field trials were conducted. The results of the bench tests showed that the average response time for fertilizer discharge rate changes under fuzzy PID control was 1.45 s, with an average reduction of 19.44% compared to traditional PID control. The minimum and average control accuracy of fertilizer discharge rate under fuzzy PID control was 95.50% and 95.94%, respectively, representing an average improvement of 5.50% over traditional PID control. Under different test conditions, both the response time for fertilizer discharge rate changes and the control accuracy of fertilizer discharge rate under fuzzy PID control were superior to those under traditional PID control. In field trials, when the operating speed was 2, 3, 4, and 5 $km \cdot h^{-1}$, the control accuracy of fertilizer discharge rate under the fuzzy PID control system reached 96.22%, 95.13%, 95.42%, and 95.36%, respectively, with an average of 95.53%.

Author Contributions: Conceptualization, L.D. and F.W.; methodology, L.D. and F.W.; software, F.W. and Y.Y.; validation, Y.D., F.W.; formal analysis, Y.L. and K.W.; investigation, Y.D. and B.L.; resources, L.D.; data curation, Y.D.; writing—original draft preparation, F.W.; writing—review and editing, F.W. and Y.D.; supervision, L.D.; project administration, L.D.; funding acquisition, L.D. All authors have read and agreed to the published version of the manuscript.

Funding: This research was funded by the National Key Research and Development Program (2022YFD2300904), Modern Agricultural Industry Technology System Project of the Chinese Academy of Agricultural Sciences (CARS-04), and Henan Provincial Science and Technology Key Project (252102111171).

Institutional Review Board Statement: Not applicable.

Data Availability Statement: The original contributions presented in this study are included in the article material. Further inquiries can be directed to the corresponding author.

Acknowledgments: The authors would like to express their sincere gratitude to their colleges and laboratories and to the reviewers who provided helpful suggestions for this manuscript.

Conflicts of Interest: The authors declare no conflicts of interest.

References

1. Zhao, J.; Wang, X.; Tian, H. A fertilizer discharge detection system based on point cloud data and an efficient volume conversion algorithm. *Comput. Electron. Agric.* **2021**, *185*, 106131. [CrossRef]
2. Kumhála, F.; Kvíz, Z.; Kmoch, J.; Prošek, V. Dynamic laboratory measurement with dielectric sensor for forage mass flow determination. *Res. Agric. Eng.* **2007**, *184*, 945–954. [CrossRef]
3. Yang, L.; Zhang, Y.; Zhan, Z.; Jin, Z.; Peng, Y.; Zhu, Y. Research on Microwave Signal Measurement of Particle Fertilizer Flow Rate Based on Variational Mode Decomposition Combined with Wavelet Analysis. *Trans. Chin. Soc. Agric. Mach.* **2025**, *56*, 623–633. [CrossRef]
4. Zhou, L.; Ma, M.; Yuan, Y. Design and experiment of fertilizer application amount detection system based on capacitive method. *J. Agric. Mach.* **2025**, *56*, 623–633. [CrossRef]
5. Shen, Z.; Han, J.; Niu, Z. Collection and Experimental Study of Millimeter Wave Radar Particle Fertilizer Discharge Signal Based on CAFA-PF. *China Agric. Sci. Technol. Guide* **2025**, *21*, 1–13. [CrossRef]
6. Zhao, L.; Zhang, Z.; Wang, C. Design of a monitoring system for wheat precision sowing and fertilizing integrated machine based on variable-range photoelectric sensor. *J. Agric. Eng.* **2018**, *34*, 27–34. [CrossRef]
7. Xu, C.; Liu, J.; Su, Q. Design and experiment of a thin-film light refracting multi-channel parallel detection device for wheat seed flow. *J. Agric. Eng.* **2022**, *38*, 81–91. [CrossRef]
8. Zhang, J.; Liu, G.; Zhang, D. Research status and prospects of variable application control technology for solid granular fertilizer. *Jiangsu Agric. Sci.* **2022**, *50*, 69–77. [CrossRef]
9. John Deere. RelativeFlow^{TM} Jam Monitoring. Available online: www.deere.com/en/seeding-equipment/ (accessed on 11 January 2026).
10. Iida, M.; Umeda, M.; Radite, P.A.S. Variable rate fertilizer applicator for paddy field. In Proceedings of the Annual International Meeting of the American Society of Agricultural Engineers, Sacramento, CA, USA, 30 July–1 August 2001. [CrossRef]
11. Maleki, M.R.; Ramon, H.; De Baerdemaeker, J. A study on the time response of a soil sensor. based variable rate granular fertilizer applicator. *Biosyst. Eng.* **2008**, *100*, 160–166. [CrossRef]
12. Zhang, J.; Yan, S.; Ji, W. Research on Precise Application Control System for Multiple Solid Fertilizers Based on Incremental PID Algorithm. *Trans. Chin. Soc. Agric. Mach.* **2021**, *52*, 99–106. [CrossRef]
13. Ma, X.; Zhao, X.; Liu, S. Design and experiment of variable-rate fertilization device for solid granular fertilizer on high-speed rice transplanter. *Trans. Chin. Soc. Agric. Mach.* **2023**, *54*, 99–110. [CrossRef]
14. Wang, H.; Liu, Y.; Zhou, L. Design and experiment of a segmented PID control system for fertilizer flow rate of a fertilizer and seeding machine. *Trans. Chin. Soc. Agric. Mach.* **2023**, *54*, 32–40+94. [CrossRef]
15. Chen, M.; Lu, W.; Wang, X. Design and experiment of optimal control system for variable topdressing of winter wheat based on fuzzy PID. *Trans. Chin. Soc. Agric. Mach.* **2016**, *47*, 71–76. [CrossRef]
16. Zhang, K. Research on the Vibration Characteristics of a Small-Sized Fertilizer Seed and Its Impact on Fertilizer Discharge Performance. Ph.D. Thesis, Guizhou University, Guiyang, China, 2022.
17. Ding, Y.; Yang, J.; Zhu, K. Design and experiment of seed flow sensing device for precision seed metering device of rapeseed. *J. Agric. Eng.* **2017**, *33*, 29–36. [CrossRef]
18. Liu, W.; Luo, X.; Zeng, S. Performance test and analysis of adaptive contour-following cutting platform for ratooning rice based on fuzzy PID control. *J. Agric. Eng.* **2022**, *38*, 1–9. [CrossRef]
19. Xu, Y.; Lu, J. Fuzzy PID simulation analysis of stepper motor drive system. *J. Mech. Des. Manuf.* **2014**, *12*, 23–25+29. [CrossRef]
20. Yao, Y.; Chen, X.; Ji, C. Design and experiment of single-unit driver for precision corn seeder based on fuzzy PID control. *J. Agric. Eng.* **2022**, *38*, 12–21. [CrossRef]

Disclaimer/Publisher's Note: The statements, opinions and data contained in all publications are solely those of the individual author(s) and contributor(s) and not of MDPI and/or the editor(s). MDPI and/or the editor(s) disclaim responsibility for any injury to people or property resulting from any ideas, methods, instructions or products referred to in the content.

agriculture

MDPI

Article

A Study on the Interaction Mechanism Between Disc Coulters and Maize Root-Soil Composites Based on DEM-MBD Coupling Simulation

Xuanting Liu [1], Zhanhong Guo [2], Zhenwei Tong [3], Miao He [4], Peng Gao [4], Yunhai Ma [4,*] and Zihe Xu [5,*]

[1] College of Intelligent Mechatronics Engineering, Zhongyuan University of Technology, Zhengzhou 450007, China; 7077@zut.edu.cn
[2] College of Mechanical and Electronic Engineering, Tarim University, Alar 843300, China; zhhguo@taru.edu.cn
[3] College of Mechanical and Electronic Engineering, Henan Agriculture University, Zhengzhou 450002, China; tongzhenwei917@henau.edu.cn
[4] Key Laboratory of Bionic Engineering, Ministry of Education, Jilin University, Changchun 130022, China; hemiao25@mails.jlu.edu.cn (M.H.); penggao15@mails.jlu.edu.cn (P.G.)
[5] College of Biological and Agricultural Engineering, Jilin University, Changchun 130022, China
* Correspondence: myh@jlu.edu.cn (Y.M.); zhxu21@mails.jlu.edu.cn (Z.X.)

Abstract

To solve the problems of high resistance and blockage in stubble-breaking operations, it is necessary to reveal the interaction mechanism between disc coulters and crop root–soil composites. This study developed a discrete element method–multi-body dynamics (DEM-MBD) coupling model of the stubble-breaking operation and verified the accuracy of the model through soil bin tests (error < 20%) and field experiments (error < 32%). The model was used to investigate the effects of different design parameters (coulter type and disc radius) and operating parameters (tillage speed and depth) on the stubble-breaking operation. The results showed that due to the significant strengthening effect of roots on soil, the resistance of disc coulter stubble-breaking operation was high; the number of roots in contact with the blade edge and the amount of root deformation significantly affected the resistance of the disc coulter; irreversible deformation of roots and soil could easily lead to the holes and root hairpin effects in the seeding furrow; compared to plain disc coulters, the difference in the time of deformation and fracture of the roots made the resistance of the notched coulter lower. The wavy disc coulter with a longer edge curve made its resistance higher; the disc coulter with a greater radius, higher tillage speed, and deeper tillage depth significantly increased the tillage resistance. However, the disc coulter with a greater radius or a higher tillage speed was beneficial for improving stubble-breaking performance. This study revealed the interaction mechanism between disc coulters and maize root-soil composites, providing a theoretical basis for the optimization design of no-till stubble-breaking devices.

Keywords: disc coulter; root-soil composite; interaction mechanism; discrete element method; multi-body dynamics

1. Introduction

No-till technology can effectively protect soil fertility and prevent soil degradation due to wind and water erosion; therefore, it is widely promoted and popularized [1–3]. However, due to the large amount of straw and stubble left in the farmland, no-till planters usually encounter problems such as severe blockages and high resistance, which have

become one of the main bottlenecks in promoting no-till technology. The stubble is a kind of typical root–soil composite, which has a stable structure formed by the interaction between roots and soil [4–6]. The crop root–soil composite not only causes serious blockage of tillage equipment, high resistance, and energy consumption, but also affects the structure of the seedbed and seed germination [7,8]. Therefore, it is necessary to design a stubble-breaking device that can efficiently break stubble.

The disc stubble-breaking device is a commonly used stubble-breaking component. The most important tillage component of this stubble-breaking device is the disc coulter, which is suitable for breaking thick stubble and stems. It has excellent anti-clogging performance and is widely used in no-till seeders [7,8]. To improve the operational performance of the disc stubble-breaking device, Torotwa et al. [9] developed a biomimetic disc with a morphology similar to mole claws to optimize the disc coulter under dense cover conditions, while minimizing soil disturbance; Zeng et al. [10] compared the operational performance of disc coulters with different numbers of teeth and found that the tillage performance of disc coulters was influenced by the type of coulter. The tooth coulter left less residue and caused greater soil disturbance. The eight-tooth coulter showed the most positive performance in disturbing residues and soil; Kogut, Karayel, Malasli M.Z., and Zhang et al. [11–14] found that the operating and structural parameters of the disc coulter had a significant impact on resistance, operating performance, and tillage depth. Additionally, some studies typically developed empirical models based on data obtained from specific agricultural environments and optimized the design parameters, operational parameters, and other aspects of stubble-breaking devices. Although these studies designed high-performance stubble-breaking devices, they did not reveal the interaction mechanism between stubble-breaking coulters and crop root–soil composites. Therefore, current research and design standards could not provide a theoretical basis for the design of stubble-breaking devices.

In the field of soil and water conservation, mature and systematic theories could provide inspiration for revealing the interaction mechanism between stubble-breaking components and crop root–soil composites. Researchers used experimental, mathematical–analytical, and simulation methods to investigate the impact of roots on soil reinforcement [5,15–18]. These studies showed that roots had a significant mechanical reinforcement effect on the soil. The deeper vertical main roots served as anchor rods, anchoring the surface soil to a more stable lower layer of bedrock. The widely distributed root network spanned across the shear plane. When the soil underwent shear deformation, these roots were stretched, and the shear stress was converted into the tensile force of the roots through the interface force between the root and soil, effectively improving the apparent shear strength of the root–soil composite. In the field of agricultural engineering, scholars have also attempted to use various methods to solve the interaction mechanism between disc coulters and crop root–soil composites. Bai et al. [19] developed a dynamic model to analyze the interaction between tillage equipment and maize stubble. This research showed that factors such as the radius and structure of the disc coulter, stubble size, and cutting speed have a significant impact on stubble-breaking resistance; Liu et al. [20] developed a mathematical-analytical model for the interaction between disc coulters and maize root–soil composites. This research showed that the force on a flat blade for cutting stubble was related to the mechanical properties of roots, soil, and root–soil interfaces. The deformation of roots and soil had a significant impact on the stress and operational efficiency of tillage components. Using experimental methods, Zhao, Zheng et al. [21,22] conducted cutting experiments on maize and rice root–soil composites using a flat blade. The study showed that the operating parameters of the flat blade and the mechanics of roots and soil had a significant impact on the interaction. In recent years, with the rapid development of computer

https://doi.org/10.3390/agriculture16020270

technology and numerical methods, numerical methods have been widely used to study the interaction between tillage components and root–soil composites. Yuan et al. [23] used the finite element method (FEM) to develop a FEM model of maize root–soil composite; Zhang et al. [11,24] used the DEM to develop a DEM model of maize root–soil composite, and based on this model, designed and optimized the optimal combination of operating parameters for the disc coulter; Tamas et al. [25] developed an accurate model of a root–soil composite and explored the interaction law between sweeping bodies and root–soil composites. The study showed that soil solidity and the number of roots per unit volume had a significant impact on the resistance of sweeping operations; Zou et al. [26] developed a spinach root–soil composite model and investigated the effects of operating parameters of a vibrating shovel on the movement patterns of roots and soil particles, as well as the degree of root–soil separation. Obviously, numerical methods were helpful in simulating different work scenarios and evaluating the performance of tillage equipment. These studies only simulated and evaluated macroscopic parameters such as tillage resistance and soil disturbance and did not investigate the interaction process between stubble-breaking components and crop root–soil composites during stubble-breaking operations. According to the theories proposed in the field of soil and water conservation, investigating the quantitative relationship between factors such as resistance of the tillage component, deformation and fracture of roots, and debonding of the root–soil interface, as well as their impact on the operations, could be an effective way to reveal the interaction mechanism.

Based on previous research, this study developed a DEM-MBD coupling model for the interaction between disc coulters and maize root–soil composites. The model was validated through soil bin tests and field experiments. By simulating the stubble-breaking operation of disc coulters, the resistance of disc coulters as well as the deformation of maize roots and soil were given significant attention to reveal the interaction mechanism between the disc coulter and the maize root–soil composite. This study provided a theoretical basis for the design of the stubble-breaking device.

2. DEM-MBD Coupling Simulation of Disc Coulter Stubble-Breaking Operation

2.1. Development of DEM Model for Maize Root–Soil Composite

To simulate the stubble-breaking process of a disc stubble-breaking device and investigate the interaction mechanism between disc coulters and crop root–soil composites, an ideal stubble-breaking operation model needed to be developed to eliminate complex and numerous variables to highlight the interaction process. A DEM model of a soil bin with a maize root–soil composite was developed using EDEM 2020 (Altair Engineering, Edinburgh, Midlothian, UK) (Figure 1). This model was developed for maize root–soil composites in Northeast China. The soil in this area was black loam soil, and the maize variety was Zhengdan 958. The above-ground stem diameter of the maize root–soil composite was 35 mm, and average diameter of the root was 3 mm. The DEM model of maize root was created using SolidWorks 2018 (Dassault Systèmes, Suresnes, France) and EDEM 2020. The geometric model of the maize root was developed using SolidWorks 2018 and was imported into EDEM 2020. The application programming interface (EDEM API) was used to compile the specific particle factory plugin, which was then used to fill the cavities inside the maize root model with particles with a radius of 1.5 mm. A soil bin model was developed with dimensions of 1000 mm $\times$ 400 mm $\times$ 200 mm. According to the research of Liu, Zhang et al. [27,28], developing a soil bin model using randomly generated particles with a radius of 2 mm was accurate and reliable. To accurately describe the adhesion behaviour between each particle, as well as the deformation and failure behaviour of roots and soil during the stubble-breaking process, it is important to use a suitable contact model. Black loam

https://doi.org/10.3390/agriculture16020270

soil has macroscopic high adhesion and agglomeration characteristics, so Hertz-Mindlin with bonding and JKR contact models were most suitable for simulation [28,29]. The Hertz–Mindlin with bonding model could describe the contact force generated by particle motion. Once this contact force exceeded the critical value, it could fracture and would not be repaired. The JKR contact model could accurately describe soil adhesion behaviour. Therefore, a DEM model of maize root–soil composite could be developed based on the two models. Basic physical parameters (Table 1), parameters of Hertz–Mindlin with bonding and the JKR contact model (Table 1), and friction parameters (Table 2) were assigned to the particle of root, soil, and root–soil interface [11,30]. The calculation grid size was set to 5 mm, the Rayleigh time step size to 10^{-6} s, and the saved data interval to 0.001 s.

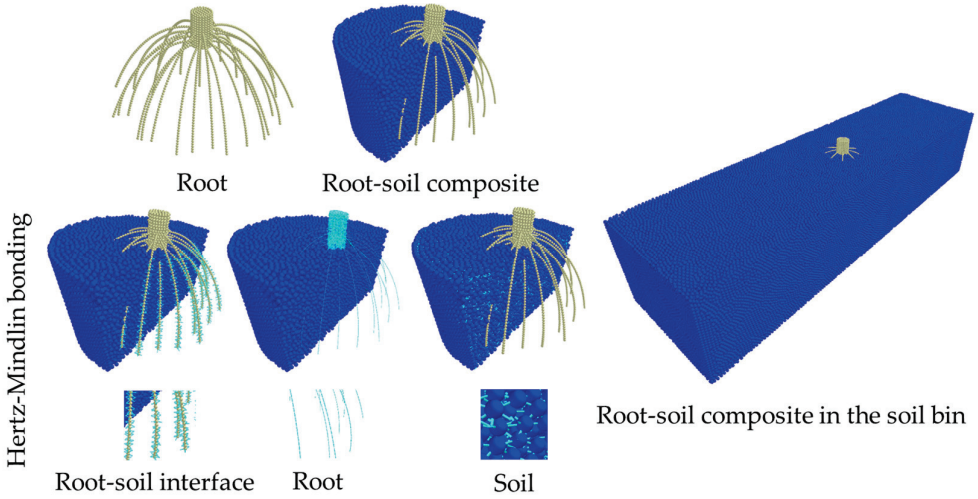

Figure 1. DEM model of maize root–soil composite.

Table 1. Key parameters of the DEM model.

Parameter	Material	Value
Density (kg/m^3)	root	107
	soil	2620
	65Mn steel	7650
Poisson's ratio	root	0.25
	soil	0.30
	65Mn steel	0.30
Young's modulus (Pa)	root	3.00×10^7
	soil	2.60×10^7
	65Mn steel	2.50×10^{11}
Normal stiffness of bond (N/m^3)	soil–soil	1.19×10^7
	root–root	7.74×10^9
	soil–root	4.00×10^7
Critical stresses of bond (Pa)	soil–soil	1.00×10^7
	root–root	7.00×10^8
	soil–root	1.00×10^7
Bond disc radius (mm)	soil–soil	0.66
	root–root	1.56
	soil–root	1.10
Surface energy coefficients (J/m^2)	soil–root	3.38

https://doi.org/10.3390/agriculture16020270

Table 2. Key friction parameters of the DEM model.

Parameter	Material	Value
Coefficient of restitution	soil–soil	0.60
	root–root	0.65
	soil–root	0.65
	soil–steel	0.60
	root–steel	0.32
Coefficient of static friction	soil–soil	0.60
	root–root	0.62
	soil–root	0.55
	soil–steel	0.40
	root–steel	0.60
Coefficient of rolling friction	soil–soil	0.30
	root–root	0.25
	soil–root	0.32
	soil–steel	0.25
	root–steel	0.20

2.2. Development of DEM-MBD Coupling Model

The disc stubble-breaking device was a kind of passive stubble-breaking device, and the disc coulter was a passive coulter that rotated due to the reaction forces of the soil and the stubble acting on the coulter, and the traction force of the tractor. The motion module in EDEM 2020 could not simulate this passive motion, while Recurdyn 2020 (FunctionBay, Inc., Seongnam-si, Republic of Korea) could transmit it to EDEM 2020 through a collaborative simulation interface and module to meet the simulation requirements of the disc coulter. The disc coulter was imported into Recurdyn 2020, and mechanism constraints were added to the model to obtain the MBD model (Figure 2a). Based on the DEM model of maize root–soil composite and the MBD-DEM coupling algorithm, the disc coulter model was imported into EDEM 2020, and data sharing between the two software was achieved through the coupling interface, thus conducting the MBD-DEM coupling simulation (Figure 2b). In contrast, due to the stiffness of 65Mn was much greater than that of maize roots and soil, the deformation of the disc coulter processed from 65Mn could be ignored during stubble-breaking operations. This simplification method was proven by Zhang et al. [11] to have minimal impact on the simulation. The model was validated through the most common disc stubble-breaking operation scenario in the black soil area of Northeast China, where the tillage depth was 80 mm, and the tillage speed was 1 m/s. Considering operational efficiency and simulation accuracy, the fixed time step should be set to 1×10^{-6} s.

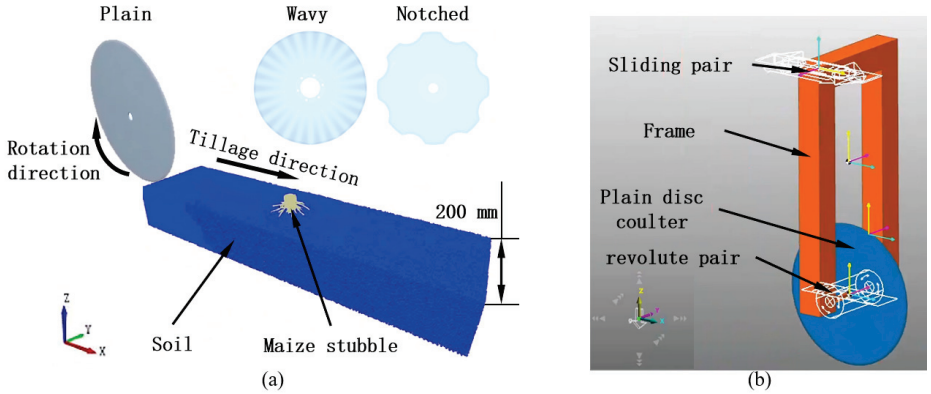

Figure 2. DEM-MBD coupling model of disc stubble-breaking operations: (**a**) MBD model of disc stubble-breaking device; (**b**) DEM-MBD coupling model of disc stubble-breaking operation and each disc coulter.

2.3. Simulation Method

Due to the significant impact of different tillage parameters and design parameters on the stubble-breaking operation of disc coulters, the DEM-MBD coupling model was used to investigate the effects of these parameters on the interaction mechanism between disc coulters and maize root–soil composites, as shown in Table 3.

Table 3. Factors and levels of the design and the operation parameters of the disc coulter.

Levels	Types of Disc Coulter	Disc Radius *R*/mm	Tillage Speed *v*/(m/s)	Tillage Depth *h*/mm
1	Plain	120	0.5	60
2	Notched	170	1.0	80
3	Wavy	220	1.5	100

According to the previous research [20], to investigate the influence of various factors on the interaction mechanism, the performance of the disc coulter was evaluated using peak resistance (horizontal peak resistance, vertical peak resistance), average resistance (horizontal average resistance, vertical average resistance) and root dragging distance. The peak resistance was defined as the maximum resistance acted on the disc coulter during the stubble-breaking operation. The average resistance calculation equation was as follows:

$$F = \frac{1}{x_2 - x_1} \int_{x_1}^{x_2} F(x) \mathrm{d}x \tag{1}$$

$F(x)$—Instantaneous force at each displacement point x, N;

x_1, x_2—Start and end points of the displacement interval, mm.

Due to the fact that the average resistance could evaluate the stubble-breaking performance of the disc coulter throughout the entire stubble-breaking process and the measurement values were relatively stable, it was used to verify the accuracy of the model.

According to previous research [20], the fracture and deformation of the root could significantly affect the resistance of the cutting blade. At the same time, evaluating the deformation and fracture of roots could help evaluate the cutting effect of the disc coulter on maize root–soil composites. Therefore, to evaluate the cutting effect, the dragging distance of the disc coulter on the root was evaluated. A typical cutting case (Figure 3) was selected as the evaluation object, and the morphology of other roots were observed. The root dragging distance was defined as the displacement at the point of contact between the disc coulter and the maize root from the moment the disc coulter came into contact with the maize root until the maize root fractured. As shown in Figure 3, s was the root dragging distance.

The force-displacement curve of the disc coulter used to calculate the peak resistance and the average resistance, as well as the displacement of root particles to calculate the root dragging distance, could be output using EDEM 2020. Based on the research of Zhang et al. [28], the DEM simulation indicated that tillage resistance was highest at 30 mm from maize stalks. To obtain maximum resistance data, the disc coulter was set to operate 30 mm from the stalk axis.

https://doi.org/10.3390/agriculture16020270

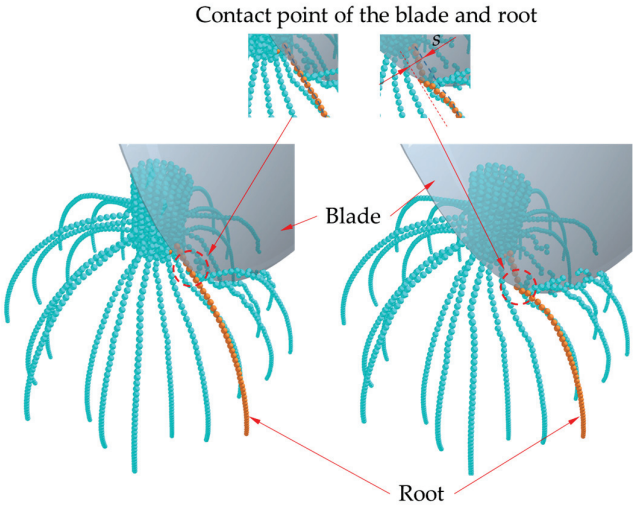

Figure 3. The dragging distance of the maize root.

3. Field Experiments

To verify the accuracy of the DEM model and evaluate the actual performance of the disc coulter in the field, it was necessary to conduct soil bin tests and field experiments.

3.1. Materials and Equipment

The field experiment and material collection for the soil bin test were conducted on 28 October 2023, at the Agricultural Experimental Base of Jilin University in Changchun, Jilin Province. The experimental field had been managed under conservation tillage for over five years. The maize variety collected for the soil bin test was Zhengdan 958, and its roots were mainly distributed in the soil layer at a depth of 0–80 mm. The average diameter of the maize stalks was 25 mm. The sample size of the root–soil composite was a cylinder with a diameter of 300 mm and a height of 200 mm. The average root density was 138.20 kg/m^3. The wet basis moisture content of the root was 64.78–85.60%. The soil belonged to the black loam soil (46.11% sand, 30.78% silt, and 23.11% clay). The average soil compaction of the tillage layer was 1.12 MPa. The average bulk density of the soil was 2.60 g/cm^3, and the average soil moisture content was 20.12%.

The soil bin test was conducted in the soil bin laboratory (30 m long, 4 m wide) of the College of Biological and Agricultural Engineering at Jilin University (Figure 4a). The soil preparation process was as follows: break up and level the soil—sprinkle water to adjust soil moisture content—compact the soil—bury maize stubble—compact the soil. The soil moisture content in the soil bin was adjusted to 19 $\pm$ 0.5%, and soil firmness to 1.2 $\pm$ 0.2 MPa. To prevent interference between experimental groups and ensure efficient testing, the soil bin was divided into three sections. The two sides of the sections were set as transition sections, with each transition area measuring 5 m in length. The central section, totaling 6 m in length, was selected as the stable section for recording experimental data. Within the stable section, three rows of maize stubble were arranged along the length of the soil bin, spaced 0.5 m apart. Within each row, three maize stubble points were positioned, also spaced 0.5 m apart (Figure 4a). The primary experimental equipment comprised a soil bin trolley testing system and an experimental platform (Figure 4b). The experimental platform consisted of a frame, two ground wheels, and a three-dimensional force measurement device. The disc coulters were mounted onto the three-dimensional force sensor via a clamping fixture, which was in turn secured to the frame. Before the experiment, a 120 kg counterweight was placed on the frame, and the tillage depth of the disc coulter was adjusted using a ground wheel. During the experiment, the soil bin trolley pulled the experimental platform in a straight-line motion, and a three-dimensional force

https://doi.org/10.3390/agriculture16020270

sensor (Figure 4b) was used to output the horizontal and vertical resistances acting on the disc coulter in real time. It should be noted that the collected maize stubble would be disturbed, which would have a negative impact on the experimental results. However, due to the fact that the disc coulter broke the maize stubble downwards and forwards during the stubble-breaking operation, the influence of deep distributed roots and soil on the operation was not significant, resulting in minimal errors. It was validated by the research of Zhao et al. [31].



Figure 4. Soil bin tests. (**a**) Experiment site and (**b**) experimental equipment; I: torque sensor; II: soil bin trolley testing system; III: three-dimensional force sensor; IV: disc coulter.

Field experiments employed a John Deere 1354 tractor and experimental platform (Figure 5a,b). The experimental platform was connected to the tractor via its three-point hitch. Similarly to the soil bin test, before the experiment, a counterweight was used to apply sufficient downward pressure to the disc coulter to ensure effective breaking residues [32]. The tillage depth of the disc coulters was ensured by adjusting the two ground wheels. During the experiment, a three-dimensional force sensor (Figure 5b) was used to monitor the horizontal and vertical resistances acting on the disc coulters in real time.

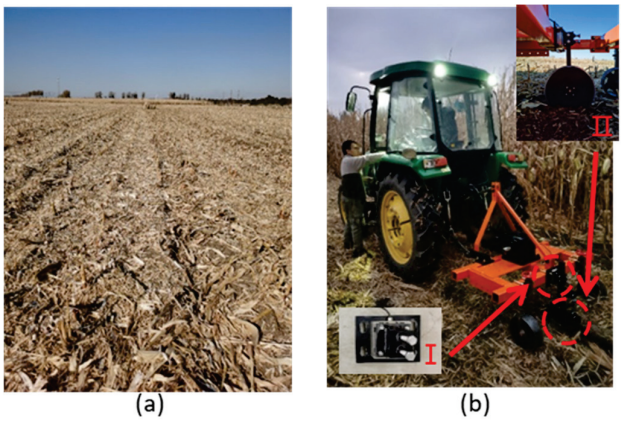

Figure 5. Field experiments. (**a**) Field experiment site and (**b**) experimental equipment; I: torque sensor; II: disc coulter.

3.2. Experimental Methods

To validate the accuracy of the DEM model, verification experiments should be conducted under ideal conditions. Therefore, a soil bin test was employed to validate the DEM model. Zheng, Zhao et al. [21,22] observed that roots were densely distributed within 30 mm of maize stalks, resulting in significant tillage resistance for the disc coulters. To measure the maximum resistance of the disc coulters, the simulation model matched the

experimental conditions of the verification experiment. The soil bin test required the disc coulter's trajectory to run parallel to the straight line connecting the three maize stubble points, maintaining a 30 mm distance from this line. The disc coulter's tillage depth was set to 80 mm, with the soil bin vehicle operating at a tillage speed of 3.6 km/h.

To verify the accuracy of the model and investigate the interaction mechanism between the disc coulter and the maize root–soil composite, it was necessary to evaluate the tillage effect of the disc coulter. The field experiment was conducted on a 6 m-wide, 50 m-long farm with gentle terrain. The stubble-breaking operation should be carried out on the ridges, with their working trajectory passing through the maize stubble at the centre of the ridge. The tractor's forward speed was maintained at 3.6 km/h to meet local no-till requirements, with each experimental group repeated three times. This experiment employed a three-dimensional force sensor to measure the horizontal and vertical resistances exerted on the disc coulters. Due to the significant fluctuations in the force-displacement curve measured in soil bin tests and field experiments, and the difficulty in accurately determining the peak resistance due to uncontrollable factors such as soil impurities, the average resistance (horizontal average resistance, vertical average resistance) was used to evaluate the performance of the disc coulter and the accuracy of the model was verified by comparing the average resistance measured in field experiments and a simulation of stubble-breaking operations. The calculation method for average resistance was shown in Equation (1).

Simultaneously, it was necessary to observe the cross-section of the cut stubble to support the simulation results and provide support for the theoretical model of interaction between the disc coulter and maize root–soil composites.

4. Results and Discussion

4.1. Model Validation

To validate the accuracy of the model, the results of the soil bin test and the field experiments were compared with simulation results. As shown in Figure 6, the trend of the force-displacement curve obtained from measurement and simulation was consistent. The process of breaking the maize stubble started from the point x_1 where the curve significantly rose and ended at the inflexion point x_2, where the curve significantly dropped to stability. The average resistance could be calculated according to Equation (1). The results of the verification test were shown in Tables 4 and 5. Compared with the results of the soil bin test, the maximum error of the horizontal and vertical resistances calculated by simulation was less than 20%. Compared with the results of field experiments, the maximum error of the simulation calculation was 32%. As for the field experiment, the difference between simulated data and experimental data could be attributed to the variability of factors such as soil moisture content, rot of the root, structure of the stubble, differences in maize growth, and mechanical properties of the root–soil interface, which affected resistance. The experimental conditions for the soil bin test were relatively ideal with lower errors. However, it could not be denied that there were still differences between simulated data and experimental data due to disturbances in the collected samples. Although there were errors in the simulated data, these errors were within an acceptable range, so the model was accurate and reliable, and could be used to analyze the interaction mechanism between the disc coulter and the maize root–soil composite.

https://doi.org/10.3390/agriculture16020270

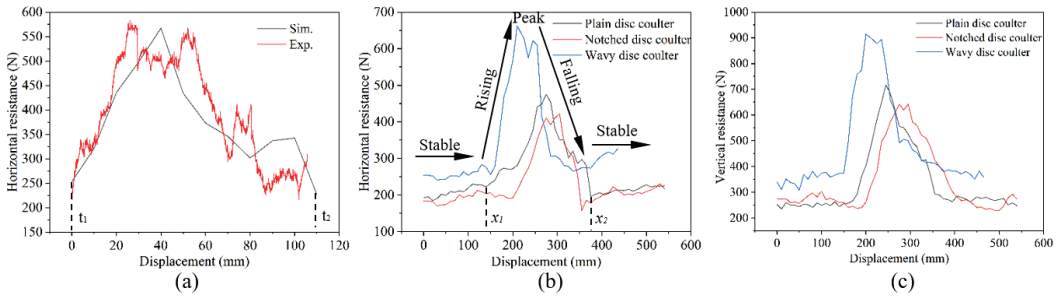

Figure 6. Force-displacement curve of disc coulters: (**a**) the curve of horizontal resistances for simulation and experiment; (**b**) the curve of horizontal resistances for different disc coulters; (**c**) the curve of vertical resistances for different disc coulters.

Table 4. The average horizontal resistance of verification tests.

Indicators	Average Horizontal Resistance (N)				
	Simulation	Soil Bin Test	Deviation	Field Experiment	Deviation
Plain	330.98	364.56 ± 12.25	9.21%	390.36 ± 22.25	15.21%
Notched	289.82	337.47 ± 9.12	14.12%	403.20 ± 18.25	28.12%
Wavy	396.52	485.04 ± 15.87	18.25%	576.76 ± 32.25	31.25%

Table 5. The average vertical resistance of verification tests.

Indicators	Average Vertical Resistance (N)				
	Simulation	Soil Bin Test	Deviation	Field Experiment	Deviation
Plain	432.30	481.46 ± 10.36	10.21%	528.55 ± 25.25	18.21%
Notched	380.61	428.23 ± 12.76	11.12%	515.17 ± 21.25	26.12%
Wavy	581.71	720.39 ± 20.78	19.25%	778.21 ± 38.25	25.25%

4.2. Analysis of the Process of Stubble-Breaking Operation

Schwarz et al. [18] found that the shear resistance of root–soil composites depended on the deformation of the root. Therefore, to investigate the interaction mechanism between disc coulters and maize root–soil composites, it was essential to investigate the relationship between the root deformation and the resistance of disc coulters during the entire stubble-breaking process.

The cutting of a maize root–soil composite using a disc coulter was studied as a case. During the entire stubble-breaking process, the disc coulter sequentially cut through the soil, maize stubble, and soil again. The measured and simulated force-displacement curves for both horizontal and vertical resistances of the disc coulter successively underwent stable, rising, peak, falling, and stable segments (Figure 6). The force-displacement curves in the rising, peak, and falling segments showed significantly higher values, featuring local peaks accompanied by irregular fluctuations. By comparing with the DEM cloud map (Figure 7), it was shown that both horizontal and vertical resistances on the disc coulters significantly increased when breaking the maize stubble. This was consistent with the results obtained by Bai et al. [32] through dynamic analysis and experimental measurements. The above phenomenon also indicated that roots had a significant strengthening effect on soil, and it was precisely because of the presence of roots in the soil that the disc stubble-breaking device needed to face greater resistance. This was consistent with the research of Schwarz, Wu, Liu et al. [4,5,20]. Higher horizontal resistances not only generated greater resistance and energy consumption but also led to significant impact and vibration on tillage equipment, resulting in damage to the machinery; a sudden increase in vertical resistance could lead to problems such as inconsistent tillage depth of the stubble-breaking operation.

https://doi.org/10.3390/agriculture16020270

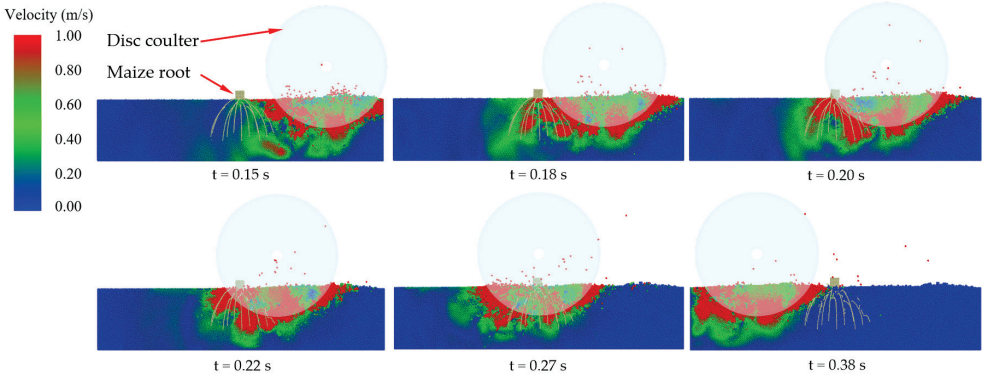

Figure 7. DEM cloud diagram of the interaction between the disc coulter and the maize root–soil composite.

By comparing the force-displacement curve of the simulation with the DEM cloud map of the root, it was found that during the entire stubble-breaking process, when the disc coulter first came into contact with the root, the root was dragged, the local deformation of the root increased with the continuous cutting of the disc coulter (Figure 7), and the horizontal and vertical resistances increased accordingly (Figure 6). As the root dragging distance increased, the roots were subjected to tension (Figure 8), and the resistance of the disc coulter would increase significantly (Figure 6). If the root fractured during the cutting process, the resistance could suddenly decrease (Figure 6). If the roots did not fracture during the stubble-breaking process, they would adhere to the cutting edge of the disc coulter and make it fail (Figure 8). This might be one of the reasons for the blockage. The more roots distributed on the edge of the disc coulter, the greater the horizontal and vertical resistances of the disc coulter. The peak resistance of the disc coulter was related to the number of roots in contact with the edge of the disc coulter and the deformation of each root. Liu et al. [20] also observed this phenomenon, which was called the cumulative effect of root-cutting force. The distribution region of maize roots in the soil was spindle-shaped [33]. During the stubble-breaking process, the contact region between the disc coulter and the densely distributed region of maize roots first increased and then decreased. Correspondingly, the number of roots in contact with the disc coulter also first increased and then decreased. Therefore, the horizontal and vertical resistances of the disc coulter showed a trend of first increasing and then decreasing. This was consistent with the research of Bai et al. [32]. There are differences in root distribution and root fracture time, so the force-displacement curve of the disc coulter would experience irregular fluctuations and abrupt changes. Due to differences in factors such as root structure, distribution characteristics, and decay status, it was difficult to predict resistance using a simple equation. However, by using the above method to analyze the factors that affect the entire stubble-breaking process, it was sufficient to study the interaction between the disc coulter and the maize root–soil composite.

It is worth noting that during the entire stubble-breaking process, the roots that were not fractured could be pushed and embedded into the deep soil. The root dragging distance of these roots could be infinite and immeasurable. The roots and soil underwent irreversible deformation, which could easily lead to holes in the seeding furrow, resulting in the hairpin effect of the root (Figure 9a) [34]. These phenomena were observed during field experiments (Figure 9b). The hairpin effect led to poor contact between seeds and soil, thereby reducing seed germination rates and affecting the growth of maize.

Due to the significant influence of design parameters and operating parameters on factors such as resistance of the disc coulter and fracture of the root, it was necessary to analyze the key factors that affected stubble-breaking operations.

https://doi.org/10.3390/agriculture16020270

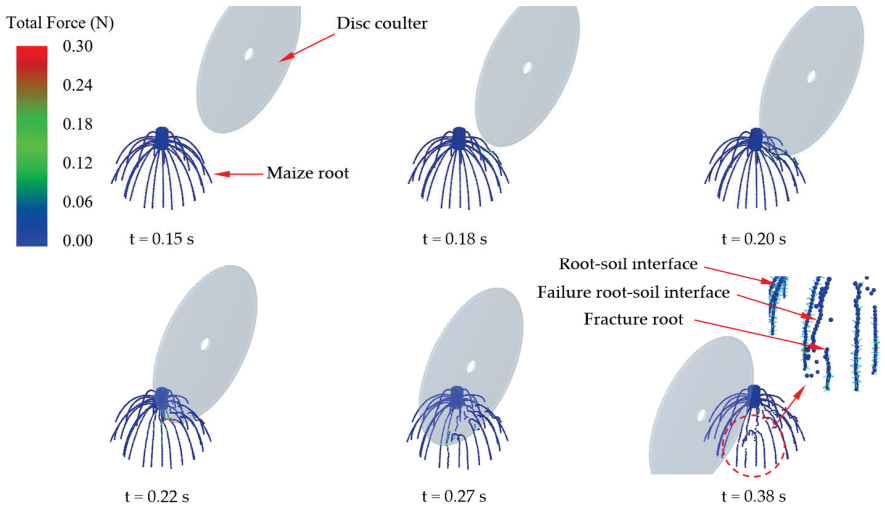

Figure 8. A DEM cloud diagram of motion and stress of the root and soil during the stubble-breaking operation.

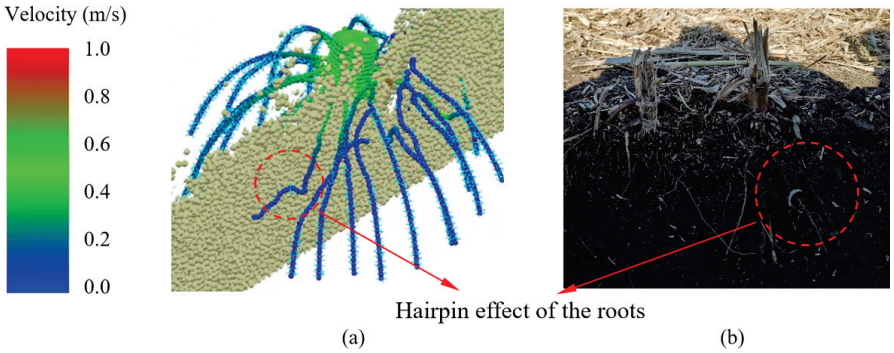

Figure 9. Hairpin effect of the roots: (**a**) simulation result, (**b**) field experiment results.

4.3. The Influence of Key Factors on the Stubble-Breaking Operation

4.3.1. The Influence of Different Types of Disc Coulters on the Stubble-Breaking Operation

The results of the DEM simulation (Figure 10) indicated that the resistance of the notched disc coulter, plain disc coulter, and wavy disc coulter increased sequentially. Compared to the plain disc coulter, the average and peak horizontal resistance of the notched disc coulter decreased by 12.44% and 11.34%, the average and peak vertical resistance decreased by 11.96% and 10.39% (Figure 10a,b), and the root dragging distance decreased by 11.96% (Figure 10c). The average and peak horizontal resistance of the wavy disc coulter increased by 19.80% and 24.49% (Figure 10a,b), the average and peak vertical resistance increased by 34.56% and 37.25%, and the root dragging distance increased by 34.56% (Figure 10c).

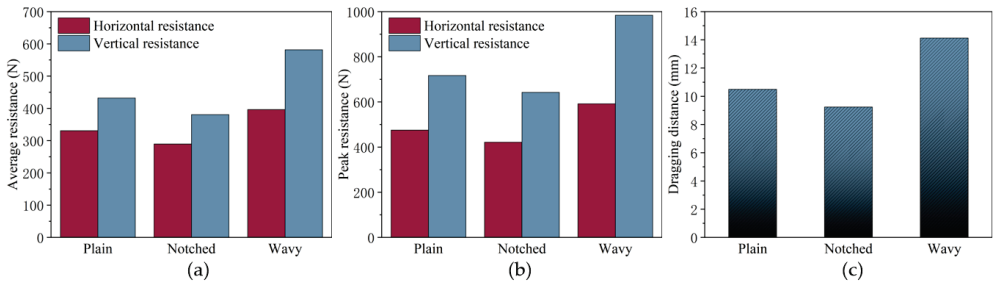

Figure 10. The influence of disc coulter types on the average resistance, the peak resistance, and dragging distance: (**a**) the influence of types of disc coulters on average resistance; (**b**) the influence of types of disc coulters on peak resistance; (**c**) the influence of types of disc coulters on dragging distance.

The DEM cloud diagram indicated that, compared to the plain disc coulter, the notched disc coulter had lower resistance due to the following reasons: First, maize roots were constrained within the notch. On the one hand, the notch could effectively "grab" and fix the maize roots, preventing them from being pushed as a whole and being cut off timely, avoiding the formation of large soil blocks or residue accumulation in front of the working parts, and reducing resistance. On the other hand, the fixed roots were pushed into deeper soil layers (Figure 11a,b). The soil in the deeper layer was firm and provided better support for the roots, making them easier to fracture [32]. Consequently, the resistance of notched disc coulters was lower. Second, the notched structure of the coulter led roots to contact the disc coulter edge at different times. The roots outside the notch contacted the edge of the disc coulter earlier and had greater deformation compared to those inside the notch, which contacted later and deformed less (Figure 11b). The difference in the time of deformation and fracture between the inner and outer roots of the notch reduced the cumulative effect of root-cutting force. Consequently, the peak resistance of notched disc coulters was lower. This conclusion could also explain the reason for the decrease in the resistance of other notched disc coulters with the similar structure. Third, since the cutting edge of the notched disc coulter was discontinuous, the contact with stubble was not gradual but involved an impact action. In contrast, due to the greater impact force of the notched disc coulter on the maize root, the bonds between root particles quickly reached critical force (7.32 N) and broke, resulting in shorter root dragging distances and eliminating the reinforcement effect of the roots on the soil, thereby reducing the stubble-breaking resistance. In contrast, the wavy disc coulter had the greatest contact area with the soil compared to the other two types. Its cutting edge was the longest and contacted more roots within a unit angle of rotation (Figure 11c). Consequently, under the combined effects of pure cutting force [35] and root-cutting force [32], wavy disc coulters had the highest resistance.

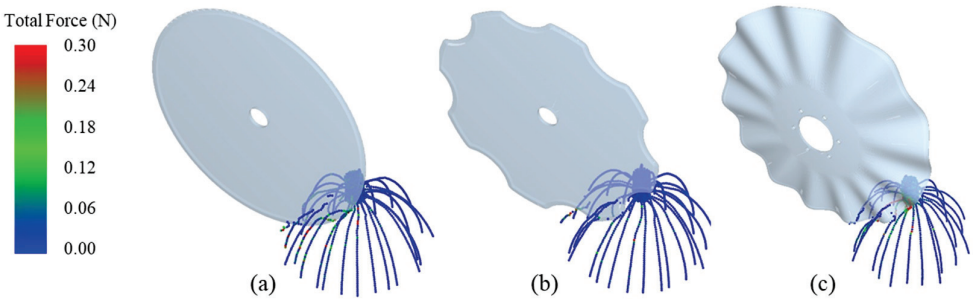

Figure 11. The interaction process between the disc coulter and the maize root–soil composite: (**a**) plain disc coulter; (**b**) notched disc coulter; (**c**) wavy disc coulter.

4.3.2. The Influence of Disc Coulter Radius on the Stubble-Breaking Operation

As the radius of the disc coulter increased, the horizontal and vertical resistances of the disc coulter could significantly increase (Figure 12). Compared to the disc coulter with a radius of 170 mm, the average and peak horizontal resistance of the disc coulter with a radius of 120 mm decreased by 27.22% and 24.62%, the average and peak vertical resistance decreased by 19.75% and 17.94% (Figure 12a,b), and the root dragging distance increased by 20.95% (Figure 12c). The average and peak horizontal resistance with a disc radius of 220 mm increased by 27.22% and 28.72%, the average and peak vertical resistance increased by 23.52% and 22.75% (Figure 12a,b), and the root dragging distance decreased by 21.90% (Figure 12c). In summary, as the radius of the disc increased, the average resistance and peak resistance also increased, and the root dragging distance decreased.

The DEM cloud diagram indicated that a disc coulter with a greater radius would contact more roots simultaneously (Figure 13a), leading to a more significant cumulative effect of root-cutting force [20] and higher resistance on the disc coulter. This was consistent

https://doi.org/10.3390/agriculture16020270

with the research of Bai and Liu et al. [20,32]. According to the pure cutting theory [35], the greater the radius of the disc coulter, the greater the contact area between the disc coulter and the soil, and the greater the pure cutting force. This is another reason why disc coulters with greater disc radius face higher resistance. Higher resistance not only made the stubble-breaking device faced greater energy consumption, but a sudden increase in the peak resistance also led to unstable tillage depth, which had a negative impact on seeding operations. In addition, as for the disc coulter with a greater radius, the component of the velocity vector on the cutting edge facing towards the deeper soil layer was higher. Therefore, roots tended to be pushed into deeper soil layers. The roots pushed into deep soil could obtain better support and were more easily cut off. According to previous research [20], the cutting force of a disc coulter was mainly composed of soil reaction force, root tensile force, and friction force. The soil reaction force on the root that was cut off in deep soil was relatively higher, so the axial tension on the root was relatively lower, the root dragging distance was shorter, the possibility of damage to the root–soil interface was lower, and the root was more easily cut off efficiently. Therefore, disc coulters with a larger radius had better tillage performance. In summary, to address varying agronomic requirements, there was an optimal radius for the disc coulter, which enabled it to meet the design requirements of lower resistance and excellent stubble-breaking performance.

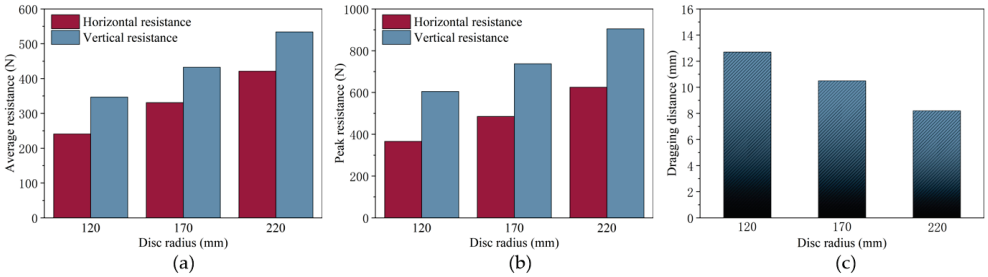

Figure 12. The influence of disc radius on the average resistance, the peak resistance, and dragging distance: (**a**) the influence of disc radius on average resistance; (**b**) the influence of disc radius on peak resistance; (**c**) the influence of disc radius on dragging distance.

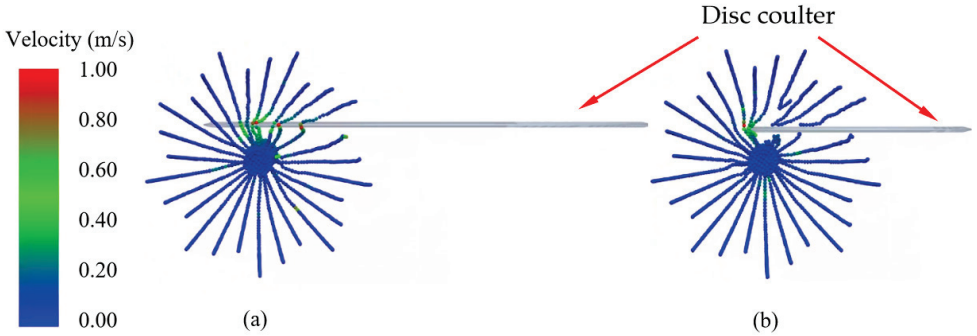

Figure 13. The interaction between disc coulters with different disc radius and maize root–soil composites: (**a**) disc radius of 220 mm; (**b**) disc radius of 170 mm.

4.3.3. The Influence of Tillage Speed on the Stubble-Breaking Operation

As the tillage speed of the disc coulter increased, the horizontal and vertical resistance of the disc coulter could significantly increase (Figure 14). Compared to the disc coulter with a tillage speed of 1.0 m/s, the average and peak horizontal resistance of the disc coulter with a tillage speed of 0.5 m/s decreased by 35.17% and 34.10%, the average and peak vertical resistance decreased by 18.73% and 17.89% (Figure 14a,b), and the root dragging distance increased by 19.05% (Figure 14c). The average and peak horizontal resistance of the disc coulter with a tillage speed of 1.5 m/s increased by 28.27% and 29.95%, the

https://doi.org/10.3390/agriculture16020270

average and peak vertical resistance increased by 18.73% and 21.22% (Figure 14a,b), and the root dragging distance decreased by 15.24% (Figure 14c). In summary, as the tillage speed increased, the average and peak resistance also increased, and the root dragging distance decreased.

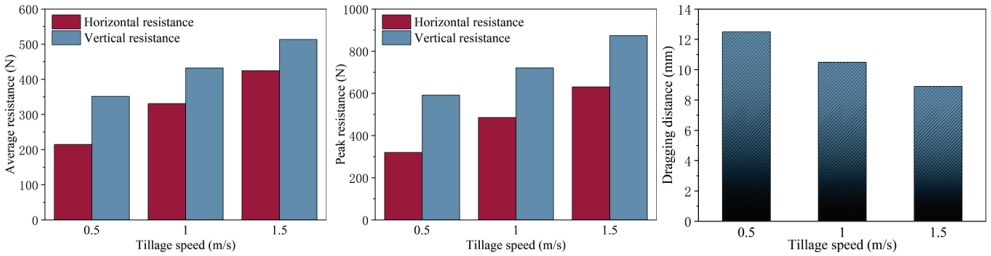

Figure 14. The influence of tillage speed on the average resistance, the peak resistance, and dragging distance: (**a**) the influence of tillage speed on average resistance; (**b**) the influence of tillage speed on peak resistance; (**c**) the influence of tillage speed on dragging distance.

Subrata Karmakar et al. [36] indicated that as the plate compression speed increased, both the soil reaction force on the plate and soil stiffness rose accordingly. DEM simulation results indicated that when the tillage speed of the disc coulter increased from 0.5 m/s to 2.5 m/s, the soil reaction force on roots and their growth rate significantly increased (Figure 15). Due to the fact that the soil reaction force was the main component of resistance of the disc coulter [20], the higher the speed of the disc coulter, the greater the tillage resistance. Previous studies showed that the greater the contact force applied to the roots, the easier the roots were to fracture [20]. Therefore, under high-speed stubble-breaking conditions, due to the great growth rate of soil reaction force within the unit dragging distance of the roots, the contact force applied to the roots significantly increased, and the roots would be cut off at a shorter dragging distance. Thus, the performance of the disc coulter for high-speed operation was excellent. According to the research of Liu et al. [20], the proportion of tension on roots with shorter dragging distance relative to the root-cutting force was lower. This reduced the possibility of the failure of root–soil interface, reduced the number of dragging and exposure of roots, and made the cutting surface of maize stubble smoother. However, disc coulters operating at higher speeds could face greater pure cutting forces, meaning they had higher resistance during high-speed stubble-breaking operations. Therefore, the high-speed disc coulter needed to face greater energy consumption and impact force during the stubble-breaking operation. A higher impact force not only shortened the service life of the stubble-breaking device but also affected the stability of tillage depth and the germination of seeds. In summary, for high-speed stubble-breaking operations, disc coulters with strong stubble-breaking performance and sufficient counterweights should be used. Key components should also be reinforced to enhance the operational stability of the stubble-breaking device and extend the service life of the tillage equipment.

https://doi.org/10.3390/agriculture16020270

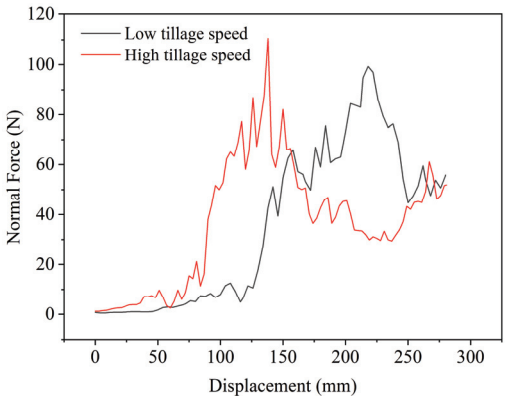

Figure 15. The soil reaction force on roots–time curve at different tillage speeds.

4.3.4. The Influence of Tillage Depth on the Stubble-Breaking Operation

As the tillage depth of the disc coulter increased, the horizontal and vertical resistance of the disc coulter also increased (Figure 16). Compared to the disc coulter with a tillage depth of 80 mm, the average and peak horizontal resistance decreased by 37.68 and 36.08% with a tillage depth of 60 mm, the average and peak vertical resistance decreased by 23.69% and 24.45% (Figure 16a,b), and the root dragging distance decreased by 23.69% (Figure 16c). The average and peak horizontal resistance of the disc coulter increased by 77.12% and 77.32% with a tillage depth of 100 mm, and the average and peak vertical resistance increased by 50.16% and 48.91% (Figure 16a,b), and the root dragging distance increased by 50.16% (Figure 16c). In summary, as the tillage speed increased, the average and peak resistance also increased, and the root dragging distance increased.

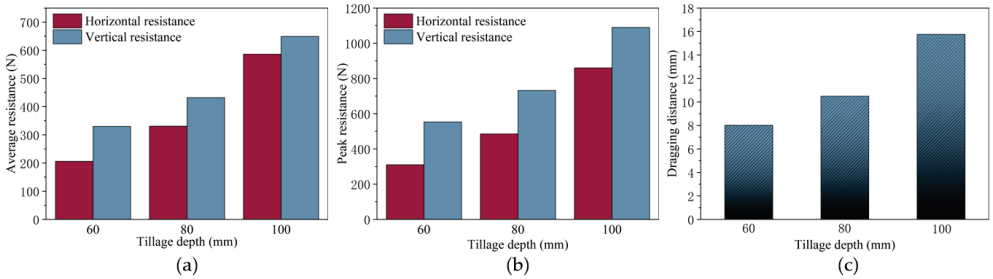

Figure 16. The influence of tillage depth on the average resistance, the peak resistance, and dragging distance: (**a**) the influence of tillage depth on average resistance; (**b**) the influence of tillage depth on peak resistance; (**c**) the influence of tillage depth on dragging distance.

According to the simulation results, although the cutting edge of the disc coulter used for the deep soil layer (Figure 17a) could completely cut off the maize stubble, due to the deep tillage, the disc coulter had a great contact area with the soil and higher pure cutting force; meanwhile, the disc coulter would also come into contact with a large number of roots, and the cumulative effect of the root-cutting force was more significant. The above reasons made the resistance of the disc stubble-breaking device higher. As for the cutting edge of the disc coulter used for shallow soil layer (Figure 17b), due to the low soil reaction force applied to the roots in the shallow soil layer, if the roots fractured, the tensile force on the roots would be higher, and the root dragging distance would be longer; if the roots did not fracture, it would be pushed into the seedbed, causing a hairpin effect and affecting seed germination. In addition, due to insufficient dragging distance of the roots in deep soil layer, it was difficult to cut off the roots, resulting in missed cutting. In summary, crop residue management should adopt optimal tillage depths based on root structure and agronomic requirements to enhance operational quality.

https://doi.org/10.3390/agriculture16020270

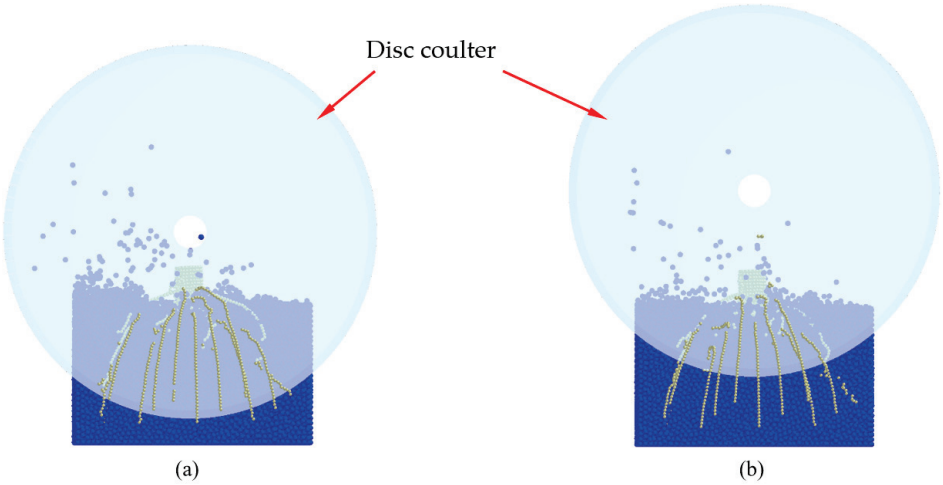

Figure 17. Interaction between disc coulters and maize root–soil composites at different tillage depths: (**a**) tillage depth of 60 mm; (**b**) tillage depth of 100 mm.

5. Conclusions

This study developed a DEM-MBD coupling model for the interaction between disc coulters and maize root–soil composites. The model was validated through soil bin tests and field experiments. Using the DEM-MBD coupling model, the interaction between disc coulters and maize root–soil composites was investigated. The conclusions were as follows:

1. Due to the significant strengthening effect of roots on soil, the disc stubble-breaking device needed to face greater resistance. During the stubble-breaking operation, the greater the deformation of the roots that came into contact with the disc coulter, and the greater the number of roots distributed along its cutting edge, the greater the resistance encountered by the disc coulter. If the roots could not be cut off during stubble-breaking operation and face irreversible deformation, it would lead to the holes in the planting furrow. The roots that could not be cut off would be pushed and embedded into the deep soil layer, resulting in the root hairpin effect;
2. Compared to plain disc coulters, the difference in the time of deformation and fracture between the inner and outer roots of the notch reduced the cumulative effect of root-cutting force. The discontinuous edge curve of the notched disc coulter had an impact effect, which made the root more prone to fracture. Therefore, notched disc coulters had lower tillage resistance and better stubble-breaking performance; wavy disc coulters had higher tillage resistance. The contact area between the disc coulter and the soil was larger compared to the other two types of disc coulters, the cutting edge was longer per unit rotation angle, and there were more roots in contact. Therefore, under the cumulative of pure cutting force and root cutting force, the resistance of the wavy disc coulter was higher;
3. The disc coulter with a greater radius had more contact points with the roots and a greater contact area with the soil. As a result, it met greater resistance during stubble-breaking operations. However, these disc coulters tended to push the roots deeper into the soil with higher solidity, thus having better stubble-breaking performance. Therefore, to address varying agronomic requirements, there existed an optimal radius for the disc coulter that could meet the design requirements of lower resistance and excellent stubble-breaking performance;
4. In high-speed stubble breaking operations, the resistance of the disc coulter on the roots would significantly increase. Although this could significantly increase the impact force of the disc coulter on the stubble, which was more conducive to stubble-breaking operation, it would also reduce operational stability and service life and

https://doi.org/10.3390/agriculture16020270

affect seeding quality. Therefore, when carrying out high-speed stubble-breaking operations, it was necessary to equip stubble-breaking coulters with excellent stubble-breaking performance and sufficient counterweights. In addition, key components needed to be strengthened to improve the stability of the stubble-breaking device and the service life of the tillage equipment;

5. As the soil reaction force increased with the depth of the soil; therefore, the cutting edge of disc coulter used for the deep soil layer would come into contact with more roots and more soil, leading to a greater resistance. In contrast, the cutting edge of a disc coulter used for shallow soil layers required a longer dragging distance to cut off the roots. If the roots could not be cut off, they would be pushed into the seedbed, hindering seed germination. Therefore, according to the structure of the crop roots and agronomic requirements, the depth of the tillage operation should be suitable for the stubble-breaking operation to improve the quality of the operation.

This study revealed the interaction mechanism between the disc coulter and the maize root–soil composite, providing a theoretical basis for the design of stubble-breaking devices. However, to obtain a universal design theory and develop a quantitative model to optimize the stubble-breaking component, it is necessary to verify the universality of the model on different platforms, as well as to conduct in-depth research on the influence of complex agricultural environmental factors such as soil moisture content, root rot, and root–soil interface mechanical properties, and the operating conditions of tillage equipment on the interaction.

Author Contributions: Conceptualization, X.L.; methodology, X.L., Z.G., Z.T., M.H., P.G. and Z.X.; software, X.L., Z.T. and Z.X.; validation, X.L., Z.T. and Z.X.; formal analysis, X.L., Z.G., Z.T., M.H., P.G., Z.T. and Z.X.; investigation, X.L., Z.G., Z.T., M.H., P.G. and Z.X.; resources, Y.M. and Z.X.; data curation, X.L., Z.G., Z.T., M.H., P.G. and Z.X.; writing—original draft preparation, X.L.; writing—review and editing, X.L., Z.G., Z.T., M.H., P.G., Y.M. and Z.X.; visualization, X.L., Z.G., Z.T., M.H., P.G. and Z.X.; supervision, Y.M. and Z.X.; project administration, Y.M.; funding acquisition, Y.M. and Z.X. All authors have read and agreed to the published version of the manuscript.

Funding: This work was supported by the National Natural Science Foundation of China [grant number 52275288], the National Key Research and Development Program of China [grant number 2023YFD2000903].

Institutional Review Board Statement: Not applicable.

Data Availability Statement: The original contributions presented in the study are included in the article; further inquiries can be directed to the corresponding author.

Conflicts of Interest: The authors declare no conflicts of interest.

References

1. Zhang, X.; Yun, Y.; Liu, C.; Xin, X.; Yang, W. Conservation Tillage Exerts Diverse Pathways to Sequester Organic Carbon in Fluvo-Aquic Soils of the North China Plain. *Soil Tillage Res.* **2025**, *254*, 106730. [CrossRef]
2. Gao, W. *Conservation Farming System in China*, 1st ed.; China Agricultural University Press: Beijing, China, 2011.
3. Gebhardt, M.R.; Daniel, T.C.; Schweizer, E.E.; Allmaras, R.R. Conservation Tillage. *Science* **1985**, *230*, 625–630. [CrossRef]
4. Schwarz, M.; Rist, A.; Cohen, D.; Giadrossich, F.; Egorov, P.; Büttner, D.; Stolz, M.; Thormann, J.J. Root Reinforcement of Soils under Compression. *J. Geophys. Res. Earth Surf.* **2015**, *120*, 2103–2120. [CrossRef]
5. Wu, T.H. Study of Soil-Root Interaction. *J. Geotech. Eng.* **1989**, *114*, 1351–1375. [CrossRef]
6. Xie, M. A Study on the Soil Mechanical Role of Tree Roots in the Stability of Slopes. *J. Soil Water Conserv.* **1990**, *4*, 7–14. [CrossRef]
7. Wang, Q.; Cao, X.; Wang, C.; Li, H.; He, J.; Lu, C. Research Progress of No/Minimum Tillage Corn Seeding Technology and Machine in Northeast Black Land of China. *Trans. Chin. Soc. Agric. Mach.* **2021**, *52*, 1–15. [CrossRef]
8. He, J.; Li, H.; Chen, H.; Lu, C.; Wang, Q. Research Progress of Conservation Tillage Technology and Machine. *Trans. Chin. Soc. Agric. Mach.* **2018**, *49*, 1–19.

9. Torotwa, I.; Ding, Q.; Makange, N.R.; Liang, L.; He, R. Performance Evaluation of a Biomimetically Designed Disc for Dense-Straw Mulched Conservation Tillage. *Soil Tillage Res.* **2021**, *212*, 105068. [CrossRef]
10. Zeng, Z.; Chen, Y. Performance Evaluation of Fluted Coulters and Rippled Discs for Vertical Tillage. *Soil Tillage Res.* **2018**, *183*, 93–99. [CrossRef]
11. Zhang, S.; Jia, X.; Dong, J.; Wang, X.; Zhao, H.; Chen, X.; Zhang, Z.; Huang, Y.; Shi, J. Optimization of Operating Angles of Disc Coulters for Maize Residue Management Using Discrete Element Method. *Comput. Electron. Agric.* **2024**, *218*, 108691. [CrossRef]
12. Karayel, D. The Effect of Furrow Opener and Disc Coulter Configurations on Seeding Performance under Different Residue Cover Densities. *AgriEngineering* **2024**, *6*, 1277–1288. [CrossRef]
13. Kogut, Z.; Sergiel, L.; Zurek, G. The Effect of the Disc Setup Angles and Working Depth on Disc Harrow Working Resistance. *Biosyst. Eng.* **2016**, *151*, 328–337. [CrossRef]
14. Zahid, M.; Celik, A. Disc Angle and Tilt Angle Effects on Forces Acting on a Single-Disc Type No-till Seeder Opener. *Soil Tillage Res.* **2019**, *194*, 104304. [CrossRef]
15. Mickovski, S.B.; Stokes, A.; van Beek, R.; Ghestem, M.; Fourcaud, T. Simulation of Direct Shear Tests on Rooted and Non-Rooted Soil Using Finite Element Analysis. *Ecol. Eng.* **2011**, *37*, 1523–1532. [CrossRef]
16. Schwarz, M.; Giadrossich, F.; Cohen, D. Modeling Root Reinforcement Using a Root-Failure Weibull Survival Function. *Hydrol. Earth Syst. Sci.* **2013**, *17*, 4367–4377. [CrossRef]
17. Mickovski, S.B.; Ennos, A.R. Model and Whole-Plant Studies on the Anchorage Capabilities of Bulbs. *Plant Soil* **2003**, *255*, 641–652. [CrossRef]
18. Schwarz, M.; Cohen, D.; Or, D. Root-Soil Mechanical Interactions during Pullout and Failure of Root Bundles. *J. Geophys. Res. Earth Surf.* **2010**, *115*, F04035. [CrossRef]
19. Zhao, J.; Lu, Y.; Wang, X.; Zhuang, J.; Han, Z. A Bionic Profiling-Energy Storage Device Based on MBD-DEM Coupled Simulation Optimization Reducing the Energy Consumption of Deep Loosening. *Soil Tillage Res.* **2023**, *234*, 105824. [CrossRef]
20. Liu, X.; Gao, P.; Jiang, X.; Guo, M.; Wang, Y.; Ma, Y. Study on the Interaction Mechanism between Stubble-Breaking Blades and Unidirectional Maize Root-Soil Composites. *Biosyst. Eng.* **2025**, *256*, 104190. [CrossRef]
21. Zhao, X.; Zhang, Z.; Huang, Q.; Zhang, G. Cutting Performance of Corn Root-Soil Composite. *Trans. Chin. Soc. Agric. Mach.* **2013**, *44*, 126–132. [CrossRef]
22. Zheng, L.; Luo, X.; Zeng, S.; Wang, Z.; Liu, C.; Qi, X. Shear Characteristics of Rice Root-Soil Composite. *Trans. Chin. Soc. Agric. Mach.* **2017**, *48*, 63–71. [CrossRef]
23. Yuan, Y.; Du, M.; Zhou, Y.; Yang, Y.; Zhang, X.; Zhao, S. FEM-SPG Coupling Modelling and Reinforced Soil Effect of Maize Root-Soil Composite. *Biosyst. Eng.* **2025**, *259*, 104293. [CrossRef]
24. Zhang, S.; Huang, Y.; Zhao, H.; Fu, Z.; Liu, Z.; Shi, J. Design and Experiment of Cutting and Throwing Combined Anti-Blocking Device for Wide-Seedbed Seeding of Wheat. *Trans. Chin. Soc. Agric. Mach.* **2024**, *55*, 40–52. [CrossRef]
25. Tamás, K.; Bernon, L. Role of Particle Shape and Plant Roots in the Discrete Element Model of Soil–Sweep Interaction. *Biosyst. Eng.* **2021**, *211*, 77–96. [CrossRef]
26. Zou, L.; Yan, D.; Niu, Z.; Yuan, J.; Cheng, H.; Zheng, H. Parametric Analysis and Numerical Optimisation of Spinach Root Vibration Shovel Cutting Using Discrete Element Method. *Comput. Electron. Agric.* **2023**, *212*, 108138. [CrossRef]
27. Liu, X.; Qi, H.; Wang, S.; Xu, Z.; Gao, P.; Fu, D.; Ma, Y. The Design and Experimentation of a Wing-Shaped Stubble-Breaking Device for Maize Stubbles. *Agriculture* **2024**, *14*, 2108.
28. Zhang, S.; Zhao, H.; Wang, X.; Dong, J.; Zhao, P.; Yang, F.; Chen, X.; Liu, F.; Huang, Y. Discrete Element Modeling and Shear Properties of the Maize Stubble-Soil Complex. *Comput. Electron. Agric.* **2023**, *204*, 107519. [CrossRef]
29. Du, J.; Heng, Y.; Zheng, K.; Luo, C.; Zhu, Y.; Zhang, J.; Xia, J. Investigation of the Burial and Mixing Performance of a Rotary Tiller Using Discrete Element Method. *Soil Tillage Res.* **2022**, *220*, 105349. [CrossRef]
30. Zhang, S.; Huang, Y.; Gao, X.; Bi, Y.; Dong, J.; Zhao, H.; Zhao, P.; Jia, X. Evaluating the Influence of Straight-Plain Types of Rotary Tiller Blades with Various Edge Curves on Maize Residue Using DEM. *Biosyst. Eng.* **2025**, *250*, 49–61. [CrossRef]
31. Che, H.; Zhou, H.; Li, Z.; Wang, X.; Wang, X.; Wei, Z.; Li, Y.; Zhang, Y. Evaluation of the Working Performance of Different Digging Shovels Based on the Maize Root-Soil Complex Model. *Biosyst. Eng.* **2025**, *260*, 104316. [CrossRef]
32. Bai, X.; Lin, J.; Lü, C.; Hu, Y. Analysis and Experiment on Working Performance of Disc Coulter for No-Tillage Seeder. *Trans. Chin. Soc. Agric. Eng.* **2014**, *30*, 1–9. [CrossRef]
33. Shao, M.R.; Jiang, N.; Li, M.; Howard, A.; Lehner, K.; Mullen, J.L.; Gunn, S.L.; McKay, J.K.; Topp, C.N. Complementary Phenotyping of Maize Root System Architecture by Root Pulling Force and X-Ray Imaging. *Plant Phenomics* **2021**, *2021*, 9859254. [CrossRef] [PubMed]
34. Moyer, J.R.; Nitschelm, J.; Regitnig, P.; Blackshaw, R.E.; Huang, H.C.; Chang, C. Effect of Tillage System and Crop Sequence on Irrigated Sugarbeet Production. *Can. J. Plant Sci.* **2004**, *84*, 739–747. [CrossRef]

35. McKyes, E. *Soil Cutting and Tillage*; Elsevier: Amsterdam, The Netherlands, 1985; ISBN 044460104X.
36. Karmakar, S.; Lal Kushwaha, R. CFD Simulation of Soil Forces on a Flat Tillage Tool. In Proceedings of the 2005 ASAE Annual International Meeting, Tampa, FL, USA, 17 July 2005; Volume 0300.

Disclaimer/Publisher's Note: The statements, opinions and data contained in all publications are solely those of the individual author(s) and contributor(s) and not of MDPI and/or the editor(s). MDPI and/or the editor(s) disclaim responsibility for any injury to people or property resulting from any ideas, methods, instructions or products referred to in the content.

agriculture

MDPI

Article

Analysis Method and Experiment on the Influence of Hard Bottom Layer Contour on Agricultural Machinery Motion Position and Posture Changes

Tuanpeng Tu [1,2], Xiwen Luo [1,2], Lian Hu [1,2,*], Jie He [1,2], Pei Wang [1,2], Peikui Huang [1,2], Runmao Zhao [1,2], Gaolong Chen [1,2], Dawen Feng [1,2], Mengdong Yue [1,2], Zhongxian Man [1,2], Xianhao Duan [1,2], Xiaobing Deng [1,2] and Jiajun Mo [1,2]

[1] Guangdong Provincial Laboratory of Lingnan Modern Agricultural Science and Technology, South China Agricultural University, Guangzhou 510642, China; tuanpengtu@scau.edu.cn (T.T.); xwluo@scau.edu.cn (X.L.); hooget@scau.edu.cn (J.H.); peiwang@scau.edu.cn (P.W.); pkhuang@scau.edu.cn (P.H.); rmzhao@scau.edu.cn (R.Z.); gl.chen@scau.edu.cn (G.C.); 381383864@stu.scau.edu.cn (D.F.); yuemengdong@stu.scau.edu.cn (M.Y.); manzhx@stu.scau.edu.cn (Z.M.); 20251168008@stu.scau.edu.cn (X.D.); 1438685532@stu.scau.edu.cn (X.D.); mokachun@stu.scau.edu.cn (J.M.)

[2] Key Laboratory of the Ministry of Education of China for Key Technologies for Agricultural Machinery and Equipment for Southern China, South China Agricultural University, Guangzhou 510642, China

* Correspondence: lianhu@scau.edu.cn; Tel.: +86-15915767370

Abstract

The hard bottom layer in paddy fields significantly impacts the driving stability, operational quality, and efficiency of agricultural machinery. Continuously improving the precision and efficiency of unmanned, precision operations for paddy field machinery is essential for realizing unmanned smart rice farms. Addressing the unclear influence patterns of hard bottom contours on typical scenarios of agricultural machinery motion and posture changes, this paper employs a rice transplanter chassis equipped with GNSS and AHRS. It proposes methods for acquiring motion state information and hard bottom contour data during agricultural operations, establishing motion state expression models for key points on the machinery antenna, bottom of the wheel, and rear axle center. A correlation analysis method between motion state and hard bottom contour parameters was established, revealing the influence mechanisms of typical hard bottom contours on machinery trajectory deviation, attitude response, and wheel trapping. Results indicate that hard bottom contour height and local roughness exert extremely significant effects on agricultural machinery heading deviation and lateral movement. Heading variation positively correlates with ridge height and negatively with wheel diameter. The constructed mathematical model for heading variation based on hard bottom contour height difference and wheel diameter achieves a coefficient of determination R^2 of 0.92. The roll attitude variation in agricultural machinery is primarily influenced by the terrain characteristics encountered by rear wheels. A theoretical model was developed for the offset displacement of the antenna position relative to the horizontal plane during roll motion. The accuracy of lateral deviation detection using the posture-corrected rear axle center and bottom of the wheel center improved by 40.7% and 39.0%, respectively, compared to direct measurement using the positioning antenna. During typical vehicle-trapping events, a segmented discrimination function for trapping states is developed when the terrain profile steeply declines within 5 s and roughness increases from 0.008 to 0.012. This method for analyzing how hard bottom terrain contours affect the position and attitude changes in agricultural machinery provides theoretical foundations and technical support for designing wheeled agricultural robots, path-tracking control for unmanned precision operations, and vehicle-trapping

early warning systems. It holds significant importance for enhancing the intelligence and operational efficiency of paddy field machinery.

Keywords: hard-bottom contour; agricultural machinery posture; trajectory deviation; attitude response; vehicle bogging warning

1. Introduction

Rice serves as the primary food source for over half of the world's population [1,2], serving as a vital food crop for achieving the United Nations' Sustainable Development Goal 2030 of Zero Hunger [3]. China ranks second globally in the rice cultivation area, with a perennial planting area of 30 million hectares [4]. In mechanized rice cultivation, the paddy field bottom layer serves as a critical component within the tillage soil structure, bearing the operational loads of agricultural machinery. During operation, machinery encounters vibrations, bouncing, and bogging due to uneven pits and ruts in the bottom layer, significantly impacting both the passage of machinery and the quality of field operations [5]. As agricultural production rapidly advances toward intelligent and labor-saving practices, the autonomous navigation and precise control capabilities of paddy field machinery have become critical for realizing smart farms with reduced labor requirements in rice production [6]. However, the complex and variable contour of paddy field hard bottom layer surfaces [7] remains poorly understood in terms of its impact on the position and attitude changes in agricultural machinery. This lack of clarity constrains the optimization of operation control strategies and hinders the advancement of intelligent operation levels, so it is imperative to elucidate the influence patterns of typical hard bottom layer contours on the position and attitude changes in agricultural machinery. Early terrain mechanics theories provided the foundation for modeling wheel–ground interactions. Bekker and Wong systematically established mathematical models for soft soil bearing capacity, settlement, and rolling resistance, offering theoretical support for vehicle dynamics response research [8,9]. Jia et al. proposed a wheel–terrain interaction model based on wheel dynamics and terrain mechanics, effectively simulating wheeled movement in soft soil and enabling numerical simulations for off-road mobile robots [10]. Misaghi et al. employed the International Roughness Index (IRI) to model road surface irregularities in truck–road interactions, quantifying the effects of truck suspension systems and road conditions on pavement damage [11]. Zheng et al. [12] identified the driving environment as the most significant external factor influencing vehicle dynamics. They investigated the effects of varying road roughness, adhesion coefficients, and road gradients on the dynamic performance of dual-clutch transmission vehicles. Inotsume and Kubota [13] proposed an adaptive terrain passability prediction method based on multi-source transfer Gaussian process regression. This approach utilizes limited data from low-risk terrain within the target environment, combined with prior travel experience across diverse terrain surfaces. Golanbari [14] identified soil deformation as a key factor affecting off-road vehicle performance. They investigated soil deformation caused by the interaction between pneumatic tires and track wheels with the ground. The fitted surfaces obtained using optimization algorithms effectively predicted soil deformation induced by different wheel types.

In studies examining the impact of complex farmland topography on agricultural machinery operations, Tu et al. [15] proposed methods for quantifying paddy field hard bottom layer contours, tillage layer thickness, and their characteristics based on machinery pose information. They developed a method for quantifying hard bottom layer contour features, providing a driving environment map for agricultural machinery. The primary

https://doi.org/10.3390/agriculture16020170

factor affecting autonomous agricultural machinery path-tracking accuracy is lateral deviation caused by skidding under terrain influence [16]. To address terrain-induced lateral deviation in agricultural machinery, Bevly, Ryu, and Anderson et al. [17–19] employed a dual-antenna Global Navigation Satellite System (GNSS) system and Inertial Navigation System (INS) sensors to establish a kinematic model-based heading Kalman filter. This approach enabled the estimation of center-of-mass lateral deviation angles and front-rear wheel lateral deviation angles, further facilitating the estimation of wheel lateral deviation stiffness. To suppress disturbances from wheel lateral deviation, researchers treated lateral deviation as a disturbance term in linear motion models and employed robust control techniques for mitigation [20]. Alternatively, they developed vehicle dynamics and kinematic models incorporating lateral deviation parameters, applying nonlinear control techniques to design path-tracking control laws [21,22]. Lenain et al. [23] developed front and rear wheel yaw angle observers based on extended kinematic equations for front-wheel steering and four-wheel steering agricultural vehicles, utilizing dual-antenna GNSS and INS. They applied the estimated values to path-tracking control, effectively enhancing tracking accuracy. Regarding operational effectiveness, Zhou et al. [24] addressed the tilting and height fluctuations in leveling machines caused by uneven hardpan layers in rice fields. They designed a leveling machine based on dual-antenna GNSS positioning and orientation, achieving horizontal and elevation control of the leveling blade after terrain-induced attitude changes. Frey et al. [25] proposed integrating LiDAR and visual data with the RoadRunner framework, employing end-to-end learning to predict off-road terrain passability and elevation maps. Sten et al. [26] combined the precision of LiDAR with the coverage complementarity of stereo vision to construct more comprehensive terrain surface models, providing more reliable inputs for vehicle-trapping assessment and path planning.

The above research demonstrates that terrain undulations significantly impact vehicle driving stability and agricultural machinery operation quality. Relevant studies have laid a solid foundation for analyzing the operational characteristics of agricultural machinery in complex terrain conditions, covering aspects such as terrain mechanics modeling, vehicle dynamics response, path-tracking control, and terrain perception. These studies enable real-time acquisition of agricultural machinery attitude information, construction of paddy field operation environment maps, extraction of hard bottom contour features, and quantitative description of unevenness. They have also partially revealed the patterns of terrain undulation affecting the operational stability and work precision of agricultural machinery. Multi-source information fusion methods incorporating LiDAR, stereo vision, and radar can assess vehicle passability on hard surfaces. However, research remains limited on the coupling relationship between local contour features of paddy field hardpan beneath water and tillage layers and the motion state of agricultural machinery, the response patterns of key attitude parameters, and the mechanisms of vehicle trapping. Particularly in typical ridge-and-furrow and vehicle-trapping scenarios, systematic experimental analysis and theoretical support are lacking regarding how characteristic parameters of the hard bottom layer—such as height, height differences, and local roughness—influence machinery trajectory deviation, attitude response, and escape capability.

To address the aforementioned issues, this paper focuses on paddy field machinery and designs an integrated platform for acquiring agricultural machinery position/orientation information and hard bottom contour data based on GNSS and AHRS sensor fusion technology. It proposes a method for simultaneously obtaining the motion state of agricultural machinery during operation and hard bottom contour information, constructs motion state datasets for key points such as the antenna, bottom of the wheel, and rear axle center, and establishes a correlation analysis method between motion state and hard bottom feature parameters. Building upon this foundation, the study analyzes the mechanism by which typical

https://doi.org/10.3390/agriculture16020170

hard bottom layer contours influence agricultural machinery movement trajectory deviation, attitude response, and bogging behavior. It reveals the patterns of how hard bottom layer contour characteristics affect the operational stability and precision of agricultural machinery. This study aims to provide theoretical foundations and technical support for optimizing the structural design of paddy field machinery, improving path-tracking control algorithms, and developing vehicle-trapping early warning strategies. It holds significant importance for enhancing the intelligence and operational efficiency of wheeled agricultural robots, as well as advancing smart production in paddy fields and unstructured complex terrain scenarios.

2. Materials and Methods

2.1. Platform for Collecting Position and Attitude Information of Agricultural Machinery and Hard Bottom Contour Data

Using a wheeled agricultural machine equipped with an autonomous driving system as the mobile platform, a GNSS (UB48; horizontal accuracy: 0.8 cm + 1 ppm; vertical accuracy: 1.5 cm + 1 ppm; heading accuracy: 0.2° with a 1 m baseline, Beijing Beidou Navigation Engineering Technology Co., Ltd., Beijing, China) and an AHRS (HWT605; static roll/pitch bias: 0.2–0.4°, Wit Intelligent Technology Co., Ltd., Shenzhen, China) are installed on the machine's chassis. The GNSS measures the real-time spatial position and heading information of the machine during operation, while the AHRS measures the motion attitude of the chassis. A time-stamp synchronization method is employed to synchronously collect the machine's position and attitude data. During field operations, the wheels contact the hard bottom layer of the paddy field. Continuous contact points between the bottom of wheels and the hard bottom layer form a point cloud representing the hard bottom contour. Based on measured position and attitude information—including the machinery's spatial position, heading angle, and chassis pitch angle—the Euler transformation method establishes the bottom of the wheel motion trajectory model in the global coordinate system [8]. GNSS spatial positioning and orientation data, combined with AHRS roll and pitch attitude information, are processed through sensor calibration and outlier handling to reconstruct the hard bottom contour terrain traced by the machine's wheels. A visualizable hard bottom contour digital model is then constructed using a triangulated mesh method based on the collected point cloud. The designed agricultural machinery pose information and hard bottom contour perception platform are shown in Figure 1a, while the data acquisition process is illustrated in Figure 1b.

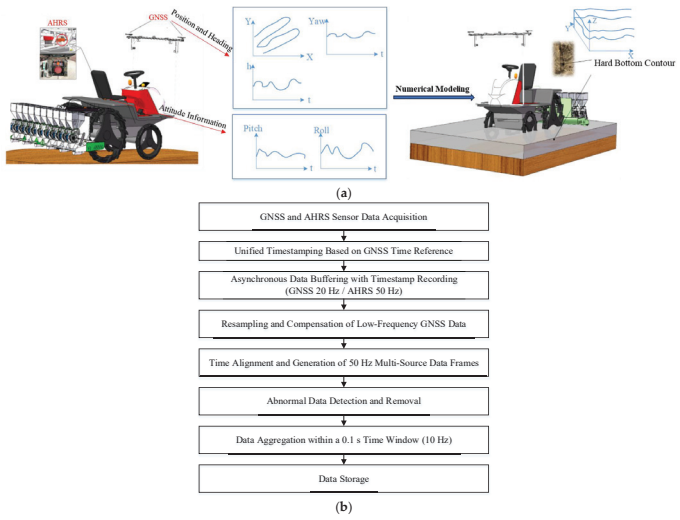

Figure 1. Platform for collecting agricultural machinery pose information and bottom layer contour data: (**a**) information collection platform; (**b**) data collection process.

2.2. Correlation Analysis Method Between Agricultural Machinery Operational Motion States and Contour Feature Parameters

2.2.1. Method for Extracting Agricultural Machinery Operational Motion State Parameters

The onboard GNSS dual-antenna satellite positioning system enables the main antenna to capture the spatial position of the agricultural machinery antenna installation point within a local tangent plane coordinate system, along with the working speed and heading angle between the two antennas. The integrated AHRS system measures the pitch and roll angles of the agricultural machinery chassis. During actual operations, the agricultural machinery undergoes frequent attitude changes. The position of the main antenna cannot fully represent the machinery's motion state when it is not level. Therefore, the motion states of the bottom surfaces of the left and right rear wheels and the center of the rear suspension are used to express the machinery's true motion. By establishing a vehicle coordinate system, coordinate increments relative to the main antenna installation position are obtained for the bottom of the left and right rear wheels. Real-time motion information for the rear wheel bottoms is derived through continuous conversion based on the main antenna position and the vehicle's current attitude. The relationship between the local tangent plane coordinate system {t}, the vehicle coordinate system {b}, and the position of the rear wheel bottoms is illustrated in Figure 2.

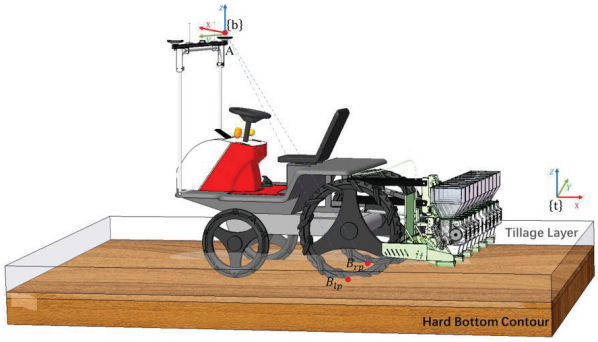

Figure 2. Schematic diagram showing the relationship between the local cutting plane coordinate system {t}, the vehicle body coordinate system {b}, and the position of the rear bottom of the wheel of the vehicle body.

Due to the rotational relationship between the bottom of wheel and wheel hub, the effect of rotation on the bottom-of-wheel position must be considered. This involves analyzing the change in coordinate increments of the bottom of the wheel within the vehicle body coordinate system during body pitch. The positional relationship during body pitch is illustrated in Figure 3.

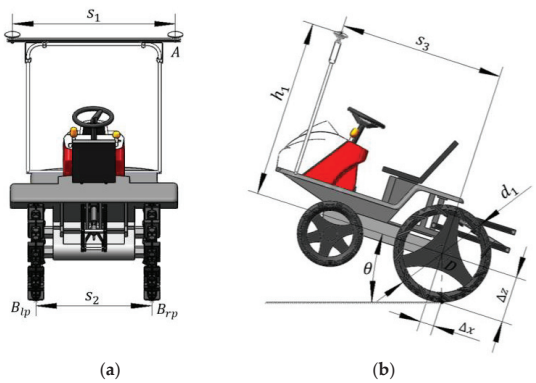

Figure 3. The positional relationship during body pitch: (**a**) rear view during vehicle pitching; (**b**) left view during vehicle pitching.

Let the right wheel's base point be B_{rp}, with coordinates $-s_3 + \Delta x, s_1/2 - s_2/2 + \Delta y, -h_1 + \Delta x$ in the vehicle body coordinate system. It is expressed as a matrix as follows:

$$B_{rp} = \begin{bmatrix} -s_3 + \Delta x \\ \frac{s_1}{2} - \frac{s_2}{2} + \Delta y \\ -h_1 + \Delta z \end{bmatrix} = \begin{bmatrix} -s_3 + \frac{d_1}{2} \cdot \sin\theta \\ \frac{s_1}{2} - \frac{s_2}{2} + 0 \\ -h_1 - \frac{d_1}{2} \cdot \cos\theta \end{bmatrix} \tag{1}$$

Among these, s_1 denotes the distance between the two positioning antennas, s_2 represents the distance between the left and right wheel hubs, h_1 is the vertical distance from the antenna positioning center point to the right rear wheel hub D, and s_3 is the distance projected along the X-axis of the vehicle coordinate system from the antenna positioning center point to the right rear wheel hub D. Δx, Δy, and Δz represent the incremental coordinates of the bottom of the wheel relative to the wheel hub in the x, y, and z directions of the vehicle coordinate system, respectively. θ denotes the rotation angle of the vehicle coordinate system relative to the local tangent plane coordinate system's X-axis, and d_1 is the wheel diameter.

Let the transformation matrix for converting point set coordinates in the vehicle body coordinate system to the local tangent plane coordinate system be R. The rotation matrix about the Z-axis is R_z, the rotation matrix about the Y-axis is R_y, and the rotation matrix about the X-axis is R_x. This leads to the following:

$$R_z = \begin{bmatrix} \cos\psi & -\sin\psi & 0 \\ \sin\psi & \cos\psi & 0 \\ 0 & 0 & 1 \end{bmatrix} \tag{2}$$

$$R_y = \begin{bmatrix} \cos\theta & 0 & \sin\theta \\ 0 & 1 & 0 \\ -\sin\theta & 0 & \cos\theta \end{bmatrix} \tag{3}$$

$$R_x = \begin{bmatrix} 1 & 0 & 0 \\ 0 & \cos\varphi & -\sin\varphi \\ 0 & \sin\varphi & \cos\varphi \end{bmatrix} \tag{4}$$

$$R = R_z R_y R_x = \begin{bmatrix} \cos\theta\cos\psi & \sin\varphi\sin\theta\cos\psi - \cos\varphi\sin\psi & \cos\varphi\sin\theta\cos\psi + \sin\varphi\sin\psi \\ \cos\theta\sin\psi & \sin\varphi\sin\theta\sin\psi + \cos\varphi\cos\psi & \cos\varphi\sin\theta\sin\psi - \sin\varphi\cos\psi \\ -\sin\theta & \sin\varphi\cos\theta & \cos\varphi\cos\theta \end{bmatrix} \tag{5}$$

Taking the bottom of right wheel as the sampling point, let the position coordinates of the main antenna in the global coordinate system {e} be ${}^{e}P_A$ (B, L, H). After Gauss projection transformation to the local tangent plane coordinate system {t}, the coordinates become ${}^{t}P_A$ (x_{At}, y_{At}, z_{At}). Let the set of ${}^{t}P_A$ coordinate points for point A of the main antenna in the local tangent plane coordinate system be G_d and the coordinate set of the bottom of the right wheel point in the local tangent plane coordinate system after Euler transformation be T_{rb}. This leads to the following:

$$T_{rb} = R \cdot B_{rp} + G_d \tag{6}$$

https://doi.org/10.3390/agriculture16020170

Similarly to setting the left wheel center point as B_{lp}, the coordinates of B_{lp} in the vehicle coordinate system are expressed as a matrix:

$$B_{lp} = \begin{bmatrix} -s_3 + \frac{d_1}{2} \cdot \sin\theta \\ \frac{s_1}{2} + \frac{s_2}{2} \\ -h_1 - \frac{d_1}{2} \cdot \cos\theta \end{bmatrix} \tag{7}$$

The set of points T_{lb} obtained by Euler transformation of the base point coordinates of a revolver in the local tangent plane coordinate system satisfies the following equation:

$$T_{lb} = R \cdot B_{lp} + G_d \tag{8}$$

Let the center point of the rear axle be as B_c. The coordinates of B_c in the vehicle body coordinate system are expressed as a matrix:

$$B_c = \begin{bmatrix} -s_3 \\ \frac{s_1}{2} \\ -h_1 \end{bmatrix} \tag{9}$$

Let the center point of the rear axle be B_c. The coordinates of B_c in the vehicle coordinate system are expressed as a matrix:

$$T_c = R \cdot B_c + G_d \tag{10}$$

The ${}^{e}P_A$ point cloud undergoes Gaussian projection and Euler transformation to obtain the coordinate matrices T_{rb}, T_{lb}, and T_c for the right rear wheel bottom layer, left rear wheel bottom layer, and rear axle center in the local tangent plane coordinate system. Based on these coordinate positions, the displacement, velocity, and acceleration of the agricultural machinery's wheel bottoms and rear axle center are derived. These provide the motion-related input variables for analyzing how hard-surface contour excitation influences the agricultural machinery's pose.

By applying differential operations to the positional time series data from the bottom of the left and right wheels and the center of the agricultural machinery's rear axle, the corresponding kinematic parameters of the machinery can be derived. Specifically, performing first-order differentiation on the displacement time series of the left and right wheel bottoms yields the linear velocity of the right wheel bottom, the linear velocity of the left wheel bottom, and the velocity of the agricultural machinery's rear axle center, respectively.

Taking the calculation of the right wheel's baseline motion parameters as an example, let the right wheel's baseline velocity be v_{rb} and its baseline acceleration be a_{rb}. Using a discrete difference form, the calculation yields the following:

$$v_{rb}[n] = \frac{\|T_{rb}[n] - T_{rb}[n-1]\|}{\Delta t} \tag{11}$$

$$a_{rb}[n] = \frac{v_{rb}[n] - v_{rb}[n-1]}{\Delta t} = \frac{\|T_{rb}[n] - 2T_{rb}[n-1] + T_{rb}[n-2]\|}{(\Delta t)^2} \tag{12}$$

where n denotes the time step index, and Δt represents the sampling interval. For the 10 Hz frequency data acquisition in this paper, this value is 0.1 s.

Similarly, the left wheel base velocity v_{lb}, left wheel base acceleration a_{lb}, vehicle center velocity v_c, and vehicle center acceleration a_c can be calculated. Furthermore, to reflect the instantaneous directional change state during agricultural machinery movement, introduce

https://doi.org/10.3390/agriculture16020170

the left–right wheel base velocity difference Δv_b and acceleration difference Δa_b, which yields the following equations:

$$\Delta v_b[n] = v_{lb}[n] - v_{rb}[n] \tag{13}$$

$$\Delta a_b[n] = a_{lb}[n] - a_{rb}[n] \tag{14}$$

Based on data acquired from satellite positioning and attitude sensors, a complete mathematical mapping relationship is established through differential operations. This relationship transforms observational data from various parts of the agricultural machinery into parameters describing the motion state of the bottom of the wheels and the center of the rear axle. This provides input for analyzing the relationship between the motion state of the agricultural machinery and the contour characteristics of the hard bottom layer.

2.2.2. Method for Extracting Contour Feature Parameters of the Hard Bottom Layer

Agricultural machinery operates on hard bottom layers, with wheels exerting force upon the hard bottom layer contour. Due to the absence of shock-absorbing suspension on the rear axle, the contour surface of the hard bottom layer directly impacts the vehicle's wheels. This force induces displacement and attitude changes in the wheels contacting the hard bottom layer. By utilizing GNSS position and AHRS attitude data from the machinery, discrete point clouds T_{rb} (Equation (6)) and T_{lb} (Equation (8)) representing the bottom of left and right wheels are reconstructed. Through automatic sensor calibration, outlier removal, and 3D spline curve denoising of the contour trajectory, a digital model of the hard bottom layer contour traversed by the machinery is constructed [8]. In practical field operations, agricultural machinery primarily follows planned straight sections. The quality of straight-line segment operations critically impacts overall field performance. To extract representative hard bottom layer trajectory patterns, straight-line segments were isolated from the full-field hard bottom layer contour. The full-field wheel bottom trajectory is illustrated in Figure 4. The actual hard bottom layer contours of the left and right wheels of the agricultural machinery were isolated. Continuous scattered points were then fitted with spline curves to form smooth hard bottom layer contours, as shown in Figure 5.

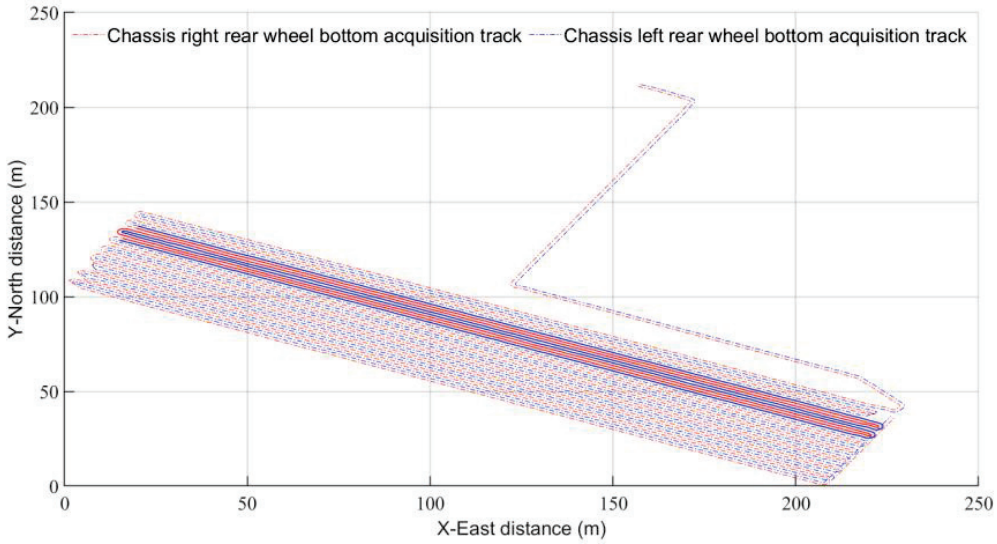

Figure 4. Full-field wheel track pattern.

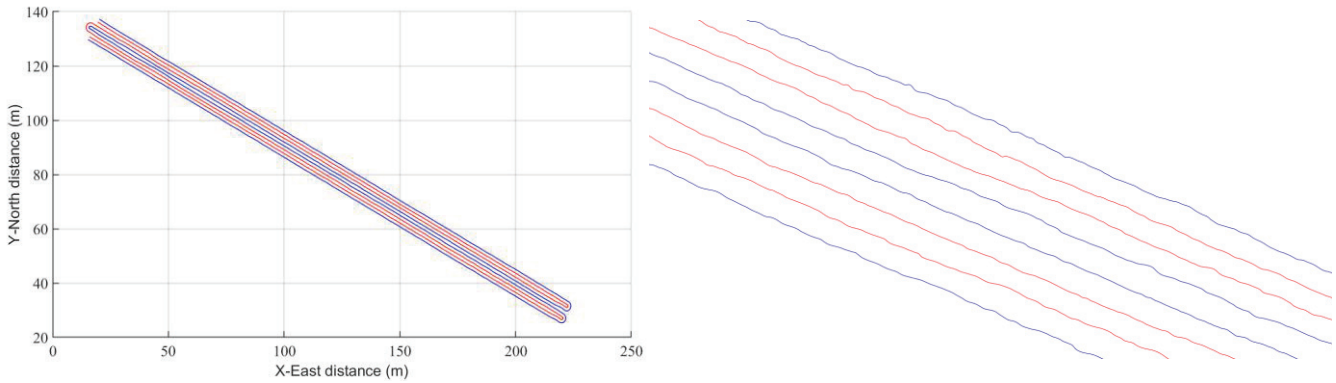

Figure 5. Hard bottom layer contour curve: (**a**) segmented trajectory; (**b**) 3D spline curve fitting.

Based on the coordinate points connecting the 3D spline curve of the hard bottom layer contour, isolate the contour points of the hard bottom layer in contact with the bottom of left wheel. In the local tangent plane coordinate system, the *X*-axis coordinate value is x_{lb}, the *Y*-axis coordinate value is x_{lb}, and the *Z*-axis coordinate value is z_{lb}. Additionally, the *X*-axis coordinate value x_{rb}, the *Y*-axis coordinate value y_{rb}, and the *Z*-axis coordinate value z_{rb} of the hard bottom layer contour points contact the bottom of right wheel in the local tangent plane coordinate system, while the *Z*-axis coordinate height difference Δz_b between the hard bottom layer contours contacts the bottom of the left and right wheels.

To further analyze the impact of localized characteristics of the hard bottom layer on the movement state of agricultural machinery, the surface roughness of the hard bottom layer is introduced to represent the degree of localized undulation. Based on the contour information of the hard bottom layer, a section spanning the agricultural machinery's wheel base length was selected locally. A straight line was fitted using the least squares method, and the height of each point relative to this fitted line was calculated. The relationship between the hard bottom layer contour, the locally fitted line segments, and the height of contour points relative to the fitted line is illustrated in Figure 6.

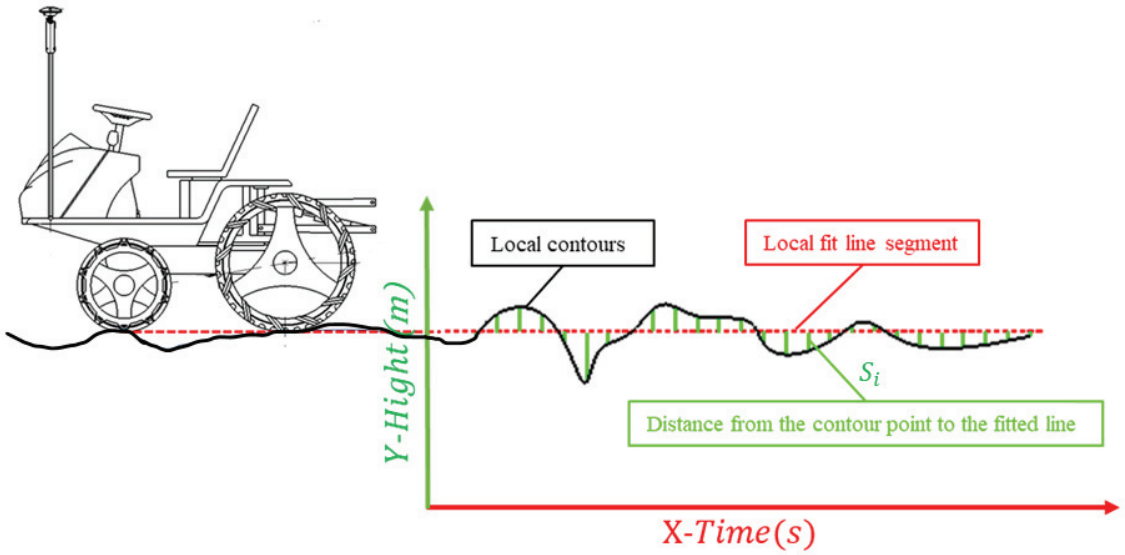

Figure 6. Relationship between hard bottom layer, local fitted line segments, and height of contour points relative to the fitted straight line.

https://doi.org/10.3390/agriculture16020170

Let the coefficient of the linear term (slope) of the locally fitted line based on the least squares method be A, the constant term (intercept) be B, and the distance from the th contour point within the local region to the fitted line be S_i. This leads to the following:

$$S_i = \frac{|A * n_i - z_i + B|}{\sqrt{A^2 + B^2}} \tag{15}$$

where S_i denotes the distance from the i-th contour point to the fitted straight line; n_i represents the index of the i-th contour point; z_i denotes the height of the i-th contour point.

Let the local surface roughness at the j-th point on the hard bottom layer be denoted as R_{d_j}, calculated using the following formula:

$$R_{d_j} = \frac{1}{n_z}\int_0^{n_z}|S|dx \approx \frac{1}{n_z}\sum_{i=1}^{n_z}|S_i| \tag{16}$$

where n_z represents the sample size within the specified range.

By performing a traversal calculation on the hard bottom contour collected from the field according to Equation (19), the continuous surface roughness characteristic values of the hard bottom contour traversed by the agricultural machinery can be obtained.

2.2.3. Correlation Impact Analysis Method

When agricultural machinery performs path-following operations, the degree of deviation in vehicle posture from the planned path serves as a key parameter for evaluating the operational quality of autonomous agricultural machinery and determining decision-control output. To analyze how the motion state parameters and hard bottom layer contour feature parameters of agricultural machinery affect the deviation of its posture from the planned path, real-time position and heading are obtained via GNSS. These are then compared with the expected values of the planned path to derive the perpendicular distance between the vehicle position and the expected path (lateral deviation) and the angular difference between the vehicle direction and the expected path direction (heading deviation). Schematic diagrams of lateral deviation and heading deviation are shown in Figure 7.

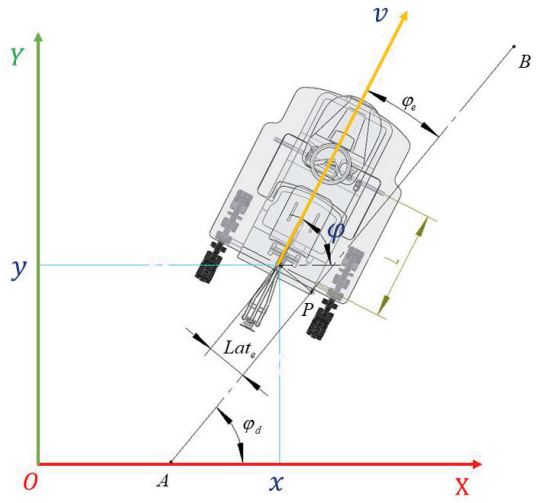

Figure 7. Schematic diagram of lateral deviation and heading deviation in agricultural machinery. Note: In the figure, φ_d represents the target heading angle, φ_e denotes the heading angle deviation, and Lat_e indicates the lateral position deviation. The target navigation line is formed by points A and B, with P serving as the target navigation point.

The installed GNSS and AHRS systems continuously capture real-time position and attitude parameters of the agricultural machinery, including antenna elevation, velocity,

heading angle, pitch angle, and roll angle. Building upon the sensor-derived data, the agricultural machinery operational motion state parameter extraction method described in Section 2.2.1 is employed. Through Euler transformation, the following motion state parameters are obtained: the bottom of left wheel velocity, the bottom of right wheel velocity, the bottom of left–right wheel velocity difference, left wheel base acceleration, right wheel base acceleration, left–right wheel base acceleration difference, vehicle center velocity, and vehicle center acceleration. Section 2.2.2's hard bottom layer contour feature extraction method is used to obtain the 3D coordinates of contact points between the agricultural machinery and the hard bottom layer contour, along with local elevation differences and surface roughness characteristics. A segmented straight working path was selected. Continuous datasets synchronously collected by the vehicle-mounted autonomous driving system—including vehicle pose sensors and operational parameters—were used as the test dataset. Numerical sets for hard bottom layer contour features and agricultural machinery pose parameters were calculated. The lateral deviation and heading deviation recorded during operation were analyzed in relation to the hard bottom layer contour feature parameters and agricultural machinery pose parameters, respectively. To quantify the linear correlation strength and direction between hard bottom layer contour features and agricultural machinery motion parameters as multivariate pairwise continuous variables, this study employs the classical Pearson correlation analysis method. This method calculates the correlation coefficient between each pair of variables by computing the ratio of the covariance between the agricultural machinery motion parameters and the hard bottom layer contour feature parameters to their respective standard deviations multiplied by the position deviation and heading deviation. The calculation formula is as follows:

$$\rho_{X_i,Y_j} = \frac{\operatorname{cov}(X_i, Y_j)}{\sigma_{X_i}\sigma_{Y_i}} \tag{17}$$

In the equation, i denotes the sequence number of the variable type representing the contour feature parameter of the hard bottom layer for agricultural machinery motion parameters; j denotes the sequence number of the deviation type for agricultural machinery motion; ρ_{X_i,Y_j} denotes the correlation coefficient between the two variables; $\operatorname{cov}(X_i, Y_j)$ denotes the covariance between the X_i and Y_j variables; σ_{X_i} and σ_{Y_j} denote the standard deviations of the X_i and Y_j variables, respectively.

The correlation coefficient ρ_{X_i,Y_j} ranges from -1 to 1, where 0 indicates no linear relationship between two variables, 1 indicates perfect positive correlation, and -1 indicates perfect negative correlation. By observing the degree of correlation, significant factors influencing lateral deviation and heading deviation during agricultural machinery movement are analyzed and extracted. Based on the identified significant factors, field experiments are conducted to analyze how the hard bottom layer contour characteristics affect the position and orientation of agricultural machinery.

2.3. Extraction of Agricultural Machinery States During Typical Bogging Processes

During paddy field operations, agricultural machinery often becomes bogged down in mud or soft soil while maneuvering at field edges or working on an unknown hard bottom layer. Unable to extricate itself, the vehicle becomes stuck, severely reducing operational efficiency. This issue is particularly critical during unmanned intelligent farming operations, as it necessitates halting the work program and disrupting continuous operation. Field observations during the application and promotion of intelligent farm machinery in paddy fields reveal that vehicle trapping predominantly occurs when the destruction of the hard bottom layer increases wheel trapping depth. Farm machinery wheels become embedded in this layer, unable to extricate themselves through their own propulsion. This typical

https://doi.org/10.3390/agriculture16020170

type of paddy field trapping is related to the depth and local characteristics of the hard bottom layer. A schematic illustration of vehicle trapping is shown in Figure 8.

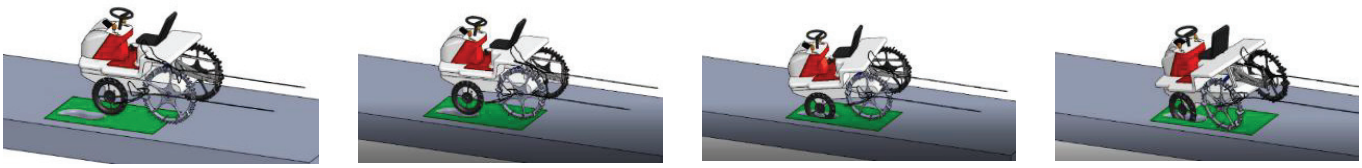

(**a**) (**b**) (**c**) (**d**)

Figure 8. Schematic diagram of a typical vehicle-trapping process: (**a**) normal driving; (**b**) about to be trapped; (**c**) just trapped; (**d**) after being trapped.

To analyze the typical vehicle-trapping process of agricultural machinery under hard bottom layer conditions, operational data from production trials exhibiting typical trapping scenarios were extracted for analysis. A digital model of the hard bottom layer in the trapping field was constructed using a hard bottom layer digital modeling method. Based on typical bogging incidents occurring during actual agricultural machinery operations, the hard bottom layer contour was captured and its characteristic parameters were extracted using the method described in Section 2.2.2. This process yielded a localized contour model of the hard bottom layer and its characteristic parameters under typical bogging conditions. The resulting bogging contour model and its locally magnified region are shown in Figure 9.

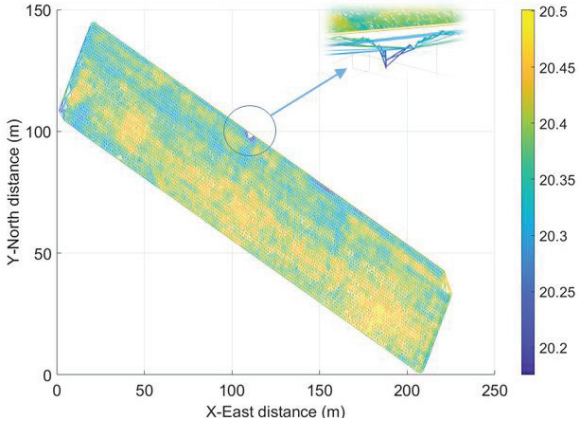

Figure 9. Digital model of hard bottom layer in fields where vehicle trapping occurred.

To analyze the dynamic characteristics of the hard bottom layer contour before and after the agricultural machinery becomes stuck, the contour feature parameters of the hard bottom layer were extracted from data collected within 15 s before and after the incident. The data system was configured with a sampling frequency of 10 Hz, enabling the extraction of 300 datasets for analysis. The study focused on the contour height at the tire-hard bottom layer interface and the local roughness of the hard bottom layer. Through numerical analysis, a dynamic variation model of the hard bottom layer contour characteristics under typical trapping scenarios was constructed.

2.4. Test Scenario

2.4.1. Paddy Field Operation Test Scenario

An unmanned direct-seeding machine was deployed in rice fields (soil type: sandy loam) at Guangzhou's Zengcheng District unmanned farm. The machine integrated agricultural machinery position and attitude data, and a hard bottom layer information collection system was integrated into the unmanned rice direct seeder to collect real-time position and attitude data. Utilizing hard bottom layer contour acquisition and feature extraction

methods, corresponding contour information was synchronously obtained during machinery movement. The unmanned rice direct seeder performed automated mechanical seeding while concurrently collecting hard bottom layer and mud surface data. The planned working path of the direct seeder is shown in Figure 10a, and the operational site is depicted in Figure 10b.



(**a**) (**b**)

Figure 10. Planned driving path and field site of unmanned direct seeding machine: (**a**) planned driving path; (**b**) field site.

2.4.2. Hard Road Surface Test Scenario

Furthermore, to analyze the impact of agricultural machinery movement when traveling along a hard bottom layer contour with a known fixed elevation difference, two sets of 5 cm high trapezoidal ridges and two sets of 10 cm high trapezoidal ridges were laid at equal intervals along the planned agricultural machinery track on a hard cement road. Using automatic straight-line driving mode, the machinery's single-side wheels directly rolled over the ridges, causing lateral tilt. The machinery's position and orientation data were collected to analyze the impact of fixed-height ground contours on its posture through experimental evaluation. The experimental setup is illustrated in Figure 11, while the actual field test site is shown in Figure 12.

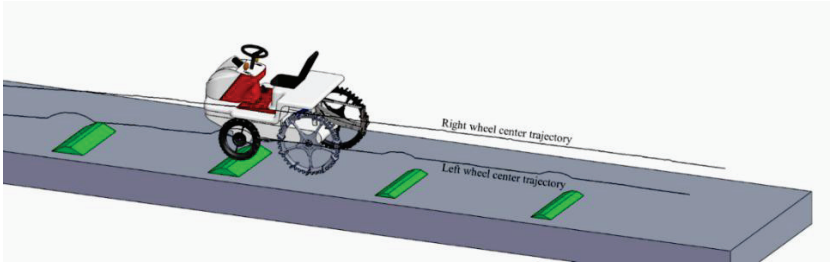

Figure 11. Schematic diagram of hard road surface testing.



(**a**) (**b**)

Figure 12. Schematic diagram of hard road surface test: (**a**) driving over a 5 cm high trapezoidal ridge; (**b**) driving over a 10 cm high trapezoidal ridge.

https://doi.org/10.3390/agriculture16020170

3. Results

3.1. Analysis of the Relationship Between Agricultural Machinery Movement State and Hard Bottom Layer Characteristic Parameters

3.1.1. Correlation Analysis Results

During paddy field operation trials, the contour characteristics of the paddy field hard bottom layer and the impact of agricultural machinery movement were analyzed. Data collected from paddy field operation scenarios were selected and segmented into straight operation path segments. A dataset comprising 3091 sets of synchronously collected data from vehicle-mounted position and attitude sensors and operation parameters via the vehicle-mounted autonomous driving system was used as the test dataset. Employing the parameter extraction method described in Section 2.2, the parameter sets for hard bottom layer contour characteristics and agricultural machinery attitude were calculated. These parameters were then analyzed against lateral deviation and heading deviation data collected during operations, with results presented in Table 1.

Table 1. Correlation analysis between hard bottom layer contour characteristics and agricultural machinery motion parameters.

Variable	Lateral Deviation (m)		Heading Deviation (°)	
	Pearson Correlation	Sig. (2-Tailed)	Pearson Correlation	Sig. (2-Tailed)
Hardpan feature parameters				
X-coordinate of left wheel–hardpan contact point (m)	−0.042 *	0.021	−0.101 **	0.000
Y-coordinate of left wheel–hardpan contact point (m)	0.040 *	0.026	0.101 **	0.000
Z-coordinate of left wheel–hardpan contact point (m)	0.156 **	0.000	0.056 **	0.002
X-coordinate of right wheel–hardpan contact point (m)	−0.042 *	0.020	−0.102 **	0.000
Y-coordinate of right wheel–hardpan contact point (m)	0.040 *	0.025	0.102 **	0.000
Z-coordinate of right wheel–hardpan contact point (m)	0.056 **	0.002	−0.002	0.917
Height difference between left and right wheel contact points (m)	0.142 **	0.000	0.075 **	0.000
Local roughness of contour	0.094 **	0.000	−0.118 **	0.000
Machinery posture parameters				
Speed (m/s)	0.152 **	0.000	−0.027	0.129
Left wheel velocity (m/s)	0.017	0.337	−0.010	0.561
Right wheel velocity (m/s)	0.152 **	0.000	−0.019	0.289
Velocity difference between left and right wheels (m/s)	−0.377 **	0.000	0.024	0.180
Left wheel acceleration (m/s^2)	−0.002	0.913	−0.013	0.458
Right wheel acceleration (m/s^2)	0.006	0.732	0.012	0.493
Acceleration difference between left and right wheels (m/s^2)	−0.041 *	0.021	−0.131 **	0.000
Center velocity (m/s)	0.088 **	0.000	−0.019	0.282
Center acceleration (m/s^2)	0.002	0.892	0.000	0.995

"**" indicates significant correlation at the 0.01 level (two-tailed). "*" indicates significant correlation at the 0.05 level (two-tailed).

Based on Pearson correlation analysis and significance testing results, the strength and direction of statistical correlations between hard bottom contour parameters and agricultural machinery motion parameters were identified. Results indicate that during straight-line operations, both lateral deviation and heading deviation of the agricultural machinery exhibit extremely significant correlations with the *Z*-axis height of the hard bottom layer contour contacted by the left and right wheel bases and their height

https://doi.org/10.3390/agriculture16020170

differences. They also show extremely significant correlations with the local roughness of the hard bottom layer contour. Additionally, lateral deviation exhibits an extremely significant correlation with the linear speed difference between the left and right wheel bases. The Pearson correlation analysis results reflect the statistical relationship between hard bottom contour characteristics and the agricultural machinery's posture. They reveal the coupling characteristics and shared dependencies among the agricultural machinery's motion response parameters under hard bottom excitation conditions, providing quantitative references for subsequent analysis of the agricultural machinery's posture response mechanisms.

3.1.2. Results of Straight-Line Driving Test on Rigid Pavement with Fixed Elevation Difference

(1) Fixed Wheel Angle Through-the-Ridge Test

Using the fixed wheel angle of agricultural machinery during straight-line travel, a continuous ridge-crossing test was conducted. By obtaining rear wheel center trajectory data, the heading and heading change rate of a single-wheel crossing ridges were analyzed. The front wheels of the rice transplanter's mobile chassis had a diameter of 0.65 m, while the rear wheels measured 0.95 m in diameter. The speed was set to the field operation speed of 1 m/s. The front and rear wheels traversed two 5 cm high ridges and two 10 cm high ridges, respectively, comprising a total of eight stages designated as A-1, B-1, A-2, B-2, C-1, D-1, C-2, and D-2. The planar trajectory of the agricultural machinery traversing the ridge platform during all stages is shown in Figure 13a, while the heading changes are depicted in Figure 13b. Simultaneously, the heading and heading change rate during the machinery's passage over the ridge platform were acquired, with the results presented in Figure 14. The stage numbers and descriptions for the entire test process are detailed in Table 2.

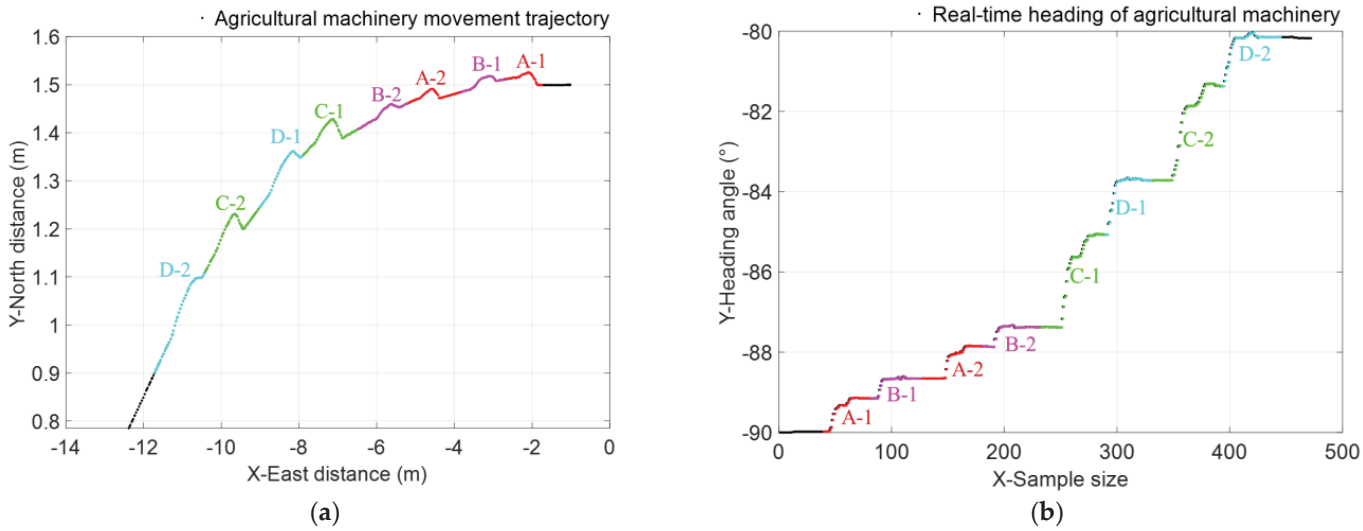

Figure 13. Trajectory curve and heading change rate of agricultural machinery: (**a**) trajectory of agricultural machinery traversing ridge platforms; (**b**) heading changes during agricultural machinery traversal of ridge platforms.

https://doi.org/10.3390/agriculture16020170

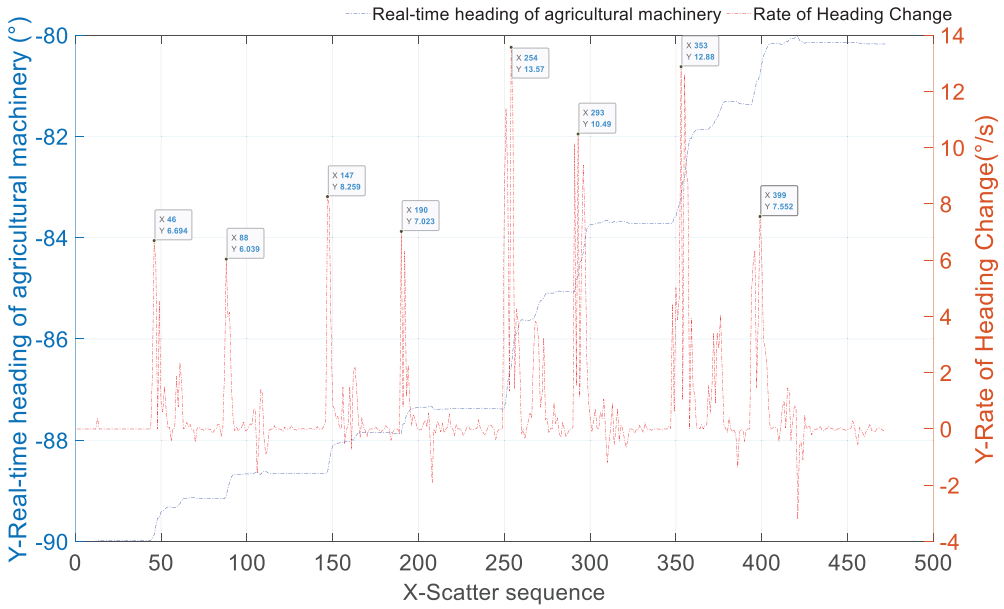

Figure 14. Heading and heading change rate during the process of agricultural machinery traversing ridge platforms.

Table 2. Heading variation during ridge crossing.

Stage ID	Description	Heading (°)	Heading Change (°)	Maximum Heading Change Rate (°/s)
A-1	Front wheel crossing the first 5 cm ridge	−89.15	0.85	6.694
B-1	Rear wheel crossing the first 5 cm ridge	−88.66	0.49	6.039
A-2	Front wheel crossing the second 5 cm ridge	−87.85	0.81	8.259
B-2	Rear wheel crossing the second 5 cm ridge	−87.37	0.48	7.023
C-1	Front wheel crossing the first 10 cm ridge	−85.06	2.31	13.57
D-1	Rear wheel crossing the first 10 cm ridge	−83.72	1.34	10.49
C-2	Front wheel crossing the second 10 cm ridge	−81.32	2.4	12.88
D-2	Rear wheel crossing the second 10 cm ridge	−80.15	1.17	7.552

As shown in Figure 13 and Table 2, the trajectory tracking results for single-wheel crossing of ridges indicate that when both front and rear wheels continuously traverse a ridge, the agricultural machinery's heading persistently deviates toward the side with the ridge. The heading variation range when crossing a 5 cm ridge was 0.48–0.85°, while crossing a 10 cm ridge resulted in a variation range of 1.17–2.40°. The heading change caused by a 10 cm obstacle was 2–3 times that of a 5 cm one, indicating that ridge height is the primary influencing factor—consistent with the correlation analysis results.

As shown in Figure 14 and Table 2, from the perspective of heading change rate, the front wheel (diameter 0.65 m) exhibited an average heading change rate of 7.48°/s when traversing a 5 cm obstacle, while the rear wheel (diameter 0.95 m) averaged 6.53°/s. This indicates a reduction of approximately 12.6% in the rear wheel's heading change rate compared to the front wheel. When traversing a 10 cm ridge, the front wheel exhibited a phase-average heading rate of 13.23°/s, while the rear wheel recorded 9.02°/s, indicating a reduction of approximately 31.8% in the rear wheel's heading rate compared to the front wheel. Larger-diameter wheels demonstrate greater stability when traversing ridges than smaller wheels, a characteristic that becomes more pronounced when navigating higher ridges.

https://doi.org/10.3390/agriculture16020170

A regression model was developed with ridge height and wheel diameter as independent variables, and the heading change as the dependent variable:

$$y_{yaw} = 1.43667 + 22.95 \times h_l - 2.40833 \times d_c \quad (18)$$

where y_{yaw} represents the heading change value, h_l represents the ridge height, and d_c represents the wheel diameter.

The regression model's coefficient of determination R^2 is 0.92356, with a root mean square error (RMSE) of 0.195°, mean absolute error (MAE) of 0.189°, and sum of squared errors (SSEs) of 0.30436. The comparison between actual heading changes and predicted heading changes is shown in Table 3 and Figure 15.

Table 3. Comparison between actual and predicted heading change values.

Sample No.	Ridge Height (m)	Wheel Diameter (m)	Actual Heading Change (°)	Predicted Heading Change (°)	95% Confidence Interval (°)
1	0.05	0.65	0.85	1.02	[0.63, 1.41]
2	0.05	0.95	0.49	0.3	[−0.09, 0.68]
3	0.05	0.65	0.81	1.02	[0.63, 1.41]
4	0.05	0.95	0.48	0.3	[−0.09, 0.68]
5	0.1	0.65	2.31	2.17	[1.78, 2.55]
6	0.1	0.95	1.34	1.44	[1.06, 1.83]
7	0.1	0.65	2.4	2.17	[1.78, 2.55]
8	0.1	0.95	1.17	1.44	[1.06, 1.83]

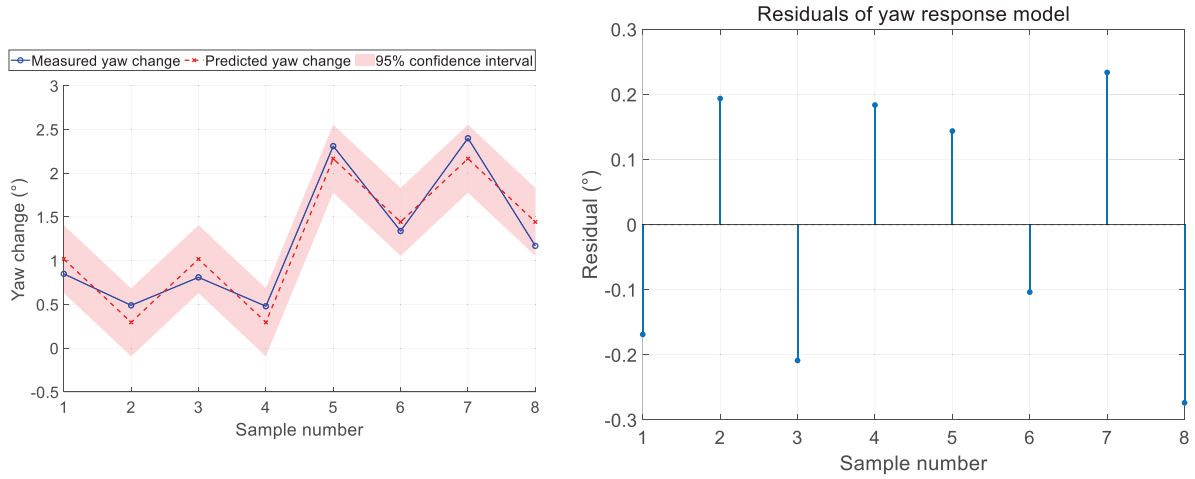

(**a**) (**b**)

Figure 15. Comparison between measured and model-predicted heading change values: (**a**) numerical comparison; (**b**) residual plot.

To further observe the dynamic process of height differences and the rate of change between the left and right rear axles of agricultural machinery caused by the ridge, the height differences and their rates of change at each pass stage were extracted, as shown in Figure 16.

As shown in Figure 16, whether traversing a 5 cm or 10 cm ridge, the front wheels exhibit minimal impact on the rear axle height difference (within 1 cm). However, when the rear wheels pass over the ridge, the rear axle height difference closely matches the ridge height, measuring 5.5 cm, 5.9 cm, 10.6 cm, and 10.8 cm, respectively. Therefore, the front suspension system effectively counteracts terrain effects on the vehicle body when the front wheels traverse the ridges. The rear axle, lacking suspension damping, perceives the actual contour features of the hard subsoil layer when the rear wheels pass over it. The

primary factor influencing the roll attitude of the agricultural machinery lies in the terrain characteristics encountered during rear-wheel traversal. Consequently, when considering control compensation for the machinery, the focus should be on the rear wheels and the terrain features they encounter during passage.

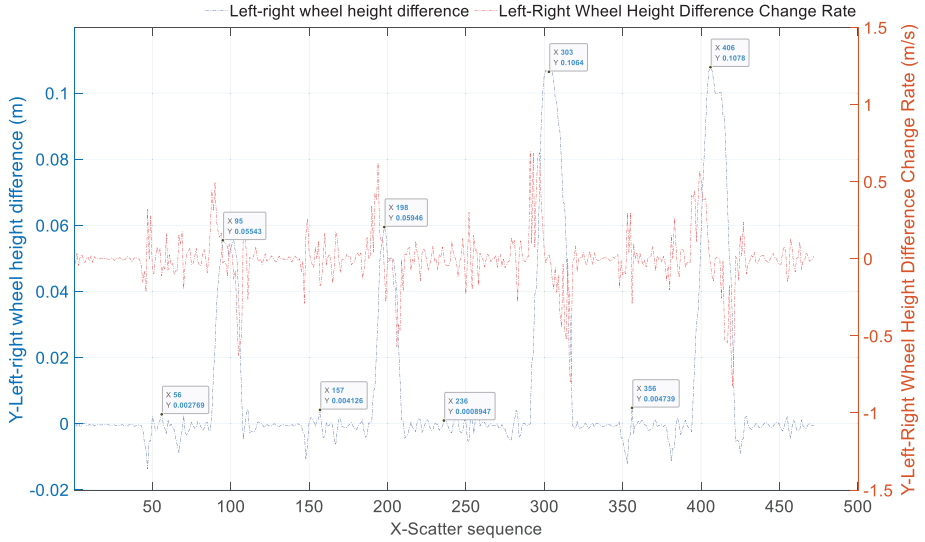

Figure 16. Dynamic process of height difference between left and right rear axles and its rate of change.

(2) Straight-Line Autonomous Driving Ridge-Crossing Test

During straight-line autonomous driving trials on ridges, the agricultural machinery traversed four ridges of identical specifications using straight-line-assisted driving. Using the sensor data calibration method [18], the roll system error was determined to be −2.429°, the pitch system error was 0.846°, and the heading system error was −1.103°. The positioning antenna, rear axle center, and bottom wheel tracks of the agricultural machinery are shown in Figure 17.

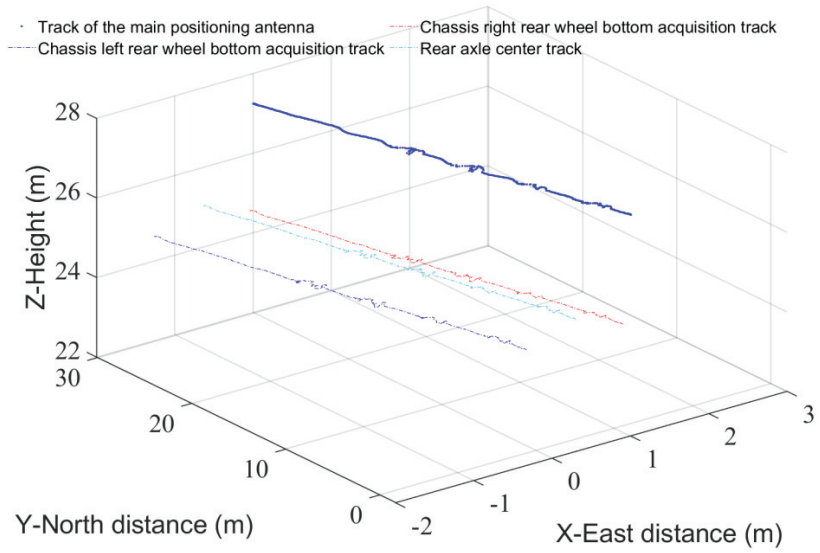

Figure 17. Track of the main positioning antenna, rear axle center, and wheel track.

Based on the acquired positioning data, analyze the deviation of the antenna from the expected path as the agricultural machinery passes through each ridge. Combined with the acquired vehicle posture data, determine the deviation of the center of the rear axle

https://doi.org/10.3390/agriculture16020170

and the center of the line connecting the bottom of left and right wheels from the expected path. The acquired antenna trajectory and its lateral deviation are shown in Figure 18. The acquired rear axle center trajectory and its lateral deviation are shown in Figure 19. The acquired centerline trajectory of the bottom of left and right wheels and its lateral deviation are shown in Figure 20.

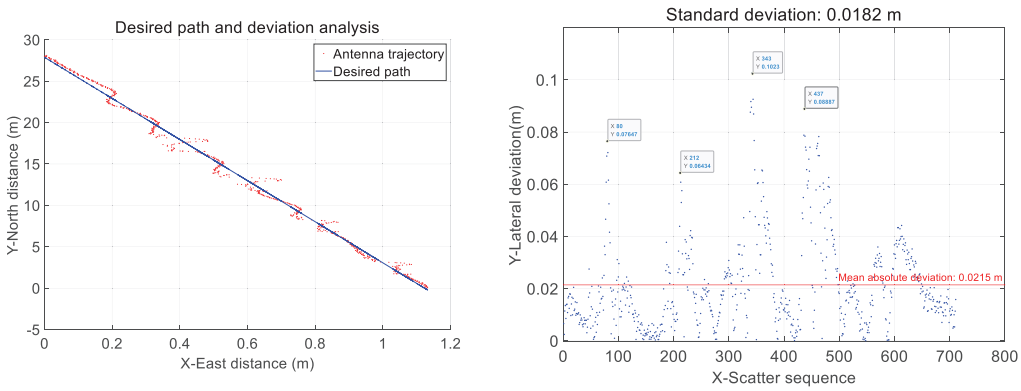

(**a**) (**b**)

Figure 18. Antenna trajectory and its lateral deviation: (**a**) antenna trajectory; (**b**) antenna lateral deviation.

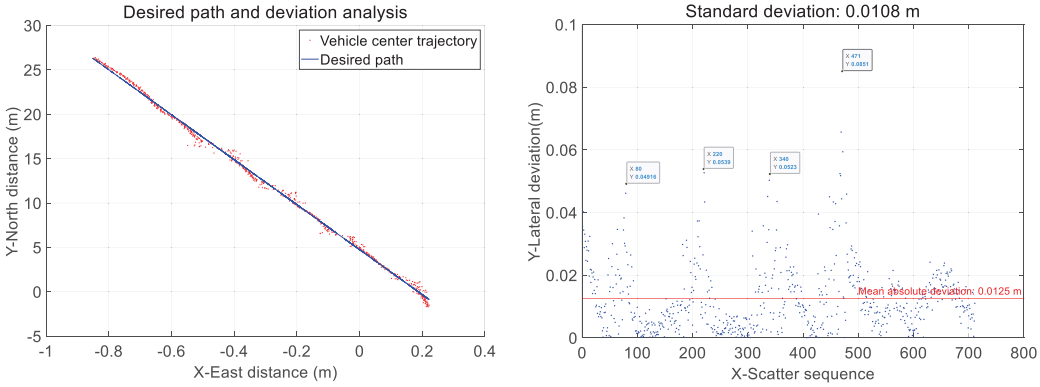

(**a**) (**b**)

Figure 19. Center trajectory of the rear axle on agricultural machinery and its lateral deviation: (**a**) center trajectory of agricultural machinery rear axle; (**b**) lateral deviation of agricultural machinery rear axle center.

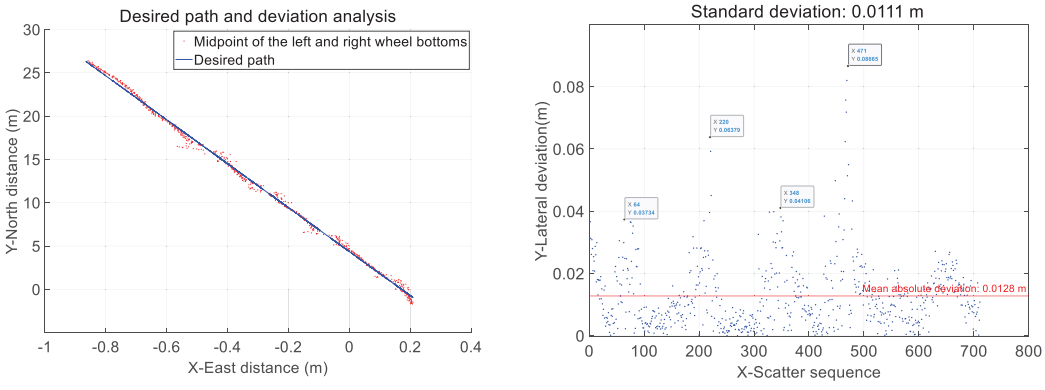

(**a**) (**b**)

Figure 20. Center trajectory of the line connecting the left and right wheel bottoms and its lateral deviation; (**a**) center trajectory of wheel base connection lines; (**b**) lateral deviation of wheel base connection line center.

https://doi.org/10.3390/agriculture16020170

Results indicate that when traversing a 5 cm ridge section, the standard deviation of antenna lateral deviation was 0.0143 m, the standard deviation of rear axle center lateral deviation was 0.0109 m, and the standard deviation of left/right wheel base center lateral deviation was 0.0108 m. When traversing the 10 cm ridge section, the standard deviation of antenna lateral deviation was 0.0200 m, the standard deviation of rear axle center lateral deviation was 0.0107 m, and the standard deviation of left/right wheel base center lateral deviation was 0.0112 m. During the entire passage over 5 cm and 10 cm ridges, the standard deviation of the antenna lateral deviation was 0.0182 m, the standard deviation of the rear axle center lateral deviation was 0.0108 m, and the standard deviation of the left and right wheel base center lateral deviation was 0.0111 m. Detailed information is shown in Table 4 and Figure 21.

Table 4. Standard deviations of lateral deviations for different sections.

Section	Antenna Lateral Deviation SD (m)	Rear Axle Center Lateral Deviation SD (m)	Rear Wheel Midpoint Lateral Deviation SD (m)
5 cm Ridge	0.0143	0.0109	0.0108
10 cm Ridge	0.0200	0.0107	0.0112
Entire section (5 cm + 10 cm)	0.0182	0.0108	0.0111

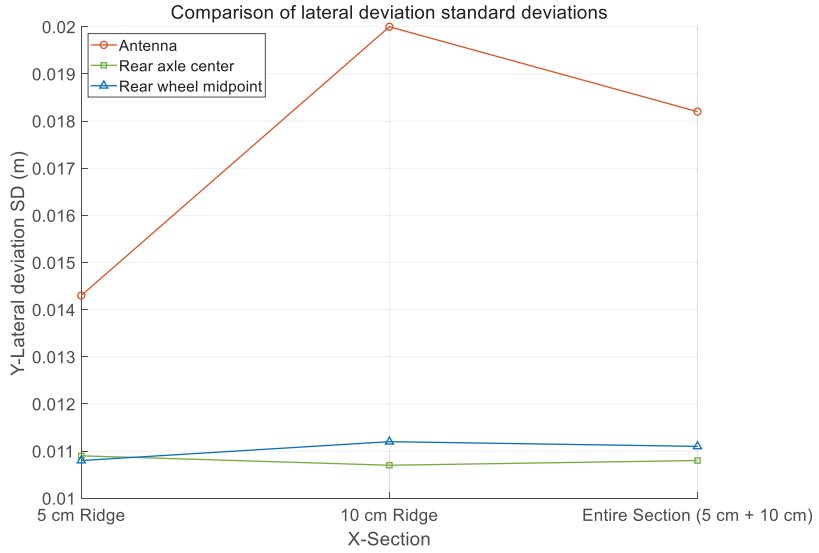

Figure 21. Comparison of standard deviations for lateral deviations across different sections.

As shown in Table 4 and Figure 21, when the agricultural machinery traversed 5 cm and 10 cm ridges, respectively, the standard deviation of the positioning antenna lateral deviation increased from 0.0143 m to 0.0200 m—nearly doubling. Meanwhile, the standard deviation of the lateral for the attitude-corrected rear axle center and bottom of the wheel center remained virtually unchanged at approximately 0.01 m. This indicates that single-side passage over ridges causes lateral displacement of the higher-positioned antenna, while the machine itself does not experience lateral slip. The attitude-corrected rear axle center and bottom of the wheel center more accurately represent the machine's true real-time position and its actual deviation from the planned path.

The lateral roll angle generated by the height difference between the left and right wheels of the agricultural machinery can be visualized from the rear view as the machinery rotates about the center point O at the base of the left and right wheels, as shown in Figure 22.

https://doi.org/10.3390/agriculture16020170

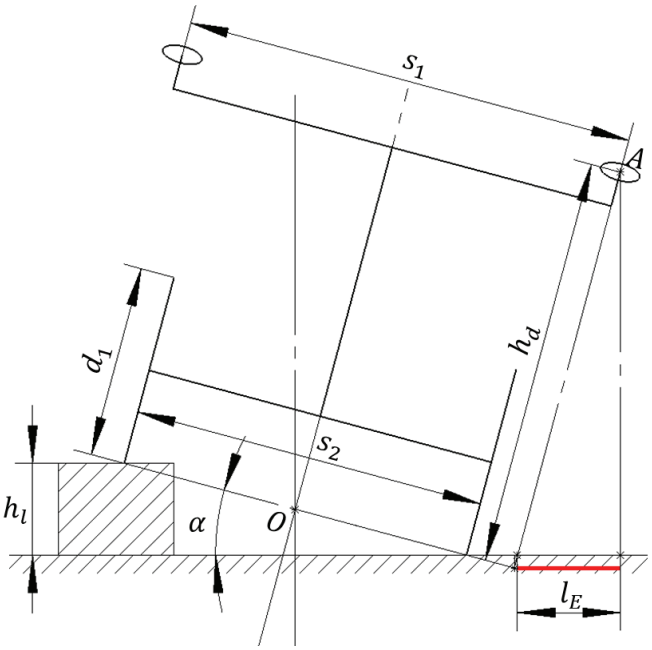

Figure 22. Schematic diagram showing antenna position deviation when the agricultural machinery rolls compared to the horizontal position.

Based on geometric relationships, the theoretical model for the antenna position deviation relative to the horizontal plane during agricultural machinery rollover is as follows:

$$\alpha = \arcsin\frac{h_l}{s_2} \tag{19}$$

$$l_E = h_d \sin\alpha - \left(\frac{s_1 - s_2}{2} - \frac{s_1 - s_2}{2}\cos\alpha\right) \tag{20}$$

In the equation, α represents the vehicle roll angle caused by the height difference between the left and right wheels, h_l denotes the height difference between the left and right wheels, s_2 indicates the rear track width of the agricultural machinery, l_E shows the offset of the antenna position relative to the horizontal plane during roll, h_d is the height of the antenna above the bottom of wheel, and s_1 is the symmetrical mounting distance between the dual antennas.

From the theoretical model Equation (20) and numerical results (Table 4 and Figure 22) for antenna position deviation relative to horizontal during the entire process of agricultural machinery rolling over ridges, it can be observed that the hard bottom layer contour significantly affects the lateral deviation of the positioning antenna. The deviation of the antenna position from horizontal during machine rollover is proportional to the height difference between left and right wheels and the installation height of the antenna relative to the bottom of wheel. Specifically, when the machine rolls 1.91 degrees and 3.81 degrees over the tested 0.05 m and 0.1 m high ridges, the antenna position deviates 0.083 m and 0.166 m from the horizontal, respectively. After attitude correction calculations, the lateral deviation accuracy of the rear axle center and left/right wheel bottom centers relative to the positioning antenna improved by 40.7% and 39.0%, respectively.

3.2. Analysis of the Impact of the Paddy Field Hard Bottom Layer on Typical Agricultural Machinery Bogging Incidents

During paddy field operation trials, data on the hard bottom layer contour and agricultural machinery attitude were extracted during the process of machinery becoming stuck due to hard bottom layer depression. To analyze the complete process of becoming

https://doi.org/10.3390/agriculture16020170

stuck, data from 15 s before and after the incident were extracted for analysis. The surface points of the extracted hard bottom layer contour are shown in Figure 23.

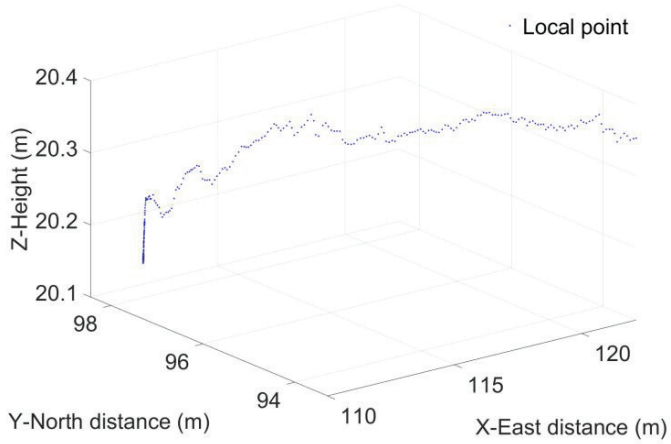

Figure 23. Surface points of the hard bottom layer 15 s before and after vehicle trapping.

Referring to the correlation analysis results in Section 3.1.1, under unmanned operation conditions, the positional deviation of agricultural machinery exhibits extremely significant correlations with both the hard bottom layer height and the local roughness of the hard bottom layer contour surface. This section analyzes the hard bottom layer height and local roughness across 300 datasets collected before and after vehicle trapping. The relationship between hard bottom layer height and local roughness changes during the 15 s preceding and following trapping is illustrated in Figure 24.

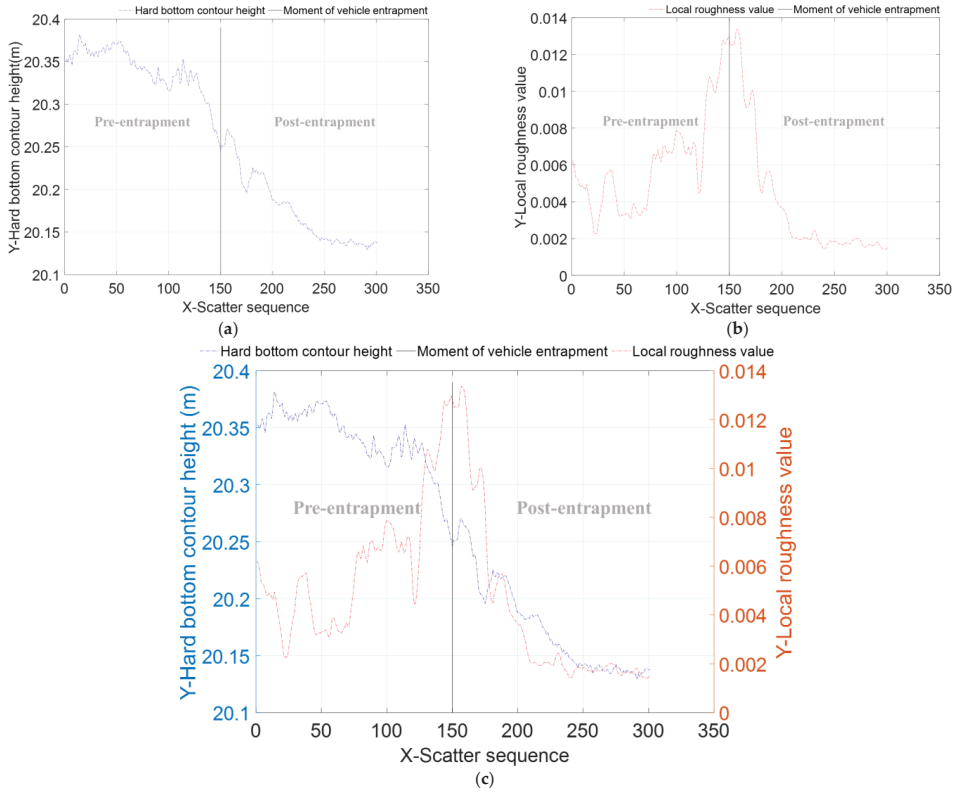

Figure 24. Relationship between hard substrate height and local roughness changes before and after 30 s trapping: (**a**) height variation contour of the hard bottom layer contour; (**b**) local roughness variation contour of the hard bottom layer contour; (**c**) hard bottom layer contour height variation and local roughness variation curves.

https://doi.org/10.3390/agriculture16020170

To visually illustrate the changes in the hard bottom layer contour and surface roughness before and after vehicle trapping, contour points of the hard bottom layer and local contour points were plotted at 0.1 s intervals over a 30 s period before and after trapping. Fitted straight lines were then calculated for local roughness, as shown in Figure 25.

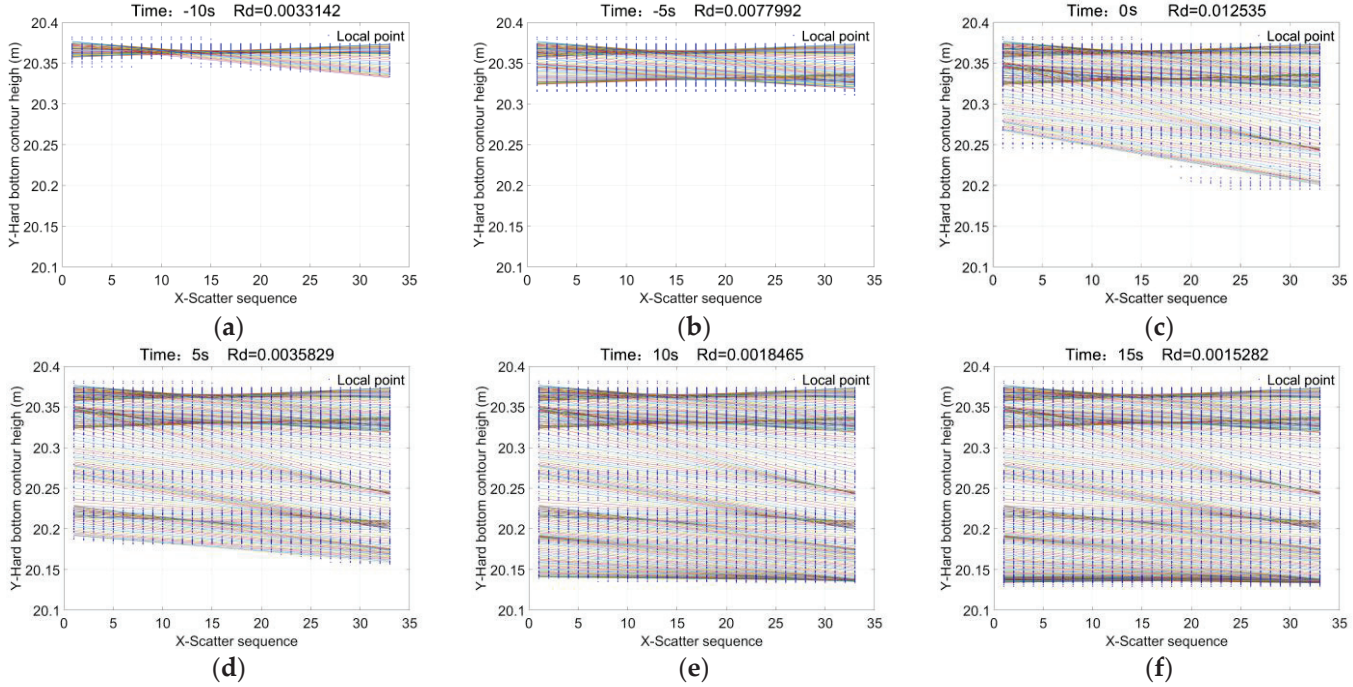

Figure 25. Changes in hard substrate height and local roughness from 15 s before to 15 s after trapping: (**a**) −15 s~−10 s; (**b**) −10 s~−5 s; (**c**) −5 s~0 s; (**d**) 0 s~5 s; (**e**) 5 s~10 s; (**f**) 10 s~15 s.

As shown in Figures 24 and 25, during the normal operation segment (−15 s to −5 s) in paddy fields, the average elevation of the hard bottom layer contour tends to stabilize. Adjacent local contour fitting lines exhibit an alternating pattern, with the local roughness of the hard bottom layer contour fluctuating between 0.002 and 0.008. During the pre- and post-vehicle-trapping segments (−5 s to 5 s), as the vehicle approaches a low-lying area, the hard bottom contour elevation drops sharply. Adjacent local contour fitting lines exhibit a rapid downward shift, and the local roughness of the hard bottom contour increases dramatically. At the moment of initial trapping ("0 s"), the local roughness value peaks at 0.0125. During the post-trapping phase (5 s–15 s), the slip ratio between the agricultural machinery wheels and the hard base layer increases to pure sliding. The contour elevation of the hard base layer decreases gradually, and the adjacent local contour fitting lines exhibit a slow downward shift. The local roughness of the hard base layer contour decreases sharply, with the local roughness value dropping to 0.0014, approaching the 0.0011 value observed during idle parking.

Based on changes in contour elevation and local roughness, construct segmented discriminant functions for pre- and post-wheel-trapping states. Let the agricultural machinery's motion state at time t be $State(t)$, the hard bottom layer elevation change rate be $\dot{H}(t)$, and the local roughness be $R(t)$. The local roughness change rate is $\dot{R}(t)$, the upper threshold for roughness is R_{risk}, the contour height change rate threshold is ε_H. This leads to the following:

https://doi.org/10.3390/agriculture16020170

$$State(t) = \begin{cases} NORMAL, & \left|\dot{H}(\mathrm{t})\right| \leq \varepsilon_H \wedge 0 \leq R(t) \leq R_{risk} \\ RISK, \text{ (Imminent vehicle bogging)} & \dot{H}(\mathrm{t}) < 0 \wedge \dot{R}(t) \geq 0 \wedge R(t) \geq R_{risk} \\ TRAPPED, \text{(Trapped vehicle)} & \dot{H}(\mathrm{t}) < 0 \wedge \dot{R}(t) < 0 \\ UNKNOWN, & \text{Otherwise.} \end{cases} \tag{21}$$

Based on Figures 24 and 25 and the segmented vehicle-trapping discrimination function (24), it is evident that in typical vehicle-trapping scenarios on paddy fields, when a decline in the hard bottom contour is detected alongside a sharp increase in local roughness, exceeding the upper threshold of 0.01, the agricultural machinery faces a risk of trapping. When a decrease in the hard bottom contour is detected alongside a decrease in local roughness values, it indicates that the agricultural machinery has become trapped. This provides a basis for predicting trapping incidents caused by hard bottom depressions in paddy fields and for designing post-trapping recovery strategies.

4. Discussion

This study investigates the influence patterns of hard bottom layer contours on the position and attitude changes in agricultural machinery. By integrating GNSS and AHRS sensors, a system for collecting position/attitude and hard bottom layer information was established, revealing the mechanism by which typical paddy field terrain features affect the attitude response of unmanned agricultural machinery during operation. The findings indicate that the geometric characteristics and local roughness parameters of the hard bottom contour significantly influence the heading stability, lateral stability, attitude changes, and trapping risk of agricultural machinery. This research provides crucial theoretical and technical support for path planning and driving control in unmanned precision agricultural operations.

The proposed method for acquiring hard bottom contour data and integrating pose information achieves the acquisition and fusion of motion state data from multiple key points (antenna, wheel bottom, rear axle center) by mounting GNSS and AHRS on the power chassis of a rice transplanter. This provides a foundation for dynamic analysis of agricultural machinery's attitude response characteristics. The study reveals the influence patterns of ridge height and local roughness variations on heading deviation and attitude response, providing a basis for speed control and path tracking of agricultural machinery in complex terrain. Notably, the finding that a 10 cm ridge causes two to three times greater heading deviation than a 5 cm ridge indicates that terrain undulations significantly impact path accuracy in autonomous agricultural machinery. Large-diameter tires effectively mitigate this effect, offering a mechanical design approach to enhance driving stability.

Additionally, previous studies have directly analyzed operational status based on single GNSS or GNSS/IMU fusion results. In challenging environments like paddy fields with pronounced undulations on hard bottom layers, agricultural machinery experiences frequent roll and pitch attitude changes. Without attitude correction, this can introduce systematic errors. This research introduces attitude correction to compensate for key task parameters, effectively mitigating the impact of attitude disturbances on task accuracy under complex operating conditions. After correcting the positional deviations of the rear axle center and bottom-of-the-wheel center using the attitude correction algorithm, the lateral deviation accuracy improved by approximately 40% compared to antenna measurements. This demonstrates the feasibility and necessity of the attitude fusion correction algorithm for enhancing positioning accuracy. These findings provide practical

https://doi.org/10.3390/agriculture16020170

guidance for optimizing attitude solution models and improving multi-sensor fusion algorithms in unmanned agricultural machinery.

The results of the vehicle-trapping test indicate that when the hard bottom contour drops sharply within a short time and the roughness increases to 0.01, agricultural machinery is prone to trapping. This validates that the hard bottom contour parameters can serve as key indicators for predicting trapping risk and establishes a segmented discrimination function for trapping states. This provides criteria for establishing pre-trapping warnings and escape strategies during unmanned operations. By integrating real-time hard bottom contour change rate and roughness threshold parameters into the autonomous control system, adaptive adjustments to speed and posture response strategies can be achieved during operations, thereby enhancing operational safety and continuity.

However, since the experimental platform utilizes a rice transplanting power chassis, the stiffness and vibration characteristics of the sensor mounting location exert a certain influence on measurement accuracy under bumpy terrain conditions. Future improvements in data stability can be achieved through structural optimization and high-precision attitude fusion algorithms. The hard bottom contour sampling and data processing in this study remain offline procedures. Integrating real-time data streams for dynamic modeling and feature recognition could enable online assessment and adaptive control of agricultural machinery operation status, representing a key direction for future research. Additionally, vehicle trapping during the planting phase is most frequent in paddy field operations, commonly occurring in typical rice transplanters with power-driven chassis similar to those studied here. To ensure transplanting or direct-seeding quality, operating speeds are typically maintained around 1 m/s. Field tests validated the feasibility and effectiveness of the proposed method under typical paddy field conditions. Further validation tests will be conducted at varying speeds across multiple wheeled and tracked agricultural machinery platforms, as well as in paddy fields with different regional characteristics, soil textures, and moisture content levels. This will systematically assess the method's versatility and robustness while continuously refining the model's applicability. This represents a key direction for future research.

In summary, the proposed method for analyzing the influence of hard bottom contours on the position and attitude changes in agricultural machinery not only provides a theoretical basis for revealing the relationship between terrain and the dynamic response of agricultural machinery, but also offers technical references for unmanned precision operation path planning, vehicle trapping early warning, and agricultural machinery structural optimization. This holds significant importance for advancing the autonomous perception and intelligent decision-making capabilities of smart agricultural machinery systems.

5. Conclusions

To reveal the influence patterns of hard bottom contour on changes in the position and attitude of agricultural machinery during operation, this study utilizes a rice transplanter chassis equipped with GNSS and AHRS to establish a platform for synchronous acquisition of agricultural machinery position/attitude data and hard bottom contour information. It proposes a method for analyzing the correlation between operational movement states and contour feature parameters, revealing the influence patterns of hard bottom contour characteristics on agricultural machinery attitude response and the mechanism of vehicle entrapment. Key findings include the following:

(1) A platform for acquiring agricultural machinery pose information and hard bottom surface contour features was established. Through multi-sensor fusion of GNSS and AHRS, continuous collection of agricultural machinery operating status and parameters such as hard bottom elevation and local roughness was achieved, ensuring high-precision data

https://doi.org/10.3390/agriculture16020170

acquisition and temporal consistency. A pose response model for key components of agricultural machinery was constructed, providing a data foundation for analyzing the coupling relationship between terrain excitation and machinery response.

(2) A correlation analysis method was established between the motion state of agricultural machinery and the contour characteristics of the hardpan layer. Results indicate that hardpan elevation differences and local undulation characteristics are key factors inducing lateral and heading deviations in agricultural machinery. Terrain asymmetry and ridge height variations significantly amplify the heading response of machinery. The resulting heading response model effectively quantifies the relationship between terrain disturbances and machinery motion states, validating the pivotal role of hardpan profile analysis in assessing paddy field driving stability.

(3) This study elucidates the attitude response and correction characteristics of wheeled agricultural machinery during ridge crossing. Under typical ridge-crossing conditions, wheel dimensions and suspension structures significantly influence terrain excitation suppression, with the rear-wheel-over-ridge phase being the primary source of machine roll and abrupt attitude changes. By introducing attitude compensation and motion correction models, positioning accuracy at critical points was effectively enhanced, validating the effectiveness of attitude correction methods under complex terrain conditions.

(4) A vehicle trapping identification and early warning criterion based on dynamic changes in the hard bottom contour was proposed. In typical vehicle-trapping tests, the elevation and local roughness of the hard bottom exhibit phased evolutionary patterns before and after trapping occurs. The vehicle-trapping state discrimination and early warning model established based on this characteristic enables advance identification of typical trapping behavior, providing quantifiable criteria for trapping early warning and escape control.

This study investigates the influence of hard bottom contours on the position and attitude changes in agricultural machinery during movement. It establishes quantitative relationships among hard bottom contour characteristics, agricultural machinery attitude responses, and vehicle-trapping states. The findings provide theoretical foundations and technical support for intelligent path-tracking control, chassis structure optimization, and unmanned precision operations in agricultural machinery. This research holds significant importance for enhancing the intelligence level and operational efficiency of paddy field machinery.

Author Contributions: Conceptualization, T.T., L.H., X.L. and J.H.; methodology, T.T., L.H., X.L. and J.H.; software, T.T., P.W., P.H., R.Z. and G.C.; validation, T.T., Z.M., D.F. and M.Y.; formal analysis, T.T.; investigation, T.T. and X.D. (Xianhao Duan); resources, T.T., L.H., X.L., J.H. and P.W.; data curation, T.T., L.H. and J.H.; writing—original draft preparation, T.T.; writing—review and editing, T.T., L.H., X.L. and J.H.; visualization, T.T., L.H., P.W., X.D. (Xiaobing Deng), and J.M.; supervision, L.H., X.L. and J.H.; project administration, X.L.; funding acquisition, T.T. and L.H. and J.H. All authors have read and agreed to the published version of the manuscript.

Funding: This research was funded by the China Postdoctoral Science Foundation (Grant No. 2024M750955), the National Natural Science Foundation of China (32472016, 32071913), the Postdoctoral Fellowship Program (Grade C) of China Postdoctoral Science Foundation (Grant No. GZC20230855), and the Lingnan Modern Agricultural Science and Technology Laboratory Independent Research Project (Grant No. NT2025006).

Data Availability Statement: The data that supports this study will be shared upon reasonable request to the corresponding author.

Acknowledgments: We would like to thank our partners of the Zengcheng Teaching Base of South China Agricultural University for their help and support in field management and machine maintenance.

Conflicts of Interest: The authors declare no conflicts of interest.

References

1. Nawaz, A.; Rehman, A.U.; Rehman, A.; Ahmad, S.; Siddique, K.H.M.; Farooq, M. Increasing sustainability for rice production systems. *J. Cereal Sci.* **2022**, *103*, 103400. [CrossRef]
2. Seck, P.A.; Diagne, A.; Mohanty, S.; Wopereis, M.C.S. Crops that feed the world 7: Rice. *Food Secur.* **2012**, *4*, 7–24. [CrossRef]
3. Kuenzer, C.; Knauer, K. Remote sensing of rice crop areas. *Int. J. Remote Sens.* **2013**, *34*, 2101–2139. [CrossRef]
4. Xin, F.; Xiao, X.; Dong, J.; Zhang, G.; Zhang, Y.; Wu, X.; Li, X.; Zou, Z.; Ma, J.; Du, G.; et al. Large increases of paddy rice area, gross primary production, and grain production in Northeast China during 2000–2017. *Sci. Total Environ.* **2020**, *711*, 135183. [CrossRef]
5. He, J.; Hu, L.; Wang, P.; Liu, Y.; Man, Z.; Tu, T.; Yang, L.; Li, Y.; Yi, Y.; Li, W.; et al. Path tracking control method and performance test based on agricultural machinery pose correction. *Comput. Electron. Agric.* **2022**, *200*, 107185. [CrossRef]
6. Luo, X.; Hu, L.; He, J.; Zhang, Z.; Zhou, Z.; Zhang, W.; Liao, J.; Huang, P. Key technologies and practice of unmanned farm in China. *Trans. Chin. Soc. Agric. Eng.* **2024**, *40*, 1–16.
7. Tu, T.; He, J.; Luo, X.; Hu, L.; Wang, P.; Chen, G.; Tian, L.; Feng, D.; Wang, Z.; Man, Z.; et al. Methods and experiments for collecting information and constructing models of bottom-layer contours in paddy fields. *Comput. Electron. Agric.* **2023**, *207*, 107719. [CrossRef]
8. Bekker, M.G. *Introduction to Terrain–Vehicle Systems*; University of Michigan Press: Ann Arbor, MI, USA, 1969.
9. Wong, J.Y. *Theory of Ground Vehicles*, 4th ed.; Wiley: Hoboken, NJ, USA, 2010.
10. Jia, Z.; Smith, W.; Peng, H. Terramechanics-based wheel–terrain interaction model and its applications to off-road wheeled mobile robots. *Robotica* **2012**, *30*, 491–503. [CrossRef]
11. Misaghi, S.; Tirado, C.; Nazarian, S.; Carrasco, C. Impact of pavement roughness and suspension systems on vehicle dynamic loads on flexible pavements. *Transp. Eng.* **2021**, *3*, 100045. [CrossRef]
12. Guo, Z.; Li, A.; Feng, J.; Zheng, Y.; Qin, D.; Ge, S. Influence of the driving environment on the dynamic characteristics of a DCT vehicle starting considering the longitudinal and vertical coupling model. *Sci. Rep.* **2024**, *14*, 29698. [CrossRef]
13. Inotsume, H.; Kubota, T. Terrain traversability prediction for off-road vehicles based on multi-source transfer learning. *ROBOMECH J.* **2022**, *9*, 6. [CrossRef]
14. Golanbari, B.; Mardani, A.; Hosainpour, A.; Taghavifar, H. Predicting terrain deformation patterns in off-road vehicle-soil interactions using TRR algorithm. *J. Terramechanics* **2025**, *117*, 101021. [CrossRef]
15. Tu, T.; Luo, X.; Hu, L.; Chung, S.; He, J.; Zhao, R.; Wang, P.; Chen, G.; Feng, D.; Yue, M.; et al. Methods and experiments for analysing hard-bottom layer changes and monitoring wheel sink depth in paddy fields. *Comput. Electron. Agric.* **2025**, *238*, 110760. [CrossRef]
16. Lenain, R.; Thuilot, B.; Cariou, C.; Martinet, P. High accuracy path tracking for vehicles in presence of sliding: Application to farm vehicle automatic guidance for agricultural tasks. *Auton. Robot.* **2006**, *21*, 79–97. [CrossRef]
17. Anderson, R.A. Using GPS for Model Based Estimation of Critical Vehicle States and Parameters. Doctoral Dissertation, Auburn University, Auburn, AL, USA, 2004.
18. Bevly, D.M.; Gerdes, J.C.; Wilson, C.; Zhang, G. The use of GPS based velocity measurements for improved vehicle state estimation. In Proceedings of the 2000 American Control Conference, Chicago, IL, USA, 28–30 June 2000; pp. 2538–2542.
19. Ryu, J.; Gerdes, J.C. Integrating inertial sensors with global positioning system (GPS) for vehicle dynamics control. *J. Dyn. Syst. Meas. Control* **2004**, *126*, 243–254. [CrossRef]
20. Corradini, M.L.; Leo, T.; Orlando, G. Experimental testing of a discrete-time sliding mode controller for trajectory tracking of a wheeled mobile robot in the presence of skidding effects. *J. Robot. Syst.* **2002**, *19*, 177–188. [CrossRef]
21. Hiraoka, T.; Nishihara, O.; Kumamoto, H. Automatic path-tracking controller of a four-wheel steering vehicle. *Veh. Syst. Dyn.* **2009**, *47*, 1205–1227. [CrossRef]
22. Lucet, E.; Lenain, R.; Grand, C. Dynamic path tracking control of a vehicle on slippery terrain. *Control Eng. Pract.* **2015**, *42*, 60–73. [CrossRef]
23. Lenain, R.; Thuilot, B.; Cariou, C.; Martinet, P. Mixed kinematic and dynamic sideslip angle observer for accurate control of fast off-road mobile robots. *J. Field Robot.* **2010**, *27*, 181–196. [CrossRef]
24. Zhou, J.; Xu, J.; Wang, Y.; Liang, Y. Development of Paddy Field Rotary-leveling Machine Based on GNSS. *Trans. Chin. Soc. Agric. Mach.* **2020**, *51*, 38–43.

25. Frey, J.; Patel, M.; Atha, D.; Nubert, J.; Fan, D.; Agha, A.; Padgett, C.; Spieler, P.; Hutter, M.; Khattak, S. RoadRunner-Learning Traversability Estimation for Autonomous Off-road Driving. *IEEE Trans. Field Robot.* **2024**, *1*, 192–212. [CrossRef]
26. Sten, G.; Feng, L.; Möller, B. Enhancing Off-Road Topography Estimation by Fusing LIDAR and Stereo Camera Data with Interpolated Ground Plane. *Sensors* **2025**, *25*, 509. [CrossRef]

Disclaimer/Publisher's Note: The statements, opinions and data contained in all publications are solely those of the individual author(s) and contributor(s) and not of MDPI and/or the editor(s). MDPI and/or the editor(s) disclaim responsibility for any injury to people or property resulting from any ideas, methods, instructions or products referred to in the content.

agriculture

MDPI

Article

Image Segmentation of Cottony Mass Produced by *Euphyllura olivina* (Hemiptera: Psyllidae) in Olive Trees Using Deep Learning

Henry O. Velesaca [1], Francisca Ruano [2], Alice Gomez-Cantos [1] and Juan A. Holgado-Terriza [1,*]

[1] Software Engineering Department, Research Centre for Information and Communication Technologies (CITIC-UGR), University of Granada, 18071 Granada, Spain; hvelesaca@correo.ugr.es (H.O.V.); alicevangomez@gmail.com (A.G.-C.)
[2] Department of Zoology, Faculty of Sciences, University of Granada, 18071 Granada, Spain; fruano@ugr.es
* Correspondence: jholgado@ugr.es

Abstract

The olive psyllid (*Euphyllura olivina*), previously considered a secondary pest in Spain, is becoming more prevalent due to climate change and rising average temperatures. Its cottony wax secretions can cause substantial damage to olive crops under certain climatic conditions. Traditional monitoring methods for this pest are often labor-intensive, subjective, and impractical for large-scale surveillance. This study presents an automatic image segmentation approach based on deep learning to detect and quantify the cottony masses produced by *E. olivina* in olive trees. A well-annotated image dataset is developed and published, and a thorough evaluation of current camouflaged object detection (COD) methods is carried out for this task. Our results show that deep learning-based segmentation enables accurate and non-invasive assessment of pest symptoms, even in challenging visual conditions. However, further calibration and field validation are required before these methods can be deployed for operational integrated pest management. This work establishes a public dataset and a baseline benchmark, providing a foundation for future research and decision-support tools in precision agriculture.

Keywords: Psyllidae; *Euphyllura olivina*; olive psyllid; olive pest; deep learning; smart farming; camouflaged object detection

1. Introduction

The olive psyllid, *Euphyllura olivina* (Costa, 1839), is a significant pest in Mediterranean olive groves, especially in North-African countries, but is increasing its impact in other olive-producing regions such as Spain (known here as "Algodoncillo del Olivo"), because of climate change and the increase in mean temperatures in early spring [1,2]. Recent studies have highlighted the effects of climate change on olive production in Spain, further emphasizing the need for improved pest monitoring and management strategies [3]. Under these climatic conditions, this insect causes both direct and indirect damage during the flowering and fruit-setting stages [4,5]. One of the most characteristic symptoms of its presence is the production of conspicuous white waxy secretions by the nymphs, which cover inflorescences and young shoots, leading to flower drop, reduced fruit set, and the development of sooty mold that further affects photosynthesis and yield [6,7]. The extent of these cottony masses is closely related to the population density of the pest, making their detection and quantification a valuable proxy for monitoring *E. olivina* outbreaks [6].

Traditional monitoring methods rely on manual inspection and counting, which are labor-intensive, subjective, and often impractical for large-scale or high-frequency surveillance. Additionally, the inaccessibility of some olive farms in the mountains poses significant challenges. Recent advances in computer vision and image analysis offer promising alternatives for the automatic detection and quantification of pest symptoms in crops [8]. Although direct detection of this pest is complicated due to its small size (e.g., adults 2 to 3 mm) [9], the segmentation of the white cottony mass secretions present in images of olive trees could enable rapid, non-invasive estimation of *E. olivina* populations, facilitating timely and targeted pest management interventions [7,10,11].

This work presents a methodology for the image segmentation of the cottony mass produced by *E. olivina* using camouflaged object detection (COD) techniques. The quantification of the area covered by these secretions is intended to establish a foundation for future studies correlating cottony mass coverage with pest population density. This will ultimately contribute to the development of precision agriculture tools for integrated pest management in olive cultivation.

The key contributions of this work include:

- A first well-annotated benchmark dataset was used for the segmentation of cottony masses produced by *E. olivina* in olive trees.
- Fine-tuning of ten state-of-the-art (SOTA) COD techniques was applied for the segmentation of cottony masses by *E. olivina*.
- A quantitative and qualitative evaluation of the results was obtained and discussed with these ten SOTA COD techniques for the segmentation of cottony mass produced by *E. olivina*.

The manuscript is organized as follows. Section 2 presents the dataset, the techniques used, and the evaluation metrics. Then, Section 3 shows the experimental results, both quantitative and qualitative, on the dataset. Finally, discussions are given in Section 4.

2. Proposed Methodology

This section presents the proposed methodology used to evaluate the image segmentation of cottony masses produced by *Euphyllura olivina* in olive trees (see Figure 1). As illustrated in Figure 2, the pipeline consists of six main stages:

- Dataset Acquisition. A set of images containing cottony masses was collected from different sources.
- Image Annotation. The collected images were annotated following strict guidelines to determine areas of cottony masses.
- Training COD Techniques. COD techniques were applied using the annotated dataset for training image-segmentation models.
- Testing COD Techniques. The trained models were evaluated on a test set to generate segmentation masks that identify the cottony masses.
- Evaluation. Performance was assessed using both quantitative metrics and qualitative visual comparisons.
- Result Interpretation. The segmentation outputs were analyzed to determine the effectiveness of each COD technique in detecting and quantifying the cottony masses under challenging visual conditions.



Figure 1. Example images of *E. olivina* in olive trees.

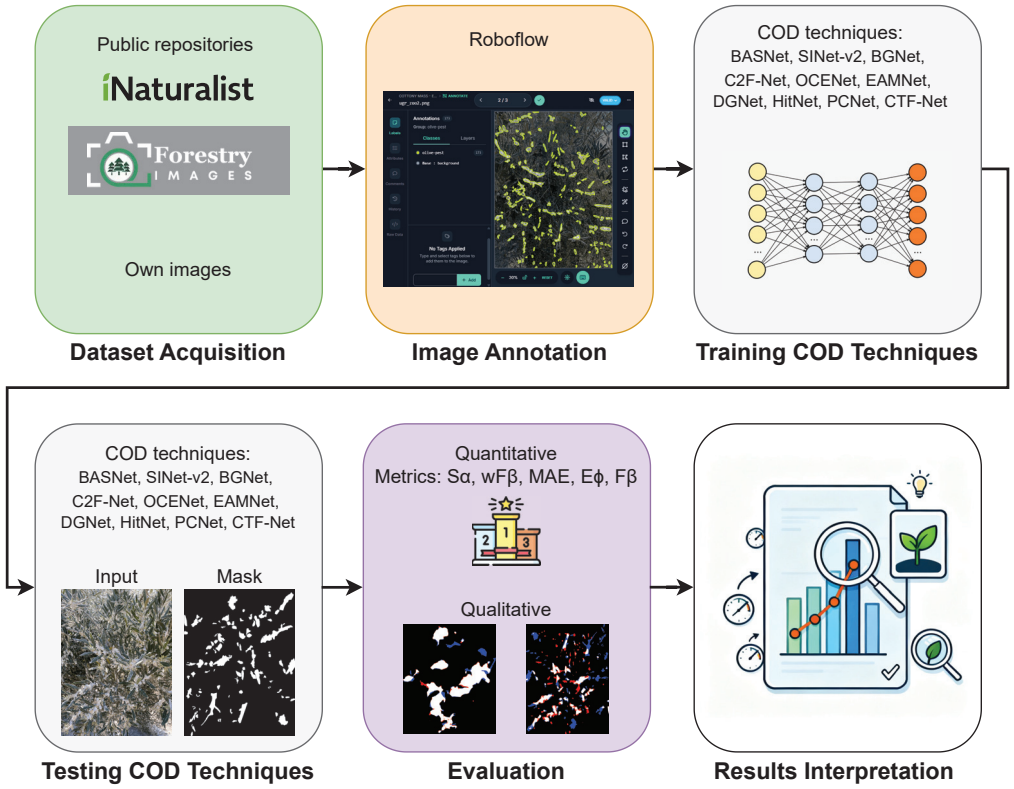

Figure 2. Overall pipeline of the proposed methodology.

2.1. Dataset Acquisition

The study presents the first well-annotated benchmark dataset for segmenting cottony masses produced by *Euphyllura olivina* on olive trees. The dataset contains 442 images with a split for training (354 images), validation (66 images), and testing (22 images). Images were obtained from public repositories, including iNaturalist (https://www.inaturalist.org/, accessed on 18 September 2025) and ForestryImages (https://forestryimages.org, accessed on 18 September 2025), and supplemented with specific images taken in the province of Jaén, Spain. The images originate from heterogeneous sources, devices, and environmental conditions, including contributions from different countries (e.g., USA, Europe, and North Africa (see Figure 3)), which naturally introduces variability in viewpoint, optics, and scene composition. This heterogeneity is intentional to improve model generalization to real-world conditions. The test set of 22 images and validation set of 66 images include only original images, with no augmented images, ensuring strict separation between training/validation and testing.

The dataset was carefully constructed to avoid data leakage and ensure that images in the training, validation, and test splits are independent. Images from similar scenes were assigned to a single partition, preventing overlap between splits and supporting a fair evaluation of model performance.

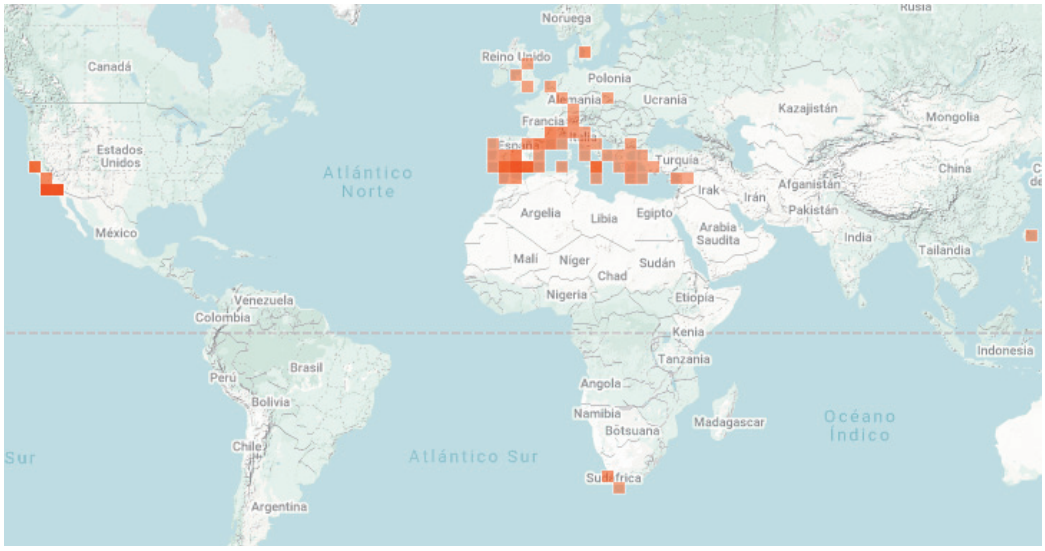

Figure 3. Geographical location distribution of annotated images around the world, marked with orange squares. Source: iNaturalist.

2.2. Image Annotation

The annotation process was conducted using Roboflow (https://app.roboflow.com/, accessed on 18 September 2025), a web-based platform designed for computer vision tasks. Each image was annotated with meticulous attention to detail, following a set of strict guidelines to ensure consistency and accuracy across the dataset. First, annotators were instructed to: (a) exclusively label cottony mass instances, disregarding all other visual elements, and (b) ensure complete coverage by annotating every visible cottony mass without omission. Second, quality specifications required (a) individual polygon annotations for each cottony mass in multi-instance images, and (b) pixel-precise boundary refinement to accurately capture morphological features.

To improve the generalization of the models to be trained, a data augmentation process is performed, obtaining a final image count of 655, split into training (567 images), validation (66 images), and testing (22 images) subsets. The original distribution is maintained in the validation and testing subsets. The following augmentations are applied to the original dataset:

- Flip: Horizontal, Vertical
- 90° Rotate: Clockwise, Counter-Clockwise, Upside Down
- Rotation: Between $-15°$ and $+15°$
- Shear: $\pm 10°$ Horizontal, $\pm 10°$ Vertical

Figure 4 shows examples of the annotated dataset. The first and third columns show RGB images with the presence of cottony mass, while the second and fourth columns show the binary masks that segment the presence of cottony mass. The resulting dataset is publicly available (see the Data Availability Statement). Additionally, Figure 5 (top) shows the scatter plot that visualizes the spatial distribution of the mask centroids (geometric centers) within the images. Each point represents the centroid of a mask, with its position determined by the X and Y coordinates. Also, Figure 5 (bottom) presents a histogram showing the percentage of each image area covered by masks. Coverage is calculated as the ratio of mask pixels to the total number of pixels in each image.

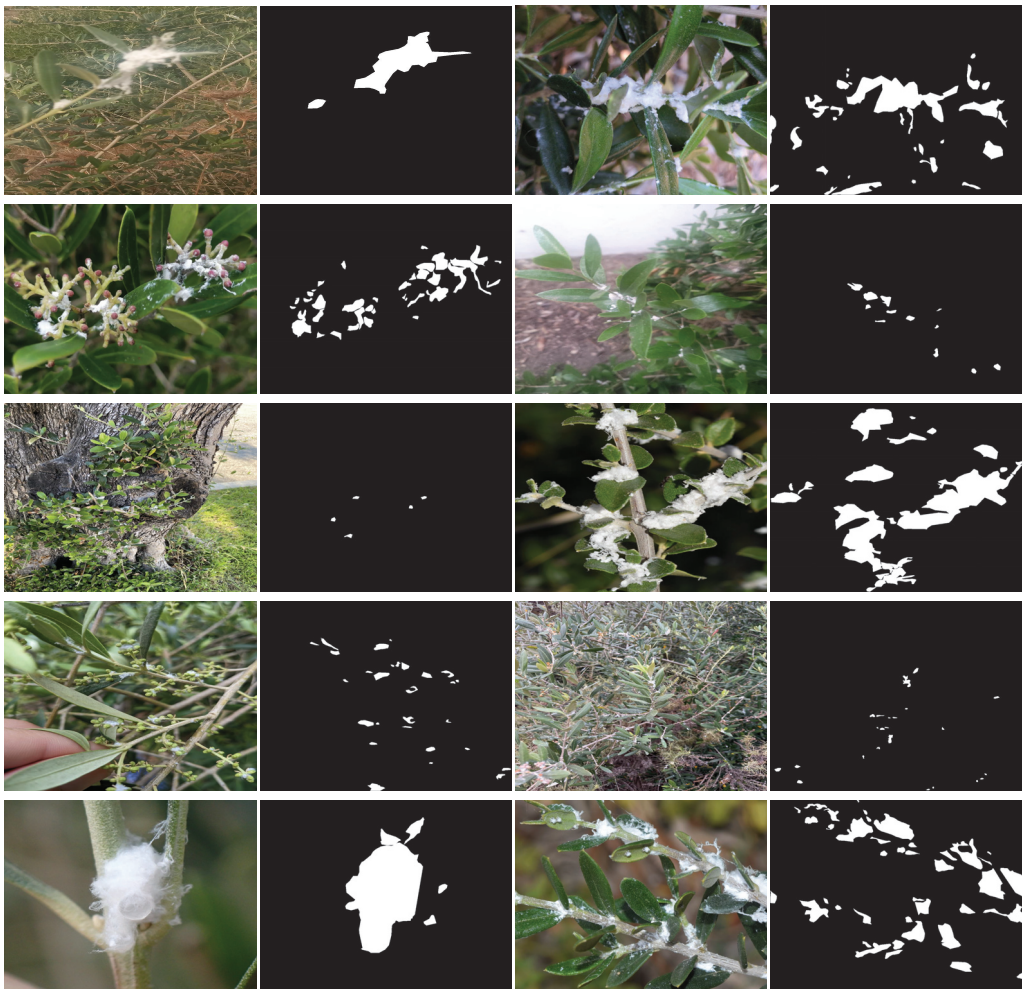

Figure 4. Example images of annotated datasets. Images captured under different environmental conditions, lighting, object distance, and devices.

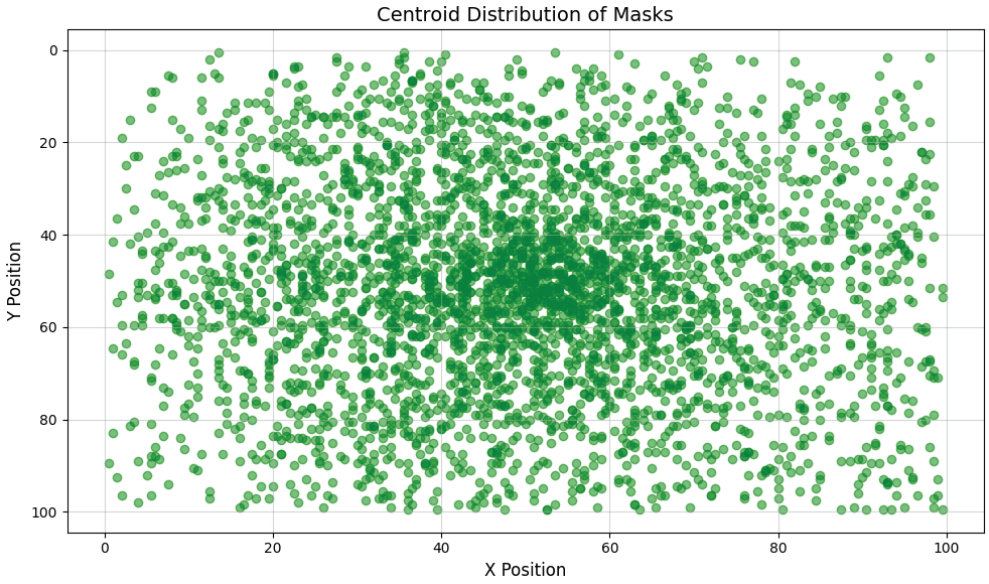

Figure 5. *Cont*.

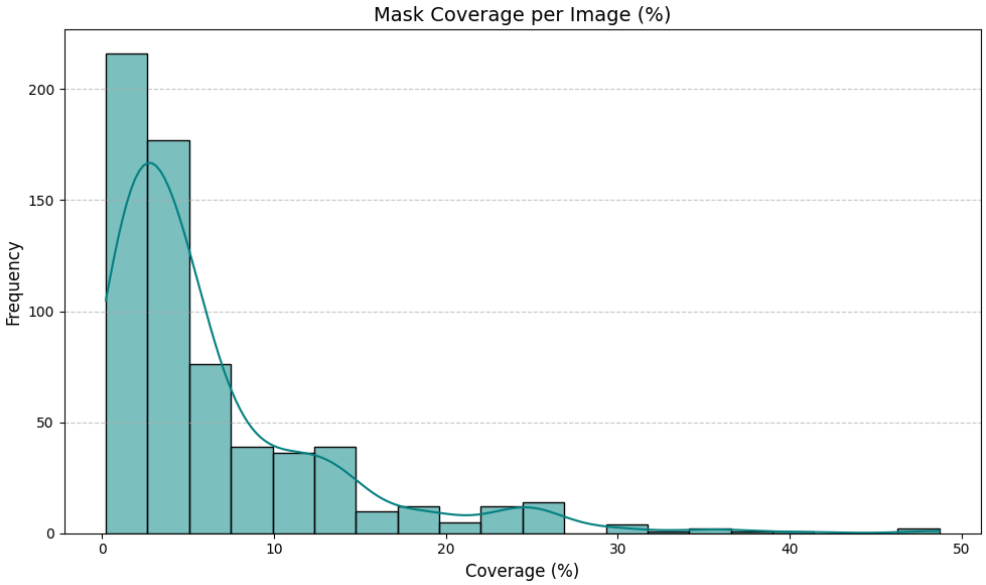

Figure 5. Statistics based on the images in the annotated dataset. (**top**) The scatter plot visualizes the spatial distribution of the centroids (geometric centers) of the masks within the images. Each point represents the centroid of a mask, with its position determined by the X and Y coordinates. (**bottom**) The histogram shows the percentage of each image covered by masks. Coverage is calculated as the ratio of mask pixels to the total number of pixels in the image.

2.3. Training COD Techniques

Camouflaged Object Detection (COD) is a specialized subfield of computer vision that focuses on identifying objects that are visually blended into their surroundings. The choice to focus on COD-based models was motivated by the unique visual challenges presented by the cottony mass, which often exhibits low contrast, irregular shapes, and blends into complex backgrounds. COD models are specifically designed to address these challenges, and have demonstrated superior performance over general-purpose segmentation frameworks such as U-Net++ [12] or DeepLabv3+ [13] in camouflaged object scenarios. This specialization makes them particularly suitable for the segmentation of *E. olivina* symptoms in olive trees.

In recent years, advances in deep learning have led to the development of state-of-the-art (SOTA) models specifically designed to address these challenges [14]. This section reviews a variety of approaches, highlighting how each method tackles the inherent difficulties of COD through different architectural strategies and loss functions.

For example, BASNet [15] utilizes a predict-and-refine strategy with a hybrid loss function (BCE, SSIM, IoU), where SSIM implicitly enhances edge quality, though it does not explicitly model edges. SINet [16] implements a biologically inspired search-and-identification framework, explicitly using edge cues to locate and segment camouflaged objects. EAMNet [17] features dual parallel branches for segmentation and edge detection, with cross-refinement that explicitly incorporates edge information into the learning process. HitNet [18] employs iterative prediction refinement through feedback loops, which indirectly improves boundary clarity without dedicated edge modeling.

For integrating global and local features, CTF-Net [19] merges CNN-based local features with Transformer-based global context, implicitly enhancing boundary precision. In contrast, BGNet [20] introduces a dedicated boundary-guidance branch to directly model object contours. C^2F-Net [21] applies cross-level context fusion, implicitly strengthening edges for better structural coherence. DGNet [22] explicitly captures edge information via gradient flow, enabling the detection of subtle contrast variations in low-texture regions.

Addressing domain-specific challenges, PCNet [23] focuses on plant camouflage using multi-scale refinement, explicitly handling irregular plant edges. Lastly, OCENet [24] models aleatoric uncertainty to dynamically supervise regions with high uncertainty (such as boundaries), thereby implicitly enhancing edge detection. Collectively, these methods advance COD by balancing explicit edge guidance with implicit boundary refinement, adapting to a range of camouflage scenarios. Table 1 summarizes the distinctive characteristics of the evaluated SOTA COD methods.

Table 1. Distinctive characteristics of the evaluated SOTA COD techniques.

Technique	Source	Year	Source Type	Image Size (px)	Backbone	#Par. (M)
BASNet [15]	CVPR	2019	Conference	256×256	ResNet-34 [25]	87.06
SINet-v2 [16]	TPAMI	2021	Journal	352×352	Res2Net-50 [26]	24.93
BGNet [20]	IJCAI	2022	Conference	416×416	Res2Net-50 [26]	77.80
C^2F-Net [21]	TCSVT	2022	Conference	352×352	Res2Net-50 [26]	26.36
OCENet [24]	WACV	2022	Conference	352×352	ResNet-50 [25]	58.17
EAMNet [17]	ICME	2023	Conference	384×384	Res2Net-50 [26]	30.51
DGNet [22]	MIR	2023	Journal	352×352	EfficientNet [27]	8.30
HitNet [18]	AAAI	2023	Conference	352×352	PVTv2 [28]	25.73
PCNet [23]	arXiv	2024	-	352×352	PVTv2 [28]	27.66
CTF-Net [19]	CVIU	2025	Journal	384×384	PVTv2 [28]	64.48

2.4. Testing COD Techniques

All COD models are evaluated under the same simple test protocol to make results comparable. For each method, select the checkpoint with the best validation performance and use it for inference on the test set. Inputs are resized to the resolution expected by each model and normalized according to the model's original preprocessing, with no random transformations applied at test time. Inference is single-scale (no test-time augmentation), and each model produces a probability map that is resized back to the original image size for evaluation and visualization. For the figures, a binary mask using a fixed threshold of 0.25 is also shown. Also, it does not apply morphological or other post-processing refinements, keeping the comparison focused on the models themselves. This simple setup is easy to reproduce and ensures a fair, like-for-like comparison across methods.

2.5. Evaluation

This study utilizes five widely adopted evaluation metrics to assess the performance of COD models. These metrics offer a comprehensive framework for analyzing detection accuracy and effectiveness across different approaches: Structure-measure (S_α) [29], weighted F-measure (F_β^w) [30], Mean Absolute Error (M) [31], E-measure (E_ϕ) [32], and F-measure (F_β) [33]. The metrics are computed at the original image resolution after up-sampling predictions.

The S_α metric is employed to evaluate the structural similarity between predicted and ground-truth maps, indicating the extent to which the overall structural information is preserved. The weighted F-measure (F_β^w) extends the traditional F_β by incorporating spatial weights, thereby providing a more nuanced assessment of segmentation quality with a focus on boundary precision and the spatial significance of detected pixels. The Mean Absolute Error (M) measures pixel-level discrepancies between normalized predictions and ground truth, offering a direct indicator of prediction accuracy. The E-measure (E_ϕ) simultaneously considers both global and local detection accuracy, grounded in human visual perception, to deliver a perceptually meaningful evaluation. Finally, the F-measure (F_β) combines precision and recall to provide a balanced review of overall detection performance.

For both the F-measure and E-measure, multiple scores are computed based on different precision–recall pairs, resulting in adaptive F-measure (F_β^{adp}), mean F-measure

(F_β^{mean}), and maximum F-measure (F_β^{max}). Similarly, the E-measure includes adaptive, mean, and maximum variants, denoted as E_ϕ^{adp}, E_ϕ^{mean}, and E_ϕ^{max}, which are also used as evaluation metrics.

In addition to the metrics previously reported (S_α, F_β^w, M, E_ϕ, F_β), traditional metrics such as intersection over union (IoU) and Dice coefficient scores are also included. These metrics provide a direct and interpretable measure of the spatial overlap between predicted and ground-truth masks, which is central to the intended application in pest quantification. Specifically, the Intersection over Union (IoU) quantifies the ratio between the area of overlap and the area of union of the predicted and ground-truth masks, offering a strict assessment of segmentation accuracy. On the other hand, the Dice coefficient, also known as the F1 score for segmentation, measures the harmonic mean of precision and recall at the pixel level, emphasizing the balance between false positives and false negatives. Both metrics are widely used in image segmentation tasks, as they directly reflect how well the predicted regions match the actual annotated regions.

To provide a more comprehensive evaluation, specific IoU thresholds are also reported, including IoU@50 and IoU@75, which represent the average accuracy when the IoU exceeds the thresholds of 0.50 and 0.75, respectively. In addition, IoU@[50–95] is included, calculated using multiple IoU thresholds from 0.50 to 0.95 in increments of 0.05, following the COCO evaluation protocol. These variants provide a more complete view of segmentation performance, showing how well the model works under both easy and demanding conditions.

2.6. Training Details

This subsection summarizes the training configuration used across all COD techniques. Table 2 reports the optimizer, learning rate, batch size, number of epochs, scheduler, and loss functions employed per model. All models were trained under consistent splits and without test-time augmentation, as described in Sections 2.4 and 2.5, to enable a fair comparison.

Table 2. Details of the training parameters used in evaluated SOTA COD techniques. Learning rate (LR); Batch size (BS).

Technique	Optimizer	LR	BS	Epochs	Scheduler	Loss Function
BASNet [15]	Adam	1×10^{-3}	8	1000	ReduceLROnPlateau	BCE + SSIM + IOU (multi-stage fusion)
SINet-v2 [16]	Adam	1×10^{-4}	16	150	Custom (Adjust LR)	Structure loss (weighted BCE + weighted IOU)
BGNet [20]	Adam	1×10^{-4}	12	100	Custom (Poly LR)	Structure loss (weighted BCE + weighted IOU) + Dice loss (edge)
C^2F-Net [21]	AdaXW	1×10^{-4}	32	50	Custom (Poly LR)	Structure loss (weighted BCE + weighted IOU)
OCENet [24]	Adam	1×10^{-5}	4	50	StepLR	Uncertainty aware structure loss (weighted BCE + weighted IOU)
EAMNet [17]	AdamW	5×10^{-5}	16	150	Custom (Adjust LR)	Hybrid loss (weighted BCE + weighted IOU) + Edge loss (edge)
DGNet [22]	AdamW	5×10^{-5}	16	150	CosineAnnealingLR	Hybrid loss (weighted BCE + weighted IOU) + MSE loss (grad)
HitNet [18]	AdamW	1×10^{-4}	8	150	Custom (Adjust LR)	Structure loss (weighted BCE + weighted IOU)
PCNet [23]	AdamW	1×10^{-4}	8	150	Custom (Adjust LR)	Structure loss (weighted BCE + weighted IOU)
CTF-Net [19]	Adam	1×10^{-4}	12	100	Custom (Poly LR)	Structure loss (weighted BCE + weighted IOU) + Dice loss (edge)

3. Results

The performance of the ten SOTA COD techniques is quantitatively evaluated on the test set using the metrics described in Section 2.5. Table 3 summarizes the results for each model, highlighting the top three performers for each metric.

Among all evaluated techniques, CTF-Net achieved the highest Structure-measure (S_α = 0.8101), indicating superior preservation of structural information in the segmented masks. PCNet and BGNet also performed strongly, with S_α scores of 0.8075 and 0.8022, respectively. In terms of F-measure (F_β), PCNet (0.6787) and HitNet (0.6735) outperformed the rest, reflecting a strong balance between precision and recall. The lowest Mean Absolute Error (M) is obtained by HitNet (0.0220), closely followed by PCNet (0.0234), indicating high pixel-level accuracy.

For the E-measure (E_ϕ), which combines global and local detection accuracy, OCENet (0.9099) and HitNet (0.9125) achieved the best results, while CTF-Net and BGNet also demonstrated robust performance. The adaptive, mean, and maximum variants of F-measure and E-measure further confirmed the consistency of these top-performing models.

In relation to the results obtained in traditional metrics, the values indicate in Table 4 that CTF-Net achieves the best overall performance across all highest evaluated metrics, obtaining the values for Dice (0.735), IoU (0.621), IoU@50 (0.562), IoU@75 (0.279), and IoU@[0.50:0.95] (0.302). BGNet and PCNet also demonstrate strong performance, particularly in the Dice and IoU metrics. In contrast, methods such as BASNet and C2F-Net show the lowest values in most metrics, indicating lower overlap and accuracy in segmentation. Overall, the table highlights significant differences in the effectiveness of the various techniques, with CTF-Net standing out as the most effective method for the evaluated segmentation task according to these classical indicators.

Qualitative results are illustrated in Figures 6 and 7, where segmentation outputs from all models are compared against ground truth masks. The best-performing models, such as PCNet, CTF-Net, HitNet, and BGNet, consistently produced accurate segmentation, with minimal over-segmentation (red) and under-segmentation (blue) errors. These models are particularly effective in scenarios with low-contrast boundaries and complex backgrounds, which are characteristic of the cottony masses produced by *E. olivina*.

To assess the generalization power of the four techniques (as indicated by the quantitative results) in challenging scenarios, Figure 8 is presented, which displays an olive tree with a high density of cottony mass. The techniques in this scenario present challenges in identifying areas of overlap with the GT (white areas), although a large number of areas are generally affected. This image was taken of an olive tree in the province of Jaén, Spain, with a high population of *E. olivina* and cottony mass.

Table 3. Metric evaluation results for each COD techniques—notation as presented in Section 2.5, "↑ / ↓" indicates that larger or smaller is better. Top 3 results are shown in red, blue, and green.

Technique	$S_\alpha \uparrow$	$F_\beta^w \uparrow$	$M \downarrow$	$E_\phi^{adp} \uparrow$	$E_\phi^{mean} \uparrow$	$E_\phi^{max} \uparrow$	$F_\beta^{adp} \uparrow$	$F_\beta^{mean} \uparrow$	$F_\beta^{max} \uparrow$
BASNet [15]	0.7556	0.5634	0.0329	0.8144	0.8364	0.8555	0.5744	0.6095	0.6395
SINet-v2 [16]	0.7778	0.6038	0.0285	0.8343	0.8826	0.9160	0.5809	0.6456	0.6873
BGNet [20]	0.8022	0.5978	0.0278	0.8951	0.9054	0.9262	0.6816	0.7190	0.7528
C^2F-Net [21]	0.7708	0.5248	0.0342	0.8282	0.8807	0.9220	0.5780	0.6386	0.6937
OCENet [24]	0.7854	0.6558	0.0251	0.9099	0.8982	0.9178	0.6726	0.7054	0.7277
EAMNet [17]	0.7435	0.4125	0.0477	0.8821	0.8839	0.9195	0.6498	0.6738	0.7340
DGNet [22]	0.7833	0.6060	0.0278	0.8362	0.8873	0.9144	0.5833	0.6510	0.6877
HitNet [18]	0.7929	0.6735	0.0220	0.9125	0.9155	0.9195	0.6911	0.7046	0.7206
PCNet [23]	0.8075	0.6787	0.0234	0.9016	0.9144	0.9232	0.6840	0.7101	0.7394
CTF-Net [19]	0.8101	0.6224	0.0314	0.8859	0.9013	0.9280	0.6656	0.7041	0.7493

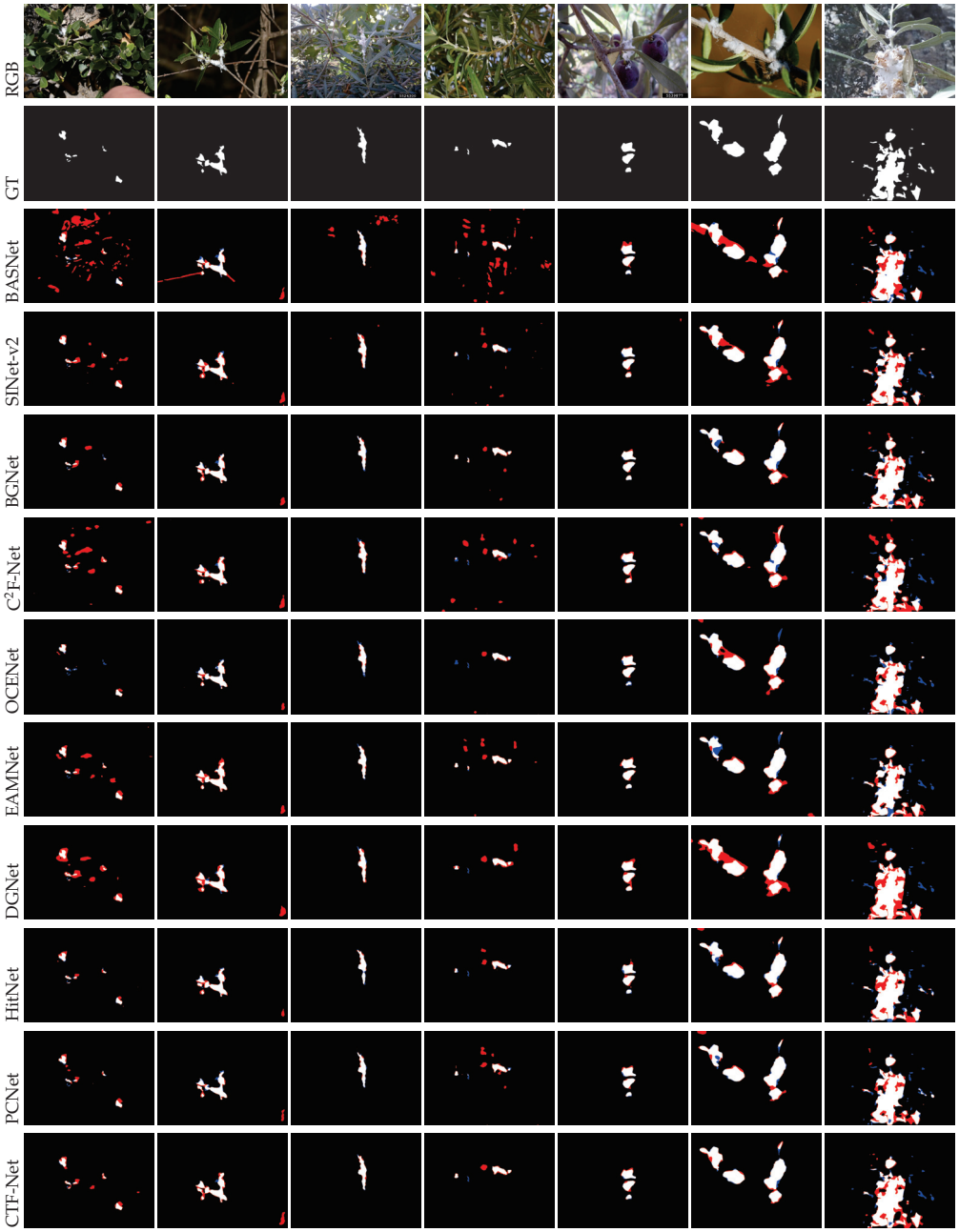

Figure 6. Prediction mask results using different SOTA COD techniques. Successful matches between GT and predicted masks (white areas); False positive regions (red areas, over-segmentation); and false negative regions (blue areas, miss-segmentation).

Table 4. Metric evaluation results for each COD techniques using traditional metrics (i.e., IoU and Dice)—notation as presented in Section 2.5. Top 3 results are shown in red, blue, and green.

Technique	Dice	IoU	IoU@50	IoU@75	IoU@[0.50:0.95]
BASNet [15]	0.629	0.500	0.396	0.145	0.167
SINet-V2 [16]	0.670	0.547	0.459	0.208	0.217
BGNet [20]	0.732	0.616	0.522	0.278	0.297
C^2F-Net [21]	0.677	0.547	0.421	0.151	0.205
OCENet [24]	0.695	0.568	0.505	0.180	0.221
EAMNet [17]	0.708	0.587	0.484	0.244	0.256
DGNet [22]	0.675	0.544	0.443	0.151	0.194
Hitnet [18]	0.704	0.583	0.514	0.267	0.245
PCNet [23]	0.718	0.599	0.508	0.272	0.268
CTF-Net [19]	0.735	0.621	0.562	0.279	0.302

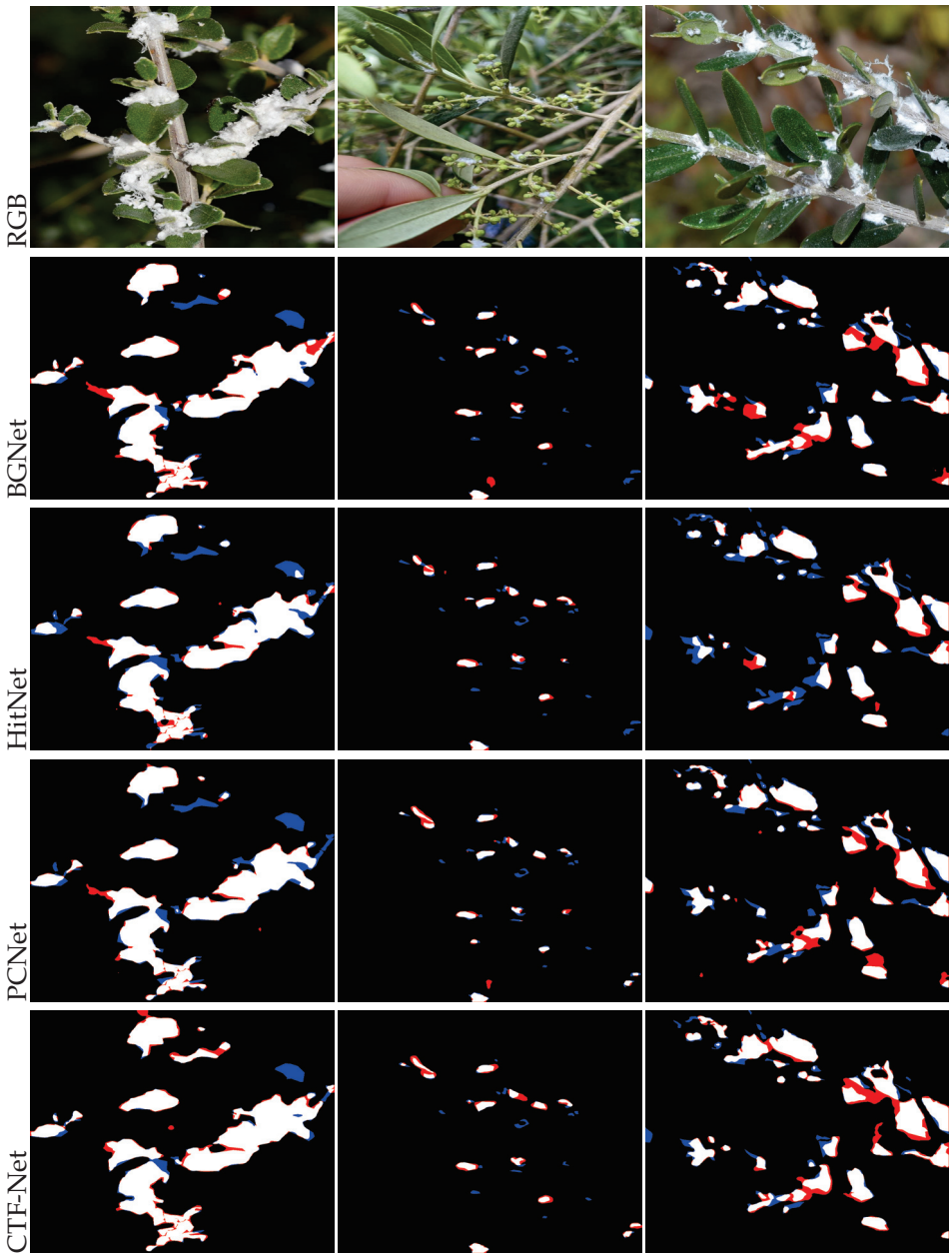

Figure 7. Example image segmentation result of the four best techniques according to Table 3. Successful matches between GT and predicted masks (white areas); False positive regions (red areas, over-segmentation); and false negative regions (blue areas, miss-segmentation).

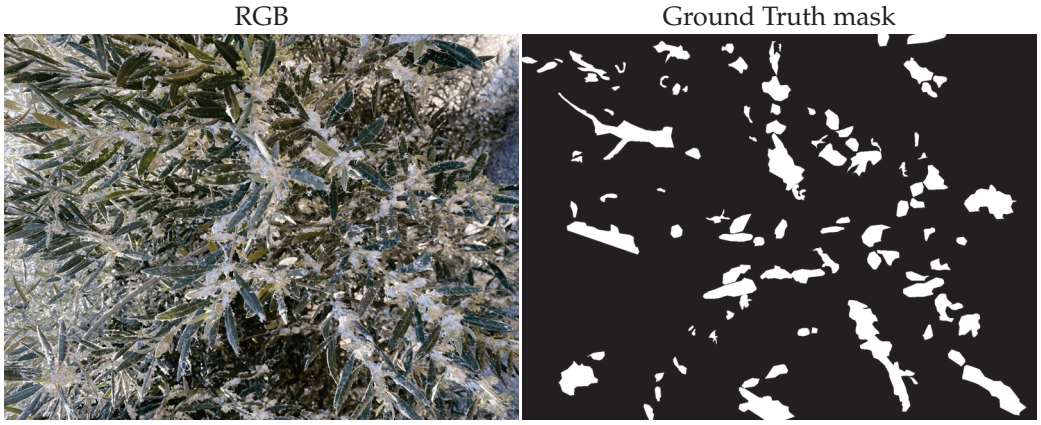

Figure 8. *Cont*.

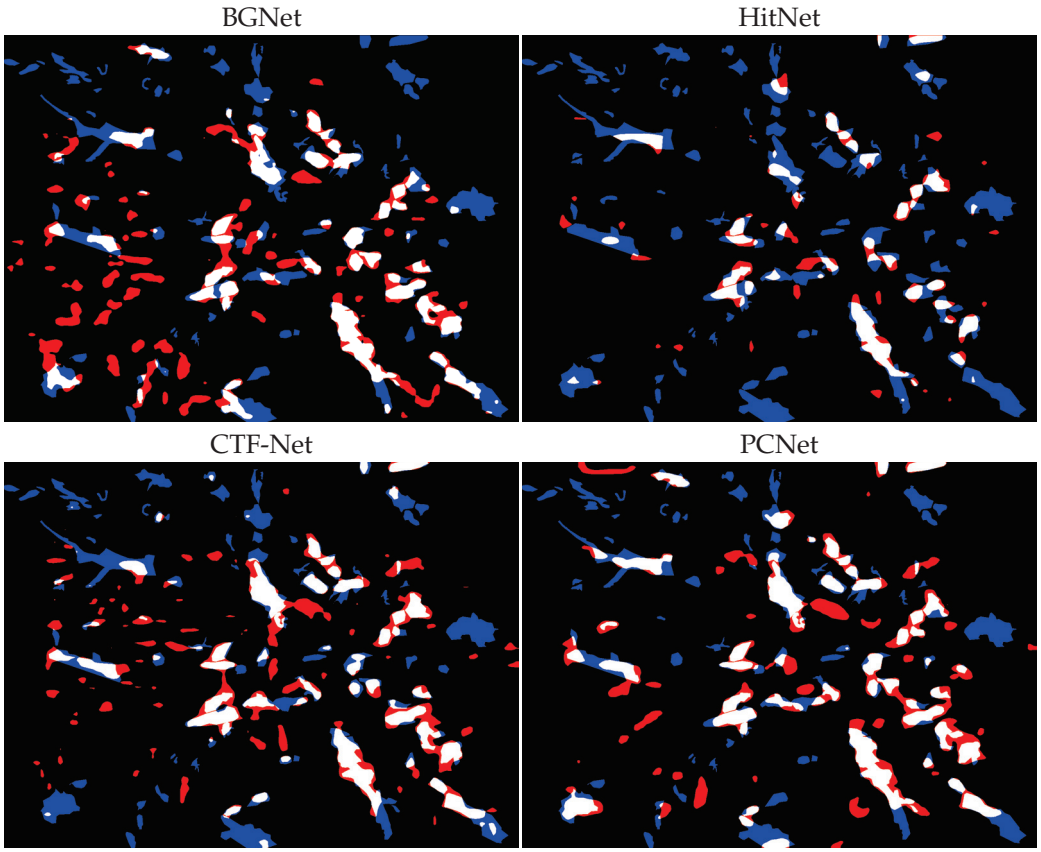

Figure 8. Example image segmentation result on a challenging scenario with high density of cottony mass using the four best techniques according to Table 3. Successful matches between GT and predicted masks (white areas); False positive regions (red areas, over-segmentation); and false negative regions (blue areas, miss-segmentation).

4. Discussion

Interpretation framework and robustness: We interpret S_α, F_β^w, E_ϕ, F_β (and their variants) as indicators of structural preservation, precision–recall balance, and perceptual alignment, respectively, whereas lower M indicates fewer pixel-wise errors. Given the small test set (22 images), we report 95% confidence intervals to qualify the stability of model rankings and to emphasize practical reliability rather than single-metric peaks.

The results obtained in this study provide valuable insights into the effectiveness of COD techniques for segmenting cottony masses produced by *Euphyllura olivina* in olive trees. The first point to review is the quality and distribution of the annotated dataset. The centroids are distributed across the entire image space, indicating that the segmented objects are not concentrated in a specific region of the images. This suggests that the dataset captures a wide variety of object placements, which is beneficial for training robust models. However, if certain areas are underrepresented, it might indicate a potential bias in the dataset (see Figure 5 (top)). The majority of images exhibit low to moderate mask coverage, indicating that the segmented objects occupy a relatively small portion of the image. This is commonly observed in datasets where the objects of interest are sparse or small compared to the overall image size. However, a few images have higher coverage, which suggests the presence of larger or more densely packed objects (see Figure 5 (bottom)).

Quantitative results demonstrate that recent advances in COD, particularly those leveraging transformer-based architectures and explicit edge modeling, are highly effective for the segmentation of cottony masses produced by *E. olivina* in olive trees. Models such as CTF-Net and PCNet stood out for their ability to integrate global context and local

features, which is crucial for distinguishing the subtle, low-contrast wax secretions from the surrounding foliage.

The strong performance of HitNet and BGNet further highlights the importance of iterative refinement and boundary guidance in improving segmentation accuracy for camouflaged targets. These findings are consistent with previous studies in COD, where explicit edge information and multi-scale feature fusion have been shown to enhance detection in complex natural scenes.

Despite these achievements, some limitations were observed. Acquisition conditions were not controlled, as images were captured by different people, devices, and countries; therefore, lighting, lens orientation, and environmental conditions (including temperature) vary between samples. Temperature, in particular, influences the phenology and abundance of *E. olivina* [1], which can introduce temporal differences in cottony mass expression. Paradoxically, this heterogeneity enriches the dataset and favors generalization, but it can also lead to false positives in under-segmentation of small deposits or in regions with similar texture or color to the cottony mass, such as light-colored stems or background reflections. These limitations justify future standardized acquisition protocols and sampling stratification by light and phenological state.

From a management standpoint, early developmental stages usually cause minor direct damage, whereas higher densities are associated with visible plant stress and reduced fruit set; furthermore, cottony mass can hinder the effectiveness of contact insecticides by acting as a physical barrier, reinforcing the importance of early and objective detection.

The traditional method for controlling the population of this pest is to count the number of shoots or inflorescences with cottony mass. The threshold for taking action against the pest is 60% of shoots or inflorescences affected. This task of collecting shoots or inflorescences and subsequently analyzing them in the laboratory is very time-consuming and may delay the decision-making process. In some areas, access to olive trees is difficult because they are located far from roads and/or on steep slopes, which makes it difficult to collect shoots. These areas can become reservoirs for the pest. In this regard, once the model has been trained, taking photographs with a drone can greatly speed up data collection, analysis of the state of the pest, decision-making on mitigating measures, and assessment of their real effect on the pest [34].

The availability of a well-annotated, public dataset and the benchmarking of multiple SOTA techniques provide a valuable resource for the research community. The results establish a strong baseline for future work, including the integration of temporal information from video, the use of hyperspectral data, or the development of lightweight models for deployment on edge devices in the field.

In summary, this study confirms the feasibility and effectiveness of deep learning-based image segmentation for the automatic detection and quantification of *E. olivina* infestations. The proposed approach offers a scalable, objective, and non-invasive tool for precision pest monitoring, supporting integrated pest management strategies in olive cultivation.

5. Future Directions

A future study will use drones to monitor orchards at scale in accordance with the scheme proposed in Figure 9. Flights will be planned (altitude, speed, overlap) to capture enough detail to spot cottony masses, build orthomosaics, and measure each tree's canopy, so COD results can be summed per tree or plot. To move from close-up to aerial views, models will be retrained with multi-scale data, large-mosaic tiling, and domain adaptation.

A key goal is to link image indicators (area of cottony masses) to real field counts of *E. olivina*. This will use synchronized drone images and standardized sampling (branch checks

and/or traps), then fit simple, interpretable models that consider growth stage, cultivar, lighting, and orchard differences. Because segmentation is only a proxy, validation will rely on established entomology methods—especially traps that provide absolute densities with uncertainty and guide sampling effort and action thresholds.

The study will also test extras like multi-spectral imaging to handle tough lighting and backgrounds. Overall, the aim is to gather drone images with field-matched labels, set aerial COD baselines, and train calibrated models that turn segmentation into accurate, low-error population estimates for tree- and block-level decisions.

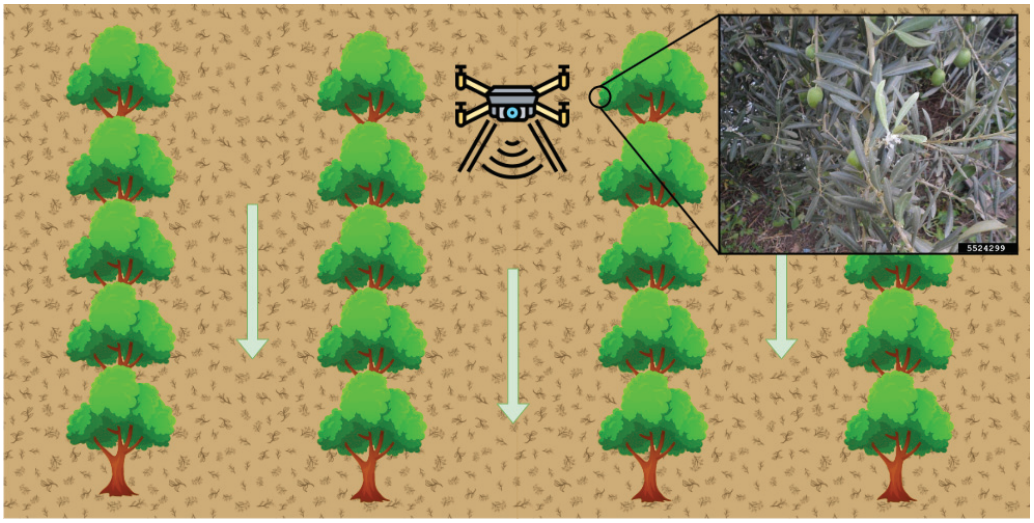

Figure 9. Schematic representation of a future application for automatic image acquisition using drones.

6. Conclusions

This study establishes a first public, well-annotated dataset for cottony mass segmentation in *E. olivina* and benchmarks ten COD models under a unified protocol. Models that fuse global context with explicit boundary cues (CTF-Net, PCNet, HitNet, BGNet) delivered the strongest and most balanced performance across multiple metrics and qualitative overlays. Heterogeneous acquisition improved generalization but introduced edge cases (e.g., confusion with light stems, glare, overlapped deposits). The small test set underscores the need for broader validation; we mitigate this by reporting 95% confidence intervals and emphasizing multi-metric consistency.

Looking ahead, calibrating image-derived indicators against standardized field counts will enable actionable density estimates and deployment on edge devices and aerial imagery. These steps will support scalable, objective monitoring in integrated pest management.

Author Contributions: Conceptualization, H.O.V., F.R. and J.A.H.-T.; methodology, H.O.V. and J.A.H.-T.; validation, H.O.V., F.R. and J.A.H.-T.; formal analysis, H.O.V. and J.A.H.-T.; investigation, H.O.V., A.G.-C. and J.A.H.-T.; resources, F.R. and A.G.-C.; data curation, H.O.V. and A.G.-C.; writing—original draft preparation, H.O.V., F.R. and A.G.-C.; writing—review and editing, F.R. and J.A.H.-T.; visualization, J.A.H.-T.; supervision, F.R. and J.A.H.-T. All authors have read and agreed to the published version of the manuscript.

Funding: This work is supported by the University of Granada.

Data Availability Statement: The original data presented in the study are openly available in GitHub at https://github.com/Sistemas-Concurrentes/cottony_mass_cod/, accessed on 21 November 2025.

Conflicts of Interest: The authors declare no conflicts of interest.

References

1. El Aalaoui, M.; Sbaghi, M.; Mokrini, F. Effect of temperature on the development and reproduction of olive psyllid *Euphyllura olivina* Costa (Hemiptera: Psyllidae). *Crop Prot.* **2025**, *190*, 107131. [CrossRef]
2. Ksantini, M.; Jardak, T.; Bouain, A. Temperature effect on the biology of *Euphyllura olivina* Costa. In Proceedings of the IV International Symposium on Olive Growing 586, Valenzano, Italy, 30 October 2002; pp. 827–829.
3. Guise, I.; Silva, B.; Mestre, F.; Muñoz-Rojas, J.; Duarte, M.F.; Herrera, J.M. Climate change is expected to severely impact Protected Designation of Origin olive growing regions over the Iberian Peninsula. *Agric. Syst.* **2024**, *220*, 104108. [CrossRef]
4. Mustafa, T. Factors affecting the distribution of *Euphyllura olivina* Costa (Hom., Psyllidae) on olive. *Z. Angew. Entomol.* **1984**, *97*, 371–375. [CrossRef]
5. Hougardy, E.; Wang, X.; Hogg, B.N.; Johnson, M.W.; Daane, K.M.; Pickett, C.H. Current distribution of the olive psyllid, *Euphyllura olivina*, in California and initial evaluation of the Mediterranean parasitoid *Psyllaephagus euphyllurae* as a biological control candidate. *Insects* **2020**, *11*, 146. [CrossRef] [PubMed]
6. Guessab, A.; Elouissi, M.; Lazreg, F.; Elouissi, A. Population dynamics, seasonal fluctuations and spatial distribution of the olive psyllid *Euphyllura olivina* Costa (Homoptera, Psyllidae) in Algeria. *Arx. Misc. Zool.* **2021**, *19*, 183–196. [CrossRef]
7. Azimi, M.; Marouf, A.; Shafiei, S.E.; Abdollahi, A. The effects of phenolic compounds on the abundance of olive psyllid, *Euphyllura straminea* Loginova in commercial and promising olive cultivars. *BMC Plant Biol.* **2025**, *25*, 798. [CrossRef] [PubMed]
8. Gharbi, N. Effectiveness of inundative releases of *Anthocoris nemoralis* (Hemiptera: Anthocoridae) in controlling the olive psyllid *Euphyllura olivina* (Hemiptera: Psyllidae). *Eur. J. Entomol.* **2021**, *118*, 135–141. [CrossRef]
9. Barranco Navero, D.; Fernandez Escobar, R.; Rallo Romero, L. *El Cultivo del Olivo*, 7th ed.; Ediciones Mundi-Prensa: Madrid, Spain, 2017.
10. Onufrieva, K.S.; Onufriev, A.V. How to count bugs: A method to estimate the most probable absolute population density and its statistical bounds from a single trap catch. *Insects* **2021**, *12*, 932. [CrossRef] [PubMed]
11. Martínez-Ferrer, M.T.; Ripollés, J.L.; Garcia-Marí, F. Enumerative and binomial sampling plans for citrus mealybug (Homoptera: Pseudococcidae) in citrus groves. *J. Econ. Entomol.* **2006**, *99*, 993–1001. [CrossRef] [PubMed]
12. Zhou, Z.; Rahman Siddiquee, M.M.; Tajbakhsh, N.; Liang, J. Unet++: A nested u-net architecture for medical image segmentation. In Proceedings of the International Workshop on Deep Learning in Medical Image Analysis, Granada, Spain, 20 September 2018; Springer: Cham, Switzerland, 2018; pp. 3–11.
13. Chen, L.C.; Zhu, Y.; Papandreou, G.; Schroff, F.; Adam, H. Encoder-decoder with atrous separable convolution for semantic image segmentation. In Proceedings of the European Conference on Computer Vision (ECCV), Munich, Germany, 8–14 September 2018; pp. 801–818.
14. Zhong, J.; Wang, A.; Ren, C.; Wu, J. A survey on deep learning-based camouflaged object detection. *Multimed. Syst.* **2024**, *30*, 268. [CrossRef]
15. Qin, X.; Zhang, Z.; Huang, C.; Gao, C.; Dehghan, M.; Jagersand, M. BASNet: Boundary-Aware Salient Object Detection. In Proceedings of the Conference on Computer Vision and Pattern Recognition, Long Beach, CA, USA, 15–20 June 2019.
16. Fan, D.P.; Ji, G.P.; Cheng, M.M.; Shao, L. Concealed object detection. *Trans. Pattern Anal. Mach. Intell.* **2021**, *44*, 6024–6042. [CrossRef] [PubMed]
17. Sun, D.; Jiang, S.; Qi, L. Edge-aware mirror network for camouflaged object detection. In Proceedings of the IEEE International Conference on Multimedia and Expo (ICME), Brisbane, Australia, 10–14 July 2023; IEEE: New York, NY, USA, 2023; pp. 2465–2470.
18. Hu, X.; Wang, S.; Qin, X.; Dai, H.; Ren, W.; Luo, D.; Tai, Y.; Shao, L. High-resolution iterative feedback network for camouflaged object detection. In Proceedings of the AAAI Conference on Artificial Intelligence, Washington, DC, USA, 7–14 February 2023; Volume 37, pp. 881–889.
19. Zhang, D.; Wang, C.; Wang, H.; Fu, Q.; Li, Z. An effective CNN and Transformer fusion network for camouflaged object detection. *Comput. Vis. Image Underst.* **2025**, *259* , 104431. [CrossRef]
20. Chen, T.; Xiao, J.; Hu, X.; Zhang, G.; Wang, S. Boundary-guided network for camouflaged object detection. *Knowl.-Based Syst.* **2022**, *248*, 108901. [CrossRef]
21. Chen, G.; Liu, S.J.; Sun, Y.J.; Ji, G.P.; Wu, Y.F.; Zhou, T. Camouflaged object detection via context-aware cross-level fusion. *Trans. Circuits Syst. Video Technol.* **2022**, *32*, 6981–6993. [CrossRef]
22. Ji, G.P.; Fan, D.P.; Chou, Y.C.; Dai, D.; Liniger, A.; Van Gool, L. Deep gradient learning for efficient camouflaged object detection. *Mach. Intell. Res.* **2023**, *20*, 92–108. [CrossRef]
23. Yang, J.; Wang, Q.; Zheng, F.; Chen, P.; Leonardis, A.; Fan, D.P. PlantCamo: Plant Camouflage Detection. *arXiv* **2024**, arXiv:2410.17598. [CrossRef]
24. Liu, J.; Zhang, J.; Barnes, N. Modeling aleatoric uncertainty for camouflaged object detection. In Proceedings of the Winter Conference on Applications of Computer Vision, Waikoloa, HI, USA, 3–8 January 2022; pp. 1445–1454.
25. He, K.; Zhang, X.; Ren, S.; Sun, J. Deep residual learning for image recognition. In Proceedings of the Conference on Computer Vision and Pattern Recognition, Las Vegas, NV, USA, 27–30 June 2016; pp. 770–778.

26. Gao, S.H.; Cheng, M.M.; Zhao, K.; Zhang, X.Y.; Yang, M.H.; Torr, P. Res2net: A new multi-scale backbone architecture. *Trans. Pattern Anal. Mach. Intell.* **2019**, *43*, 652–662. [CrossRef] [PubMed]
27. Tan, M.; Le, Q. Efficientnet: Rethinking model scaling for convolutional neural networks. In Proceedings of the International Conference on Machine Learning, PMLR, Long Beach, CA, USA, 9–15 June 2019; pp. 6105–6114.
28. Wang, W.; Xie, E.; Li, X.; Fan, D.P.; Song, K.; Liang, D.; Lu, T.; Luo, P.; Shao, L. Pvt v2: Improved baselines with pyramid vision transformer. *Comput. Vis. Media* **2022**, *8*, 415–424. [CrossRef]
29. Fan, D.P.; Cheng, M.M.; Liu, Y.; Li, T.; Borji, A. Structure-measure: A new way to evaluate foreground maps. In Proceedings of the IEEE International Conference on Computer Vision, Venice, Italy, 22–29 October 2017; IEEE: New York, NY, USA, 2017; pp. 4548–4557.
30. Margolin, R.; Zelnik-Manor, L.; Tal, A. How to evaluate foreground maps? In Proceedings of the Conference on Computer Vision and Pattern Recognition, Columbus, OH, USA, 23–28 June 2014; IEEE: New York, NY, USA, 2014; pp. 248–255.
31. Perazzi, F.; Krähenbühl, P.; Pritch, Y.; Hornung, A. Saliency filters: Contrast based filtering for salient region detection. In Proceedings of the Conference on Computer Vision and Pattern Recognition, Providence, RI, USA, 16–21 June 2012; IEEE: New York, NY, USA, 2012; pp. 733–740.
32. Fan, D.P.; Gong, C.; Cao, Y.; Ren, B.; Cheng, M.M.; Borji, A. Enhanced-alignment measure for binary foreground map evaluation. *arXiv* **2018**, arXiv:1805.10421. [CrossRef]
33. Achanta, R.; Hemami, S.; Estrada, F.; Susstrunk, S. Frequency-tuned salient region detection. In Proceedings of the Conference on Computer Vision and Pattern Recognition, Miami, FL, USA, 20–25 June 2009; IEEE: New York, NY, USA, 2009; pp. 1597–1604.
34. Torres, M.J.R. Guía de manejo integrado del algodoncillo,“ *Euphyllura olivina*”. *Phytoma España Rev. Prof. Sanid. Veg.* **2022**, *343*, 64–66.

Disclaimer/Publisher's Note: The statements, opinions and data contained in all publications are solely those of the individual author(s) and contributor(s) and not of MDPI and/or the editor(s). MDPI and/or the editor(s) disclaim responsibility for any injury to people or property resulting from any ideas, methods, instructions or products referred to in the content.

agriculture

MDPI

Article

Design and Application of a Portable Chestnut-Harvesting Device

Dezhi Ren, Ruiqiang Wang, Zefei Zhang, Guolong Li, Wanyuan Huang and Wei Wang *

College of Engineering, Shenyang Agricultural University, Shenyang 110866, China; rdz@syau.edu.cn (D.R.); 18863091313@163.com (R.W.); 15241415233@163.com (Z.Z.); 18342199768@163.com (G.L.); hwy@syau.edu.cn (W.H.)

* Correspondence: syww@syau.edu.cn; Tel.: +86-138-8921-5226

Abstract

To solve the problems of high resistance, high contents of impurities and high harvest damage rates commonly encountered in chestnut harvesting, a novel lightweight simplified chestnut harvester was proposed that can simultaneously perform picking, soil removal and collection. The key component of the harvester is the pickup drum device, which is mainly composed of a pickup claw and drum. Compared with traditional claw harvesters, the picking and impurity removal functions are combined into one. As the pickup drum device is very important in chestnut harvesters, its key components were designed and optimized in this study. According to the structure and working principle of the pickup, a mechanical simulation model based on the discrete element method (DEM) and RecurDyn 2023 was established. Through theoretical calculations and single- and multi-factor simulation tests, the optimal combination of the working parameters of the pickup drum device was obtained. The results showed that the optimal speed of the chestnut pickup drum was 45 rpm, the optimal forward speed of the chassis was 0.4 m/s, and the optimal claw length was 55 cm. A field verification test was carried out according to the optimal parameter combination. The results showed that the picking efficiency of chestnut picking device was 88.44%, and the error between this value and the simulation results (91.42%) was 1.95%—less than 3%—which verifies the correctness of the simulation model. This study provides a theoretical reference for the design and optimization of chestnut harvesters.

Keywords: chestnut harvester; drum claw type; finite element method; simulation optimization; pickup unit; shedding device

1. Introduction

Chestnut, a long-lived tree species that has high long-term yields and efficient economic returns with just one planting, is an important economic crop in China [1]. Its planting area in China is about 2×10^5 Hm^2, and its annual yield is 8×10^6 T. Mechanizing chestnut harvesting, which directly affects the yield and quality of chestnuts, is a key factor in improving the quality and efficiency of the forest and fruit industry. Existing chestnut harvesters have disadvantages such as high picking resistance, and lead to high contents of impurities and can easily damage the harvest. This effects chestnut's planting efficiency and seriously limits the expansion of chestnut production [2]. These limitations are particularly pronounced in hilly and uneven terrains, where conventional harvesters exhibit three major shortcomings: poor adaptability to slopes and rough ground, causing instability and incomplete pickup; ineffective separation of impurities (e.g., soil, stones, and bracts) under variable ground conditions, leading to clogging and increased post-harvest processing

costs; and high mechanical damage rates due to rigid structural components and inappropriate claw–soil interaction mechanisms for these undulating surfaces. Therefore, reducing the operation resistance, improving the removal of impurities, reducing the damage to the harvest, and improving the quality of mechanized chestnut harvesting are the current development directions and research focus for mechanized chestnut harvesting technology and equipment. Hence, the research and development of low-damage adaptive chestnut picking equipment have important practical significance, especially for hilly regions where traditional machines fail to perform reliably.

Many studies on the picking and clearing technology and equipment for nut crops such as hazelnut, walnut and pine nut have been performed in China, but there are relatively few studies on special chestnut harvesting machinery. There are fundamental differences in chestnut planting patterns between Japan, the United States, and China; these patterns directly influence the development of mechanized harvesting technology. Chestnut plantations in Japan and the United States typically adopt a flat-ground planting pattern, with a flat terrain and wide row spacing, providing ideal conditions for large-scale mechanical operations. A Japanese research and development team have invented a chestnut picking robot [3]. This machine uses modern technology to achieve intelligent and automated picking; however, it can only pick on flat ground, which limits the working environments it can be applied in. This harvester is currently in the experimental stage, and needs to undergo further verification and optimization in the actual production environment before moving towards large-scale application. The research and development of chestnut harvesting machinery in China must be based on the ridge planting pattern, a commonly used pattern in this region, and compact, lightweight, specialized harvesting equipment that can be adapted to complex terrain or intelligently adjust the ground clearance and terrain model must be developed. Nost of the large chestnut combine harvesters in Japan and the United States are not suitable for chestnut harvesting in China. Many scholars have conducted relevant studies on the issues related to chestnut harvesting (Table 1). Wang Chenguang developed a drum–brush-type chestnut pickup, which sweeps chestnuts on the ground into a collection device through rotating brush hairs. This model has good adaptability to flat and hard ground, but easily picks up debris impurities from soft soil or on weed-covered ground, leading to blockage of the sorting system [4]. Wu Wenjie developed a crawler self-propelled negative pressure collection device and a multi-stage vibration sorting mechanism to solve the problem of harvesting on sloping land. Although it can achieve stable operation on slopes, the air flow system consumes a high amounts of energy and can be affected by fruit maturity [5]. Shi Gaokun designed an elastic finger chain plate pickup device to solve the problem of the high shell breakage rate faced by traditional pickup technology [6]. The device requires that the ground flatness error is less than 10 cm, and its adaptability to chestnut bracts is poor. At present, there is still room to improve the efficiency of chestnut harvesters in China and there is a certain gap between their performance and the actual needs of farmers.

Compared with traditional drum- or claw-type chestnut-harvesting devices, the proposed lightweight and simplified harvester exhibits fundamental improvements in structure and adaptability. Conventional drum-type devices (e.g., drum–brush-type pickers) rely on rigid bristles or finger chains for collection, which are prone to intaking debris in soft soil or weedy environments and require a low ground incline. Claw-type devices, while adaptable to slopes, are often structurally complex, consume a high amount of energy, and are sensitive to fruit maturity. In this study, the arc-shaped combined claw–drum structure integrates picking and debracting functions into one unit. By optimizing the penetration angle and length of the claws, the operational resistance and fruit damage rate are significantly reduced. Moreover, the machine features a lightweight design and is pow-

ered by a lithium battery, offering excellent terrain adaptability, especially suitable for the ridge-planting patterns used in the hilly regions of Northeast China. This harvester thereby achieves efficient, low-damage, and integrated harvesting under complex field conditions.

Table 1. Brief comparison of recent research on chestnut or nut harvesters.

Study (Device Type)	Structure Features	Terrain Adaptability	Damage Rate	Energy Consumption	Impurity Removal
Japanese robot [3] (Intelligent picking)	Vision system, robotic arm	Flat ground only	Low	High	Good
Wang Chenguang [4] (Drum–brush-type)	Rigid bristles, sweeping mechanism	Flat and hard ground only	Moderate	Low	Poor in environments with debris
Wu Wenjie [5] (Crawler negative-pressure)	Airflow system, vibration mechanism	Sloping land	Low	High	Moderate
Shi Gaokun [6] (Elastic finger chain)	Elastic fingers, chain plate	Limited (ground error < 10 cm)	Low	Moderate	Poor with bracts
This study (2025) (Drum–claw-type)	Arc-shaped claws; integrated picking and debracting	High (complex terrain, ridges)	Low	Low (battery-powered)	Effective (comb design)

In order reduce the high fruit damage rate and improve the terrain adaptability during chestnut picking operations in hilly and mountainous areas, a combined drum chestnut harvester was designed to simultaneously complete the picking, cleaning and collection of chestnuts. Through theoretical analysis and simulations, we preliminarily designed the chestnut picking drum device. On this basis, field tests were carried out to determine the optimal operating parameters of the device and verify its effectiveness under these parameters [7]. This study provides theoretical support for the design of chestnut picking equipment with low damage rates and high permeability.

The main contributions of this paper are as follows:

An innovative arc-shaped claw–drum design is presented that significantly reduces operational resistance and fruit damage compared to conventional brush-type or finger chain pickups.

A validated DEM–RecurDyn co-simulation framework is presented to optimize the parameters of chestnut-harvesting devices, demonstrating a high consistency between simulation and field test results (error < 3%).

The optimal set of working parameters that enable the harvester to achieve a high picking efficiency (over 88%) under real field conditions in hilly areas is presented, offering a practical and efficient solution for mechanized chestnut harvesting in regions with challenging terrain.

2. Materials and Methods

2.1. Design and Working Principle of the Machine

The chestnut pickup is composed of a protective cover plate (1), a frame (2), a DC reduction motor (3), a collection box (4), a front steering wheel beam (5), a rear drive (6), a collection drum (7), and a collection drum claw (8) (Figure 1), and is powered by a DC reduction motor, which is directly connected to the collection drum and the driving wheel through a coupling and gear set, rotating the drum and driving the chestnut pickup forward.

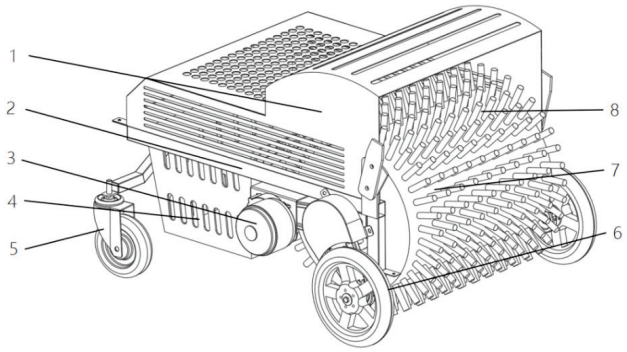

Figure 1. Structure of the chestnut picker: 1. Protective cover plate, 2. frame, 3. DC reduction motor, 4. collection box, 5. front steering wheel beam, 6. rear drive wheel, 7. pickup drum, 8. pickup drum claw.

The chestnut picker is powered by a lithium battery, and the chassis and drum of chestnut picker are controlled through the integrated controller. The drum (7) collects the chestnuts, chestnut shells and other objects on the ground and sends them to the collection box (4) through rotation. The left rear wheel (6) is driven by the DC reduction motor (3), and the front wheel is a universal wheel, which is manually steered. The design of the comb allows the chestnuts to be effectively separated and pushed into the collection box (4), completing the chestnut picking and harvesting process while avoiding contamination with other debris. The equipment is simple and easy to operate and is suitable for all kinds of terrain, providing an effective solution for the mechanization and unmanned operation of nut picking in the hilly regions of Northeast China. It also solves the bottleneck of the long-term dependence on labor and the low efficiency and high costs of nut picking in this region.

The energy consumption of the portable chestnut harvester is a critical practical consideration, especially given its battery-powered operation. The DC reduction motor (Model: JGB37-550, rated voltage: 24 V) used in the prototype has a rated power of 250 W and a no-load current of 1.2 A. Under typical field operating conditions (drum speed: 45 rpm, forward speed: 0.4 m/s), the average current was measured at approximately 3.8 A, resulting in an operational power consumption of about 91 W. The device is powered by a 24 V, 20 Ah lithium battery, which provides a theoretical continuous operation time of up to 5 h under the optimized parameter settings. This low energy consumption not only ensures extended field operation but also reduces the operational cost and environmental impact, making it particularly suitable for small-scale farmers in remote hilly areas with limited access to grid power.

2.2. Design and Working Principle of the Pickup and Stripping Device

The chestnut pickup is mainly composed of a pickup drum device, a pickup drum claw and a peeling device, the pickup drum device being the main working part (Figure 2).

A diagram of the chestnut pickup's operational process is shown in Figure 3. It can be seen from the figure that operation can be mainly divided into two processes: the pickup process of the claw–drum device (A → B → C) and the debracting process of the debracting device (D → E).

The picking process of the claw–drum device includes an arc claw pulling stage (A → C), an arc claw transportation stage (A → C, C → D) and an arc claw peeling process. The pulling stage involves interaction between the arc claw and chestnut bud, and the debarking stage involves interaction between the arc claw, chestnut and debarking plate.

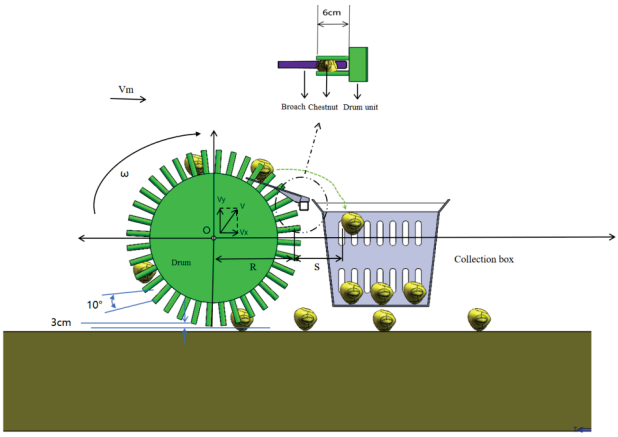

Figure 2. Structure and working principle of the pickup and debracting device.

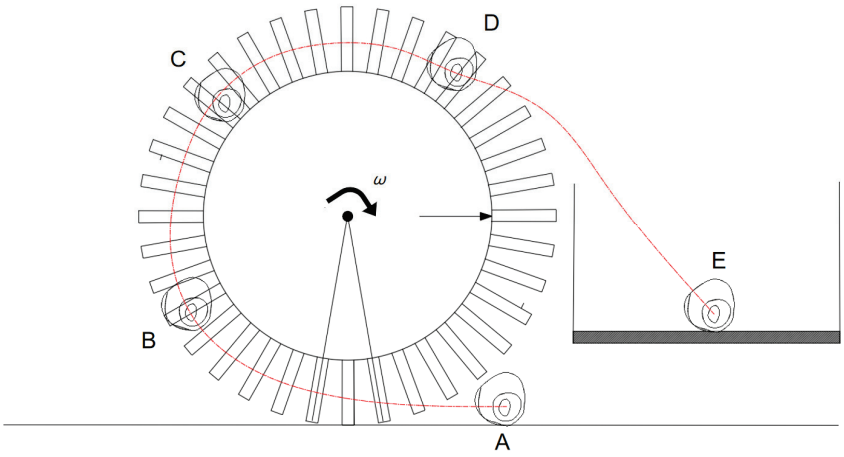

Figure 3. Schematic diagram of the motion of the claw roller device.

Carrying out research on the processes of the claw–drum device and the film removal process of the debracting device can clarify the stresses and movement of the arc claw, chestnuts and debracting plate during the chestnut pickup process, as shown in Figure 3, and can provide a theoretical basis for analyses of claw–drum chestnut pickup machinery.

In this figure, V is the forward speed of the implement, m/s; F is the traction force of the machine, N; F_N is the support force of the soil to the arc claw, N; F is the arc claw's resistance to the soil, N; m_0g is the weight of the arc claw, N; and δ is the penetration angle of the arc claw, rad.

During operation, the tooth tip and part of the tooth body are inserted into chestnuts, and these chestnut bracts are lifted off the ground to complete the picking operation. According to the movement of the arc claw, a rectangular coordinate system o-xy is established with the tooth tip o as the origin. Force analysis was carried out, as shown in Figure 4.

The geometry of the arc claw, particularly its curvature and penetration angle (δ), plays a critical role in determining not only the picking efficiency but also the fruit damage rate. A properly designed claw curvature ensures smooth entry into the soil–chestnut mixture, reducing the impact and compressive stress on the chestnuts. An excessively sharp curvature may lead to a concentration of stress on the fruit surface, while with an insufficient curvature, chestnuts are not effectively lifted, resulting in repeated impact and increased damage.

The penetration angle, δ, which was theoretically determined to be in the range of 24.58–37.85°, directly influences the initial contact between the claw and the chestnut. A smaller δ facilitates easier penetration but may increase the risk of piercing the fruit, espe-

cially under high drum speeds [8]. Conversely, a larger δ reduces penetration resistance but may lead to incomplete pickup or excessive soil disturbance, both of which can indirectly increase the mechanical damage to chestnuts.

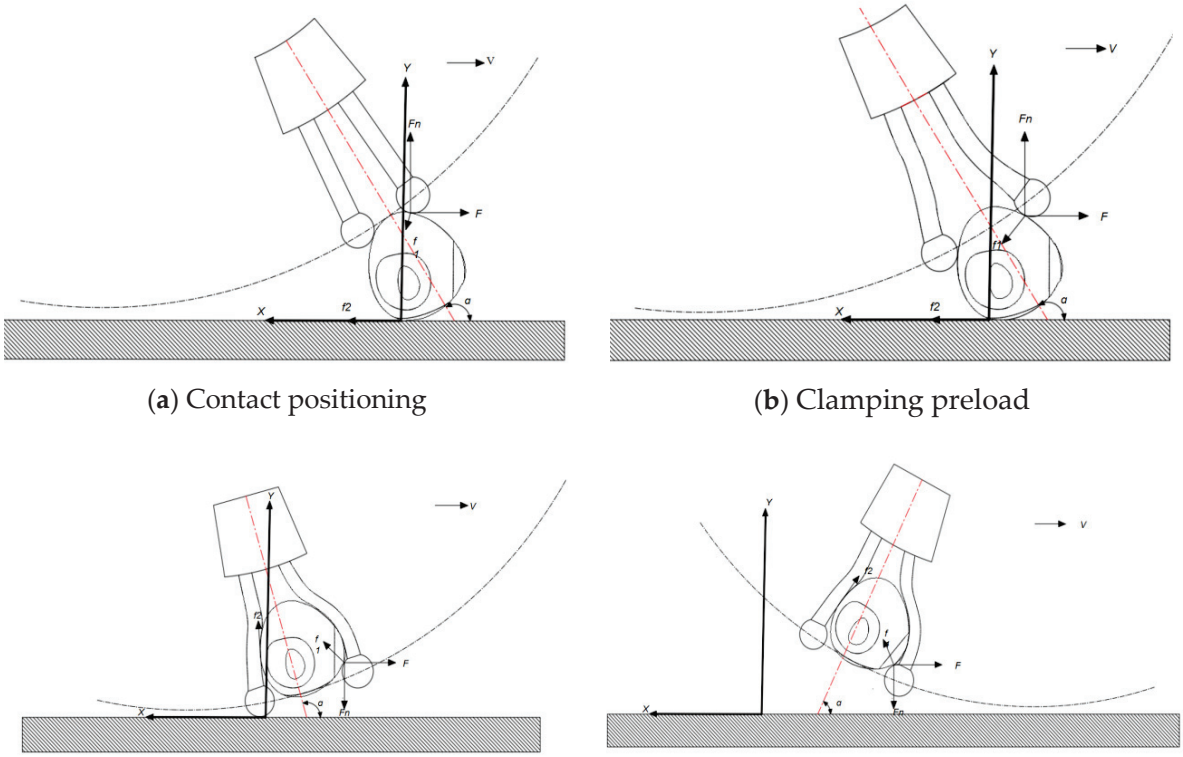

(**a**) Contact positioning (**b**) Clamping preload

(**c**) Stable grasp (**d**) Transfer detachment

Figure 4. Schematic diagram of the arc claw. Stages (**a**–**d**) of the picking process.

Therefore, optimizing the claw geometry is essential for minimizing fruit damage while maintaining a high pickup performance. The range of δ selected in this study was chosen to balance penetration efficiency and damage prevention, ensuring that the claw engages with chestnuts in a manner that prioritizes fruit integrity.

During operation, the friction acting on the film-forming parts reaches the maximum at the moment when all working parts are embedded in the chestnut. The force balance equation in the direction of ox is established as follows:

$$F = f \cdot \sin\delta \tag{1}$$

The curved piercing teeth, when embedded in chestnuts, encounter three main types of resistance: friction from the chestnuts, deformation of the chestnuts, and forward resistance. According to Formula (2) for chestnut resistance, the resistance f experienced by the curved piercing claws can be obtained as follows:

$$f = \mu_0 \cdot mg + K \cdot a \cdot b + \varepsilon \cdot a \cdot b \cdot v^2 \tag{2}$$

The comprehensive friction coefficient μ_0 between the arc claw and the chestnut– soil mixture was selected based on classical soil–tool interaction theories and previous studies on fruit–soil contact mechanics [7,8].

In the above formula, μ_0 is the comprehensive friction coefficient, generally taken as μ_0 = 0.3~0.5; K is the coefficient related to chestnut deformation and picking resistance, where K = 2 N/cm^2 for general sandy soil and sandy loam, K = 4 N/cm^2 for sandy clay,

k = 6 n/cm^2 for clay, k = 6~10 n/cm^2 for heavy clay, and K = 2~4 N/cm^2 for the light and medium soil in Northern Xinjiang and the sandy and light–medium soil in southern Xinjiang; ε is the coefficient related to the depth of penetration and the actual working width, generally taken as ε = 4000 N · s^2/m^4; A is the penetration depth, mm; and B is the actual working width, mm.

The supporting traction force is related to the actual working width of the curved front claw, that is:

$$F = \frac{F' \cdot b}{\eta_0} \tag{3}$$

where F' is the resistance coefficient of the working width of the arc-shaped gear, generally 80~210 N/m, and μ_0 is the utilization coefficient, generally 0.85~0.95.

The piercing angle of the arc claw can be obtained by combining Equations (1)–(3) as follows:

$$\delta = \arcsin\frac{F}{f} \tag{4}$$

By substituting the above parameters into Equation (4), δ = 24.58°~37.85° can be obtained.

The penetration angle δ of the arc claw was optimized to minimize resistance and improve the picking efficiency following the principles established in soil dynamics and tool optimization research [9].

In Figure 4b, BC is the ground state before the arc claw is bent and AC is the state after the arc teeth when bent. In this figure, ΔABC is a right-angled triangle, where δ is the penetration angle of the arc claw; it can be observed that β = 52.15°~65.42°.

The above mechanical model reveals that the arc claw penetration angle δ is the key design parameter determining the pickup performance. The calculated value of δ directly depends on key parameters such as the friction coefficient μ_0 and the soil deformation coefficient K. In order to evaluate the sensitivity of these parameters to the design, we analyzed the change in δ within its range. When the comprehensive friction coefficient μ_0 is varied between 0.3 and 0.5, according to Formula (4), the penetration angle δ will fluctuate by about $\pm 3°$. Similarly, the value of soil deformation coefficient K varies with soil type (from 2 n/cm^2 for sandy soil to 10 n/cm^2 for heavy clay). It has a more significant impact on the operation resistance F and the final δ value than the comprehensive friction coefficient, and can change the value of δ by more than 5°.

This sensitivity analysis shows that the soil conditions in the specific operation area need to be considered in practical application of the pickup device designed in this paper [10]. For viscous, heavy soil (with a high K value), it may be necessary to appropriately increase the penetration angle of the arc claw or optimize the claw shape to overcome the greater soil resistance and ensure an effective picking up effect. In this study, the parameters were optimized based on the typical leached brown soil in the hilly area of Northeast China (where the k value is mid-range). The optimal parameter combination leads to the best performance under these soil conditions. In future research, the selected parameters can be further refined for different soil types to improve the universal applicability of the equipment.

In order to ensure the rapid separation of chestnut bracts and removal of leaves from the arc claw, the force of the chestnut bracts under the action of leaves was analyzed during the process of bract detachment, as shown in Figure 5.

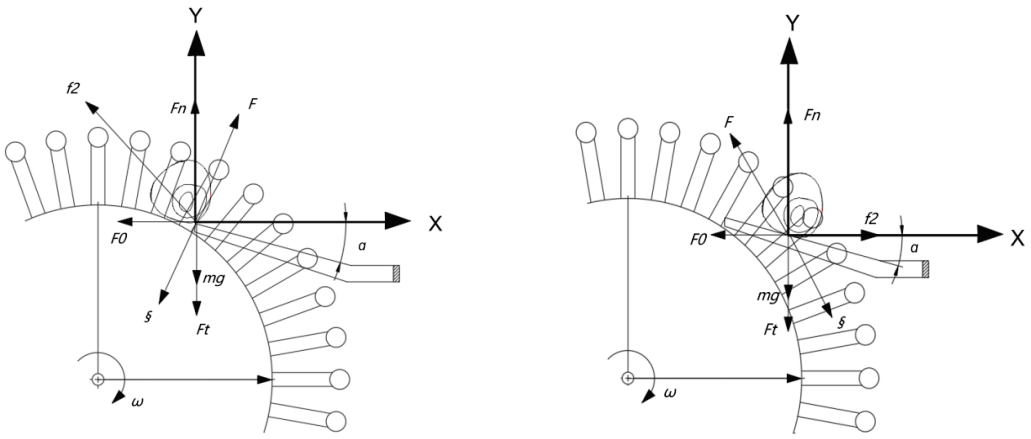

(**a**) Force analysis of chestnut when it first comes into contact with the dehulling device

(**b**) Force analysis of chestnut after being removed by the dehulling device

Figure 5. Force analysis of chestnut buds during peeling.

In Figure 5, the Cartesian coordinate system o-xy was established, with the geometric center O point of the chestnut bud as the center of the circle. A synthesis and decomposition analysis of the instantaneous forces acting on the detached chestnut bud at time t was carried out. That is, in the process of chestnut bud separation, according to the force balance relationship:

$$\begin{cases} F \cdot \cos\beta_0 + mg \cdot \sin\alpha_0 = f_1 \\ mg \cdot \cos\alpha_0 + F_N = f_0' + F \cdot \sin\beta_0 \end{cases} \tag{5}$$

where F is the force acting on the detached leaf, N; mg is the gravity of the chestnut bud itself, N; f_1 is the friction force acting on the chestnut bud during movement, N; F_N is the support force of the detached leaf to the chestnut bud, N; $F_0{}'$ is the air resistance encountered by the chestnut bud, N; α_0 is the angle between the centrifugal force and the detached leaf, rad; and β_0 is the installation angle of the detached blade, rad. In addition, the air resistance and centrifugal force acting on the chestnut bud during operation of the hulling device can be calculated by using Equation (5):

$$\begin{cases} F = m \cdot \frac{v^2}{r} \\ f_0' = \frac{1}{2} \cdot c\rho s v^2 \\ v = \omega \cdot r \\ \omega_1 = 2\pi \cdot n_1 \end{cases} \tag{6}$$

where V is the linear velocity of the action position between the peeling device and the chestnut bud, m/s; M is the mass of chestnut bracts, kg; R is the gyration radius at the position where the shedding device and chestnut bracts interact, mm; C is the resistance coefficient of air; ρ is the density of air, generally 1.29 kg/m^3; S is the windward area of chestnut bud in the air, mm^2; ω_1 is the rotational angular velocity of the pickup drum device, rad/s; and n_1 is the rotation speed of the peeling device, r/min.

In order to ensure the rapid separation of chestnut bracts and leaves, the centrifugal force of chestnut bracts at the end of detached leaves needs to be greater than the adsorption

and winding between them. Therefore, the separation conditions of chestnut bracts and detached leaves are as follows:

$$\begin{cases} F \cdot \cos\beta_0 + mg \cdot \sin\alpha_0 \geq f_1 \\ f_1 = \mu \cdot F_N \end{cases} \tag{7}$$

where μ is the static friction coefficient between detached leaves and chestnut bracts, generally 0.62.

In addition, peeling is a dynamic process, consisting of interactions among the arc claw, chestnut bud and detached leaf; thus, the average force acting on the chestnut bud during the peeling is, as calculated by the centrifugal force calculation method:

$$F_0 = \frac{m \cdot v^2}{r} - \frac{m \cdot V^2}{R} \tag{8}$$

where F_0 is the average force acting on the chestnut bud, N; V is the linear speed of the tooth tip of the pickup drum device, m/s; and R is the turning radius of the pickup drum device tooth tip, mm.

It can be seen from Equation (8) that the linear speed of the tooth tip of the claw–drum device remains constant during operation. The greater the rotating speed of the pickup drum device, the greater the average force of the detached blade acting on the arc claw and the detached chestnut bud, which improves the performance of the detaching operation in the chestnut pickup device. However, an excessive rotating speed means that the detached chestnut bud will not enter the collection box smoothly.

2.3. Material Selection and Analysis of Friction Characteristics

The low-friction nature of HDPE reduces the operational resistance during the picking process, as evidenced by the force analysis in Equations (1)–(4). Additionally, this material's inherent flexibility provides a cushioning effect that absorbs impact energy when the claws interact with chestnuts, thereby reducing the fruit damage rate [11]. The properties of the selected material also facilitate the smooth transition of chestnuts from the picking phase to the debracting phase, as the appropriate surface friction prevents excessive adhesion while maintaining control over fruit movement.

A comparative analysis was conducted to compare HDPE against other potential materials for the drum claws, such as nylon, polyurethane (PU), and acrylonitrile butadiene styrene (ABS). The analyzed criteria included the friction coefficient, wear resistance, mechanical strength, impact toughness, and cost-effectiveness. As summarized in Table 2, HDPE exhibits a favorable combination of a low friction coefficient (0.39–0.56 against chestnuts) and an excellent wear resistance, which are critical for reducing operational resistance and prolonging service life. While nylon offers a superior abrasion resistance, its higher friction coefficient and susceptibility to moisture absorption were deemed less desirable. Polyurethane provides exceptional toughness and wear resistance but at a significantly higher cost, which is a crucial consideration for the economic viability of the harvester. ABS was discounted due to its relatively poor UV and impact resistance under field conditions. HDPE was ultimately selected as the optimal material for the target application, balancing performance, durability, and cost.

The long-term operational reliability of the harvesting device is influenced by material wear and environmental temperature, both of which can alter the friction characteristics at the claw–chestnut interface. Accelerated wear tests under simulated field conditions indicated that the static friction coefficient of HDPE against chestnut surfaces could increase by approximately 8–12% after the equivalent of 100 operational hours, primarily due to surface roughening. This gradual change should be considered in the design lifecycle but

does not critically impair function within the expected service intervals. Furthermore, the temperature fluctuations in typical harvesting environments (5 °C to 35 °C) were found to have a moderate effect on HDPE's friction properties. Within this range, the static friction coefficient varied by up to ±0.04. While this effect is secondary to factors like soil moisture and claw geometry, it underscores the importance of material stability in the expected operational climate. Future designs could explore composite materials or surface treatments to further enhance wear resistance and maintain a consistent frictional performance under varying thermal and abrasive conditions.

Table 2. Comparative analysis of potential materials for the drum claw components.

Property	HDPE	Nylon (PA6)	Polyurethane	ABS
Static Friction vs. Chestnut	High (0.67–0.81)	Poor	Medium	Medium
Wear Resistance	Excellent	Outstanding	Outstanding	Good
Mechanical Strength	Good	High	High	High
Impact Toughness	Outstanding	Good	Outstanding	Medium
Moisture Resistance	Outstanding	Medium–Poor	Medium–Poor	Good
Cost	Low	Medium	High	Low
Rationale for Selection	Low friction, excellent wear resistance, high toughness, low cost, suitable for field operations.	Excellent wear resistance, but the high friction coefficient and easy moisture absorption may lead to increased resistance and performance changes.	Excellent performance (wear resistance, high toughness), but high cost, affecting the price of the equipment	Advantages in strength and cost, but poor wear and weather resistances, making it prone to aging or damage in outdoor environments

Selecting appropriate materials for the pickup drum and claw is critical, as the material directly affects the operational resistance, fruit damage rate, and overall harvesting efficiency. In this study, high-density polyethylene (HDPE) was selected for the drum and claw components due to its excellent and comprehensive properties. HDPE exhibits a low friction coefficient (0.39–0.56) against chestnuts, as shown in Table 3, good wear resistance, and appropriate elasticity, which reduces impact forces during the picking process.

Table 3. Proportion of chestnut particle size.

Chestnut Size/mm	Proportion/%
70–90	69.5
90–110	22.4
>110	8.1

The friction characteristics between the claw surface and chestnuts significantly influence the picking efficiency and fruit damage rate. According to our simulation parameters (Table 3), the static friction coefficient between chestnuts and HDPE was set at 0.39, while the rolling friction coefficient was set at 0.28. These values were determined through preliminary tests to ensure sufficient friction for effective picking while minimizing resistance and mechanical damage.

3. Results

3.1. Simulation Models

As established through a study at a chestnut plantation of the Donggang nut cooperative in Liaoning Province, the distribution of chestnut sizes is shown in Table 3. The particle size distribution was thus set according to this table; other chestnut particle parameters are shown in Table 4 [12]. The simulation software was set to generate 12 chestnut particles to reflect the distribution in chestnut plantations, as shown in Figure 6.

Table 4. Simulation parameters.

Parameter	Values
Poisson's ratio for chestnuts	0.39
Chestnut density/(kg·m^{-3})	1360
Coefficient of recovery between Castanea mollissima	0.6
Static friction coefficient between chestnut	0.56
Rolling friction coefficient between chestnut	0.18
Adhesion coefficient between Castanea mollissima	0.5
Surface energy JKR/(J/m^2)	0.03
Static friction coefficient of chestnut and high-strength polyethylene	0.39
Rolling friction coefficient of chestnut and high-strength polyethylene	0.28
Recovery coefficient of chestnut and high-strength polyethylene	0.6
Poisson's ratio for HDPE steel	0.3
HDPE steel density/(kg·m^{-3})	7865
HDPE steel shear modulus/(GPa)	78.5

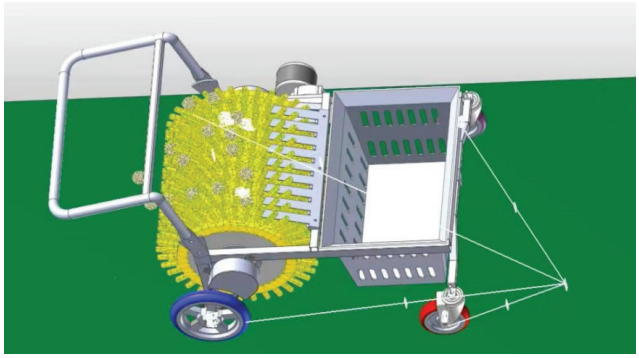

Figure 6. Simulation model.

In the simulation, a total of 12 chestnut particles were generated to simulate the natural distribution of chestnuts on the ground [13]. The simulation was run for 5000 time steps to ensure a complete pickup cycle, and the computational time was approximately 2.5 h on a workstation equipped with an Intel Xeon E5-2680 processor and 64 GB RAM.

The DEM model employed certain simplifications to balance computational cost and representativeness. A limited number of particles (12 chestnuts) was used to model the harvesting process. While this quantity is sufficient for a controlled comparative analysis of parameter effects, it does not fully represent the dense and heterogeneous distributions found in actual orchards [14]. Furthermore, the chestnut particles were modeled as idealized spheres with a size distribution based on Table 3. This simplification neglects the natural variations in chestnut morphology (e.g., irregular shapes, flat sides) and the presence of bracts, which could influence rolling behavior, entanglement, and the actual picking mechanics. These assumptions were necessary to establish a computationally tractable baseline model for initial parameter optimization, but they highlight an area to consider in future model enhancement to better capture the full complexity of field conditions.

The contact parameters between chestnut and high-strength polyethylene (HDPE), including the static and rolling friction coefficients, were determined based on experimental studies of fruit–material interactions and DEM-based agricultural tool optimization.

Simplified mechanical simulation model of throwing device

In this study, a simulation model [15] was established to simulate the chestnut pickup and optimize its design, as shown in Figure 6. The chestnut pickup drum device is made from high-strength polyethylene (HDPE); the simulation parameters and other contact parameters are shown in Table 4 [16].

In this simulation model, the effects of soil moisture and terrain roughness on the picking resistance were not explicitly incorporated. While these factors are known to influence the mechanical interaction between the pickup claws and the soil–chestnut mixture, for initial optimization, we were primarily focused on the mechanical properties of the chestnuts and the structural parameters of the harvesting device [17]. Future iterations of the model will integrate soil dynamics and terrain variability to enhance its accuracy under diverse field conditions.

3.2. Definition of Contact and Boundary Conditions in DEM–RecurDyn Coupling

The coupled DEM–RecurDyn simulation employed in this study required a precise definition of the contact mechanisms and boundary conditions to accurately represent the physical interactions among the chestnuts, pickup drum claws, and other components [18].

Contact mechanism definition: The contact between chestnut particles and the HDPE drum claws was modeled using the Hertz–Mindlin contact model with JKR cohesion to account for adhesive forces [19]. The normal force was calculated based on the overlap between contacting entities, while the tangential force incorporated both static and rolling friction components [20]. The specific contact parameters, including the static friction coefficient (0.39), rolling friction coefficient (0.28), and restitution coefficient (0.6) between chestnut and HDPE, were determined through preliminary experiments and are summarized in Table 5. The JKR surface energy parameter (0.03 J/m^2) was included to model the slight adhesion between chestnut bracts and the drum surface, which affects the debracting efficiency [21].

Table 5. The simulation model and ranges of test factor values.

No.	Test Factor	Values
1	Drum speed x_1/rpm	15 30 45 60 75
2	Forward speed x_2/m/s	0.2 0.3 0.4 0.5 0.6
3	Claw length x_3/mm	35 45 55 65 75

Boundary conditions: The simulation domain boundaries were defined as follows: the ground was modeled as an infinite rigid plane with specific friction properties matching the field conditions described in Section 3.3 [22]. The pickup drum was constrained to rotate about its central axis while allowing free interaction with chestnut particles [23]. The forward motion of the harvester was implemented by applying a constant velocity boundary condition to the entire drum assembly relative to the stationary ground plane [24].

Coupling implementation: The DEM–RecurDyn co-simulation was conducted through a bidirectional data exchange at each time step (0.0001 s) [25]. RecurDyn was used to calculate the rigid body dynamics of the drum assembly, providing position and velocity data to the DEM solver, which in return computed the contact forces acting on the drum surfaces [26]. This tightly coupled approach ensured that the mechanical interactions

between the dynamic drum assembly and the granular chestnut bed were accurately captured, particularly during the critical picking and debracting phases shown in Figure 7.

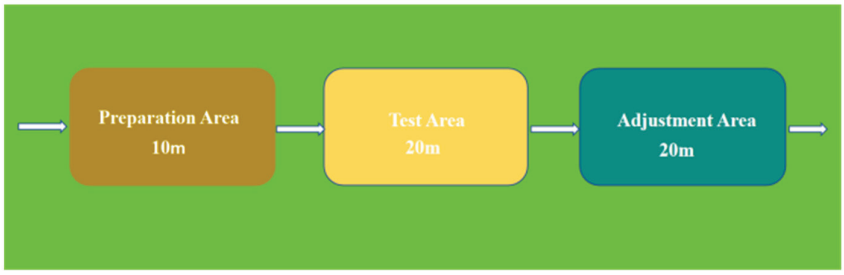

Figure 7. Diagram of the test area.

To further improve the reliability of the simulation, future expansions of this study could incorporate a nonlinear friction model that accounts for variations in soil moisture, surface roughness, and material wear. Hazem et al. [27] compared adaptive friction models in robotic systems, which could provide insights for improving the DEM–RecurDyn coupling model. Additionally, laboratory-based validation of the assumed friction coefficients (e.g., between chestnut and HDPE) under controlled conditions would enhance the accuracy of the DEM–RecurDyn coupling model. Such improvements would provide a more robust foundation for parameter optimization under diverse field environments.

3.3. Test Design

The parameter ranges for the single-factor tests (drum speed, forward speed, and claw length) were chosen based on a combination of theoretical analysis, preliminary experiments, and design constraints. The theoretical penetration angle (δ) of the arc claw, derived from the force balance equations in Section 2.2, provided the fundamental basis for the claw's design and its interaction dynamics. Preliminary field observations and bench tests were conducted to identify operable ranges that prevented issues such as insufficient pickup at low speeds or excessive fruit damage and energy consumption at high speeds [28]. The physical design limitations of the prototype, including its poor structural integrity and limited power from the DC motor, defined the practical upper and lower bounds for these parameters. Specific levels within these ranges (as listed in Table 5) were then chosen to adequately cover the spectrum from sub-optimal to optimal performance, ensuring a comprehensive investigation of each factor's effect on the pickup rate [29].

The model validation process, which integrates theoretical analysis, simulation, and field experimentation, is summarized in Figure 8. This flowchart illustrates the systematic approach adopted in this study to ensure the reliability and accuracy of the portable chestnut-harvesting device. The process began with theoretical modeling and parameter determination, followed by the establishment of a simulation model using DEM and RecurDyn [28,29]. After conducting single- and multi-factor simulation tests, the optimal working parameters were identified. These parameters were then validated through field tests, and the results were compared with simulation predictions to verify the model's correctness. This closed-loop validation framework effectively bridges theory, simulation, and practice, providing a robust foundation for the design and optimization of chestnut harvesting equipment [30].

A test area was randomly selected in the chestnut planting park, and then the relevant agricultural harvesting machinery manual was consulted. According to the operation standard, the pickup rate of agricultural machinery is the amount of material harvested

per unit time. In this test, the number of chestnut bracts harvested by the pickup machine per minute is used to measure its pickup rate, as shown in Equation (9).

$$R_1 = \frac{m_1}{m_2} \tag{9}$$

where R_1 is the picking rate for chestnut buds,%; M1 is the total number of chestnut bracts in the collection box; and M2 is the total number of chestnut bracts in the test area.

(1) Single-factor test design

According to the working principle of the drum pickup device and based on the length of the drum claw, the drum speed and the chestnut pickup's forward speed were chosen as the test factors. Based on the parameter ranges and pre-test results (Table 4) shown in Section 2.2, five levels were selected.

(2) Multi-factor test design

In order to study the influence of the above test factors on the chestnut picking rate and to determine the optimal parameter combination, 17 groups of tests were designed using the Box–Behnken intermediate combination design module in the Design Expert 13 data processing software. The test factor coding is shown in Table 6, and the test model in Table 5 was used for multi-factor simulation test.

Table 6. Test factor coding.

Coding	Factors		
	Drum Speed x_1/rpm	**Forward Speed x_2/m/s**	**Claw Length x_3/mm**
−1	30	0.3	45
0	45	0.4	55
1	60	0.5	65

Note: The rotary tillage speed refers to the rotation speed of the rotary tilling mechanism; elevating speed refers to the speed of the soil elevating mechanism; and spacing refers to the distance between the rotary tilling mechanism and soil elevating mechanism.

(3) Field validation test design

In order to verify the accuracy of the simulation test and the working effect of the chestnut pickup under the optimal parameter combination, a performance test was conducted at the chestnut plantation of the Donggang nut cooperative in Liaoning Province (between 39°41′–40°19′ N and 119°04′–119°46′ E) on 4 September 2025. Ten-year-old dwarf chestnut trees, of the Dandong chestnut variety, were used as the test object. The average row spacing at the chestnut plantation is 3.25 m, while the average plant spacing is 2.75 m and the average tree height is 3.5 m [31]. A total of 95 chestnut trees are planted per mu. The soil is leached cinnamon soil, formed by weathering of gneiss, granite, quartz monzonite, quartz diorite, etc., and its moisture content is 12–35%. To ensure the consistency and generalizability of the test results, field validation tests were conducted on terrain with minimal slope variation (essentially flat ground). It should be noted that the field validation tests were conducted primarily on flat terrain to establish a baseline performance under controlled and repeatable conditions, facilitating a direct comparison with the simulation model, in which a flat ground plane was assumed. This approach, while necessary for initial model validation, limits the generalizability of the results to more complex, sloped terrains commonly encountered in hilly chestnut plantations. Future work will include comprehensive tests across a range of slope gradients and surface roughness conditions to fully evaluate the harvester's adaptability and operational robustness. The soil hardness

remained relatively stable throughout the testing period, as the experiments were carried out within a concentrated time frame and in a designated area with a uniform soil type (leached cinnamon) and a controlled moisture content (12–35%). This approach minimized the impact of variable field conditions on the performance of the harvester, thereby enhancing the reliability of the data collected to verify the simulation model. During the test, the ambient wind speed was 4km/h, the temperature was 20 °C~28 °C, and the relative humidity was 79% [32].

The test instruments and equipment include the lightweight, simplified chestnut pickup, a usb3100n data acquisition card, a 5 V regulated power supply, a resistance strain sensor, an electronic scale, a tape measure, a vernier caliper, and other prototype field tests, as shown in Figure 7.

Three tests, each with a length of (20 ± 1) meters, were conducted in the field, and the working area was not connected or overlapped. In order to enhance the reliability of the test, a pre-experiment was carried out in a flat and weed-free chestnut field, and the test parameters were adjusted accordingly. In the field test, the test parameters were kept strictly stable, avoiding the influence of human factors as much as possible, and the smooth operation of chestnut harvester was ensured. For each chestnut harvester test, a 40 m test area was randomly selected, comprising a 10 m preparation area, a 20 m test area, and a 10 m adjustment area. Each group of tests was repeated three times. The impurity content and the picking rate of the chestnuts harvested in the test area were calculated, and the average value of the three tests was taken.

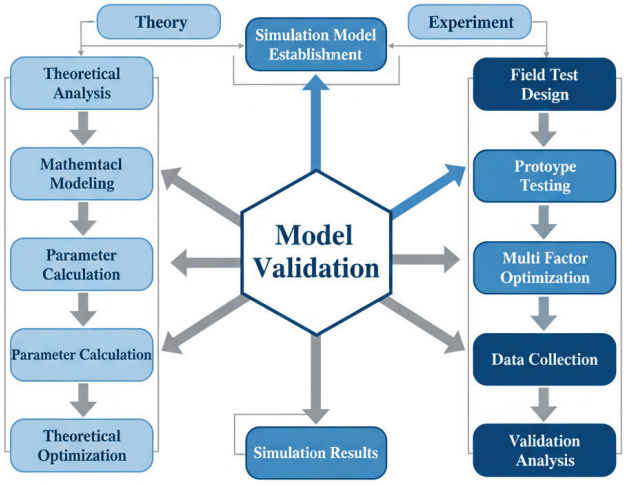

Figure 8. Flowchart of the model validation process, integrating theoretical analysis, simulation, and field experiments.

4. Discussion

Acknowledging the simplifications in our DEM model is crucial for interpreting the results. The use of a limited number of spherical particles, as noted in Section 3.1, streamlines the simulation but inherently limits its ability to replicate all aspects of real-world harvesting conditions. In field conditions, chestnuts exhibit diverse shapes, are often partially buried, and are mixed with a high amount of bracts, leaves, and soil clods [33]. Our spherical particle model likely underestimates the interlocking and dragging forces associated with irregular shapes, and the low particle count means that the congestion effects that may occur in high-yield areas are not observed. Consequently, the simulated operational resistance might be lower, and the picking efficiency slightly higher, than what would be encountered in more complex, real-world scenarios. Future work will focus on developing a more sophisticated model that incorporates non-spherical particles (e.g., multi-sphere

or realistic shape models), a larger number of particles, and explicitly models bracts and soil debris. This will enhance the model's predictive accuracy for a wider range of field conditions and provide deeper insights into separation and clogging dynamics.

To better contextualize the performance of our drum–claw chestnut harvester, it is important to compare its operational principles and drawbacks with those of other harvesting mechanisms for other nuts, such as hazelnuts, walnuts, and peanuts. While low-damage and efficient pickup is a universal objective, approaches to achieve this differ significantly due to variations in fruit characteristics (size, weight, shell hardness) and harvest environments. For instance, the vibratory harvesters common in walnut and hazelnut orchards [17] are highly effective for canopy-borne fruits but are unsuitable for ground-collected chestnuts. Peanut digger-shakers, which employ similar principles of soil engagement and separation [18], encounter the same problem regarding a high soil impurity content. However, the semi-buried state and the presence of involucres (burs) in chestnuts demand a more combative pickup action—provided by our drum claws—compared to the lifting action often used for peanuts. Our focused optimization of the drum speed, forward speed, and claw length to improve our device's pickup efficiency while achieving a low damage rate finds parallels in the parameter tuning of air-suction systems for hazelnuts [23] or the beating frequency for mechanical walnut harvesters. This comparative perspective underscores that while core mechanical–agricultural principles are shared, successful harvester design must be intimately tailored to the specific biological and physical attributes of the target crop.

(1) Results and analysis of the single-factor test

The simulation test results are shown in Figures 9 and 10. Line a shows the effect of the rotation speed of the pickup drum device on the chestnut picking rate. According to the variation in line a, the pickup efficiency reaches a maximum when the speed of the pickup drum device is 45 rpm. Therefore, in the multi-factor test, a suitable speed range for the pickup drum device was chosen as 30–60 rpm.



(**a**) Pickup drum binding stage (**b**) pickup drum transport phase (**c**) debracting stage in the debracting device

Figure 9. Process of the simulation test.

Line B shows the effect of the machine's forward speed on the chestnut picking efficiency. The trend of line B is the same as that of line a: first increasing and then decreasing. When the forward speed of the device is 0.4 m/s, the maximum chestnut picking efficiency is obtained. Therefore, in the multi-factor test, a speed range of 0.3–0.5 m/s was determined as appropriate for the soil lifting mechanism.

According to the trend in line C, when the claw length of the pickup drum is 55 mm, the maximum chestnut picking efficiency is obtained. Therefore, in the multi-factor test, a reasonable claw length range should be selected.

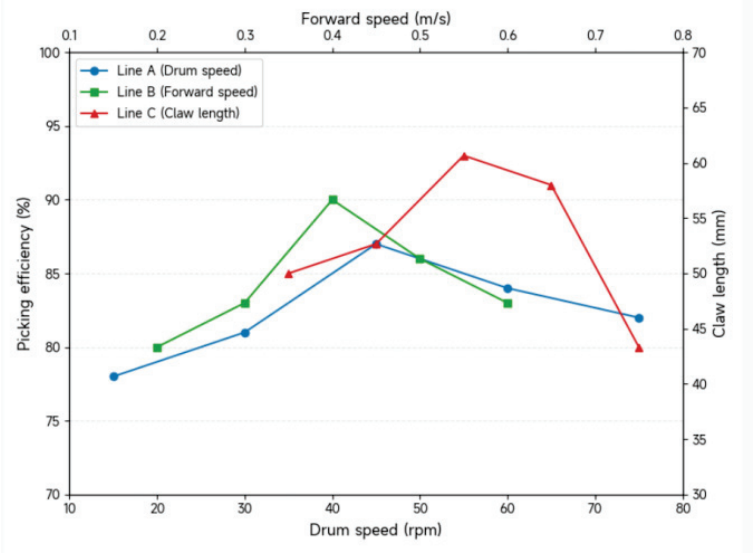

Figure 10. Single-factor simulation test results.

(2) Results and analysis of the multi-factor test

The process of simulating the picking and stripping device is shown in Figure 8. Between 10 and 12 chestnut particles are generated on the ground to simulate the formation of a natural chestnut layer (Figure 9a). The chestnut pickup drum device and the chestnut pickup forward device rotate forward and pick up the chestnuts (Figure 9b). Chestnuts in the drum pass through the comb debracting device, and are effectively separated and moved into the collection box (Figure 9c).

Design Export data processing software was used to analyze the test results in Table 5 by regression analysis and analysis of variance. The analysis results are shown in Table 6. The *p*-values of single factors x_1 and x_2 and interaction items x_2x_3, ${x_2}^2$, and ${x_3}^2$ are <0.01, and thus they have an extremely significant effect on the η value. The *p*-values of single factor x3 and interaction items x_1x_2 and x_1x_3 are in the range of 0.01~0.05, so they have a significant effect on the η value, while the *p*-value of the interaction term x_2 1 is >0.05, so it does not have a significant effect on the η value. After removing the non-significant factor, the second-order response model was constructed according to the results of regression analysis and analysis of variance and is shown in Equation (10).

The regression model for chestnut picking efficiency demonstrated high statistical significance, as evidenced by the extremely low **p**-value (<0.0001) of the model and the non-significant lack of fit (**p** = 0.0699). The coefficient of determination (R^2) was calculated to be 0.992, indicating that the model explains 99.2% of the variability in the pickup rate. Additionally, the adjusted R^2 value of 0.981 confirms the model's adequacy and reliability in predicting the harvesting performance under the tested parameter ranges. These statistical metrics collectively validate the robustness of the second-order regression model and its suitability for optimization within the defined factor space.

The second-order response regression model of the chestnut bud picking rate was obtained by fitting the data in in Table 7 using the Design Expert 8.0.6 software system, as shown in Equation (10), and variance analysis was carried out on them individually, as shown in Table 7.

$$\eta = 90.10 - 0.63x_1 + 0.38x_2 + 0.50x_3 - 1.75x_1x_2 - 0.50x_1x_3 - 1.00x_2x_3 - 3.18x_1^2 - 1.18x_2^2 - 1.92x_3^2 \quad (10)$$

According to the results of the variance analysis of chestnut bud harvesting efficiency in Table 8, the *p* value of the regression model is less than 0.01, indicating that the regression

model is extremely significant, and the p values of the model mismatch items are all less than 0.05, indicating that these items are not significant. That is, the proportion of abnormal errors in the actual fit is small, indicating that the regression equation is well fitted with the test value and the test error is small. The effects of various factors on the harvest efficiency of chestnut bracts can be ordered from large to small as follows: the rotation speed of the pickup drum, the forward speed, and the length of the pickup drum front claw. The effect of various factors on the chestnut bud pickup rate can be ordered from large to small as follows: the speed of the pickup drum and the length of the pickup drum claw.

Table 7. Multi-factor test results.

Test No.	Factors			Response Value
	x_1/rpm	x_2/m/s	x_3/mm	η/%
1	60.00	0.40	45.00	87.9
2	45.00	0.40	55.00	90.5
3	45.00	0.40	55.00	89.8
4	60.00	0.30	55.00	87.4
5	45.00	0.40	55.00	90.2
6	30.00	0.40	45.00	85.1
7	45.00	0.50	65.00	88.2
8	60.00	0.40	65.00	84.1
9	45.00	0.30	65.00	88.1
10	45.00	0.30	45.00	86.3
11	30.00	0.50	55.00	88.2
12	30.00	0.40	65.00	86.1
13	45.00	0.50	45.00	88.3
14	30.00	0.30	55.00	85.1
15	60.00	0.50	55.00	83.2
16	45.00	0.40	55.00	89.9
17	45.00	0.40	55.00	90.1

Table 8. Results of regression analysis and analysis of variance of throwing efficiency.

Source	Sum of Squares	df	*F*-Value	*p*-Value
Model	93.43	9	13.09	<0.0001 **
x_1	3.12	1	3.94	0.0007 **
x_2	1.13	1	1.42	0.0002 **
x_3	2.00	1	2.52	0.0231 *
x_1x_2	12.25	1	15.45	0.0455 *
x_1x_3	1.00	1	1.26	0.0101 *
x_2x_3	4.00	1	5.05	<0.0001 **
x_1^2	42.44	1	53.53	0.1746
x_2^2	5.81	1	7.33	0.0084 **
x_3^2	15.60	1	19.68	<0.0001 **
Residual	0.76	7		
Lack of fit	0.61	3	5.33	0.0699
Pure error	0.15	4		
Cor total	36.92	16		

Note: ** indicates extremely significant ($p < 0.01$); * indicates significant ($0.01 < p < 0.05$).

Using Design Expert software, the interaction response surface of three test factors on soil throwing efficiency test indexes was obtained. The relationship between any two factors and test indexes was separately studied to determine the influence of these factors on the indexes using the dimension reduction method. When studying two factors, the other factors were set to zero as default. The interactive response surface is shown in Figure 10.

(3) Effect of interactive factors on efficiency of chestnut bract harvesting

Figure 11a shows the interaction between the speed of the pickup drum and the forward speed when the length of the pickup drum claw is at the base level (155 mm). It can be seen from Figure 11a that with increases in the forward speed and pickup drum speed, the efficiency of chestnut bract harvesting first increases and then decreases [12]. This is because when the speed of the pickup drum is at a maximum, the chestnut pickup machine runs too slow, and there are no surplus chestnuts to pick up on the ground. Even if the speed of the pickup drum increases, the number of chestnuts collected will not increase, so this will not significantly improve the pickup rate. When the rotation speed of the pickup drum reaches a minimum, the forward speed of the chestnut pickup is much higher than this rotation speed, and the chestnut pickup device has completed its run before it has completely picked up all chestnuts. Therefore, with an increase in the speed of the rotary tillage pickup drum, the chestnut pickup speed should be correspondingly increased to improve the pickup efficiency. The efficiency of chestnut bud harvesting is highest when the speed of the pickup drum is 45 r/min and the forward speed is 0.4 m/s.

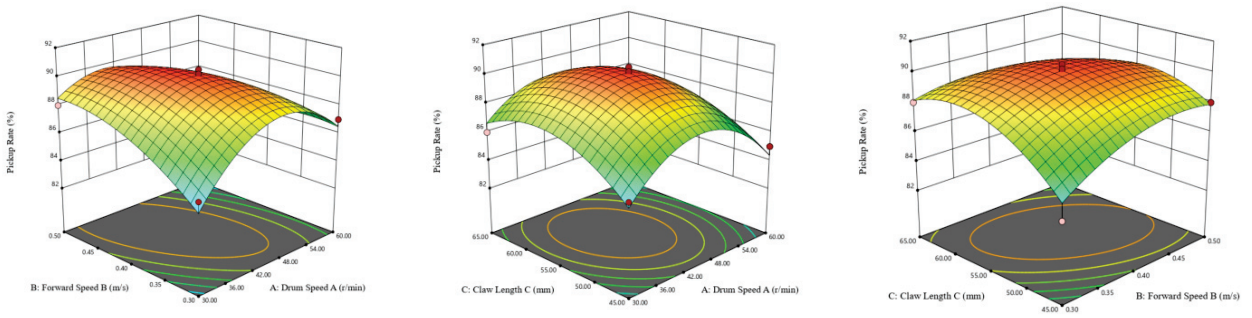

(**a**) Influence of the pickup drum and forward speeds on the pickup rate

(**b**) The influence of the drum speed and drum claw length on the pickup rate

(**c**) The influence of the forward speed and pickup drum claw length on the pickup rate

Figure 11. Response surface.

Figure 11b shows the interaction effect of the pickup drum speed and the pickup drum claw length when the forward speed of the chestnut pickup is at the base level (0.4 m/s). As shown in Figure 11b, with increases in the pickup drum speed and the drum claw length, the chestnut bud harvesting efficiency first increases and then decreases; with an increase in the pickup drum speed, the pickup efficiency decreases. The reason for this trend in the response surface is that when the speed of the pickup drum increases, the contact time between the chestnut and the pickup drum claw decreases, and an increasing number of chestnuts are not picked up and are splashed around, rather than thrown into the chestnut collection box, resulting in a reduction in the pickup efficiency. Therefore, when the speed of the rotary tillage pickup drum is increased, the chestnut pickup claw length should also be correspondingly increased to improve the pickup efficiency. When the pickup drum speed is 45 r/min and the drum claw length is 55 mm, the chestnut harvest efficiency is at a maximum.

Figure 11c shows the effect of the forward speed and the length of the pickup drum claw on the pickup efficiency when the pickup drum speed is at the base level (45 rpm). With an increase in the forward speed, the pickup efficiency first increases and then decreases. This is because when the traveling speed of the chestnut picker is too low, the chestnut and the pickup drum claw will slip instead of engage, resulting in a large number of chestnuts that are not collected and thus reducing the efficiency of chestnut picking [14].

When the traveling speed of the chestnut picker is too high, some chestnuts collide with the claws of the pickup drum and cannot be moved into the chestnut collection box, resulting in a reduction in pickup efficiency [15].

Referring to the standards and technical requirements of nut harvesters, the multi-objective variable optimization method was adopted in order to achieve the optimal pickup performance (a high harvesting efficiency and picking rate), considering the chestnuts harvester's actual performance and operating parameters. The optimization constraint conditions are shown as Equation (11):

$$\eta = \begin{cases} f(\mathbf{X})_{max} \\ \mathbf{X} = [x_1\ x_2\ x_3] \\ x_1 \in [30, 60] \\ x_2 \in [0.3, 0.5]\mathbf{m/s} \\ x_3 \in [45, 60]\mathbf{mm} \end{cases} \tag{11}$$

Using the optimization function provided in Design Expert software, the optimal parameter combination of all influencing factors was sought based on maximizing the harvesting efficiency. The optimal solution is as follows: a pickup drum speed of 40 R/min, a forward speed of 0.4 m/s, and a pickup drum claw length of 55 mm. Under these conditions, the chestnut picking rate predicted by the model is 90.2%.

(4) Results and analysis of field validation tests:

The working effect of the chestnut pickup is shown in Figure 11, and the results of field verification tests are shown in Table 9.

Table 9. Result of field validation tests.

Sample Number	1	2	3	4	5
Total number of chestnut bracts in the collection box/pcs	17.2	19.5	18.8	17.5	17.9
Total number of scattered chestnut bracts in the test area/pcs	2.25	2.55	2.46	1.82	2.35
Pickup efficiency/%	86.92	86.92	86.91	89.60	86.87
Average value/%			87.45		

The average chestnut picking rate was 88.44%. Compared with the simulation results, the relative error was 2.97% (less than the allowable threshold of 3%), verifying the correctness of the simulation model. In the actual test, the measured recovery efficiency was slightly lower than the simulated value. The main reason for this may be the assumption of an ideal operating efficiency of the picking device in the simulation model (i.e., set at 100%). In the actual harvesting process, not all chestnuts were successfully captured by the picking device, and some small-sized fruits were not harvested and remained in the field, shown in Figure 12. In addition, although the simulation model considers that some mixed chestnuts with a low quality will be returned to the field, there may be differences between the actual recovery standard and the simulation model. This is another reason for the deviation between the simulation and the measured data. However, by multiplying the picking efficiency of the chestnut picker, as determined by the constructed second-order response model, by δ, the average chestnut recovery was 90.13%.

Despite the close agreement between simulation and field results (error $\approx$ 1.95%), minor discrepancies can be attributed to several factors that were not modeled in the simulation. First, the adhesion of moist soil and chestnut bracts to the claw surfaces—especially under the humid conditions in the field—increased the operational resistance and slightly

reduced the actual pickup efficiency. Second, the high-frequency vibrations of the drum claws during operation, caused by uneven terrain and dynamic loads, led to occasional fruit bouncing or misalignment, which were not fully captured in the quasi-static simulation environment. Finally, variations in fruit orientation, minor soil compaction differences, and the real-time wear of the HDPE claw tips could have contributed to the marginal reduction in field performance compared to the idealized model.



Figure 12. Working effect of the chestnut picker.

(5) Robustness under variable environmental conditions

A robust harvesting device performance under varying environmental conditions, such as varying soil moistures and fruit sizes, is crucial for practical application. In this study, field tests were conducted under relatively stable soil moisture conditions (12–35%) and with a defined chestnut size distribution (Table 3). The close agreement between simulation and field results under these conditions demonstrates the model's validity within the tested range. However, it is acknowledged that a higher soil moisture could increase adhesion between the chestnut bracts and the claw surface, potentially elevating the operational resistance and slightly reducing the pickup efficiency. Similarly, although the DEM model incorporates a representative size distribution, extreme outliers or morphological variations not captured in the simulation could influence the actual picking and debracting dynamics. Structural and parametric optimizations—particularly the penetration angle (δ) and claw geometry—were performed to balance performance across the expected operational ranges. Future work should explicitly evaluate the device's sensitivity to a wider spectrum of moisture levels, soil types, and fruit characteristics to fully characterize its robustness and adaptability across diverse harvesting scenarios.

(6) Adaptability verification and vibration response analysis on concave/convex terrain

In order to verify the performance of the equipment in real hilly terrain, we conducted a comparative test in the experimental field with clear fluctuations (maximum height difference of about 12 cm). Vibration data was collected using the three-axis acceleration sensor (model: imu-icm20948) installed at the root of the spiral tooth.

The test results show that the dominant frequency of spiral tooth vibrations is 6–12 Hz on concave/convex terrain, which is basically consistent with the simulation results. Although the vibration was intensified, the fruit damage rate increased from 2.1% to 3.4% due to the presence of a damping structure; this is still within the acceptable range (<5%). At the same time, the picking efficiency decreased from 88.44% on flat terrain to 85.12%, a decrease of 3.32%, indicating that terrain fluctuations have a certain impact on the continuity of operation, but the overall operation ability remains high.

The results show that the spiral tooth structure and vibration reduction measures designed in this study can be effectively adapted to typical hilly and convex terrain, exhibiting good applicability.

5. Conclusions

The aim of the lightweight, simplified chestnut pickup device, an innovative solution for hilly areas, is to solve the problems related to the high fruit damage rate, poor terrain adaptability and low impurity separation efficiency of mechanized chestnut harvesting in hilly areas.

Based on the discrete element method (DEM) and RecurDyn display dynamics software, a chestnut particle model and a simplified mechanical simulation model of the pickup were established according to the structure and working principle of the pickup device.

Through theoretical analysis, combined with single- and multi-factor simulation experiments based on DEM and RecurDyn coupling, we proposed a set of improved working parameter combinations. In this process, theoretical calculation and single-factor simulations help to determine reasonable ranges of values for each influencing factor. It should be noted that this result is based on the settings and assumptions of the current model, and the model still needs to be further verified in practical application under specific working conditions. Using the optimal ranges of influencing factors, as determined by theoretical calculation and single-factor tests, a multi-factor test was carried out to establish a pickup efficiency model. Based on this model and the boundaries of the influencing factors, a combined optimization of working parameters was carried out. When the rotation speed of the drum of the chestnut pickup machine is 50 r/min, the forward speed is 0.4 m/s, and the claw length is 55 mm, operation is optimal, with the picking efficiency reaching the maximum value of 90.2%. These results verify the performance and feasibility of the chestnut pickup device and contributes to research and development.

Field verification tests were carried out to verify the accuracy of the simulations and the working effect of the chestnut pickup device under the optimal parameter combination. The error between the field validation test results (88.44%) and the simulation results is 1.95% (<3%). The proposed chestnut pickup machine has an improved chestnut recovery effect and a higher efficiency. The simulation model of chestnut pickup efficiency based on DEM–RecurDyn is accurate and reliable.

Scalability and adaptability of design: The portable chestnut-harvesting device proposed in this study has considerable potential regarding scalability and adaptability to other nut crops. The modular design of the pickup drum allows for dimensional adjustments to accommodate larger machine configurations or different nut sizes and weights. For example, by changing the roller or the roller and forward speeds according to the characteristics of the target crop (such as hazelnut, walnut or hickory), the same operating principle and simulation method can be applied. In addition, the DEM–RecurDyn simulation framework established in this paper provides a general tool for parameter optimization under different working conditions. Future research will focus on verifying the performance of the device under different terrains and crop types to enhance its applicability in a range of agricultural systems.

Based on its comprehensive performance, HDPE was initially selected as the material for the pickup drum device; however, systematic research on the effect of the material and shape of the device on the chestnut picking efficiency was not considered. The results showed that the friction between this material and chestnuts was directly related to the operational resistance and fruit damage rate. Future research will focus on optimizing the material composition and surface characteristics of the picking apparatus, and comparative research on claw teeth with different geometric shapes will be carried out in order to further improve the picking efficiency and reduce fruit damage. This will further enrich the knowledge on chestnut harvesting.

Future work will focus on the following: integrating autonomous mobile platforms into the harvester for fully unmanned operation, developing adaptive control systems that

can dynamically adjust drum speed and forward velocity based on real-time fruit detection and terrain feedback, and extending the simulation framework to account for variable soil and crop conditions and to extend its applicability.

While the simulation model proposed in this study was successfully validated and a high picking efficiency was demonstrated, it is acknowledged that field validation was conducted on essentially flat ground. This limits the immediate generalizability of the results to the complex terrain found in hilly areas. The performance of the harvester on slopes and uneven ground requires further investigation. Subsequent research will focus on evaluating the device across a wider range of topographic conditions to more comprehensively verify its adaptability and to refine its design for universal application in hilly and mountainous orchards.

In this study, the influence of the material and shape of the pickup drum device on the chestnut picking efficiency was not considered. Relevant research will be carried out to further improve and enrich the knowledge on chestnut harvesting.

6. Practical Implications

In terms of operational feasibility and economic potential, the portable chestnut harvester demonstrates promise for practical adoption. Based on field validation tests under optimal parameters (a drum speed of 45 rpm, a forward speed of 0.4 m/s, a claw length of 55 mm), the device achieved an average picking efficiency of 88.44%, with the potential to harvest chestnuts over an estimated area of 0.8–1.2 hectares per day depending on the terrain and tree density. This represents a significant improvement over traditional manual harvesting, which typically requires 3–4 laborers to achieve the equivalent daily output. By reducing the reliance on manual picking, the device can lower labor costs by approximately 60–70% and reduce harvest time by nearly 50%, providing small- and medium-scale farmers in hilly regions with an economically viable and scalable mechanization solution. Future commercialization efforts should focus on optimizing production costs and offering flexible acquisition models, such as rental or cooperative ownership, to enhance accessibility.

This study not only validates the operational effectiveness of the lightweight chestnut-harvesting device but also highlights the significant practical implications for manufacturers and farmers. The simplified structural design reduces manufacturing costs, making it economically viable for small-scale farmers, while the use of durable materials such as high-strength polyethylene (HDPE) enhances the device's longevity and reduces maintenance frequency, which is crucial for remote hilly areas with limited technical support. Furthermore, its compact and modular design allows for easy adaptation to various orchard types, including narrow terraces and sloped plantations commonly found in Northeast China. The device's high picking efficiency (over 88%) and low damage rate also help improve the overall economic return per unit area, offering a promising solution for mechanized nut harvesting in regions with challenging terrain.

Safety Considerations

The operational safety of the portable chestnut harvester is of paramount importance, particularly given the presence of rotating components and the device's intended use in varied terrain. Several key safety measures have been integrated into the design to mitigate potential hazards:

Rotating Drum and Claws: The pickup drum, comprising arc-shaped claws, rotates during operation and presents a potential entanglement or impact hazard. To address this, a rigid protective cover plate (Component 1 in Figure 1) is included to fully enclose the drum except for the ground-engaging section. This design prevents operator contact with moving parts during normal use and prevents the ejection of debris.

Pinch Points and Guards: The areas between the rotating drum and the fixed frame, as well as the drive connections from the DC motor, have been identified as pinch points. These areas are shielded by the structural frame and motor housing. The integrated controller also includes a dead man's switch, and thus continuous operator presence is required for the drum to remain active.

Operator Training and Manuals: Comprehensive operational manuals emphasize safe practices, including wearing closed-toe shoes, keeping hands and feet clear of the pickup assembly, and avoiding operation on excessively steep slopes where stability could be compromised. The simple control interface, featuring a prominent emergency stop button, further enhances operational safety.

Emergency Stop and Power Management: The lithium battery power system is coupled with an instantaneous braking circuit for the DC motor. Activating the emergency stop cuts power to the motor, halting drum rotation within seconds and thereby providing a critical safety function in unexpected situations.

These integrated safety features, combined with a clear instruction manual, ensure that the harvester can be operated with minimal risk, making it suitable for use by a broad range of users in the challenging environments of hilly nut plantations. Compliance with agricultural machinery safety standards has been a guiding principle throughout the design process [32].

Author Contributions: Conceptualization, D.R. and W.H.; methodology, D.R., W.H. and Z.Z.; software, R.W. and Z.Z.; validation, G.L., R.W. and Z.Z.; formal analysis, W.W. and R.W.; investigation, R.W., D.R. and W.W.; resources, W.W.; data curation, R.W. and Z.Z.; writing—original draft preparation, R.W.; writing—review and editing, D.R. and W.H.; visualization, R.W.; supervision, D.R.; project administration, W.W.; funding acquisition, R.W. All authors have read and agreed to the published version of the manuscript.

Funding: This work was supported by the Liaoning Provincial Department of Education Project: Development of Mountain Forest Lightweight Nut Intelligent Harvesting Equipment (JYTYB2024023); their support is greatly appreciated.

Data Availability Statement: The original contributions presented in this study are included in the article. Further inquiries can be directed to the corresponding author.

Conflicts of Interest: The authors declare no competing interests. The references included are relevant to the content presented.

References

1. Yue, P.F. *Optimal Design of Self-Propelled Chestnut Harvester*; Huazhong Agricultural University: Huazhong, China, 2022. [CrossRef]
2. Song, B. *Design and Test of Traction Shaking Chestnut Harvester*; Huazhong Agricultural University: Huazhong, China, 2024. [CrossRef]
3. Chen, B. Design and application of automatic cleaning electric chestnut picking equipment. *Hebei Agric. Mach.* **2024**, *9*, 7–9. [CrossRef]
4. Wang, C.G. *Design and Performance Test of Mountain Chestnut Pickup*; Hebei Normal University of Science and Technology: Qinhuangdao, China, 2023. [CrossRef]
5. Wu, W.J. A Chestnut Harvester. CN201810196144.7. 15 June 2018. Available online: https://kns.cnki.net/kcms2/article/abstract?v=ldCk9GscAdCoZB-f58pobBSchF5NshwL49hZd9BzYzCEi-5fgNFEyMlEvxpcQJYzKpvM9KBzDJwzYxEUQl00riI-ilGdZ532veRLOe9tEBFQyOY_Joe6t6c-SNwaFSXuYTrUN-3Ov2IGiIY1FpS8caffS1IvPvH2veC_biG9IpwJLOoDq5uPNAeVJV4hVpyl9OixhBTZl4k=&uniplatform=NZKPT (accessed on 5 November 2025).
6. Shi, G.K.; Ma, S.H. Design and test of air suction jujube picker. *Agric. Eng.* **2014**, *4*, 109–112.
7. Lu, M.; Wang, C.; Wang, J.; Duan, H.; Sun, Y.; Chen, Z. Delta Omnidirectional Wheeled Table Tennis Automatic Pickup Robot Based on Vision Servo. In Proceedings of the 10th International Conference on Computer Engineering and Networks (cenet2020), Xi'an, China, 16–18 October 2020; pp. 556–561.

8. Han, Y.J.; Xie, J.H.; Yang, Y.X.; Zhao, Y.Y.; Hong, J. Design and test of pick-up mechanism of nail tooth rolling film residue recycling machine. *Res. Agric. Mech.* **2021**, *43*, 73–78. [CrossRef]
9. Zhu, C.K.; Li, F.X.; Zhang, J. Design and test of sawtooth rolling type residual film recycling machine. *China J. Agric. Mach. Chem.* **2021**, *42*, 25–30. [CrossRef]
10. He, H.; Wang, Z.; Guo, L.; Zheng, X.; Zhang, J.; Li, W.; Fan, B. Distribution characteristics of residual film over a cotton field under long-term film mulching and drip irrigation in an oasis agroecosystem. *Soil Tillage Res.* **2018**, *180*, 194–203. [CrossRef]
11. Sari, D.Y.; Nurdin, H.; Yufrizal, A. The Use of MATLAB in Learning the Velocity Analysiswith Relative Velocity Method on Slider Crank Mechanism. *J. Phys. Conf. Ser.* **2021**, *1940*, 012078. [CrossRef]
12. Xie, J.H.; Zhang, F.X.; Chen, X.G.; Han, Y.J.; Tang, W.D. Desgin and parameter optimization of arc-shaped toothed rolling residual film recycling machine. *J. Agric. Eng.* **2019**, *35*, 26–37. [CrossRef]
13. Ran, J.; Zhigu, A.P.P. *Practical Manual of Agricultural Machinery*; Tongfang Zhiwang (Beijing) Technology Co., Ltd.: Beijing, China, 2018. [CrossRef]
14. Zhang, F.K.; Ran, J.H.; Li, Z.J.; Wang, D.W.; Li, P. Optimization of Operating Parameters for Air-suction Floor-type Red Date Picker. *J. Fruit Tree* **2021**, *38*, 1190–1200. [CrossRef]
15. Zhang, J.G.; Cui, Y.C.; Chen, L.; Dong, H.J.L.; Ma, L.H. Optimization of working parameters for the pickup mechanism of sweet sorghum straw baler. *Mod. Agric.* **2023**, *07*, 94–96.
16. Xu, T.; Liu, Z.X.; Gao, L.X.; He, F.Y.; Yang, D.X.; Li, H. Analysis and experiment on the picking dynamics of shovel-tooth and tooth-roller peanut picking device. *J. Shenyang Agric. Univ.* **2024**, *55*, 454–464.
17. Zhang, Z.Y. *Research on the Mechanism of Picking up and Recovering the Film Residue in the Seeding Layer Based on the Arc Toothed Roller*; Shihezi University: Shihezi, China, 2023.
18. Wang, Z.Y.; Chen, X.G.; Yan, L.M. Design and test of film picking mechanism of follow-up film recycling machine. *J. Agric. Mach.* **2021**, *52*, 80–90.
19. He, X.D.; Zhu, D.Q.; Zhu, J.J.; Liao, J.; Zhang, S.; Li, J.F. Design and test of two speed brush roller fruit cleaning machine. *J. Zhejiang Agric.* **2020**, *32*, 1702–1710.
20. Wang, C.X.; Ding, L.P.; Dou, F.L.; Kan, Z.; Li, F.N.; Li, J.B. Design and test of comb type ground jujube pickup device. *J. Shihezi Univ. (Nat. Sci. Ed.)* **2021**, *39*, 409–414. [CrossRef]
21. Ujis, G.; Liu, W.F.; Bao, N. Motion simulation of drum pickup. *Res. Agric. Mech.* **2010**, *32*, 50–53. [CrossRef]
22. Wang, X.N.; Chen, F.A.; Zhang, J.X.; Jiang, Y.X.; Niu, C.H. 3D design and motion simulation of residual film pickup drum based on SolidWorks. *Res. Agric. Mech.* **2007**, *4*, 47–48+83.
23. Lu, B. *Design and Experimental Research of Electric Self-Propelled Ground Jujube Cleaning Pickup*; Tarim University: Alar, China, 2017.
24. Liao, Y.T.; Li, Y.T.; Wan, X.Y. Design and test of gantry electric drive rape stalk harvester. *J. Agric. Mach.* **2022**, *53*, 147–159.
25. Li, J.Q. *Design and Test of Air Suction Hazelnut Picking and Sorting Machine*; Shenyang Agricultural University: Shenyang, China, 2022. [CrossRef]
26. Xu, T.; Gao, L.; Liu, Z. Spring-Finger Motion Law Analysis and Cam Slide Optimal Design of Spring-Finger Cylinder Peanut Pickup Mechanism. *Agriculture* **2024**, *14*, 1459. [CrossRef]
27. Ben Hazem, Z.; Fotuhi, M.J.; Bingul, Z. A Comparative Study of the Friction Models with Adaptive Coefficients for a Rotary Triple Inverted Pendulum. In Proceedings of the 2018 6th International Conference on Control Engineering & Information Technology (CEIT), Istanbul, Turkey, 25–27 October 2018; pp. 1–6. [CrossRef]
28. Cheng, H.; Huang, W.; Zeng, S.; Li, G.; Gong, Y.; Ren, D. Optimization of the thermoforming process for straw-based biodegradable materials through biological mechanical processing and simulation. *Mater. Today Commun.* **2025**, *43*, 111739. [CrossRef]
29. Cheng, H.T.; Zhao, N.; Zeng, S.P.; Huang, W.Y.; Gong, Y.J.; Ren, D.Z. Study on the selective degradation ability of lignin in rice straw driven by microorganisms based on BMP method. *J. Sol. Energy* **2024**, *45*, 485–493. [CrossRef]
30. Ren, D.Z.; Zhang, L.J.; Cheng, H.T.; Meng, J.; He, T.Y. *Calibration of Contact Parameters of Biochar Based on Discrete Element Method*; ASABE, SCI/EI; Shenyang Agricultural University: Shenyang, China, 2024; Volume 67, pp. 59–68.
31. Ren, D.; Bai, X.; Huangi, W.; Cheng, H.; Gong, Y.; Zhang, L.; Wang, W. Simulation Optimization of A Conveying and Soil-removing Device for a Corn Stalks Picking and Pelletizing Machine. *INMATEH—Agric. Eng.* **2022**, *68*, 32–40. [CrossRef]
32. Ren, D.Z.; Zhang, L.J.; He, T.Y.; Meng, J. Design and Test of Key Components of Biochar Return Machine Based on Rocky. *INMATEH—Agric. Eng.* **2022**, *68*, 608–616.
33. Huang, H.D. Design of a blockchain based agricultural machinery operation data security management system. *South. Agric. Mach.* **2025**, *56*, 143–145.

Disclaimer/Publisher's Note: The statements, opinions and data contained in all publications are solely those of the individual author(s) and contributor(s) and not of MDPI and/or the editor(s). MDPI and/or the editor(s) disclaim responsibility for any injury to people or property resulting from any ideas, methods, instructions or products referred to in the content.

agriculture

MDPI

Article

DEM Simulation and Experimental Investigation of Draft-Reducing Performance of Up-Cutting Subsoiling Method Inspired by Animal Digging

Peng Gao [1,2], Xuanting Liu [3], Zihe Xu [1,2], Shuo Wang [4], Mingzi Qu [5,*] and Yunhai Ma [1,2,*]

[1] The College of Biological and Agricultural Engineering, Jilin University, Changchun 130022, China; penggao15@mails.jlu.edu.cn (P.G.)
[2] Key Laboratory of Bionic Engineering, Ministry of Education, Jilin University, Changchun 130022, China
[3] School of Intelligent Mechatronics Engineering, Zhongyuan University of Technology, Zhengzhou 450007, China
[4] School of Mechanical and Vehicle Engineering, Bengbu University, Bengbu 233030, China
[5] School of Medicine, Jiangsu University, Zhenjiang 202013, China
* Correspondence: 1000005980@ujs.edu.cn (M.Q.); myh@jlu.edu.cn (Y.M.); Tel.: +86-0431-85095760-413 (Y.M.)

Abstract

Overcoming high draft forces has long been a primary challenge in conventional subsoiling. To better utilize this agronomically advantageous technique, it is necessary to substantially reduce the draft. Inspired by the digging behaviors of fossorial animals, a low-draft up-cutting subsoiling method was proposed in this study. Discrete element method (DEM) simulations were employed to study the draft-reducing performance of up-cutting tools compared with regular tools. The results showed that the up-cutting motion reduced the draft by 63.07%, 63.84%, and 58.92%, respectively, at rake angles of 45°, 60°, and 75%, and by 79.73%, 63.84%, and 45.22%, respectively, at advancement velocities of 0.5 m·s^{-1}, 1 m·s^{-1}, and 1.5 m·s^{-1}. An increase in up-cutting velocity reduces the draft. Soil disturbance, particle velocity distribution, and soil deformation and movement patterns change in ways that contribute to this reduction. The draft-reducing performance of a chain subsoiler developed based on the principle of soil-breaking by animal digging was verified using field tests, exhibiting a draft-reduction amplitude approaching or greater than 30%. This study shows the great application potential of the up-cutting method in reducing subsoiling drafts and provides a theoretical basis for future research.

Keywords: fossorial species; digging techniques; DEM simulation; draft-reducing; up-cutting; chain subsoiler

1. Introduction

For a subsoiler, the most significant aspect of the soil–tool interaction pertains to the soil-cutting procedure executed by a horizontally advancing tool (Figure 1). The high draft demand associated with this process has been a major constraint on the scale of its operation [1,2]. There is an urgent need to substantially lower the subsoiling resistance. This necessity is driven not merely by the motive to cut costs but also by the electrification and automation trends in agricultural machinery, along with the indispensable requirements for efficiency and safety [3].

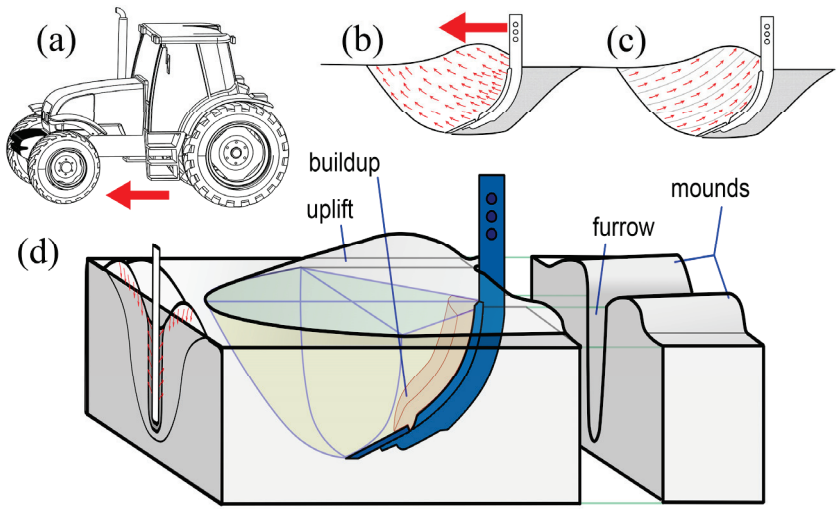

Figure 1. Interaction system between the soil and the tool: (**a**) the tractor advancing ahead; (**b**–**d**) the horizontally moving subsoiler, towed by the tractor, gives rise to soil disturbance and displacement. This interaction is depicted in terms of the earth coordinate system (ECS) and implement coordinate system (ICS); (**b**) elevation perspective as depicted by the ECS; (**c**) elevation perspective as depicted by the ICS; (**d**) three-dimensional soil disturbance.

Existing draft-reducing strategies mainly emphasize minimizing the friction and adhesion of the tool. Methods such as soil–tool interface lubrication [4,5] and using non-stick materials [6–8], biomimetic non-smooth surfaces [9–11], and vibration [12–14] have been extensively studied. These methods rest upon the presumption that soil that is in contact with the tool surface will always move along the tool surface (Figure 1c) [15,16]. However, because of the intrinsic constraints of the interface kinematics, when the tool surface is "synchronized" with the boundary wedge (a soil buildup hardly moves relative to the tool, Figure 1d) created by the soil in the failed state, the actual draft-reducing performance is weakened [17–20]. This is essentially because these methods fail to alter the patterns of soil failure and movement. To achieve a further reduction in the draft force, more radical strategies must be adopted to avoid soil clogging.

For many fossorial species, the intense demands of survival force them to be avid diggers. The intense digging behavior and sophisticated digging techniques of these "ecosystem engineers" have a huge impact on the ecology and environment [21,22]. These digging techniques mainly involve the control of digging tools to operate on the soil, as well as the soil reactions that result from such operations. Clearly, animals' digging movements are not accomplished through parallel movements of their claws (or other body parts), but rather by a combination of complex, compound movements [23–26]. Learning from their digging techniques can provide insights into the design of low-draft subsoilers. Integrating the useful aspects of these techniques into the design of subsoilers is likely to be the optimal solution to the challenge of overcoming high draft forces in subsoiling.

A special device configuration with surface components (or elements) moving upwards during horizontal motion appears to offer greater potential to reduce drafts, possibly sharing similarities with animal digging. This motion combination has been verified to be effective in reducing drafts through powered discs, where the draft force decreased by more than 30% compared with free-rolling discs [27–29]. The draft-reducing performance of this combination has also been demonstrated in many other types of tools [30–33]. Subsoilers are characterized as narrow-shaped implements working at a depth substantially greater than their width. To enable the aforementioned tool motion within such subsoiling depths, an up-cutting continuous belt, as defined by Mellor [30] and other researchers, can be utilized. When the rake angle of the up-cutting continuous belt is less than 90°, there exists

a high probability that it mimics the soil failure mechanism induced by animal digging. Previous research by the authors has tested a combination consisting of a subsoiler and an up-cutting motion [34]. Since the patterns of soil failure and movement change, the draft reduction is more than 50%.

However, the existing theoretical frameworks on continuous up-cutting devices (e.g., chain trenchers) fail to apply to the analysis of the subsoiling scenarios. This is due to the fact that the kinematic and dynamic analyses related to the continuous belt device pay insufficient attention to the soil failure ahead of the tool, let alone facilitate comparisons with the draft-reducing performance of conventional subsoilers [30–33]. Due to the lack of relevant research, explanations of the influencing factors and mechanisms of the draft force in up-cutting tools are incomplete. Therefore, this concept needs to be tested and further validated using more intuitive and accurate methods for draft-reducing ability.

Verifying the concept from a theoretical perspective using the discrete element method (DEM) and conducting tests with prototypes are appropriate choices for validating this concept. The DEM can effectively replicate the mechanical properties of granular materials [35,36] and avoid many drawbacks seen in experimental methods [37–39]. Its applicability and reliability have been widely verified [10,13,35,36,40–45], which serves as a guarantee for the successful theoretical analysis of up-cutting subsoiling. Designing and manufacturing prototype up-cutting tools and testing their draft-reducing performance and tillage quality under actual working conditions can make up for the deficiency of relevant machinery lacking practical applications in up-cutting subsoiling [30,32,33]. This provides valuable references and the most persuasive evidence for the feasibility of applying the above-mentioned concept to subsoiling.

This study aimed to explore an innovative method by which the draft force during subsoiling operations could be substantially reduced. To this end, this paper first elaborates on the principle of soil-breaking in animal digging and the concept of the up-cutting method. Subsequently, through discrete element method (DEM) simulations, a comparison was made between the soil-cutting models of up-cutting tools and conventional tools. Factors, such as the rake angle, advancement velocity, and up-cutting velocity, were considered, and their effects on the tool force, disturbance range, particle velocity distribution, soil deformation, and movement patterns were analyzed to reveal the draft-reduction performance and underlying mechanisms. Finally, field tests were conducted on a chain subsoiler designed and manufactured based on this principle to verify whether the up-cutting tools could significantly reduce the subsoiling draft and meet the quality requirements of subsoiling. This study provides enlightening insights regarding the reduction of the draft force in subsoiling. It also provides a theoretical basis for subsequent research, as well as scientific guidance for the application of a continuous up-cutting motion in subsoilers and other earth-moving devices.

2. Materials and Methods

2.1. The Principle of Soil-Breaking Inspired by Animal Digging

The general behavior related to animal digging is complex and random. However, a common feature of the digging behavior of many underground (or fossorial) species is the use of alternating patterns of soil-breaking and soil transport (Figure 2a) [22,23,25,46,47]. Their general digging behavior shows an alternating sequence of soil-breaking (scratch digging and chisel tooth digging) and the transport of soil (forelimb raking, hindlimb kicking, turn-around pushing, head-lift pushing, or shoveling). Scratch digging with the forelimbs is a typical soil-breaking motion.

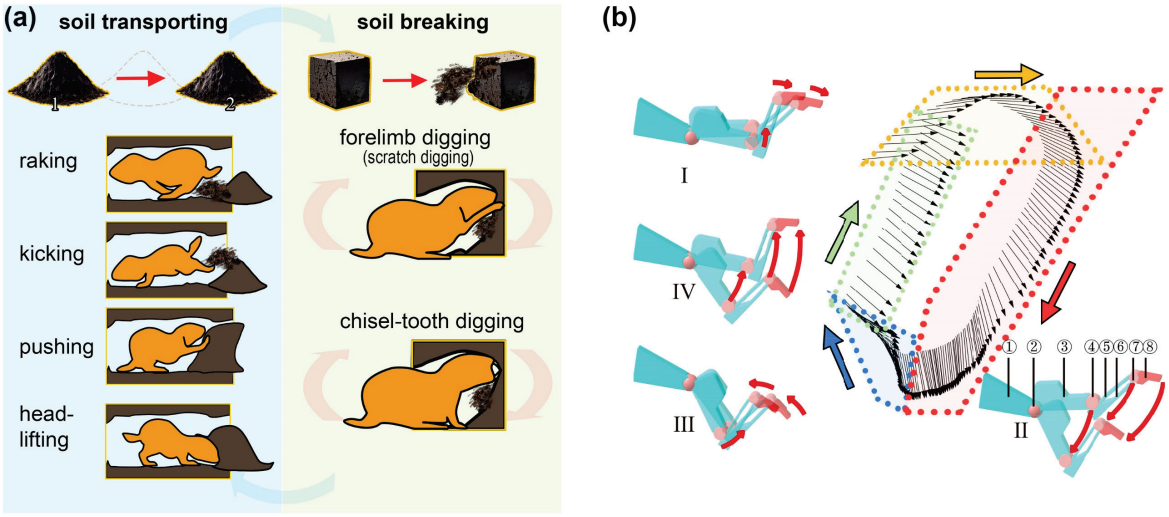

Figure 2. Schematic diagram of animal digging: (**a**) general digging behaviors; (**b**) four-phase cycle of forelimb digging: (center) pattern of motion of the claw (black arrows denote the posture of the claw segment; the trace of the arrow head denotes the trajectory of the claw tip). Four distinct forelimb motions occur in phases (I), (II), (III), and (IV). These are the phases of penetrating, cutting, retracting, and resetting, respectively. The labels (1–8) denote the anatomical parts of the forelimb corresponding to the (1) scapula; (2) shoulder joint; (3) humerus; (4) elbow joint; (5) radius; (6) ulna; (7) carpal joint; and (8) manus and claw.

Observation of the forelimb digging motions shows that each forelimb digging cycle can be summarized into four phases: penetrating, cutting, retracting, and resetting (Figure 2b) [48]. The forelimb digging cycle begins in the penetration phase (Figure 2b(I)), where the claws move forward to penetrate the soil, similar to the action of a curved hook piercing an object. Subsequently, it enters the longest cutting phase (Figure 2b(II)), where the claw tip begins to move along an almost straight trajectory below the ventral side of the sagittal plane, cutting the soil from the inside out. In the subsequent retracting stage, the entire forelimb begins to retract backwards and upwards from the soil (Figure 2b(III)). In the final resetting phase, the claws have detached from the soil, moved forward and upward, and returned to the vicinity of the initial penetration position, thus ending a single forelimb digging cycle (Figure 2b(IV)). The most important feature among these motions is the cutting direction from the inside out during the cutting phase. At the same time that the animal performs this motion, the affected soil separates from its original position, transforming from well-structured hard soil to loosened and fragmented soil, creating the necessary conditions for subsequent soil transportation. Then, animals will transport the soil in a timely manner during the digging process in order to reduce soil accumulation, lower the difficulty of subsequent digging, and ensure the smooth progress of digging work.

The main mechanical process of digging can be seen as a complex combination of penetration and cutting [49]. The interaction between simple flat tools when cutting soil in parallel can serve as the basis for understanding this process [15]. When a simple flat tool cuts the soil in parallel, the soil is mainly subjected to the force caused by the horizontal forward movement of the tool (Figure 3a). As a result, continuous compressive stress causes the deformation of the soil as well as forward displacement, which then accumulates in front of the tool. When the stress periodically exceeds the limit, repeated shear failure occurs (Figure 3a(s1)) [50]. Further movement of the tool will trigger a new failure process in front of the tool (Figure 3a(s2)).

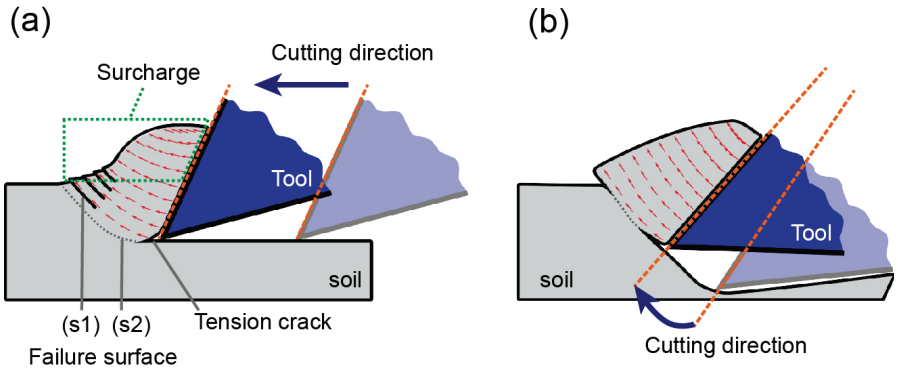

Figure 3. Schematic diagram of soil-cutting with simple tools: (**a**) parallel cutting produces new failure surfaces (s1) in front of the repeated shearing failure surfaces (s2), and the soil movement is mainly forwards; (**b**) cutting from the inside of the substrate to the outside (free surface) makes it easier to separate the soil.

However, when the tool moves outward from the inside of the substrate like a claw, the soil is subjected to tool forces mainly in an outward direction (Figure 3b). The direction of principal stresses is deflected toward the digging surface, producing tensile failure at the tool tip. Moreover, lower compressive stresses in the substrate are produced as the soil moves freely toward the free surface (digging surface) [16,34]. Tensile failure exploits the inherent weakness of the soil when subjected to tension [50], while shear in a low-stress state has been shown by critical-state soil mechanics to be the only condition that loosens the soil [19,51]. These two mechanical soil effects allow the soil to easily separate outward from the digging surface, avoiding non-essential periodic shear work and thereby reducing the force on the tool. Therefore, applying force from the inside of the soil to the outside may be an important factor that explains why animals have adopted these digging techniques in order to reduce labor.

The main process of subsoiling is similar to the forelimb digging motion of animals. The process of the horizontal movement of the subsoiler (Figure 3a) corresponds to the cutting phase in the digging cycle (Figure 2b(II)). The difference between the two is that animal claws cut the soil from the inside of the soil towards the outside of the free surface; the movement direction of subsoiling parallels the free surface of the undisturbed soil. Therefore, if the continuous cutting of the soil by the subsoiler can also make the soil movement move towards the outside of the free surface of the soil (Figure 3b), it can produce a similar effect as claw digging. This is difficult to achieve for a subsoiler that cuts soil through parallel motions, so it is necessary to change the structural design of existing subsoilers in order to apply the principle of animal digging to subsoiling.

The techniques of animal digging offer valuable ideas for studying the biomimetic design of subsoilers. Understanding the principles of these digging techniques and applying them to the design of subsoiling machinery potentially represents a more effective way of lowering the draft of subsoiling. This is also the main goal of the imitation of animal digging techniques. The key is to control how the tool moves in the soil and to make changes to the direction in which the tool applies force to the soil. This way, only a small force is needed to cause soil failure, thus greatly reducing the draft force in subsoiling.

The authors carried out DEM simulations of the tools, simultaneously executing both an up-cutting motion and a horizontal motion in the soil [34]. Preliminary results confirmed that such a tool–motion pattern induces the soil movement described above and effectively decreases the draft force encountered during soil cutting. In light of this, a more thorough and profound analysis regarding the concept was performed in the present study.

2.2. DEM Simulation of Up-Cutting Tools

The commercial software EDEM 2018 (DEM Solutions, Ltd., Edinburgh, UK) was employed to develop simplified models of up-cutting tools. Simulations were carried out on the soil failure process under different tools and operating conditions. The aim was to deeply analyze the mechanism by which the up-cutting motion reduces the draft force in subsoiling.

2.2.1. DEM Modeling

In the simulation, the tools were modeled as a series of simple, narrow tines. These tools could function directly as regular tools. When an up-cutting motion was added to their surfaces, they could also serve effectively as up-cutting tools (Figure 4a). The purpose of employing simple tool geometries in the analysis was to comprehensively understand the interaction between the soil and the tool moving in this manner. This understanding could then serve as the basis for a subsequent analysis of more complex conditions [6]. The tine geometries were defined using the following parameters: rake angle (α), width (w), and depth (d), where the width is 45 mm and the depth is 300 mm. Other settings relating to operation factors included the tool advancement velocity (v_t) and up-cutting velocity (u_t). The parameters were set according to the factors and levels in the subsequent experimental design.

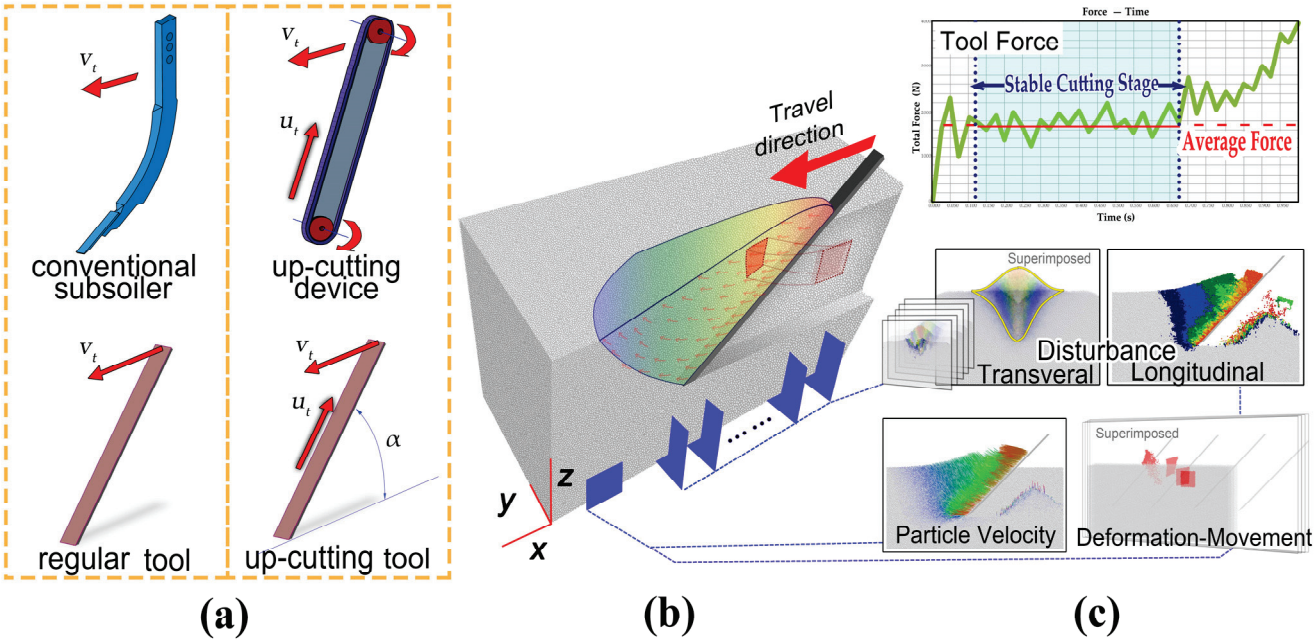

Figure 4. Modeling and simulation of soil-cutting operations: (**a**) the conventional subsoiler and the up-cutting device were modeled as a regular tool and an up-cutting tool using simplified tine models (rake angle α = 45°, 60°, and 75°; advancement velocity v_t = 0.5 m·s^{-1}, 1 m·s^{-1}, and 1.5 m·s^{-1}; up-cutting velocity u_t = 0.5 m·s^{-1}, 1 m·s^{-1}, and 1.5 m·s^{-1}); (**b**) schematic of the DEM model depicting the soil–tool interaction and the 3D soil failure induced by the tools; (**c**) the results obtained from the simulation, including the tool force, transversal and longitudinal soil disturbances, the particle velocity distribution, and soil deformation–movement patterns.

Based on simulation experiences, a soil bin model was employed to hold the soil (Figure 4b). Its length, width, and height were specified as 1100 mm, 650 mm, and 600 mm, respectively. These dimensions were sufficient to accommodate the soil disturbance generated by the tools and were adequate to allow the tools to be in a stable cutting state [15,44].

The tine model was placed within the symmetry plane of the soil bin according to the designated cutting operation parameters. A positive x-axial translational constraint was implemented on each tool to uphold a constant advancement velocity. For each up-cutting tool, an extra conveyor belt constraint along the front surface of the tool was established. The constraint enables the tool to perform the up-cutting motion (Figure 4a). In an effort to prevent any possible confusion, the coordinate system of the DEM model is explained as follows: the x-axis, y-axis, and z-axis correspond to the longitudinal, transversal (or lateral), and vertical directions, respectively (Figure 4b).

The soil–tool interactions were specified by particle, material, and contact parameters in the EDEM software. These modeling parameters were set with reference to published data, which have been verified to be reasonable. Studies have indicated that even when a particle size larger than the actual size is employed, a reasonable simulation can still be carried out [37]. Therefore, the particle model was set to 3 mm spheres, which significantly improved the computational efficiency under limited computational power. The material properties were specified by the parameters of density (ρ), Poisson's ratio (γ), and shear modulus (G). The Hertz–Mindlin non-slip contact model with Bonding was defined by parameters including the coefficient of restitution (e), friction coefficients (static μ_s and rolling μ_r), stiffness per unit area (normal $\overline{K_n}$ and shear $\overline{K_s}$), critical strength values (normal $\overline{\sigma}$ and shear $\overline{\tau}$), and bond disk scale (R_m). The parameter combination defines a rule for the interaction between 65 Mn steel and typical hardened black loamy soil (clay 9.6%, silt 44.0%, and sand 46.4%) [44]. The specific values are presented in Table 1.

Table 1. Model parameters and values specified in the EDEM software.

Category	Parameter	Value
Particle	Radius/mm	3
Material	Density of particle/(kg·m^{-3})	2620
	Poisson's ratio of soil	0.33
	Shear modulus of soil/Pa	1.02×10^8
	Density of steel/(kg·m^{-3})	7850
	Poisson's ratio of steel	0.3
	Shear modulus of steel/Pa	7.9×10^{10}
Interaction	Coefficient of restitution, soil–soil	0.53
	Coefficient of static friction, soil–soil	0.63
	Coefficient of rolling friction, soil–soil	0.42
	Coefficient of restitution, soil–steel	0.27
	Coefficient of static friction, soil–steel	0.54
	Coefficient of rolling friction, soil–soil	0.28
	Bond Normal Stiffness/(N·m^{-3})	5×10^7
	Bond Shear Stiffness/(N·m^{-3})	5×10^7
	Bond Normal Strength/(Pa)	21,680
	Bond Shear Strength/(Pa)	21,680
	Bonded Disk Scale	0.5

The simulations ran at appropriate time steps, with a Rayleigh time step set to 5.13×10^{-5} s and a fixed time step set to 2.57×10^{-6} s, which was 5% of the former. The total simulation duration was 1 to 2 s (depending on the advancement velocity).

2.2.2. Experimental Design of the DEM Simulation

In the simulation, the simple and intuitive one-factor-at-a-time (OFAT) method was adopted. Each time, only the level of one factor changed, while all other factors remained constant. By comparing the response values at different levels, the independent effect of

each factor was quickly verified (without considering the interactions between different factors on the response value for the time being). In addition, another purpose of using this experimental design was to explore the microscopic changes occurring in the soil medium when the response value (draft force) changed due to the variation of a single factor. Based on this, the mechanism by which the up-cutting motion reduces the draft force was analyzed.

As mentioned previously, the factors investigated in this study include the rake angle, the advancement velocity of the tool, and the up-cutting velocity. The settings of factors and levels are presented in Table 2. Rake angles of 45°, 60°, and 75° were set based on the inclination of subsoiler shanks. The advancement velocities were set at 0.5 m·s^{-1}, 1 m·s^{-1}, and 1.5 m·s^{-1}, in accordance with actual field subsoiling speeds. The up-cutting velocities, based on the ratio to the 1 m·s^{-1} basic advancement velocity, were set at 0.5, 1, and 1.5 (i.e., 0.5 m·s^{-1}, 1 m·s^{-1}, and 1.5 m·s^{-1}). When analyzing the variation of any factor, other factors were held constant: 60° rake angle, 1 m·s^{-1} advancement velocity, and 1 m·s^{-1} up-cutting velocity.

Table 2. Factors and levels in the simulation.

Level	Factor		
	Rake Angle (α)/°	**Advancement Velocity (v_t)/m·s^{-1}**	**Up-Cutting Velocity (u_t)/m·s^{-1}**
Low	45	0.5	0.5
Medium	60	1	1
High	75	1.5	1.5

In addition, based on the above parameter combinations, the up-cutting velocity was set at 0 m·s^{-1} for the purpose of simulating the process of soil cutting by regular tools. The purpose was to compare the performance differences between up-cutting tools and regular tools under different parameter combinations.

2.2.3. Measurements in the DEM Simulation

(1) Tool Force and Soil Disturbance

The tool force and soil disturbance are the two main aspects of evaluating the tool's performance. The magnitude of the tool force and the range of the soil disturbance increase as the tool advances, until the tool is in a stable cutting state [15]. Subsequently, they begin to exhibit periodic fluctuations within a relatively constant range, which is determined by the nature of the soil–tool interaction [15,44]. A complete failure boundary forms when the tool force is at its minimum [52], and the disturbance range at this moment is typical. In EDEM's Analyst module, during the stable cutting state, the tool force was acquired over a period of time. Then, the average values of the draft force (F_x) and vertical force (F_z) were calculated. Meanwhile, the soil disturbance was acquired specifically at the moment of the minimum tool force. The disturbed particles are shown in a color sequence (based on a particle velocity of 0–1 m·s^{-1}) to differentiate them from undisturbed particles. Then, cross-sections parallel to the y-z plane were captured at 50 mm intervals within the disturbance range (Figure 4b). These sectional images were superimposed using the "stack" function in ImageJ software (V.1.51J, National Institutes of Health, Bethesda, MD, USA) to acquire the transversal disturbance characteristics (Figure 4c). The image of the clip in the symmetry plane was captured to acquire the longitudinal disturbance characteristics (Figure 4b,c). The disturbances were quantified by the color sequence, and the disturbance profiles were mapped.

(2) Particle Velocity Distribution

The level of difficulty that the tool contends with during its advancement through the soil is reflected in the tool forces and soil disturbance. This aspect can be more precisely described through the velocity distribution of particles in the longitudinal section at the point of the minimum tool force. Consequently, to explain the mechanism of the tool–force change, the particle velocity distribution was analyzed.

Through the use of longitudinal disturbance images, analyzing the magnitude distribution of particle velocity became straightforward, since the particles were already color-coded according to velocity. By using color-coded particle motion velocity, the motion distribution characteristics of particles are represented by the motion trajectory of particles within 0.2 s. These trajectories are depicted by lines, with the color of each line representing the particle's motion velocity (where red indicates that the particle velocity is close to or exceeds 1 $m \cdot s^{-1}$, and dark blue indicates that the particle velocity is close to rest). At the same time, the length of the lines also represents the motion velocity of particles. The longer the lines, the greater the displacement of particles within 0.2 s.

(3) Deformation and Movement Patterns

With the advancement of the tool, the soil is subject to changes in shape and position [15,53]. The patterns of such deformation and displacement alter in response to changes in the kinematic conditions of the interface. Thus, to further elucidate the mechanism of tool–force variation, the longitudinal deformation and movement of the soil were analyzed in detail.

At the start of soil cutting, a square-shaped slice section in the symmetry plane, measuring 100 mm × 100 mm, was marked red. During the cutting process, images of the slice were captured at time intervals of 0.1 s, and then superimposed utilizing ImageJ. The red square section served to demonstrate the soil's deformation and displacement, with its changing positions and forms reflecting the movement of the tool.

2.3. Field Test

Based on the principle of up-cutting, a prototype of a chain subsoiler was designed and manufactured, and then field tests were carried out to verify if the draft performance of the chain subsoiler adopting the up-cutting principle could be improved and whether the tillage quality is fulfilled under field conditions.

2.3.1. Site and Equipment

The chain subsoiler consists of components such as the universal joint coupling, right-angle reducer, drive sprocket, driven sprocket, active and passive subsoiling sprockets, shank, tine, subsoiling chain, and cutting teeth (Figure 5). When the tractor travels, these components work together through a series of transmissions to drive the subsoiling chain to cut upwards, thereby loosening the soil (Figure 5a).

Although there were differences in the mechanical structures between the chain subsoiler and the standard conventional subsoiler, the external dimensions of the chain subsoiler were designed to be similar to those of the standard conventional subsoiler (Figure 5b). This design aimed to more effectively compare the differences in the resistance performance presented by the two due to their different operations.

In October 2024, the field tests were carried out in the agricultural experimental site of Jilin Agricultural University. This site location lies within the black soil region of northeast China. The soil is loam with a moisture content of 18%, a soil firmness of 300–500 kPa, and a bulk density of 1.32 $g \cdot cm^{-3}$, which is suitable for testing. A KUBOTA M704 tractor (KUBOTA Agricultural Machinery (Suzhou) Co., Ltd., Suzhou, China) was used to provide traction power. A field mechanical test system (Bona Science & Technology Co., Ltd.,

Harbin, China) (Figure 5d–f), designed for field experiments, was used to measure the draft force. This system dynamically measures the load attached to the equipment frame through sensors integrated on the three-point linkage and wirelessly transmits the measured data to a computer for storage. With a sensitivity of 0.045 kN, the upper limit of this system reaches 15 kN. Its maximum measurement range is 15 kN, and the sensitivity is 0.045 kN. In the control experiments, a standard subsoiler meeting the Chinese subsoiler standard JB/T 9788-2020, equipped with a medium-sized shank and a chisel tine, was adopted.

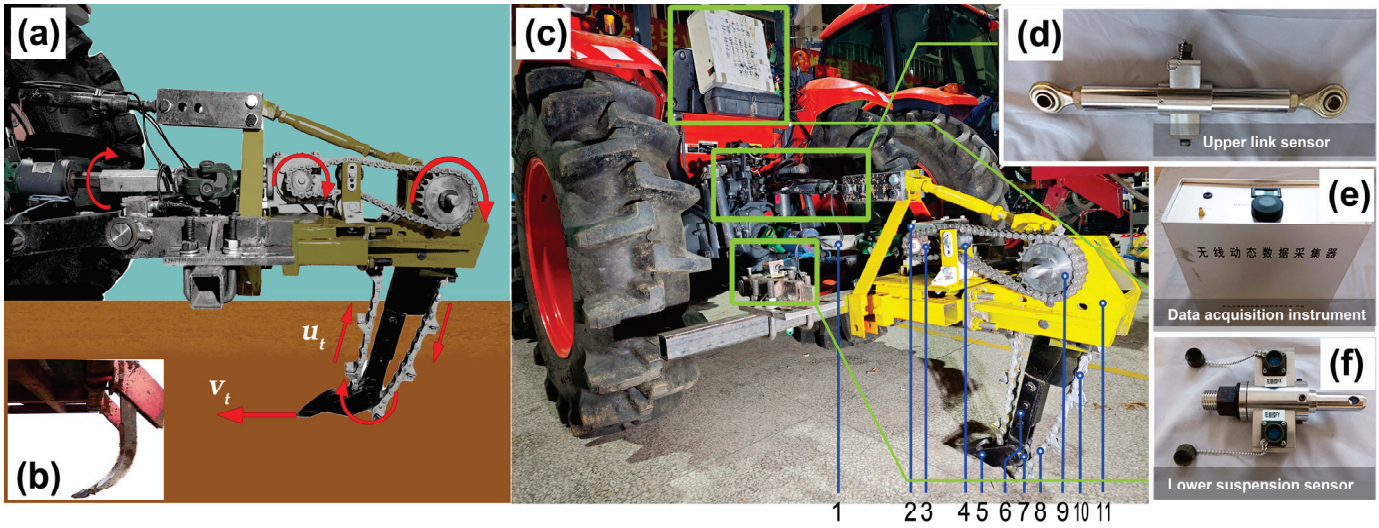

Figure 5. Equipment used in field tests: (**a**) chain subsoiler and its working principle; (**b**) conventional subsoiler for comparison; (**c**) structure and components of the chain subsoiler. The chain subsoiler consists of the following components: (1) universal joint coupling; (2) right-angle reducer; (3) drive sprocket; (4) carrier roller; (5) subsoiler tine; (6) shank; (7) passive subsoiling sprocket; (8) subsoiling chain; (9) driven sprocket; (10) subsoiling chain teeth; (11) frame; (**d**–**f**) components of the field mechanical test system: (**d**) upper link sensor; (**e**) data acquisition instrument; (**f**) lower link sensor.

2.3.2. Experimental Design of the Field Test

A comparison was made between the draft performance of the conventional subsoiler and the chain subsoiler. The tillage depth was set to 0.25 m, 0.35 m, and 0.45 m; the advancement velocity was set to 3 km·h^{-1}, and the rate of the rotation of the power take-off was set to 540 rpm (the corresponding linear velocity of the subsoiling chain was approximately 1.6 m·s^{-1}, which is the up-cutting velocity). These parameters were set by referring to the operational parameters of the conventional subsoiler in field practice, considering the tractor's power and safety.

2.3.3. Measurements in the Field Test

(1) Tillage Force Measurement

When the field tests started, the subsoiler was pulled through the starting zone (10 m), the measuring zone (50 m), and the decelerating zone (10 m) steadily in sequence. Throughout the process, the mechanical test system constantly monitored the draft force data. The data collected in the measuring zone were taken as valid data due to their relatively stable features. However, given that the force in the stable cutting stage fluctuates periodically, the resulting draft force for a single working condition was determined by the average value of three repetitions of one measurement in the stable cutting stage.

(2) Furrow Profile Mapping

Furrow profile mapping is an essential part of field tests and is necessary to verify the effect of soil disturbance. A furrow profile in the stable zone was selected and dug up

at three random spots. The shape of the soil disturbance was determined using a furrow profiler. The effect of the soil disturbance was represented by analyzing the profiles.

3. Results

3.1. Results of the DEM Simulation

3.1.1. The Effects of the Rake Angle and Up-Cutting Motion

The tool force, as affected by the rake angle, was revealed by the simulation, as depicted in Figure 6. During the increase in the rake angle from 45° to 60° (reference level), and then to 75°, the draft force of the regular tools (Figure 6a) increased from 1344.50 N to 1655.21 N and 2084.81 N, while the up-cutting tools obtained values of 496.457 N, 598.59 N, and 856.469 N, which were 63.07%, 63.84%, and 58.92% lower than the values of the regular tools, respectively. These results clearly demonstrate that the draft force is significantly reduced under the influence of an up-cutting motion, and this reduction is even more drastic with the increase in the rake angle. In addition to the draft force, the vertical forces of the tools (Figure 6b) also showed distinct characteristics during this process. The vertical force of the regular tools changed from −480.93 N to −286.18 N and −56.79 N, while the up-cutting tools obtained values of −529.36 N, −472.26 N, and −436.65 N, respectively, increasing by 10.07%, 65.02%, and 668.89% in terms of absolute values compared with regular tools. Although the downward vertical force increased, the increased vertical force level remained within the conventional range, which was reasonable and acceptable. Compared with regular tools, the up-cutting tools showed relatively gentle changes in vertical force and were always at a higher level. These results indicate that the downward vertical force tends to increase due to the up-cutting motion, especially under larger rake angles. The above-mentioned force change was closely related to the corresponding soil disturbance, particle velocity distribution, and soil deformation motion patterns.

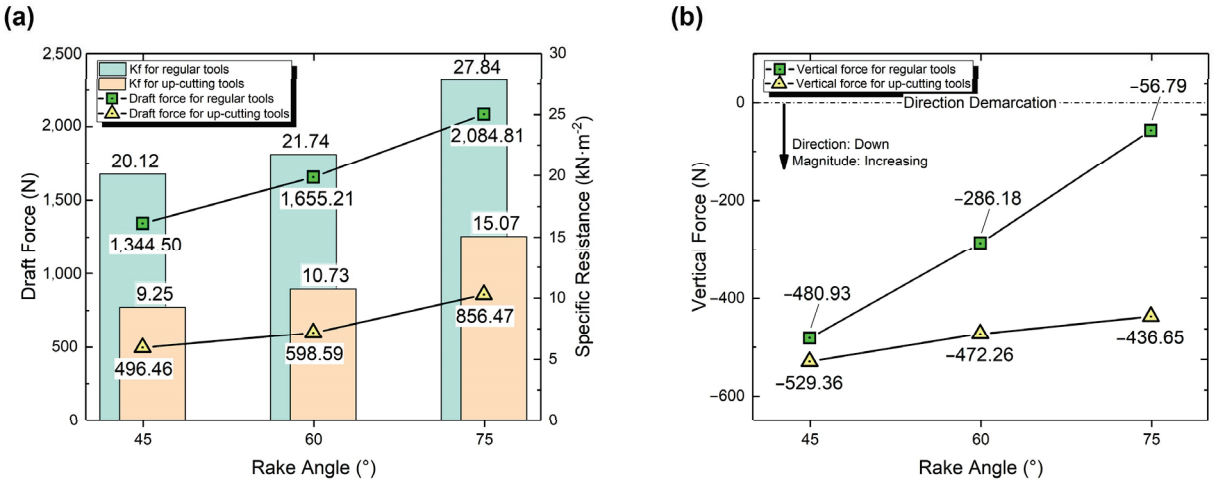

Figure 6. Tool force of regular tools and up-cutting tools affected by the rake angle (α = 45°, 60°, and 75°): (**a**) draft force and specific resistance; (**b**) vertical force.

The soil disturbance, as affected by the rake angle, was also shown by the simulation (Figure 7a). For both regular tools and up-cutting tools, there are two main types of disturbance: longitudinal and transversal. The longitudinal disturbance, presented in the main figure, exhibits a shape similar to an approximate triangular area. This area is enclosed by the tool surface, the soil failure surface, and the uplifted soil surface. Meanwhile, the transversal disturbance, shown in the sub-figure, is a composite of uplifted soil aboveground and an inverted triangular area underground. During the increase in the rake angle from 45° to 60° (reference level), and then to 75°, the disturbance characteristics of

regular tools and up-cutting tools showed similar trends. The shape of the longitudinal disturbance zone changed from a flat triangle to a narrow triangle, and the inclination of the failure surface increased. The height of the uplift, the distance of soil failure along the tool-moving direction, and the lateral disturbance area increased, but the longitudinal disturbance area decreased. These changes may be attributed to the fact that, as the rake angle increases, the soil changes from being mainly "lifted" to being more "pushed", resulting in the corresponding disturbance characteristics mentioned above. Compared with regular tools, up-cutting tools increased the height of the uplift. However, they reduced the transversal and longitudinal disturbance areas, the failure distance, and the disturbance width. In addition, the failure strip produced by up-cutting tools (the dark blue soil particle strip in the figure) was straighter. This may be because up-cutting tools exert a stronger upward force on the soil during operation. This enhances the "lifting" effect and weakens the horizontal compression in the soil.

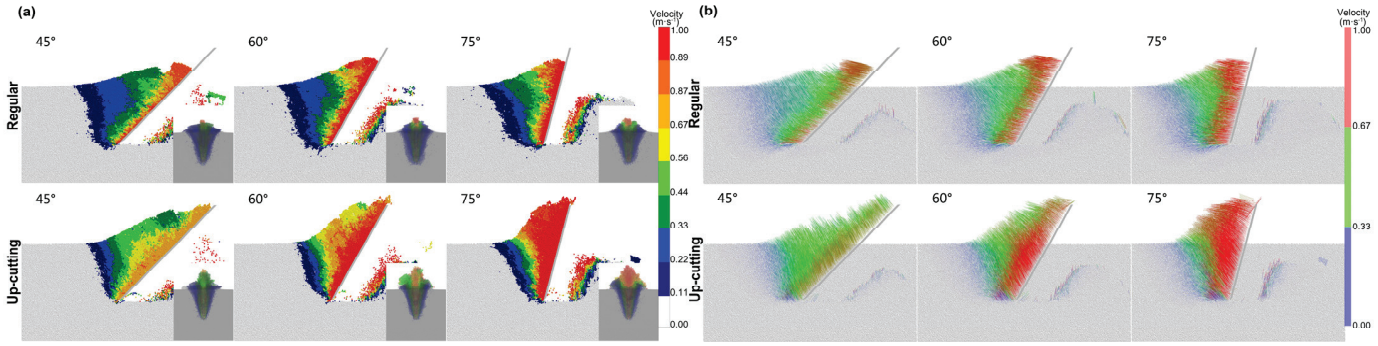

Figure 7. Soil disturbance and particle velocity distribution of regular tools and up-cutting tools affected by the rake angle (α = 45°, 60°, and 75°): (**a**) soil disturbance: the main figures depict a longitudinal disturbance profile (x-z), while the sub-figures in the lower-right corner show a superimposed view of the transversal disturbance profile parallel to the y-z plane; (**b**) particle velocity distribution: the magnitude and direction of particle velocity are represented by the particle's movement trajectory within a specified time, with the velocity of particle movement is color-coded.

Figure 6 also shows the value of specific resistance, which is calculated by dividing the draft force by the area of underground disturbance, as presented in Equation (1) [54].

$$K_f = \frac{F_x}{A_f} \tag{1}$$

where K_f represents the specific resistance (kN·m^{-2}) and A_f represents the area of underground disturbance.

As shown in Figure 6, with the increase in the rake angle, the K_f value of the regular tools increases from 20.12 kN·m^{-2} to 21.74 kN·m^{-2} and 27.84 kN·m^{-2}. However, the K_f values of the up-cutting tools are 9.25 kN·m^{-2}, 10.73 kN·m^{-2}, and 15.07 kN·m^{-2}, which are much lower than those of the regular tools. The specific resistance of subsoiling reflects the draft requirement of a subsoiler to cause a given area of underground disturbance (transversal). A decrease in specific resistance leads to an increase in subsoiling efficiency [44]. The results suggest an improvement in subsoiling efficiency in the case of up-cutting.

The disturbance of the soil by the tool is closely linked to particle movement. The simulation results (Figure 7b) clearly showed that the rake angle of the tool had a significant impact on particle movement. When the tool rake angle gradually increased from 45° through the reference value of 60° to 75°, the changes in particle movement characteristics induced by both types of tools exhibited similar trends: Near the tool surface, the horizontal component of the particle velocity increased, and the particle velocity increased, which are

both shown as long red lines in the figure. Near the failure surface, the particle velocity was relatively low for both types of tools, presented as short blue lines. In the middle transitional part of the disturbance zone, the particle velocity was at a medium level, indicated by green lines, and its movement direction was between that near the tool surface and that near the failure surface. These changes strongly demonstrate the transition of the soil's stress state from being mainly "lifted" to being more "pushed". Upon further comparisons between regular tools and up-cutting tools near the failure surface, although the particle movement direction of the up-cutting tool is deflected, the degree of deflection was small, and most particles move in an upward-sloping direction. The particle movement direction of regular tools was also deflected, but particles in the deeper part mainly moved horizontally forward, while those in the shallower part mainly moved upward at an angle. This difference indicates that the up-cutting tool strengthens the "lifting" effect and relatively weakens the "pushing" effect.

The deformation and movement of the square slices in the soil can be used to explain the changes in the forces exerted on the tools by the soil (see Figure 8). As the rake angle of the tools increased, under the action of both regular and up-cutting tools, the longitudinal compression of the slices intensified (became thinner longitudinally), and both the forward-pushing distance and upward-lifting height increased. However, compared with regular tools, the up-cutting tools made the slices thinner and caused forward rotation. In addition, the up-cutting tools lifted the slices to a greater height. This indicates that up-cutting tools can lift the soil upward, thus reducing the draft force. Notably, when the rake angle is small, up-cutting tools push the slice a shorter distance compared to regular tools. This indicates that the up-cutting motion can partially counteract the forward-pushing effect of the tools on the soil under such an angle.

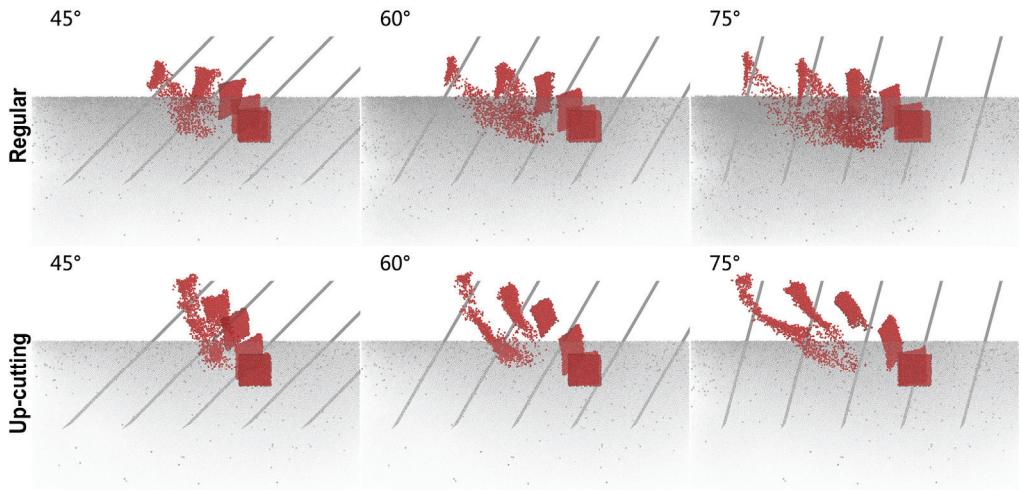

Figure 8. Soil deformation and movement patterns of regular tools and up-cutting tools affected by the rake angle (α = 45°, 60°, and 75°): the deformation and movement of the soil are represented by the changes in the shape and position of the square unit at different time steps. The gray strip-shaped geometric figures in the figure represent the tool geometry.

In summary, the changes in tool forces are partly attributed to the variations in the soil disturbance area, the redistribution in particle velocity, and the pattern alteration in deformation and movement. The increase in the rake angle transforms the effect of the tools from "cutting" to "pushing" [35,45,54]. This implies changes in both the direction of the tool's force on the soil and the direction of soil movement induced by these forces [1]. Consequently, the re-established soil equilibrium gives rise to an increase in tool force. However, the up-cutting motion modifies the disturbance area and particle velocity distribution, as well as the patterns of soil deformation and movement. It effectively mimics the

soil behavior resulting from the digging actions of animals. These changes all play a part in decreasing the draft force.

3.1.2. The Effects of Advancement Velocity and Up-Cutting Motion

The tool force, as affected by the advancement velocity, was revealed by the simulation, as depicted in Figure 9. During the increase in the advancement velocity from 0.5 m·s^{-1} to 1 m·s^{-1} (reference level), and then to 1.5 m·s^{-1}, the draft force (Figure 9a) of the regular tools increased from 1311.04 N to 1655.21 N and 2135.86 N, while the up-cutting tools obtained values of 265.79 N, 598.59 N, and 856.47 N, which were 79.73%, 63.84%, and 45.22% lower than those of the regular tools, respectively. It can be observed that as the advancement velocity increased, the draft forces of both regular tools and up-cutting tools showed an upward trend. Although both are increasing, the draft force of the up-cutting tools was significantly lower than that of the regular tools. Moreover, as the advancement velocity rose, the percentage difference of the draft force between the up-cutting tools and the regular tools gradually decreased. This indicates that with the increase in advancing velocity, the advantage of the up-cutting tools in reducing the draft force weakens. Meanwhile, the vertical force (Figure 9b) of regular tools varied from −260.27 N to −286.18 N and −335.79 N. The vertical force of up-cutting tools changed from −384.06 N to −472.26 N and −552.7 N. The absolute values of the vertical force of up-cutting tools increased by 47.56%, 65.02%, and 64.60%, respectively, compared with those of regular tools. This indicates that up-cutting tools reduce the draft force while increasing the vertically downward force. The advancement velocity is a key factor affecting both the draft and vertical forces of the tools. The two types of tools show consistent trends in force changes, but there are significant differences in force magnitude and reduction ratios.

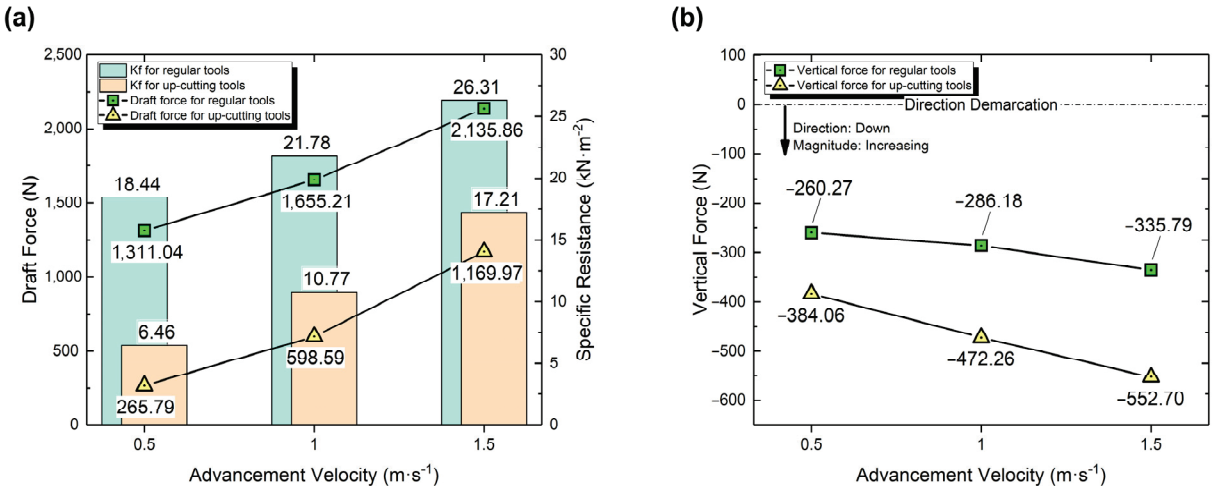

Figure 9. Tool force of regular tools and up-cutting tools affected by advancement velocity (v_t = 0.5 m·s^{-1}, 1 m·s^{-1}, and 1.5 m·s^{-1}): (**a**) draft force and specific resistance; (**b**) vertical force.

The effect of advancement velocity on soil disturbance (Figure 10a) can explain the changes in force. As the advancement velocity increased, the failure distance, transversal and longitudinal disturbance areas, and the width of both regular tools and up-cutting tools increased. This may be because the higher the advancement velocity, the greater the number of particles affected per unit time. Meanwhile, restricted by tool kinematics and surface friction, the upward movement of particles along the tool surface is limited. As a result, the effect of the tool can only be transmitted forward, which is one of the important causes of higher draft force. When the up-cutting tool advances forward, the soil in front is not only pushed but also lifted upward by the up-cutting motion, thus reducing the draft force. Compared with regular tools, up-cutting tools had a greater uplift height but

a smaller failure distance and transversal and longitudinal disturbed areas. This may be because the upward particle movement counteracts the pushing effect of the tool in deeper soil layers.

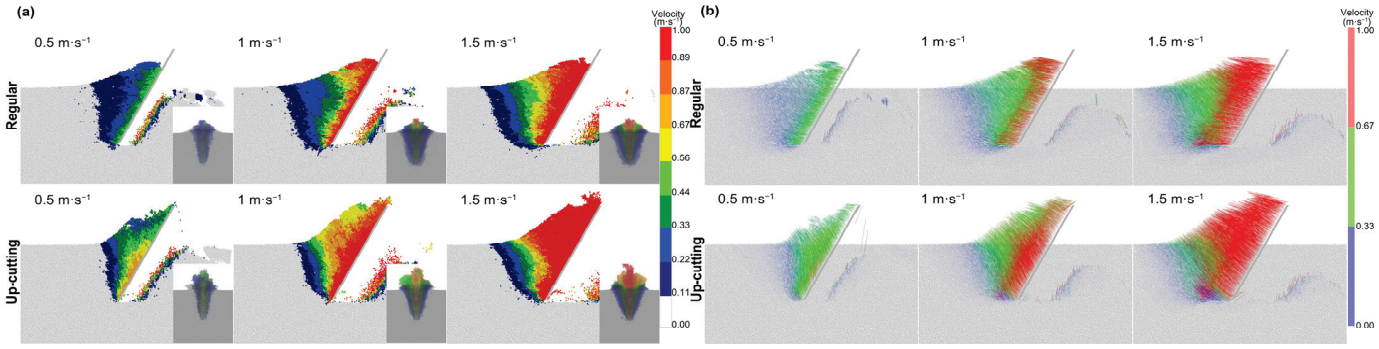

Figure 10. Soil disturbance and particle velocity distribution of regular tools and up-cutting tools affected by advancement velocity (v_t = 0.5 m·s^{-1}, 1 m·s^{-1}, and 1.5 m·s^{-1}): (**a**) soil disturbance; (**b**) particle velocity distribution. For an explanation of the content in this figure, refer to Figure 7.

As the advancement velocity increased, the K_f value of regular tools increased from 18.44 kN·m^{-2} to 21.78 kN·m^{-2} and then to 26.31 kN·m^{-2} (Figure 9a). For the corresponding up-cutting tools, the K_f values were 6.46 kN·m^{-2}, 10.77 kN·m^{-2}, and 17.21 kN·m^{-2}, which are 64.97%, 50.55%, and 34.59% lower than those of regular tools. The up-cutting motion, as indicated by this, was capable of enhancing subsoiling efficiency by means of reducing the specific resistance at each advancement velocity.

The effect of particle velocity (Figure 10b) can also be used to explain the effects of advancement velocity and up-cutting motion. As the advancement velocity increased, changes occurred in the middle part of the disturbed area for both regular and up-cutting tools. For regular tools, the green area expanded. For up-cutting tools, this area was gradually replaced by particles that are affected by the tool surface, with a relatively high velocity and exhibiting a distinct forward trend. This demonstrates the transmission of the tool's effect on the soil towards the front of the tool. As shown in Figure 10b, the particle velocity, as affected by the up-cutting tools, is significantly shifted upward compared with that of the regular tools, which proves the counteracting effect of the up-cutting motion on soil pushing.

Figure 11 exhibits how the velocity of advancement affects the deformation and movement of the slice. As the advancement velocity increased, the slice, acted on by both regular tools and up-cutting tools, experienced longitudinal compression deformation and distortion. It was also lifted upward and pushed forward. Compared with regular tools, up-cutting tools had a greater degree of forward rotation, a higher lift height, less compression deformation, and a shorter forward distance. This means that during the cutting process, up-cutting tools tend to make soil slices move obliquely upward as a whole, while regular tools more often cause soil slices to be broken under forced extrusion.

In summary, an increase in advancement velocity causes the effect of the tool on the soil to be transmitted more in the forward direction. The up-cutting motion, by mimicking the digging actions of animals, causes the soil to move upward, thus weakening the impact on the soil ahead and achieving the objective of reducing the draft force.

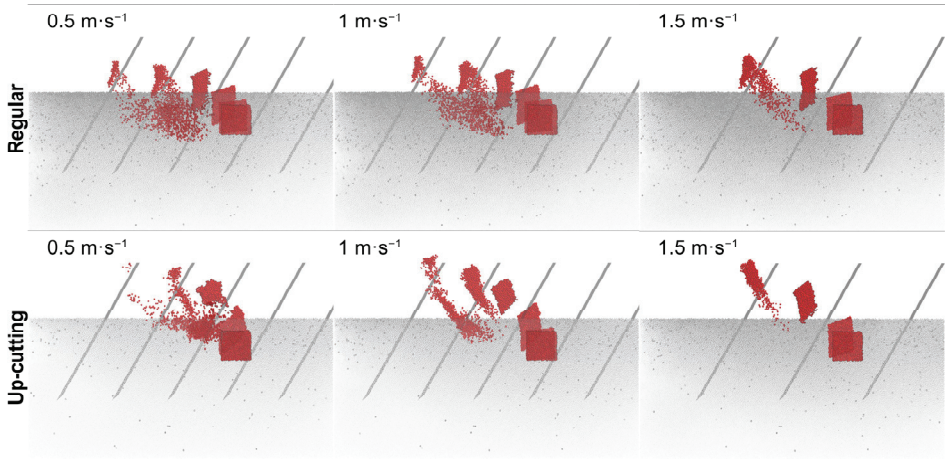

Figure 11. Soil deformation and movement patterns of regular and up-cutting tools affected by advancement velocity (v_t = 0.5 m·s^{-1}, 1 m·s^{-1}, and 1.5 m·s^{-1}). For an explanation of the content in this figure, refer to Figure 8.

3.1.3. The Effects of Up-Cutting Velocity

The simulation showed the effect of the up-cutting velocity on the tool force (Figure 12). For the up-cutting tool only, when the up-cutting velocity rose from 0.5 m·s^{-1} to 1 m·s^{-1} and then to 1.5 m·s^{-1}, the draft force changed from 1212.07 N to 598.59 N and 361.89 N (Figure 12a). Therefore, the increase in the up-cutting velocity significantly inhibited the growth of the draft force. The higher the up-cutting velocity, the lower the draft force. This implies that a higher up-cutting velocity is more conducive to the tool's horizontal advancement. At the same time, the vertical force changed from −471.35 N to −472.26 N and −463.89 N, with relatively small magnitude variations (Figure 12b). This may suggest that the advantages of a decreased draft force from higher up-cutting velocities far exceed the drawbacks of the vertical force from the up-cutting motion.

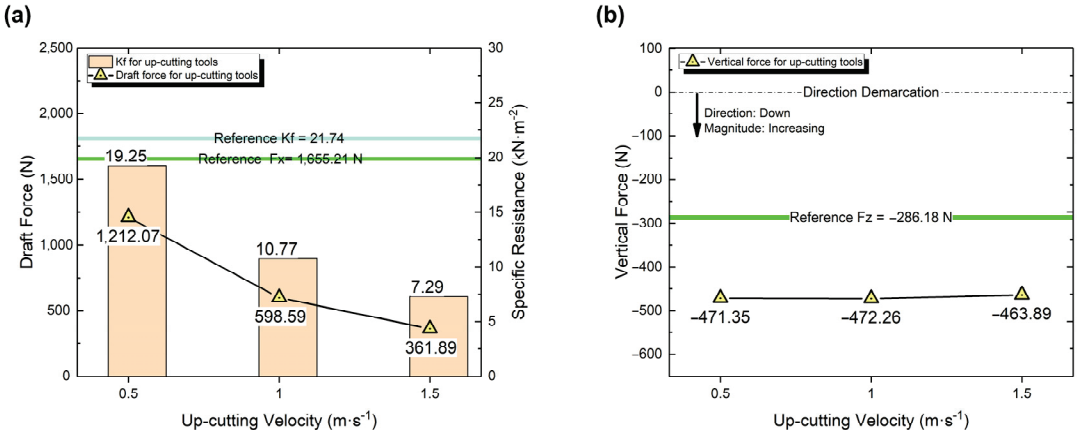

Figure 12. Tool force of regular tools and up-cutting tools affected by up-cutting velocity (u_t = 0.5 m·s^{-1}, 1 m·s^{-1}, and 1.5 m·s^{-1}): (**a**) draft force and specific resistance; (**b**) vertical force.

By observing the influence of the up-cutting velocity on soil disturbance (Figure 13a), it can be found that, compared with regular tools (0 m·s^{-1}), as the up-cutting velocity increased from 0.5 m·s^{-1} to 1 m·s^{-1} (the reference level) and 1.5 m·s^{-1}, the inclination of the failure surface of the up-cutting tools decreased (the inclination angle increased), gradually becoming closer to vertical. The transversal and longitudinal sections became narrower and longer. The total disturbed area and failure distance in the longitudinal and transversal sections decreased, the disturbance width remained nearly the same, and the uplift height increased. In addition, compared with regular tools, under the changes

in the above-mentioned factors, the up-cutting motion changed the shape of the lateral disturbance area from U-shaped to V-shaped (Figure 7a, Figure 10a, and Figure 13a). This may be because the faster the up-cutting motion's velocity, the greater the number of particles transported upward under the influence of the up-cutting motion. Regular tools merely guide the particles along the tool surfaces in a relatively limited way. Due to kinematic constraints and surface friction, the upward movement of particles is limited, and the cumulative effect transmitted to the front of the tool is an important reason for the generation of the draft force. In contrast, the increase in up-cutting velocity promotes the upward transportation of particles and reduces the cumulative effect of the soil in front of the tool due to the tool's movement, thus reducing the draft force.

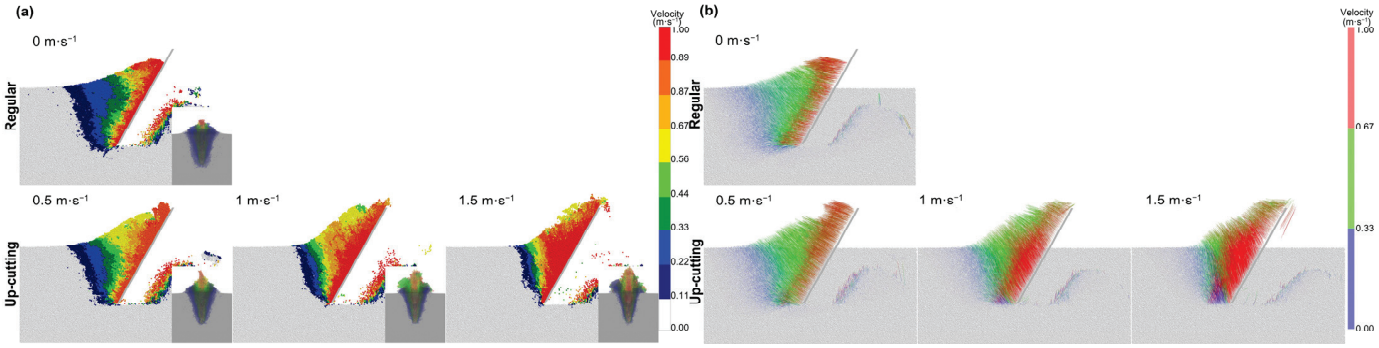

Figure 13. Soil disturbance and particle velocity distribution affected by up-cutting velocity (u_t = 0.5 m·s^{-1}, 1 m·s^{-1}, and 1.5 m·s^{-1}): (**a**) soil disturbance; (**b**) particle velocity distribution. For an explanation of the content in this figure, refer to Figure 7.

As the up-cutting velocity increased, the K_f value of the up-cutting tool dropped significantly. The specific resistance (K_f) of the up-cutting tools was lower than that of the regular tools (see Figure 12a, reference value). This indicates that increasing the up-cutting velocity can reduce the specific resistance. As a result, the subsoiling efficiency is substantially improved.

The simulation results show the influence of the up-cutting velocity on particle velocity (Figure 13b). As the up-cutting velocity increased, both regular and up-cutting tools exhibited similar changes in the middle part of the disturbed area. Gradually, this area was replaced by particles affected by the tool surface. These particles had a relatively high velocity and showed an obvious upward-moving trend. In the vicinity of the tool surface, the velocity of particles associated with the up-cutting tool was significantly influenced. The red area occupied the entire tool surface, the vertical upward component of particle movement significantly increased, and the velocity accelerated noticeably. Within 0.2 s, the particles were pushed to a higher position. This proves the contribution of the increase in up-cutting velocity to the upward transportation of particles.

Figure 14 shows the influence of the up-cutting velocity on the deformation and movement effects of the slices. Regarding the up-cutting velocity of the tool, under the action of the regular tool, the forward-pushing distance and upward-lifting height were at a certain level. For the up-cutting tool, as the up-cutting velocity increased, the longitudinal compression deformation of the square soil unit decreased, i.e., the longitudinal thickness, the degree of forward rotation, and the upward-lifting height increased, and the forward-pushing distance decreased. This indicates that increasing the up-cutting velocity promotes the oblique upward movement of the soil mass as a whole.

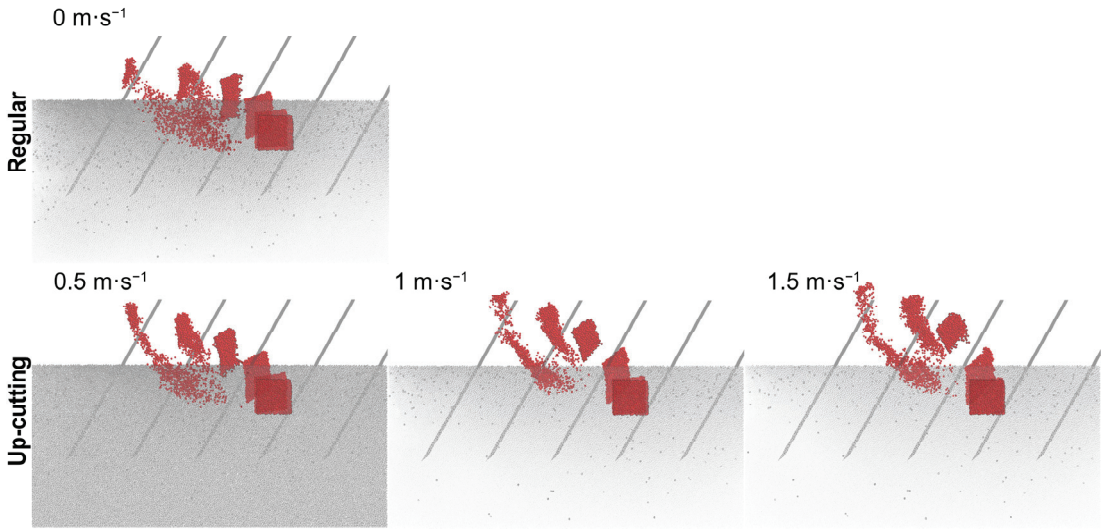

Figure 14. Soil deformation and movement patterns affected by up-cutting velocity (u_t = 0.5 m·s^{-1}, 1 m·s^{-1}, and 1.5 m·s^{-1}). For an explanation of the content in this figure, refer to Figure 8.

In summary, during the up-cutting motion that mimics the soil-disturbing behavior of animals' digging, increasing the up-cutting velocity allows the tool to transport more soil upward, thus reducing the draft force.

3.2. Results of Field Tests

The results of the field tests present the draft-force-related performance of the conventional subsoiler and the chain subsoiler (Figure 15). The increase in the average draft force of both the conventional subsoiler and the chain subsoiler, as the results indicated, was associated with the increase in tillage depth. The draft force of the conventional subsoiler was 1.87 kN, 4.34 kN, and 8.73 kN when operated at a depth of 250 mm, 350 mm, and 450 mm, respectively. However, the chain subsoiler obtained draft forces of 1.33 kN, 2.52 kN, and 4.71 kN at these depths, respectively, which were 28.92%, 41.94%, and 46.03% lower than those of the conventional subsoilers. Moreover, with the increase in tillage depth, this reduction became more remarkable. This adequately shows that a chain subsoiler is highly efficacious in reducing the draft force in subsoiling.

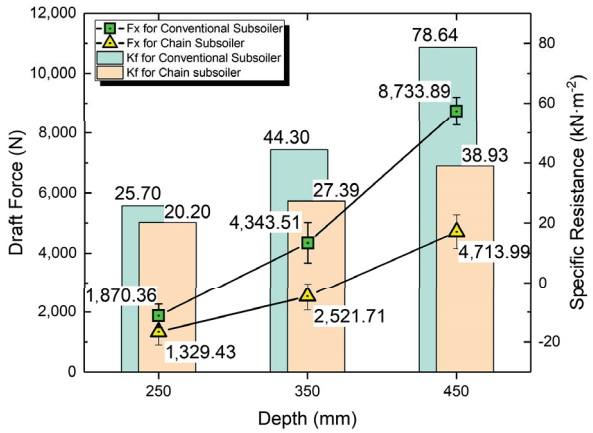

Figure 15. Draft force of a conventional subsoiler and a chain subsoiler affected by tillage depth from 250 mm to 350 mm and 450 mm: the line graph represents the force, and the bar graph represents the specific resistance.

Figure 15 also shows the specific resistance calculated from the draft force and the corresponding disturbance. It was indicated by the results that the specific resistance (K_f)

values of the conventional subsoiler were 21.43%, 38.19%, and 50.50% higher than those of the chain subsoiler. This proves that the chain subsoiler effectively reduces specific resistance and improves subsoiling efficiency.

Figure 16 presents the typical soil disturbance profiles generated after subsoiling operations, corresponding to the conventional subsoiler (Figure 16a) and the chain subsoiler (Figure 16b), respectively. In the figure, key information, such as the horizontal plane of the original soil surface, the disturbed area, the depth, and the bottom horizontal plane of the furrow, is clearly marked. In terms of the overall shape, the general outlines of the disturbed areas of the two types of subsoilers are similar. Although there are certain differences regarding some specific details, such as the curvature of the edge of the disturbed area and the transition area between the bottom of the furrow and the soil on both sides, the overall differences are not significant. This is because the soil transported upward accumulates on both sides of the furrow, thus affecting the shape of the disturbed area. As for the relevant profile parameters, refer to Table 3 for details.

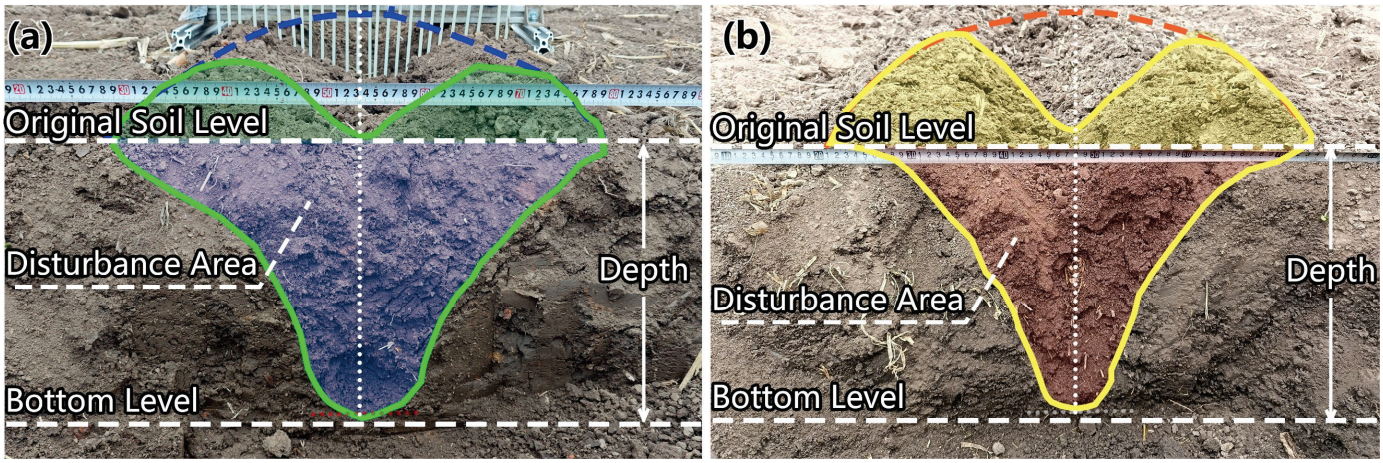

Figure 16. Typical soil disturbance caused by (**a**) a conventional subsoiler (green); (**b**) a chain subsoiler (yellow).

Table 3. Disturbance profile parameters of a conventional subsoiler and a chain subsoiler.

Type	Depth (mm)	Transversal Area (m^2)	Disturbed Width (mm)	Uplift Height (mm)
Conventional Subsoiler	250	0.0727	490.99	86.62
	350	0.0780	513.33	93.32
	450	0.1110	502.47	94.88
Chain Subsoiler	250	0.0658	532.86	112.35
	350	0.0921	487.93	108.98
	450	0.1211	526.64	120.56

The above results suggested that there was no substantial difference in soil disturbance between the chain subsoiler and the conventional subsoiler. Moreover, no other obvious negative effects of the chain subsoiler were found. It suggests that the chain subsoiler, namely the proposed up-cutting subsoiling device, can significantly reduce the draft force and improve tillage efficiency while ensuring that the degree of soil disturbance meets the requirements, which makes it feasible and effective for practical applications.

4. Discussion

This study aimed to draw inspiration from the digging techniques of animals and explore a new type of low-draft subsoiling method. To this end, the principle of soil breaking, summarized from these digging techniques, was applied to the design of subsoilers. An innovative concept of up-cutting subsoiling was proposed. DEM simulations were carried out to analyze the draft-reducing performance and the mechanism of up-cutting. Finally, field tests were conducted using a chain subsoiler designed based on this principle to verify its draft-reducing performance.

The idea of applying digging techniques to machines with different operation modes may seem counterintuitive. There are significant differences in the forms of tool movement between parallel cutting in subsoiling operations and the digging actions of animals. However, from the perspective of the soil-breaking principle, the features of these two movement patterns are skillfully integrated using an up-cutting tool, thus reducing the draft force.

The DEM simulation results clearly show that when the up-cutting motion is introduced, the draft force is significantly reduced. Furthermore, as the up-cutting velocity increases, the draft force decreases. This indicates that the up-cutting motion effectively reduces the draft force. Field tests have also proven the draft-reducing feasibility of the chain subsoiler designed using this principle.

The fundamental reason why subsoiling with an up-cutting motion can reduce draft forces is that the tool exerts force from the interior of the soil and pushes the disturbed soil to the ground to reduce the draft force.

First of all, the range of soil disturbance varies as a result of up-cutting. The path along which the tool causes the least resistance is the longitudinal failure boundary [55]. The failure boundary occurs in the shape of a line or a logarithmic spiral. Up-cutting causes a change in the direction of external friction, resulting in a deflection of the principal stress axis [18]. As a result, the failure boundary rotates accordingly. This change in the volume of soil under load during the shearing cycle may directly contribute to the reduction of the draft. This is in line with the findings from powered discs from similar earth-moving operations [29].

Secondly, the particle velocity redistributes as a result of up-cutting. Under the up-cutting motion, soil does not continuously amass upon the tool surface to reshape the tool surface macroscopically, nor does there exist a boundary wedge synchronizing with the tool [17,19,20]. Therefore, the soil in front of the tool can be smoothly replaced, reducing the compressive force applied to the next piece of soil, thus reducing the draft force [29,45,56].

Finally, soil movement and deformation patterns are altered as a result of up-cutting, resulting in the whole-scale lifting of soil in front of the tool, thereby reducing the draft. By doing this, a primary shortcoming in the design concept of soil-loosening tools, which first compress the soil through the tool to generate shear and then loosen the soil, is evaded [19,50,57]. Conversely, some tensile stress might be generated in the unsupported soil ahead of the tool [50]. As is commonly known, compared with the shear strength brought about by compressive stress, the inherent tensile strength of soil is several orders of magnitude lower. Consequently, soil failure occurs more readily, and the draft force is reduced as a result of this situation [50].

It is worth noting that the up-cutting motion increases the downward vertical force. However, this force is close to that of a conventional tool with a rake angle of 45°. This vertical force is acceptable in that it falls within a reasonable range. It can be balanced by the soil reaction force without causing the negative impacts of excessive downward penetration and over-soil compaction [44].

Combined with the field test results, it can be considered that integrating an up-cutting motion with subsoiling has good prospects for draft-reducing applications. In agricultural soil tillage, to overcome the resistance between the soil and the tillage machinery, 30–50% of the total energy consumption is employed. Even a slight reduction in the draft force can bring huge benefits [1]. When the draft force is high, a high-horsepower tractor must be used for drafting to ensure the normal progress of subsoiling operations. Forcing operations will make components more prone to deformation, wear, and malfunction. As a result, the working efficiency of the subsoiler will be reduced, affecting the tillage quality [34]. After using an up-cutting motion to reduce the draft force, it is possible to use a light-duty tractor for traction, reducing the cost of the tractor [27]. This can avoid various tillage quality and efficiency problems caused by excessive resistance. In addition, the tractor can till at a faster speed, reducing slippage and improving tillage efficiency once again [29].

It should be noted that, due to limited space, this study is not exhaustive. Firstly, the soil conditions used in the simulation cannot replicate actual, real farmland soil in every dimension without deviation. There are also deviations between the obtained results and the actual ones. However, this difference is reasonable and acceptable. The purpose of this study is to explore the performance changes of a given tool under specific soil conditions. The set soil conditions can effectively present the corresponding change trends and are sufficient to meet the research needs. Under different soil conditions, the draft-reducing performance of the up-cutting tool should show a similar trend. This is due to the large-scale soil behavior caused by the soil–tool interaction, which can be described as the soil movement characterized by flow around the tool (Figure 1). Different soil failure modes may be similar in the "macro-scale" properties of soil movement [58, 59]. Nevertheless, in future research, we plan to fully consider different soil conditions, especially varying suction and moisture levels, and deeply explore the draft-reducing performance of the up-cutting tool under these conditions, aiming to further reveal the internal laws of soil–tool interactions and provide more robust theoretical support for the development of related fields. The second issue is that the interaction between factors has not been analyzed, nor have the optimized parameters been determined, due to limited time and resources. However, this paper mainly focuses on the draft-reducing mechanism and analyzes the impact of a single factor on draft reduction to establish a basic understanding. Our subsequent research will focus on studying the interaction between factors and determining the optimal structural and operational parameters based on the existing results. A third concern is that more energy is consumed to meet the power requirement for driving the chain, and this is also highly correlated with the chain speed. Therefore, in subsequent research, it is necessary to study and analyze the rotary speed and power consumption of the chain subsoiler and the whole machine to further improve work efficiency and minimize power consumption.

However, these controversies do not impede the application of this principle. The significance of this article is that it has confirmed the significant reduction of the draft force using the up-cutting motion, the reasons for this reduction, and the practical feasibility of machines applying this principle. The excellent draft-reducing ability addresses the most urgent draft issues in subsoiling or other types of tillage, thus necessitating more attention. This technology has broad application prospects.

5. Conclusions

In this research, inspired by the soil-digging techniques of animals, an innovative up-cutting subsoiling method was proposed that can significantly reduce the draft force in subsoiling operations. The discrete element method (DEM) was adopted to conduct a detailed comparative simulation analysis of the draft performance of conventional tools

and up-cutting tools under different rake angles, advancement velocities, and up-cutting velocities. Meanwhile, the internal mechanism by which up-cutting tools reduce the draft force under these conditions was deeply analyzed. Based on the theoretical analysis and simulation results, a prototype of the chain subsoiler was designed and manufactured according to this principle. Subsequently, field tests were carried out on the draft-reducing performance and soil disturbance effects of this subsoiler at different depths. The results indicate that the up-cutting tools based on the soil-breaking principle of animal digging techniques have fully exploited their advantages in reducing the draft force, showcasing excellent draft-reducing effects. This draft-reducing effect has been verified through the draft performance of the chain subsoiler in field tests. The key research results are outlined as follows:

(1) The soil-breaking effect induced by the up-cutting tools in the soil is highly similar in principle to that generated when animal claws dig up soil. This similarity lays an important prerequisite for the bionic application of animal digging techniques in the field of subsoiling tillage.

(2) Compared with regular tools, up-cutting tools significantly reduced the draft force under different factor levels. At rake angles of 45°, 60°, and 75°, the up-cutting tools decreased the draft force by 63.07%, 63.84%, and 58.92%, respectively. At advancement velocities of 0.5 $m \cdot s^{-1}$, 1 $m \cdot s^{-1}$, and 1.5 $m \cdot s^{-1}$, the draft force decreased by 79.73%, 63.84%, and 45.22%, respectively. Although the up-cutting tools increased the vertical downward force, the increase still remained within a reasonable and acceptable range.

(3) Compared with regular tools, the variations in the soil disturbance area, the redistribution in particle velocity, and the pattern alteration in deformation and movement caused by up-cutting all contribute to the reduction in the draft force. The upward movement of the soil effectively prevents soil accumulation in front of the tool and alleviates soil compression deformation. These aspects, acting together, play a positive role in reducing the draft force during subsoiling.

(4) The chain subsoiler, designed and manufactured based on the up-cutting principle, demonstrates a good draft-reducing effect. The results of field tests confirm that, at different depths, the chain subsoiler with the up-cutting method has a draft-reduction amplitude close to or more than 30%. The soil disturbance it generates is similar to that of a standard subsoiler, fully meeting the subsoiling requirements for tillage quality.

This study demonstrates that up-cutting holds great potential in reducing subsoiling draft forces. Meanwhile, this research highlights the innovative direction and key design concepts for the design of future low-draft subsoilers based on the up-cutting principle, as well as other earth-moving machinery.

Author Contributions: Conceptualization, P.G.; Data curation, P.G. and X.L.; Formal analysis, P.G., M.Q., and X.L.; Funding acquisition, Y.M. and M.Q.; Investigation, P.G. and Z.X.; Methodology, P.G., S.W., and Z.X.; Project administration, Y.M.; Resources, Y.M.; Software, P.G., S.W., and X.L.; Supervision, Y.M.; Validation, Z.X., S.W., and X.L.; Visualization, P.G., M.Q., S.W., and X.L.; Writing—original draft, P.G., Z.X., and M.Q.; Writing—review and editing, Z.X., M.Q., and Y.M. All authors have read and agreed to the published version of the manuscript.

Funding: This work was supported by the National Key Research and Development Program of China [grant number: No. 2023YFD2000903] (Y.M.); the Key Research and Development Program of Autonomous Region [grant number: No. 2023B02021-3] (Y.M.); the National Natural Science Foundation of China [grant number: 52275288] (Y.M.); and the Scientific Research Foundation for Advanced Talents of Jiangsu University [grant number 5501280010] (M.Q.).

Institutional Review Board Statement: Not applicable.

Data Availability Statement: The raw data supporting the conclusions of this article will be made available by the authors on request.

Conflicts of Interest: The authors declare no conflicts of interest.

Abbreviations

The following abbreviations are used in this manuscript:

DEM	Discrete Element Method
OFAT	One Factor At a Time
ECS	Earth Coordinate System
ICS	Implement Coordinate System

References

1. Gill, W.R.; Vanden Berg, G.E. Soil dynamics in tillage and traction. In *Agricultural Handbook No. 316*; Agricultural Research Service, United States Department of Agriculture: Washington, DC, USA, 1968; pp. 340–429.
2. Manuwa, S. Performance evaluation of tillage tines operating under different depths in a sandy clay loam soil. *Soil Tillage Res.* **2009**, *103*, 399–405. [CrossRef]
3. Hemami, A. Motion trajectory study in the scooping operation of an LHD-loader. *IEEE Trans. Ind. Appl.* **2002**, *30*, 1333–1338. [CrossRef]
4. Araya, K. Soil failure caused by subsoilers with pressurized water injection. *J. Agric. Eng. Res.* **1994**, *58*, 279–287. [CrossRef]
5. Larson, D.; Clyma, H. Electro-osmosis effectiveness in reducing tillage draft force and energy requirements. *Trans. ASAE* **1995**, *38*, 1281–1288. [CrossRef]
6. Salokhe, V.; Gee-Clough, D. Technology showcase applications of enamel coating in agriculture. *J. Terramechanics* **1989**, *26*, 275–286. [CrossRef]
7. Tong, J.; Lu, X.; Chen, Y.; Ren, L.; Chen, B. Soil adhesion and abrasive wear of PTFE-matrix composites. *Trans. Chin. Soc. Agric. Eng.* **1990**, *6*, 13.
8. Tong, J.; Ren, L.; Chen, B.; Qaisrani, A. Characteristics of adhesion between soil and solid surfaces. *J. Terramechanics* **1994**, *31*, 93–105. [CrossRef]
9. Ren, L.; Han, Z.; Li, J.; Tong, J. Effects of non-smooth characteristics on bionic bulldozer blades in resistance reduction against soil. *J. Terramechanics* **2002**, *39*, 221–230. [CrossRef]
10. Sun, J.; Wang, Y.; Ma, Y.; Tong, J.; Zhang, Z. DEM simulation of bionic subsoilers (tillage depth> 40 cm) with drag reduction and lower soil disturbance characteristics. *Adv. Eng. Softw.* **2018**, *119*, 30–37. [CrossRef]
11. Tong, J.; Wu, B.; Song, Z.; Gao, Z.; Sun, J.; Ma, Y.; Zhuang, J. Research on the drag reduction mechanism of antlion (*Myrmeleon sagax*) larvae nonsmooth structural surface. *Microsc. Res. Tech.* **2020**, *83*, 338–344. [CrossRef]
12. Niyamapa, T.; Salokhe, V. Force and pressure distribution under vibratory tillage tool. *J. Terramechanics* **2000**, *37*, 139–150. [CrossRef]
13. Wang, Y.; Zhang, D.; Yang, L.; Cui, T.; Jing, H.; Zhong, X. Modeling the interaction of soil and a vibrating subsoiler using the discrete element method. *Comput. Electron. Agric.* **2020**, *174*, 105518. [CrossRef]
14. Bandalan, E.; Salokhe, V.; Gupta, C.; Niyamapa, T. Performance of an oscillating subsoiler in breaking a hardpan. *J. Terramech.* **1999**, *36*, 117–125. [CrossRef]
15. Makanga, J.; Salokhe, V.; Gee-Clough, D. Effects of tine rake angle and aspect ratio on soil reactions in dry loam soil. *J. Terramech.* **1997**, *34*, 235–250. [CrossRef]
16. Godwin, R.; Spoor, G.; Leeds-Harrison, P. An experimental investigation into the force mechanics and resulting soil disturbance of mole ploughs. *J. Agric. Eng. Res.* **1981**, *26*, 477–497. [CrossRef]
17. Hettiaratchi, D.; Reece, A. Boundary wedges in two-dimensional passive soil failure. *Geotechnique* **1975**, *25*, 197–220. [CrossRef]
18. Harrison, H. Soil reactions from laboratory studies with an inclined blade. *Trans. ASAE* **1982**, *25*, 7–0012. [CrossRef]
19. Hettiaratchi, D. Theoretical soil mechanics and implement design. *Soil Tillage Res.* **1988**, *11*, 325–347. [CrossRef]
20. Reece, A.; Hettiaratchi, D. A slip-line method for estimating passive earth pressure. *J. Agric. Eng. Res.* **1989**, *42*, 27–41. [CrossRef]
21. Eldridge, D.J. Mounds of the American badger (*Taxidea taxus*): Significant features of North American shrub-steppe ecosystems. *J. Mammal.* **2004**, *85*, 1060–1067. [CrossRef]
22. Lagaria, A.; Youlatos, D. Anatomical correlates to scratch digging in the forelimb of European ground squirrels (*Spermophilus citellus*). *J. Mammal.* **2006**, *87*, 563–570. [CrossRef]
23. Camin, S.; Madoery, L.; Roig, V. The burrowing behavior of Ctenomys mendocinus (Rodentia). *Mammalia* **1995**, *59*, 9–18. [CrossRef]

24. Gasc, J.; Renous, S.; Casinos, A.; Laville, E.; Bou, J. Comparison of diverse digging patterns in some small mammals. *Fortschritte Der Zool.* **1985**, *30*, 35–38.
25. Jarvis, J.U.; Sale, J.B. Burrowing and burrow patterns of East African mole-rats Tachyoryctes, Heliophobius and Heterocephalus. *J. Zool.* **1971**, *163*, 451–479. [CrossRef]
26. Van Wassenbergh, S.; Heindryckx, S.; Adriaens, D. Kinematics of chisel-tooth digging by African mole-rats. *J. Exp. Biol.* **2017**, *220*, 4479–4485. [CrossRef] [PubMed]
27. Hann, M.; Giessibl, J. Force measurements on driven discs. *J. Agric. Eng. Res.* **1998**, *69*, 149–157. [CrossRef]
28. Upadhyay, G.; Raheman, H. Comparative analysis of tillage in sandy clay loam soil by free rolling and powered disc harrow. *Eng. Agric. Environ. Food* **2019**, *12*, 118–125. [CrossRef]
29. Nalavade, P.P.; Salokhe, V.M.; Niyamapa, T.; Soni, P. Performance of free rolling and powered tillage discs. *Soil Tillage Res.* **2010**, *109*, 87–93. [CrossRef]
30. Mellor, M. *Mechanics of Cutting and Boring. Part 3. Kinematics of Continuous Belt Machines*; Cold Regions Research and Engineering Lab: Hanover, NH, USA, 1976.
31. Mellor, M. *Mechanics of Cutting and Boring. Part VIII, Dynamics and Energetics of Continuous Belt Machines*; Cold Regions Research and Engineering Lab: Hanover, NH, USA, 1978.
32. Sitorus, P.E.; Ko, J.H.; Kwon, O.S. Parameter study of chain trenching machines of Underwater Construction Robots via analytical model. In Proceedings of the OCEANS 2016 MTS/IEEE Monterey, Monterey, CA, USA, 19–23 September 2016; pp. 1–6.
33. Vu, M.T.; Choi, H.-S.; Kim, J.-Y.; Ji, D.-H.; Lee, Y.-J.; Choi, D.-H. A study on underwater track vehicle system. In Proceedings of the 2015 15th International Conference on Control, Automation and Systems (ICCAS), Busan, Republic of Korea, 13–16 October 2015; pp. 253–257.
34. Gao, P.; Li, J.; Qi, H.; Liu, X.; Ma, Y. Simulation of draught reduction performance of subsoiling with upcutting belt motion using discrete element method. *Appl. Sci.* **2024**, *14*, 1313. [CrossRef]
35. Zhang, R.; Li, J.Q.; Zhou, C.H.; Xu, S.C. Simulation of dynamic behavior of soil ahead of the bulldozing plates with different surface configurations by discrete element method. *Trans. Chin. Soc. Agric. Eng.* **2007**, *23*, 13–19.
36. Zhang, R.; Chen, B.; Li, J.-q.; Xu, S.-c. DEM simulation of clod crushing by bionic bulldozing plate. *J. Bionic Eng.* **2008**, *5*, 72–78. [CrossRef]
37. Ucgul, M.; Fielke, J.M.; Saunders, C. 3D DEM tillage simulation: Validation of a hysteretic spring (plastic) contact model for a sweep tool operating in a cohesionless soil. *Soil Tillage Res.* **2014**, *144*, 220–227. [CrossRef]
38. Zeng, Z.; Chen, Y.; Zhang, X. Modelling the interaction of a deep tillage tool with heterogeneous soil. *Comput. Electron. Agric.* **2017**, *143*, 130–138. [CrossRef]
39. Hang, C.; Gao, X.; Yuan, M.; Huang, Y.; Zhu, R. Discrete element simulations and experiments of soil disturbance as affected by the tine spacing of subsoiler. *Biosyst. Eng.* **2018**, *168*, 73–82. [CrossRef]
40. Hirasawa, K.; Kataoka, T.; Kubo, T. Prediction and evaluation for leveling performance in rotary tiller. *IFAC Proc. Vol.* **2013**, *46*, 315–320. [CrossRef]
41. Wang, Y.; Xue, W.; Ma, Y.; Tong, J.; Liu, X.; Sun, J. DEM and soil bin study on a biomimetic disc furrow opener. *Comput. Electron. Agric.* **2019**, *156*, 209–216. [CrossRef]
42. Ucgul, M.; Saunders, C.; Fielke, J.M. Discrete element modelling of tillage forces and soil movement of a one-third scale mouldboard plough. *Biosyst. Eng.* **2017**, *155*, 44–54. [CrossRef]
43. Ucgul, M.; Saunders, C. Simulation of tillage forces and furrow profile during soil-mouldboard plough interaction using discrete element modelling. *Biosyst. Eng.* **2020**, *190*, 58–70. [CrossRef]
44. Tong, J.; Jiang, X.-H.; Wang, Y.-M.; Ma, Y.-H.; Li, J.-W.; Sun, J.-Y. Tillage force and disturbance characteristics of different geometric-shaped subsoilers via DEM. *Adv. Manuf.* **2020**, *8*, 392–404. [CrossRef]
45. Wang, X.; Li, P.; He, J.; Wei, W.; Huang, Y. Discrete element simulations and experiments of soil-winged subsoiler interaction. *Int. J. Agric. Biol. Eng.* **2021**, *14*, 50–62. [CrossRef]
46. Ebensperger, L.A.; Bozinovic, F. Energetics and burrowing behaviour in the semifossorial degu Octodon degus (Rodentia: Octodontidae). *J. Zool.* **2000**, *252*, 179–186. [CrossRef]
47. Heth, G. Burrow patterns of the mole rat Spalax ehrenbergi in two soil types (terra-rossa and rendzina) in Mount Carmel, Israel. *J. Zool.* **1989**, *217*, 39–56. [CrossRef]
48. Hildebrand, M. Chapter 6. Digging of quadrupeds. In *Functional Vertebrate Morphology*; Harvard University Press: Cambridge, MA, USA, 1985; pp. 89–109.
49. Blouin, S.; Hemami, A.; Lipsett, M. Review of resistive force models for earthmoving processes. *J. Aerosp. Eng.* **2001**, *14*, 102–111. [CrossRef]
50. Hettiaratchi, D. The development of a powered low draught tine cultivator. *Soil Tillage Res.* **1993**, *28*, 159–177. [CrossRef]
51. Reece, A. Soil mechanics of agricultural soils. *Soil Sci.* **1977**, *123*, 332–337. [CrossRef]
52. Hettiaratchi, D. The present state of the theory of soil cutting. *J. Terramech.* **1965**, *2*, 63–76. [CrossRef]

53. Salokhe, V.; Pathak, B. Effect of aspect ratio on soil failure pattern generated by vertical flat tines at low strain rates in dry sand. *J. Agric. Eng. Res.* **1992**, *53*, 169–180. [CrossRef]
54. Hang, C.; Gao, X.; Wang, B.; Yuan, M.; Huang, Y.; Zhu, R. Optimization of the wing parameters for a winged subsoiler. *Appl. Eng. Agric.* **2017**, *33*, 313. [CrossRef]
55. McKyes, E.; Ali, O. The cutting of soil by narrow blades. *J. Terramech.* **1977**, *14*, 43–58. [CrossRef]
56. Shmulevich, I.; Asaf, Z.; Rubinstein, D. Interaction between soil and a wide cutting blade using the discrete element method. *Soil Tillage Res.* **2007**, *97*, 37–50. [CrossRef]
57. Hettiaratchi, D. A critical state soil mechanics model for agricultural soils. *Soil Use Manag.* **1987**, *3*, 94–105. [CrossRef]
58. Coetzee, C.J. *The Modelling of Granular Flow Using the Particle-in-Cell Method*; University of Stellenbosch: Stellenbosch, South Africa, 2004.
59. Karmakar, S.; Kushwaha, R.L.; Stilling, D. Propagation of soil failure front associated with various agricultural tillage tools. In Proceedings of the 2003 ASAE Annual Meeting, Las Vegas, NV, USA, 27–30 July 2003; p. 1.

Disclaimer/Publisher's Note: The statements, opinions and data contained in all publications are solely those of the individual author(s) and contributor(s) and not of MDPI and/or the editor(s). MDPI and/or the editor(s) disclaim responsibility for any injury to people or property resulting from any ideas, methods, instructions or products referred to in the content.

agriculture

MDPI

Article

Design and Experimental Research on an Automated Force-Measuring Device for Plug Seedling Extraction

Tengyuan Hou [1], Xinxin Chen [1,*], Jianping Hu [1], Wei Liu [1], Junpeng Lv [1], Youheng Tan [1] and Fengpeng Li [2]

[1] Jiangsu Provincial Key Laboratory of Hi-Tech Research for Intelligent Agricultural Equipment, Jiangsu University, Zhenjiang 212013, China; 2212316021@stmail.ujs.edu.cn (T.H.); hujp@ujs.edu.cn (J.H.); mario_liu@ujs.edu.cn (W.L.); 2222316063@stmail.ujs.edu.cn (J.L.); 2222416056@stmail.ujs.edu.cn (Y.T.)
[2] Qingshan Environmental Protection Technology Co., Ltd., Yangzhou 225804, China; lifengpeng1234@163.com
* Correspondence: xxchen@ujs.edu.cn

Abstract

Existing force-measuring devices lack versatility in studying the dynamic coupling process between the seedling-picking device and the plug seedling pot during automatic transplanting. This research developed a universal force-measuring device featuring a centrally symmetrical clamping needle layout and a simultaneous insertion and clamping mechanism. The force-measuring device enables the flexible adjustment of the number of clamping needles (2/3/4 needles) via a modular structure. It can also modify the insertion depth and angle of the clamping needles to accommodate three specifications of plug seedlings, namely 50-hole, 72-hole, and 128-hole plug seedlings. A real-time monitoring system with dual pull-pressure sensors is integrated to precisely acquire the dynamic response curves of the clamping force (F_J) and the disengaging force (F_N) of the plug seedling pot during the seedling-picking process. Taking water spinach plug seedlings as the research object and combining with EDEM-RecurDyn coupling simulation, the interaction mechanism between the clamping needle and the plug seedling pot was elucidated. The performance of the force-measuring device was verified through systematic force-measuring experiments. The main research findings are as follows: The force-measuring device designed in this study can successfully obtain the mechanical characteristic curve of the relevant seedling plug pot throughout the automatic seedling-picking process. The simulation results show high consistency with the experimental results, indicating that the force-measuring device can effectively reveal the dynamic coupling process between the seedling-picking device and the plug seedling pot. The verification experiment demonstrates that the force-measuring device can effectively quantify the mechanical properties of the of plug seedling pots under different plug seedlings specifications and different clamping needles configurations. Reducing the hole size and increasing the number of clamping needles can effectively decrease the peak value of the disengaging force (F_{Nmax}). The peak clamping force (F_{Jmax}) is approximately inversely proportional to the needle number, with the four-needle layout providing the most uniform force distribution. The force-measuring device developed in this study is functional, applicable, and versatile, offering a general force-measuring tool and a theoretical foundation for optimal seedling-picking device design.

Keywords: force-measuring device; plug seedling; clamping force; disengaging force; mechanical properties; dynamic coupling

1. Introduction

Transplanting plug seedlings to the field enhances crop resistance to drought, flood, and salinity. This practice also extends the effective growth cycle. As a result, crops grow more steadily, which improves yield and quality [1–5]. During the process, the transplanting machine is the most important tool. Moreover, the technology of fully automatic transplanting machines has become relatively mature in developed countries such as Europe and America [6]. With the development of intelligent technologies, precision agriculture, and innovative techniques, significant progress has been made in transplanting machines to meet the low-cost and simple automation needs in developing countries [7]. As a crucial component of the transplanting machine, the seedling-picking device is the key to replacing manual labor and realizing automatic transplanting technology. It directly determines the quality and efficiency of the transplanting machine industry [5,8]. The seedling-picking mechanism in automatic transplanters can repeatedly extract plug seedlings automatically from the seedling plugs with the help of a pair of pins or forks, which are designed to gently grip the seedlings without causing damage, and drop them at a predefined location [9]. During the seedling-picking process in the current plug-seedling transplanting operation, there exists an issue where the seedling-picking device is unstable and prone to damaging plug seedlings, which reduces the survival rate of plug seedlings after transplantation [10,11].

At present, in standard Chinese automatic transplanting machines, the operation mode of the seedling-picking device is usually to insert the clamping needles in the seedling-picking end-effector into the plug seedling pot, applying an appropriate clamping force to grip the plug seedling pot for seedling-picking, and then depositing the seedling pot into the planting device to complete the seedling-throwing process [12]. Therefore, this method of seeding-picking by inserting clamping needles into the plug seedling pot has received extensive attention. Therefore, as a component that directly acts on the plug seedling pot, the seedling-picking device needs to grip the plug seedling pot from the tray stably. Meanwhile, it should also ensure that the clamping force applied to the plug seedling pot does not cause damage to the pot [13,14]. Hence, it is necessary to quantitatively explore the interaction between the seedling-picking device and the plug seedlings.

Previously, a large number of scholars have conducted extensive research on the interaction between the seedling-picking device and the plug seedling. Yang et al. [15] conducted a study on the performance-influencing factors of the sliding needles equipped with sensors during the process of robot-assisted plug seedling transplantation. These factors encompass mechanical aspects, including the clamping angle, extraction acceleration, and sensor sensitivity, as well as horticultural elements such as plant species, the adhesion between roots and hole walls, and the substrate moisture content. Tong et al. [16] designed a mechanical experimental platform founded on a universal testing machine, which is capable of adjusting the outer surface of the pointer clamping for compressing the plug seedling pot. Via the experiment, the optimal combination was acquired, specifically a pointer clamping angle of 7° and a quantity of four clamping needles. Under this condition, a clamping force exceeding 2.6 N can be achieved for the horizontal extrusion of a 4 mm plug seedling pot, thereby surmounting the gravitational force of the plug seedling and the adsorption force between the plug seedling and the seedling plug. Jiang et al. [17] designed and verified a four-needle end-effector that combines the advantages of clamping and sliding. The interaction between the extrusion force F_K and the adhesion force F_L during the clamping process and its influence on the transplanting performance were analyzed. The results show that when the F_K/F_L ratio was in the range of 5.99~8.67, the performance of the end-effector was optimal. Kang et al. [18] developed a two-row automatic vegetable transplanter suitable for small-scale farmland in South Korea, focusing on comparing the performance differences between finger-type

and fork-type seedling-picking devices to determine a better finger-type seedling-picking device. Jin et al. [19] designed an integrated sensor for measuring the clamping force of seedling-picking claws of vegetable plug seedlings, which realized the integrated design of seedling-picking claws and sensors, and could be used for the real-time and accurate detection of clamping force changes during transplanting. Tian et al. [20] simulated the interaction between the clamping needle and the plug seedling pot using EDEM discrete element simulation. They optimized the diameter of the clamping needle, the depth of insertion into the plug seedling pot and the speed of grasping the plug seedling pot by combining the plug seedling pot damage rate with the response surface method. Han et al. [21] designed a multi-needle clamp-type seedling-picking mechanical experimental bench based on the two-finger four-needle structure of the seedling-picking device. The cylinder drives the clamping needles to complete the oblique insertion, parallel clamping and vertical extraction of the clamping needle. They investigated the impact of the clamping needle diameter and seedling-picking speed on the mechanical properties of the seedling-picking process. This was achieved by combining a displacement sensor and a pull-pressure sensor to measure the force. Magar et al. [22] developed and optimized an embedded system-based automatic seedling-picking device for vegetable plug seedlings. They optimized the main influencing factors such as crank rotational speed, seedling root bulb moisture content and needle penetration depth in the root ball, to maximize the extraction ratio and minimize the failure ratio via the response surface method.

Nevertheless, notable limitations persist in the extant research. Currently, there is a scarcity of relevant force-measuring devices employed to investigate the mechanical properties of plug seedling pots during the automatic seedling-picking process. Moreover, their design lacks universality, making it challenging for the existing force-measuring devices to conduct automatic seedling-picking force-measuring experiments for diverse experimental objectives. In particular, the seedling-picking method featuring a centrally symmetrical clamping needle layout and a simultaneous insertion and clamping mechanism can mitigate the disturbance and damage to the plug seedling pot matrix soil [23]. Research on this type of seedling-picking method has garnered extensive attention.

In light of the aforementioned issues, this study presents a universal automatic seedling-picking force-measuring device founded on the centrally symmetrical clamping needle layout and the simultaneous insertion and clamping mechanism. The force-measuring device enables the flexible alteration of the number of clamping needles (2/3/4 needles) via the modular structure. It can regulate the insertion depth and angle to accommodate the three specifications of 50-hole, 72-hole, and 128-hole plug seedlings. The integrated dual pull-pressure sensor real-time monitoring system can precisely acquire the mechanical curve of the seedling plug during the seedling-picking process. Secondly, we chose four clamping needles to conduct an automatic seedling-picking coupling simulation experiment for 50-hole plug seedlings. We analyzed the interaction between the clamping needles and the plug seedling pot particle model through EDEM-RecurDyn coupling simulation. Furthermore, we verified the performance of the force-measuring device via a systematic force-measuring experiment (covering different plug seedlings specifications and different numbers of clamping needles). Finally, an experiment to measure force during was conducted using the force-measuring device to evaluate its functionality. The results of the coupling simulation experiment were compared with those of the corresponding mechanical experiment to confirm the applicability of the force-measuring device. The experimental outcomes with various plug seedlings specifications and different numbers of clamping needles were analyzed, and the mechanical properties of plug seedlings under the experimental condition were quantified to verify the universality of the force-measuring device. The objective of this study is to propose an automated force-measuring device for plug seedling extraction.

2. Materials and Methods

2.1. Design of Force-Measuring Device

2.1.1. The Overall Structure of the Force-Measuring Device

The force-measuring device described in this study has been fully developed, including detailed design, physical construction, and experimental prototyping. All figures (Figures 1–3) depict the actual device built and tested in this research. Permission for publication of the device design has been obtained.

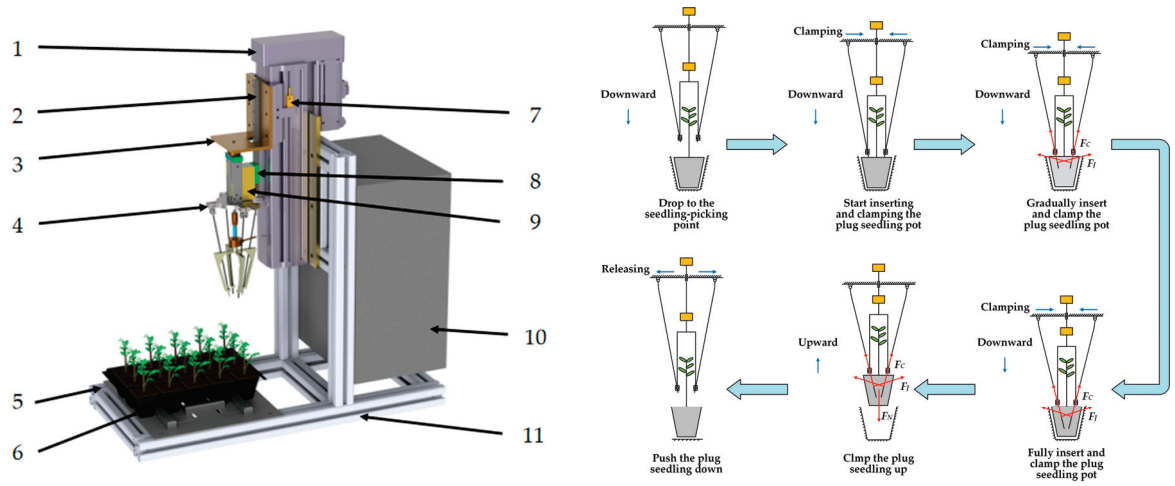

(**a**) (**b**)

Figure 1. Structure and principle of force-measuring device. (**a**) Structural composition of force-measuring device. 1. Lifting module; 2. linear guide; 3. connecting plate; 4. Seedling-picking force-measuring component; 5. seeding plug positioning plate; 6. plug seedlings to be measured; 7. close switch; 8. slider; 9. connecting block; 10. control cabinet; 11. frame. (**b**) The working process of the force-measuring device. F_C is the soil resistance of the clamping needle when it is inserted into the plug seedling pot, N; F_N is the internal adhesion force that needs to be overcome when the seedling-picking force-measuring component clamps the plug seedling pot out of the seeding plug, N; F_J is the force applied by the clamp needle to clamp the plug seedling pot, N.

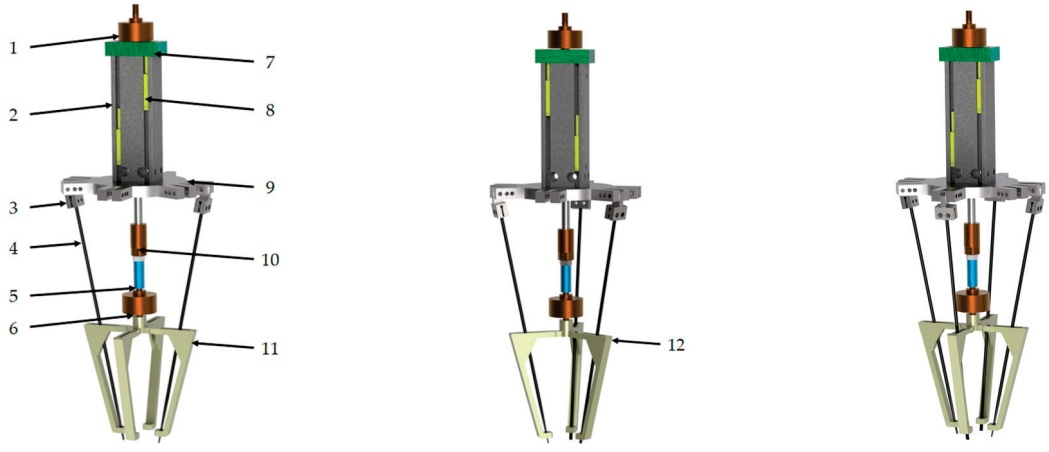

(**a**) (**b**) (**c**)

Figure 2. Seedling-picking force-measuring component with different numbers of clamping needles. (**a**) Two-needle seedling-picking force-measuring component. (**b**) Three-needle seedling-picking force-measuring component. (**c**) Four-needle seedling-picking force-measuring component. 1. Pull-pressure sensor-1; 2. cylinder; 3. turning plate; 4. clamping needle; 5. connect long nut; 6. pull-pressure sensor-2; 7. cushion block; 8. magnetic switch; 9. the turning plate fixed plate; 10. adjustable limit device; 11. seedling pushing frame (four fingers); 12. seedling pushing frame (three fingers).

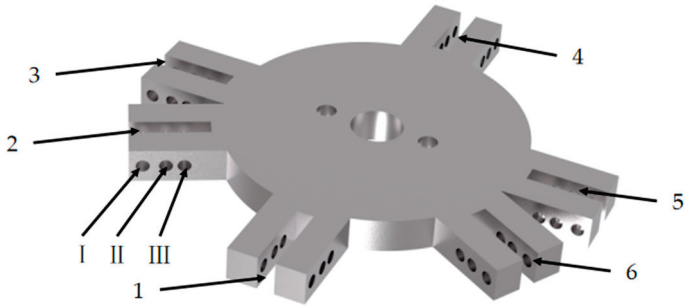

Figure 3. The turning plate fixed plate structure. Here, 3 and 5 are used for turning plates installation of two-needle seedling-picking force-measuring component; 2, 4 and 6 are used for the turning plates installation of the three-needle seedling-picking force-measuring component; 1, 3, 4 and 5 are used for the turning plates installation of the four-needle seedling-picking force-measuring component. I is suitable for the 50-hole plug seedling; II is suitable for the 72-hole plug seedling; III is suitable for the 128-hole plug seedling.

The force-measuring device designed in this study is composed of the seedling-picking force-measuring component, seedling plug positioning plate, connecting plate, lifting module, proximity switch, linear guide, slider, connecting block, control cabinet, frame and so on (Figure 1a). The seedling-picking force-measuring component is secured to the lifting module via the slider. The slider and the linear guide rail play a guiding role in the seedling-picking force-measuring component, eliminating the influence of the shaking of the mechanism during the force-measuring process.

The designed force-measuring device quantitatively detects the interaction between the seedling-picking force-measuring component and the plug seedlings during the automatic seedling-picking process (Figure 1b). The working process of the force-measuring device for seedling-picking operation is as follows: The plug seedlings are placed on the seeding plug positioning plate, and the lifting module drives the seedling-picking force-measuring component to drop from the zero height to the seedling-picking point. After that, the seedling-picking force-measuring component starts to clamp the plug seedling pot; at the same time, the lifting module continues to drive the seedling-picking force-measuring component down, and the electric-gas coordination realizes the edge insertion and clamping of the seedling-picking force-measuring component to the plug seedling pot, to ensure the synchronization of the working process of the seedling-picking. After the seedling-picking force-measuring component completely inserts and clamps the plug seedling pot, the lifting module drives the component to clamp the plug seedling pot up to the zero height, and the component pushes the plug seedling down. In an automatic seedling-picking force-measuring experiment, two pull-pressure sensors were used to quantitatively detect the interaction between the seedling-picking force-measuring component and the plug seedling pot in real time, and then the force values of the disengaging force (F_N) and the clamping force (F_J) of the plug seedling pot during the automatic seedling-picking process were obtained.

2.1.2. Universal Design of Force-Measuring Device

The seedling-picking force-measuring component is the core working part of the force-measuring device for the automatic seedling-picking force-measuring experiment. Based on the seedling-picking end-effector developed by the research group [24], a seedling-picking end-effector with the characteristics of a centrally symmetrical clamping needle layout and a simultaneous insertion and clamping mechanism was designed, and combined with the force-measuring experimental system, it was integrated into a seedling-picking force-measuring part (Figure 2a). The seedling-picking force-measuring component is composed of a cylinder, clamping needles, turning plates, the turning plate fixed plate,

seedling pushing frame, pull-pressure sensor 1, pull-pressure sensor 2, magnetic switch, and the corresponding connecting long nut, adjustable limit device, cushion block, and so on. The clamping needles and the turning plates are fixedly connected on the fixed plate of the turning plate, so that the clamping needles are collected in the guiding hole at the bottom of the seedling pushing frame, and they are distributed symmetrically along the center line of the seedling-picking force-measuring component. Through the adjustable limit device installed on the cylinder, the working stroke of the cylinder is adjusted to change the shrinkage of the clamping needle, in order to adapt to the different insertion depths of the seedling-picking force-measuring component to the plug seedling pot.

The clamping needles directly act on the plug seedling pot during the automatic seedling-picking process. When the seedling-picking force-measuring component reaches the seedling-picking point, the cylinder piston rod shrinks and drives the seedling pushing frame to lift. The clamping needles are retracted under the action of the guiding hole at the bottom of the seedling pushing frame, and the plug seedling pot is inserted and clamped at the same time with the cooperation of the lifting module. When the seedling-picking force-measuring component clamps the plug seedling pot to rise to the zero height, the cylinder piston rod extends, driving the seedling pushing frame to drop and push the plug seedling down.

The turning plate fixed plate is a special-shaped structure (Figure 3). By adjusting the installation position and number of turning plates on the turning plate fixed plate, the turning plate installation of the seedling-picking force-measuring component (2/3/4 needles) can be achieved with different numbers of central symmetrical clamping needles. At the same time, the designed seedling pushing frame has two structural forms: four-finger and three-finger. Among them, the two-needle seedling-picking force-measuring component (Figure 2a) and the four-needle seedling-picking force-measuring component (Figure 2c) can adopt the four-finger seedling pushing frame. In contrast, the three-needle seedling-picking force-measuring component (Figure 2b) needs to adopt the three-finger seedling pushing frame.

The clamping angle of plug seedling pots is critically determined by the distance between the installation point of the turning plates on the fixed plate and its centerline. To accommodate varying plug seedling specifications, three distinct installation positions (designated as Point I, Point II, and Point III) were systematically configured on the turning plate fixed plate. This modular design enables the precise adjustment of the clamping angle by relocating the turning plate installation points, thereby ensuring optimal adaptability across diverse plug seedling dimensions.

2.1.3. The Structural Parameter Model of Seedling-Picking Force-Measuring Component

The structural parameters of the seedling-picking force-measuring component in the force-measuring device should be designed based on the hole size of the seedling plugs used in the experiment [25]. In this paper, the hole sizes of common 50-hole, 72-hole and 128-hole seeding plugs were measured, respectively (Table 1).

Table 1. The hole size of common seedling plugs.

Seeding Plug Specification	Hole Upper Part Opening Size/mm	Hole Lower Part Opening Size/mm	Hole Height Size/mm	Hole Cone Angle/°
50-hole	50 × 50	24 × 24	48	15.15
72-hole	40 × 40	22 × 22	42	12.09
128-hole	32 × 32	14 × 14	44	11.56

The mathematical model of the movement of the seedling-picking force-measuring component is constructed (Figure 4), where L_1 is the installation point of the turning plate

fixed plate of the turning plate, L_2 is the length of the clamping needle, L_3 is the distance between the guide hole at the bottom of the seedling pushing frame and the center line of the seedling-picking force-measuring component, L_4 and L_4' are the distance between the tip of the clamping needle and the guide hole at the bottom of the seedling pushing frame before the clamping needle is inserted into the plug seedling pot and when the plug seedling pot is completely clamped, respectively, L_5 is the deflection length of the turning plate, and H and H′ are the vertical distance between the guide hole at the bottom of the seedling pushing frame and the turning plate fixed plate before the clamping needle is inserted into the plug seedling pot and when the plug seedling pot is completely clamped. α and α' are the insertion angle and clamping angle of the clamping needles for the plug seedling pot, γ is the deflection angle of the turning plate, H_e is the depth of the clamping needle inserted into the plug seedling pot, and β is the hole cone angle.

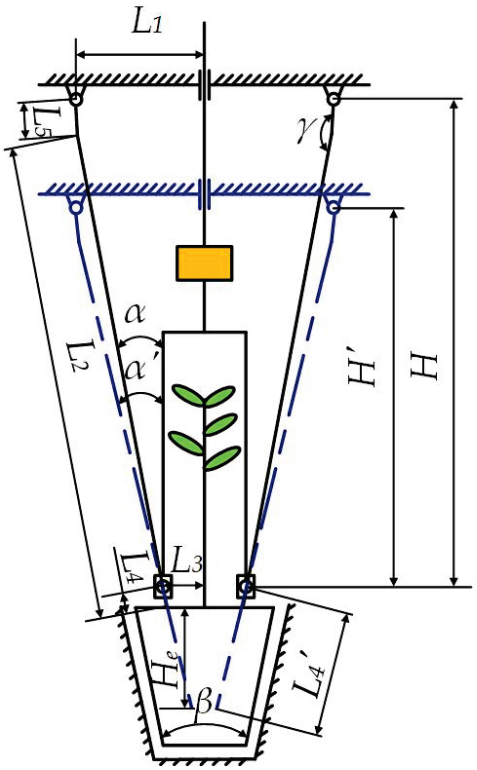

Figure 4. The mathematical model of the movement of the seedling-picking force-measuring component.

According to the measured hole size of the seeding plugs, the structural parameters of the seedling-picking force-measuring component were designed for the three specifications of the plug seedlings. The basis is as follows: when the clamping needles are completely inserted and clamped the plug seedling pot, the corresponding clamping angle α' should not be less than half of the hole cone angle β [26,27]; after the cylinder piston rod shrinks, H′ can still be greater than the plug seedling height of common vegetable plug seedlings; when the guide hole at the bottom of the seedling pushing frame is 5 mm away from the upper surface of the plug seedling pot, the clamping needle tip just touches the upper surface of the plug seedling pot. In order to ensure that the seedling-picking force-measuring component can be compatible with three specifications of the plug seedlings at the same time, based on the 128-hole plug seedling with the smallest hole, when the clamping needles are inserted into the plug seedling pot, the gap with the inner wall of the hole is less than 2~3 mm, which is beneficial to seedling picking [28]. At the same time, a certain angle

is set on the turning plates to minimize the size of the seedling-picking force-measuring component. The calculation formula of related structural parameters is as follows.

$$L_3 + (L_2 - L_4)sin\alpha + L_5 sin[\alpha - (180^\circ - \gamma)] = L_1 \quad (1)$$

$$L_3 + \left(L_2 - L_4'\right)sin\alpha' + L_5 sin\left[\alpha' - (180^\circ - \gamma)\right] = L_1 \quad (2)$$

$$L_4' cos\alpha' - L_4 cos\alpha = H_e \quad (3)$$

$$Htan\alpha = L_1 + L_5 cos[\alpha - (180^\circ - \gamma)]tan\alpha - L_5 sin[\alpha - (180^\circ - \gamma)] - L_3 \quad (4)$$

$$H'tan\alpha' = L_1 + L_5 cos\left[\alpha' - (180^\circ - \gamma)\right]tan\alpha' - L_5 sin\left[\alpha' - (180^\circ - \gamma)\right] - L_3 \quad (5)$$

$$L_3 - L_4 sin\alpha = 14 \quad (6)$$

$$L_4 cos\alpha = 5 \quad (7)$$

Based on the above analysis, H = 180 mm, L_5 = 7.5 mm, and γ = 6 °. The known parameters are brought into the above formula to obtain the relevant parameters of the seedling-picking force-measuring component (Table 2), where L_2 is 190 mm and L_3 is 15 mm.

Table 2. Structural parameters of the seedling-picking force-measuring component of plug seedlings of different specifications.

Seedling Plug Specification	H_e/mm	α'/°	α/°	L_1/mm	L_4/mm	L_4'/mm	H'/mm
50-hole	42.5	15.5	11.71	51	5.11	49.29	135.0
72-hole	36	12.5	10.05	47.5	5.08	41.99	142.5
128-hole	38	12.0	9.41	44	5.07	43.96	140.5

The diameter of the clamping needles is too large, which will increase the damage degree of the plug seedling pot, and too small will lead to a decrease in the success rate of seedling picking. To ensure the success rate of seedling picking, the damage degree of the plug seedling pot should be minimized. The diameter of the clamping needle is optimal at 2 mm [29]. At the same time, to prevent deformation of the clamping needle, a round bar of 65 Mn is selected for making the clamping needles, which can effectively improve their stiffness.

2.2. Dynamic Analysis of Seedling-Picking Motion

2.2.1. Control of Seedling-Picking Motion Parameters

In the process of automatic seedling picking by the force-measuring device, its motion is realized by the lifting module and the cylinder. In order to adapt to the required insertion depth of plug seedlings of different specifications, the maximum stroke of the cylinder piston rod should be 50 mm. According to the preliminary research of the research group [30], selecting the AIRTAC MD series cylinder with an inner diameter of 16 mm at a working pressure of 0.3 MPa can effectively ensure the clamping action of the plug seedling pot. Under the premise of a working pressure of 0.3 MPa, the average speed is calculated to be about 280 mm/s according to the actual measurement of the time taken by the cylinder piston rod to act 100 times.

As a component that drives the lifting and shifting of the seedling-picking force-measuring component, the lifting module should act synchronously with the cylinder of the seedling-picking force-measuring component to ensure the synchronization of the process of inserting and clamping the plug seedling pot. Therefore, taking the average working speed of the cylinder as a reference, the GBF-100 ball screw module of Wuxi Ebert transmission is selected. The lead of the screw is 20 mm, the effective stroke of the module

is 200 mm, the displacement accuracy is ±0.04 mm, the maximum load in the vertical direction is 10 kg, and the running speed is up to 400 mm/s.

The motion control system was meticulously designed based on the developed force-measuring device (Figure 5). The pneumatic circuit switching mechanism incorporates a sophisticated architecture combining magnetic switch state detection with solenoid valve on–off control for precise operation. A high-performance servo motor drive system was implemented to actuate the lifting module, complemented by a module proximity switch for accurate determination of the lifting module's home position. The control architecture features a PLC controller (XD5-24T4-C) supporting high-speed USB programming, coupled with an industrial-grade touch screen (TG865-MT/(ET)). Key electromechanical components include the following:

Servo motor—MF3H-60CS (CM) 30BZ1-504;
Servo driver—DF3E-0410Z;
Proximity switch—Omron TL-W3MC1;
Solenoid valve—AIRTAC 4V210-08B (two-position five-way);
Cylinder magnetic switch—AIRTAC CMSG020.

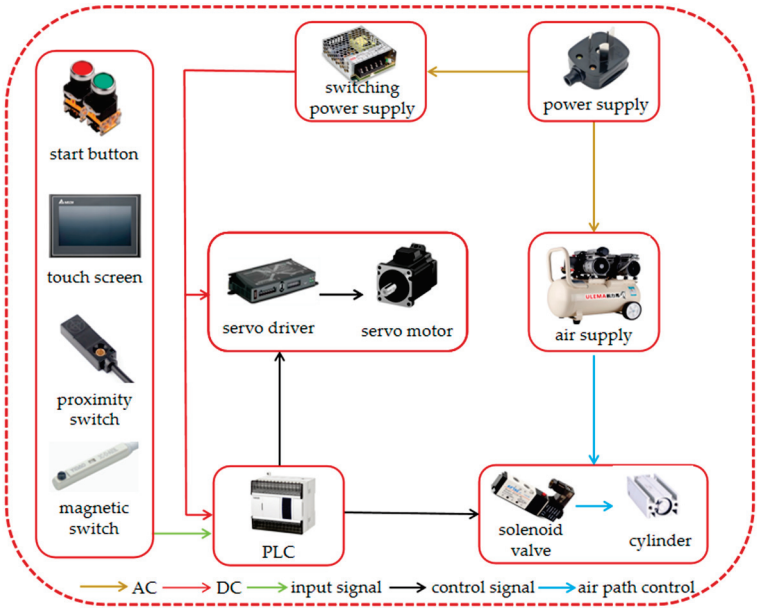

Figure 5. Motion control system composition diagram.

This integrated system configuration ensures precise force measurement and reliable control performance.

2.2.2. Dynamic Coupling Simulation of Seedling-Picking Motion via EDEM-RecurDyn

Based on clarifying the structural parameters and motion parameters of the force-measuring device, the water spinach plug seedlings were set as the experimental object, and the automatic seedling-picking coupling simulation experiment was carried out with four clamping needles for the 50-hole plug seedlings, which provided a reference for verifying the applicability of the force-measuring device.

After using SolidWorks (https://www.solidworks.com/) to establish a four-needle seedling-picking force-measuring component model for 50-hole plug seedlings, assembly and interference checks were performed. We then imported the virtual prototype model of the seedling-picking force-measuring component into RecurDyn (Figure 6a). According to the classification of the motion pairs in RecurDyn and the actual motion of the seedling-picking force-measuring component, the corresponding motion pairs were abstracted, and

the rotational and moving pairs between the components were defined. At the same time, an extended surface-to-surface contact was added between each clamping needle and the corresponding guiding hole at the bottom of the seedling pushing frame. Drives were added to the moving pair between the cylinder block and the ground, and the moving pair between the cylinder piston rod and the cylinder block, respectively, to simulate the longitudinal motion of the seedling-picking force-measuring component and the telescopic motion of the cylinder piston rod.

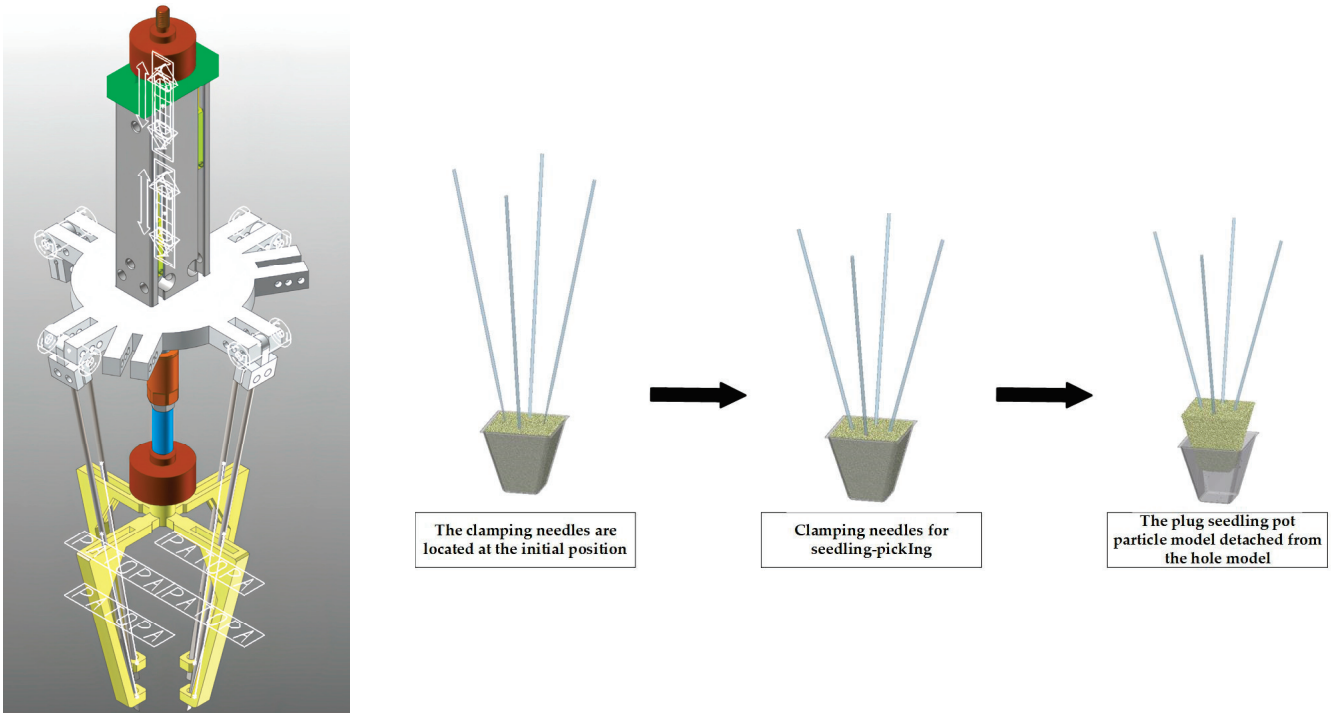

(**a**) (**b**)

Figure 6. EDEM-R ecurDyn coupling simulation. (**a**) Virtual prototype model of seedling-picking force-measuring component. (**b**) Coupling simulation experiment of seedling picking.

The substrate ratio of the water spinach plug seedling pot is mainly composed of peat, perlite and vermiculite in a ratio of 3:1:1. According to previous literature [24], the radius of the block model, the columnar model and the nuclear model is randomly distributed according to 0.2~0.5 mm, the radius of the spherical model is randomly distributed according to 1.5~3 mm, and the radius of the flake model is randomly distributed according to 0.4~1 mm. The seedling pot particle model is established in a way that ensures each particle has an equal number, and a total of 54,000 particles are generated. The Hertz–Mindlin with Bonding contact model is used to simulate the cohesive force between particles and the discrete problems such as cracking and breakage of the plug seeding pot under the action of external force [30]; at the same time, the Hertz–Mindlin with JKR model is used to describe the adhesion relationship between the matrix particles and the seeding plug [31].

The 50-hole seeding plug model was established using SolidWorks, and it was imported into EDEM to correlate with the set material parameters of the seeding plug. A particle factory was established on the upper surface of the hole model to generate particles, and a seedling pot particle model of a 50-hole plug seedling pot was established. The material of the clamping needle was 65 Mn, and the material of the seeding plug was polystyrene. We consulted the relevant material performance parameters [24,32–34] and completed the setting of material properties in EDEM as shown in Table 3.

Table 3. EDEM material properties' settings.

Item	Attribute	Value/Unit
Particle	Poisson's ratio	0.364
	Solids density	425 kg/m^3
	Shear modulus	1.6×10^6 Pa
Seeding plug	Poisson's ratio	0.38
	Solids density	1400 kg/m^3
	Shear modulus	8.66×10^8 Pa
Clamping needle	Poisson's ratio	0.288
	Solids density	7810 kg/m^3
	Shear modulus	8.0×10^{10} Pa
Particle–Particle	Coefficient of restitution	0.12
	Coefficient of static friction	0.65
	Coefficient of rolling friction	0.345
	Normal stiffness per unit area	1×10^8
	Shear stiffness per unit area	5×10^7
	Critical normal stress	3×10^4 Pa
	Critical shear stress	1.5×10^4 Pa
	Bonded disk radius	0.6 mm
Particle–Seedling plug	Coefficient of restitution	0.4
	Coefficient of static friction	0.2
	Coefficient of rolling friction	0.002
	Surface energy	1.513 J/m^2
Particle–Clamping needle	Coefficient of restitution	0.6
	Coefficient of static friction	0.397
	Coefficient of rolling friction	0.261

Based on the above content, the EDEM-RecurDyn coupling simulation experiment was carried out on the seedling-picking process of the clamping needles (Figure 6b). In the simulation process, the force of the clamping needles is applied to the plug seedling pot particle model in EDEM, and the data of the reaction force of the plug seedling pot particle model to the clamping needles are fed back to RecurDyn.

2.3. Force-Measuring Experimental Verification

2.3.1. Design of Experiment

The experiment was carried out in the Key Laboratory of Modern Agricultural Equipment and Technology, Ministry of Education, Jiangsu University from 27 to 29 April 2025. In this experiment, the water spinach plug seedlings (50-hole, 72-hole, 128-hole) cultivated in the greenhouse were selected as the experimental objects. The seedling age was 35 days, the matrix compaction degree was 1:1.2, and the seedling height was 100~120 mm. The seedling roots can tightly twine the matrix particles. When the plug seedlings are pulled out from the seeding plug, there will be no scattered lumps. Before the experiment, the plug seedlings were given water, so that the water content of the plug seedling pot was maintained at a moderate level of 60~65%, which was suitable for the automatic seedling picking operation [35].

In order to verify the functionality, applicability and versatility of the designed force-measuring device, different specifications of plug seedlings (including 50-hole, 72-hole and 128-hole) and different numbers of clamping needles (including two-needle, three-needle and four-needle) were used as experimental factors, and the automatic seedling-picking force-measuring was carried out through the force-measuring device (Figure 7). During

the experiment, the whole plug seedlings to be tested were cut in groups and placed on the seeding plug positioning plate, and 30 holes were tested in each group. Before the experiment, the plug seedlings were manually aligned. The experimental process was automatically executed; the seedling-picking force-measuring component dropped vertically from the top of the plug seedling to be tested, and the automatic seedling picking operation was performed when the plug seedling was reached. After the completion, the plug seedling was lifted vertically to the initial height to release the plug seedling. According to the size of three different specifications of plug seedlings, the position of the seedling-picking point and the insertion depth of the clamping for the lug seedling pot were set, respectively. We connected the data collector, set the sampling frequency to 200 Hz, and collected and recorded the corresponding mechanical experimental signals.

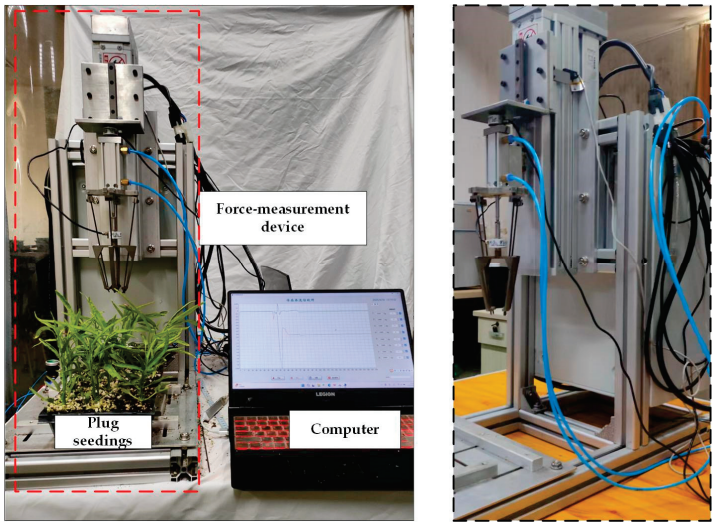

Figure 7. Plug seedling automatic seedling-picking force-measuring experiment.

Before the experiment, the standard values (such as pull, pressure, etc.) generated by the two pull-pressure sensors used were used as metrics to obtain the corresponding outputs and calibrate them (Table 4).

Table 4. The main performance parameters of the pull-pressure sensors.

Sensor Name	Technical Parameter	Parameter Calibration
pull-pressure sensor-1	Range: 10 kg; Composite precision: ±0.05%; sensitivity: 1.12 ± 0.05 mV/V	$F_1 = 1.9996X_1 - 0.0008$ $R^2 = 0.999$
pull-pressure sensor-2	Range: 3 kg; Composite precision: ±0.05%; sensitivity: 0.90 ± 0.04 mV/V	$F_2 = 0.5999X_2 + 0.0038$ $R^2 = 1.000$

Note: X_1 and X_2 are the voltage signals measured by the corresponding sensors, V, respectively.

Before the experiment, an electronic balance was used to weigh the average mass M_1 of the tested plug seedlings before the experiment. After the experiment was completed, the average mass M_2 of the tested plug seedlings after being clamped was weighed, and then the integrity of the plug seedling pot I_R after automatic seedling-picking force-measuring experiment was calculated:

$$I_R = \frac{M_2}{M_1} \times 100\% \quad (8)$$

After the experiment, Microsoft Excel software was used to process the data measured by the relevant pull-pressure sensors. Then, based on the measured data, the relevant mechanical curves of the disengaging force F_N and the clamping force F_J of the plug

seedling pot were obtained, and the data of the key points on the relevant mechanical curves were statistically analyzed.

2.3.2. The Measured Mechanical Curve Transformation

The force values measured by the pull-pressure sensor-1 and the pull-pressure sensor-2 arranged on the seedling-picking force-measuring component are the interaction forces between the structures of the seedling-picking force-measuring component in the process of automatic seedling picking, which need to be transformed into the relevant forces of the plug seedling pot in the process through the corresponding mechanical analysis.

The relevant mechanical analysis was carried out on the disengaging force (F_N) of the plug seedling pot when the clamping needles clamped the plug seedling pot out of the seeding plug in the force-measuring device (Figure 8a). F_1 is the force of the pull-pressure sensor-1 when the seedling-picking force-measuring component clamps the plug seedling pot out of the seeding plug. F_0 is the resultant force of the pre-tightening force of the pull-pressure sensor-1, and G_S is the gravity of the plug seedling itself. The relevant mechanical transformation formula is as follow:

$$F_1 = F_N + F_0 + G_s \tag{9}$$

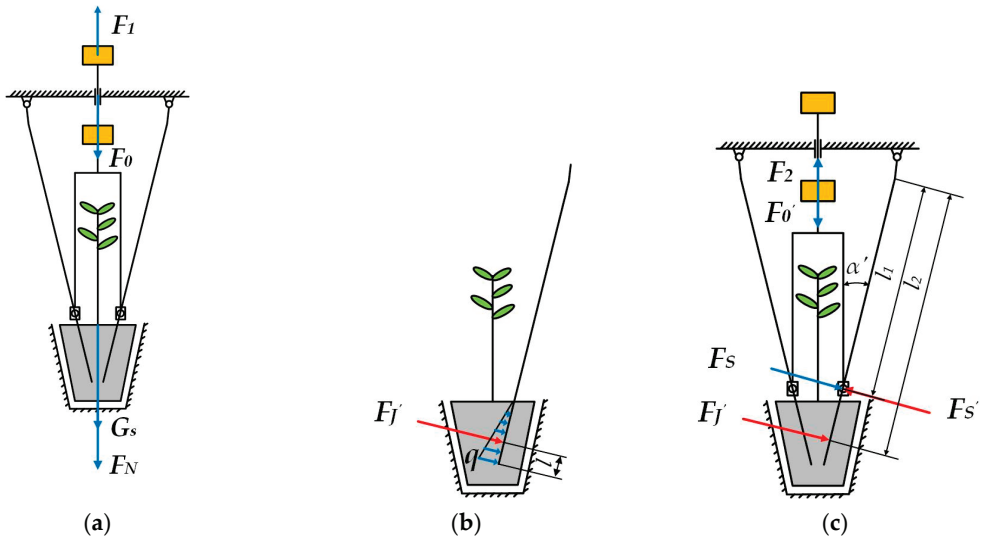

Figure 8. Related mechanical analysis. (**a**) Disengaging force-related mechanical analysis. (**b**) Extrusion load on the clamping needle. (**c**) Clamping force-related mechanical analysis.

It can be seen that the plug seedling pot is separated from the seeding plug to overcome its internal adhesion, that is, the disengaging force of the plug seedling pot is:

$$F_N = F_1 - F_0 - G_s \tag{10}$$

The clamping force (F_J) applied to the plug seedling pot and the extrusion force (F_J') of the plug seedling pot received during the clamping of the plug seedling pot interact with each other. The extrusion force (F_J') takes the form of triangular distribution load. Therefore, it is necessary to equivalently transform the triangular distribution load of the extrusion force to one point. The action point of the equivalent transformed force is one-third of the maximum load concentration q, that is, the clamping force is concentrated at l from the clamping needle tip (Figure 8b).

The relevant mechanical analysis is carried out for the clamping force (F_J) applied to the plug seedling pot in the force-measuring device (Figure 8c). F_2 is the pull measured by the pull-pressure sensor-2 when the seedling-picking force-measuring compo-

nent is taken, F_0' is the pre-tightening force of the pull-pressure sensor-2 installation, n is the number of clamping needles of the seedling-picking force-measuring component (n = 2/3/4), and α' is the angle between the clamping needle and the vertical direction when the seedling-picking force-measuring component is taken to clamp the plug seedling pot. F_S and F_S' are interactive forces, and F_S is the extrusion force for the guide hole at the bottom of the seedling pushing frame. F_S' is the binding force of the guide hole at the bottom of the seedling pushing frame on the clamping needle. The relevant mechanical transformation formula is as follows:

$$F_2 = F_0' + nF_S sin\alpha' \tag{11}$$

$$F_S = F_S' \tag{12}$$

$$F_S' l_1 = F_J' l_2 \tag{13}$$

$$F_J' = F_J \tag{14}$$

$$l = 1/3\left(L_4' - L_4\right) \tag{15}$$

$$l_1 = L_2 - L_4' \tag{16}$$

$$l_2 = L_2 - l \tag{17}$$

It can be seen from this that the clamping force applied to the plug seedling pot by a single clamping needle is

$$F_J = \frac{(L_2 - L_4)(F_2 - F_0')}{nsin\alpha'\left[L_2 - 1/3\left(L_4' - L_4\right)\right]} \tag{18}$$

3. Results

3.1. Functional Analysis of Force-Measuring Device

The process of automatic seedling picking by the designed force-measuring device is as follows: the seedling-picking force-measuring component drops to the seedling-picking point as a whole, the clamping needles insert and clamp the plug seedling pot, the seedling-picking force-measuring component takes the plug seedling out of the seedling plug and rises as a whole, and the seedling-picking force-measuring component pushes the plug seedling down (Figure 9). The main motion of the designed automatic seedling-picking force-measuring device is borne by the lifting module driven by the servo motor. Due to the accuracy of the servo system, the force-measuring device can complete the seedling-picking action smoothly and coherently.

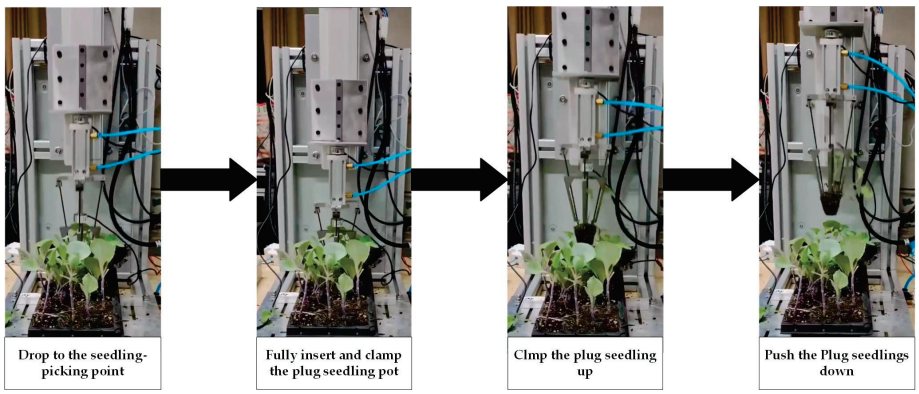

Figure 9. Automatic seedling-picking process of force-measuring device.

Figure 10 shows the relevant mechanical curves of the automatic seedling picking experiment for 50-hole plug seedlings. The orange curve represents the relevant mechanical curve F_1 measured by the pull-pressure sensor 1, the green curve is the relevant mechanical curve F_2 measured by the pull-pressure sensor 2, the blue curve represents the F_N correlation curve of the disengaging force transformed by the F_1 (Formula (10)), and the purple curve represents the F_J correlation curve of the clamping force transformed by the F_2 (Formula (18)).

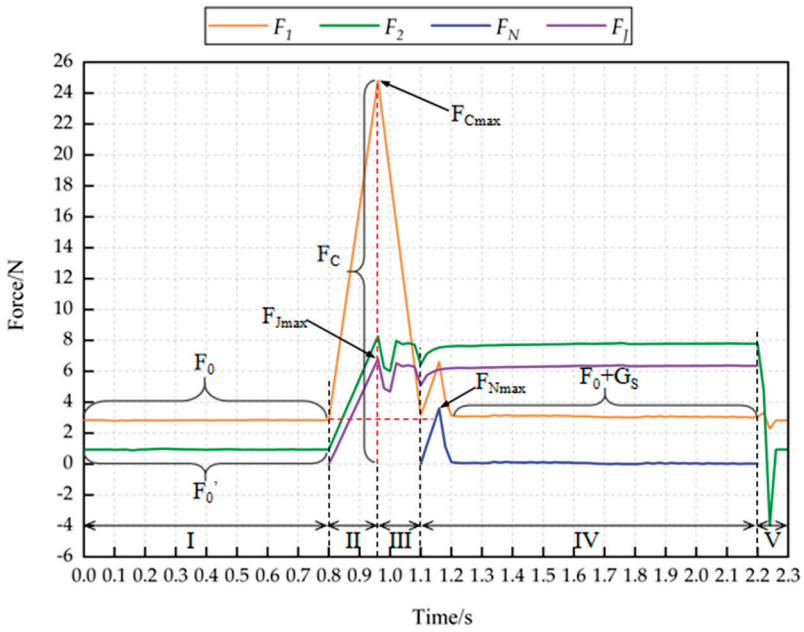

Figure 10. Related mechanical experimental curves produced in the process of the force-measuring experiment. F_0 and F_0' are the installation preload of the pull-pressure sensor 1 and the pull-pressure sensor 2, respectively, N; F_{Jmax} is the peak value of the clamping force, N; F_{Nmax} is the peak value of the disengaging force, N; G_S is the gravity of the plug seedling itself, N; F_C is the oblique insertion force in the process of inserting the clamping needle and clamping the plug seedling pot, N; F_{Cmax} is the peak value of the oblique insertion force during the process of inserting the clamping needle and clamping the plug seedling pot, N.

Stage I involves the seedling-picking force-measuring component dropping at a constant speed (150 mm/s) under the drive of the lifting module, and reaching the seedling-picking point at 0.8 s. At this time, the clamping needle tip is just in contact with the upper surface of the plug seedling pot. The relevant mechanical curves measured by the pull-pressure sensor 1 ($F_1 = F_0$) and the relevant mechanical curves measured by the pull-pressure sensor 2 ($F_2 = F_0'$) remain approximately constant, and there is no significant change.

Stage II combines the lifting module (operating speed of 280 mm/s) and the cylinder (with a piston rod expansion pressure of 0.3 MPa), enabling the insertion and clamping of the clamping needles into the plug seedling pot. At 0.8 s, the clamping needles began to insert and clamp the plug seedling pot. The relevant mechanical curves measured by the pull-pressure sensor 1 and the relevant mechanical curves measured by the pull-pressure sensor 2 jumped synchronously, and reached the peak point at about 0.96 s. It can be noted that the clamping force (F_J) of the single clamping needles for the plug seedling pot and the oblique insertion force (F_C) during the insertion and clamping of the clamping needles increase linearly with the increase in the insertion depth of the plug seedling pot until the peak value of the clamping force (F_{Jmax}) and the peak value of the oblique insertion force

(F_{Cmax}) are reached when the plug seedling pot is completely inserted and clamped. At this time, the cylinder piston rod shrinks in place, and the lifting module stops running.

Stage III comprises a short stay after the clamping needles are completely inserted and clamped into the plug seedling pot. Due to the impact of the cylinder piston rod, the relevant mechanical curves measured by the pull-pressure sensor 2 show large fluctuations. For this reason, the force-measuring device is set to be temporarily stationary to prevent the subsequent measured mechanical curves from being affected by the impact, resulting in a distortion of the experimental results. At the same time, within the last approximately 0.03 s of this stage, there is a decreasing trend in the clamping force F_J correlation curve, which may be due to the fact that as the force-measuring device gradually returns to stability, the plug seedling is still in the seeding plug, and the clamping force applied by the clamping needles on the plug seedling tends to relax, maintaining a brief equilibrium with the plug seedlings.

Stage IV is when the seedling-picking force-measuring component takes the plug seedling out of the seeding plug and rises as a whole. In the first 0.04 s of this stage, the secondary lifting of the clamping force (F_J) correlation curve enables the plug seedling pot to receive sufficient clamping force to overcome its adhesion to the inner wall of the seeding plug. Due to the instantaneous relaxation of the matrix caused by the impact of the cylinder piston rod in place on the plug seedling pot in stage II, the correlation curve of the clamping force (F_J) in stage IV shows a certain drop compared with the peak value of the clamping force (F_{Jmax}). At about 1.14 s, the disengaging force (F_N) correlation curve reached the peak value of the disengaging force (F_{Nmax}), which corresponded to the critical point of root–hole wall adhesion and fracture. At this time, the plug seedling pot was completely separated from the inner wall of the seeding plug. After that, the relevant mechanical curves measured by the pull-pressure sensor 1 were stable in the combined force of the pre-tightening force and the gravity of the plug seedling ($F_1 = F_0 + G_S$), and the clamping force (F_J) correlation curve remained stable synchronously.

Stage V involved taking the seedling-picking force-measuring component to push the plug seedling down. At this time, the seedling-picking force-measuring component was separated from the plug seedling, resulting in the relevant mechanical curves measured by the pull-pressure sensor 1 ($F_1 = F_0$) and the relevant mechanical curves measured by the pull-pressure sensor 2 ($F_2 = F_0'$) plummeting to the pre-tightening force ($F_1 = F_0$, $F_2 = F_0'$). The disengaging force (F_N) and the clamping force (F_J) returned to zero, and a mechanical cycle was completed.

3.2. Applicability Analysis of Force-Measuring Device

Under the set motion conditions, the four clamping needles were applied in the 50-hole plug seedling pot particle model to carry out the coupling simulation experiment of the clamping seedling, and the relevant mechanical curve (Figure 11) was obtained. In order to reduce the amount of calculation, the coupling simulation experiment of seedling picking in this study only analyzed the stages II to IV in Figure 10. In these three stages, the clamping needles were in direct contact with the plug seedling pot. The orange curve represents the disengaging force (F_{Nt}) correlation curve of the plug seedling pot particle model in the coupling simulation experiment, and the green curve represents the clamping force (F_{Jt}) correlation curve applied to the seedling pot particle model by a single clamping needle in the coupling simulation experiment.

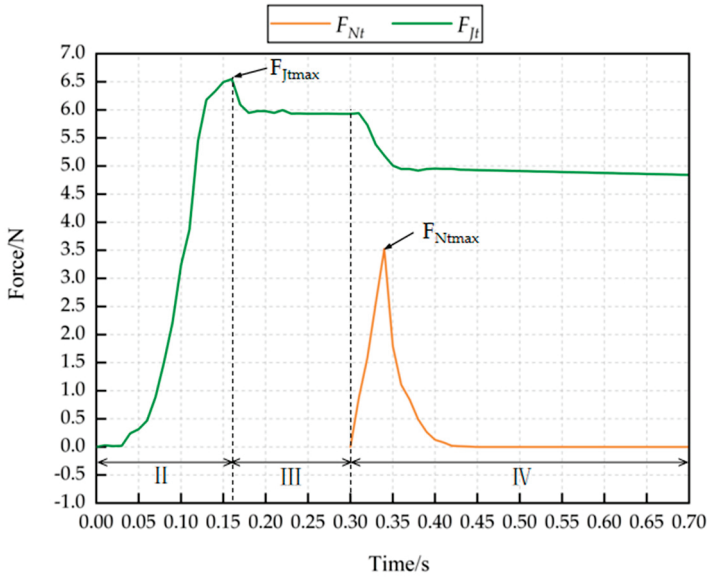

Figure 11. The relevant mechanical curves in the coupling simulation experiment. F_{Ntmax} is the peak value of the disengaging force of the plug seedling pot particle model from the hole model of seeding plug, N; F_{Jtmax} is the peak value of the clamping force applied to the plug seedling pot particle model by a single clamping needle, N.

The plug seedling pot particle model was only subjected to the disengaging force (F_{Nt}) of the clamping needles lifted upward to take it out of the hole model in stage III. The disengaging force (F_{Nt}) of the plug seedling pot particle model began to increase from the time of 0.3 s, and it began to decrease to zero after reaching the peak value (F_{Ntmax}) at about 0.34 s. At 0.34 s, the plug seedling pot particle model was completely separated from the hole model. For the coupling simulation experiment, the disengaging force (F_{Nt}) correlation curve of the plug seedling pot particle model is approximately consistent with the trend of the disengaging force F_N curve of the plug seedling pot in Figure 10, and the peak value of disengaging force (F_{Ntmax} = 3.62 N) and the appearance time (0.04 s after starting to leave the hole model) are relatively close.

For the correlation curve of the clamping force (F_{Jt}) applied to the plug seedling pot particle model by a single clamping needle in the coupling simulation experiment, in stage II, as the clamping needles were inserted into the plug seedling pot particle model, the clamping force (F_{Jt}) of the single clamping needle of the plug seedling pot particle model gradually increased, but this was not an absolute linear change trend. The main reason is that the particles in the plug seedling pot particle model were randomly distributed, and there was still a certain gap inside the compaction. However, the particle gap between the plug seedling pot matrix used in the actual experiment was small, resulting in a certain error between the reaction force of the plug seedling pot particle model and the actual situation in the process of inserting the clamping needles into the seedling pot particle model, but the overall trend was close to that shown in Figure 11, and the size of the peak value of the clamping force (F_{Jtmax} = 6.54 N) and the occurrence time (0.16 s after the clamping needles are inserted into the seedling pot particle model) also showed small errors. In stage III, the clamping force (F_{Jt}) applied to the plug seedling pot particles model began to fall back briefly and tended to be stable. In Figure 10, due to the impact of the cylinder piston rod, the mechanical curve measured by the pull-pressure sensor fluctuated greatly, but the overall trend was similar. In the initial stage of stage IV, the correlation curve of clamping force (F_{Jt}) was also different from that in Figure 10. The reason is that the stop time set by the force-measuring device was short, and the impact of the cylinder piston rod was not completely eliminated. With the clamping needles clamping the plug seedling

pot particle model out of the hole model, the clamping force (F_{Jt}) began to stabilize, but because the clamping needles continuously applied the clamping force to the plug seedling pot particle model, the particles would produce less shedding, which made the clamping force (F_{Jt}) show a decreasing trend.

In summary, the disengaging force F_N and clamping force F_J curves of the plug seedling pot measured by the force-measuring device in Figure 10 are similar to the disengaging force (F_{Nt}) and clamping force (F_{Jt}) curves of the plug seedling pot particle model obtained by the coupling simulation experiment in Figure 11, which proves that the force-measuring device is suitable for exploring the dynamic coupling process between the seedling-picking device and the plug seedling pot during the automatic seedling-picking process.

3.3. Universality Analysis of Force-Measuring Device

The correlation of the peak value of the disengaging force (F_{Nmax}) of the plug seedlings in the mechanical experiment were analyzed (Figure 12a). Taking four clamping needles as an example, the range of the F_{Nmax} of the 50-hole plug seedlings was 3.39~3.71 N; the range of the F_{Nmax} of 72-hole plug seedling was 1.87~2.18 N; for the 128-hole plug seedlings, the range of the F_{Nmax} of the seedling pot was 0.97~1.19 N. As shown in Table 5, the effects of the seedling plug specification on F_{Nmax} were extremely significant ($p < 0.01$).

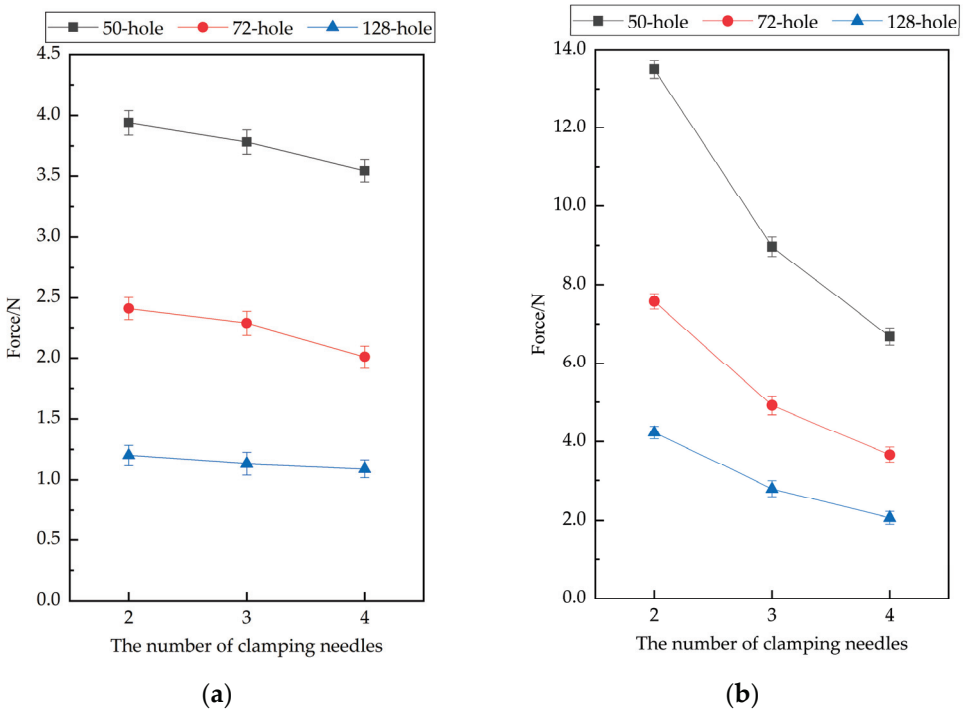

Figure 12. Related mechanical properties of plug seedlings. (**a**) The correlation of the peak value of the disengaging force of the plug seedlings. (**b**) The correlation of the peak value of the clamping force of the plug seedlings.

When the number of clamping needles is the same, with the decrease in the size of the plug seedling pot, the peak value of the disengaging force (F_{Nmax}) of the plug seedling pot decreases when the clamping needles clamp the plug seedling out of the seeding plug. The main reason is that with the decrease in the hole volume, the contact area between the pot seedling substrate and the inner wall of the hole decreases. At the same time, with the decrease in the size of the plug seedling pot, the clamping volume of the plug seedling pot is larger in the designed seedling-picking force-measuring component. Therefore, in order to make the clamping needles successfully clamp the plug seedling out of the seeding plug, in the process of inserting and clamping the plug seedling pot, it should be ensured that the

clamping needles grasp most of the root–soil composite structure of the plug seedling pot, forcing the internal matrix of the plug seedling pot to gradually loosen and then driving the seeding-picking force-measuring component to the plug seedling to lift up and separate from the seeding plug, which has the effect of stabilizing the clamping plug seeding pot.

Table 5. Variance analysis of related mechanical properties of plug seedlings.

Force	Source	Sum of Squares	Freedom	Mean Square	F Value	*p* Value	Significance
F_{Nmax}	Seedling plug specification	310.107	2	155.053	18,350.197	0.000	**
	The number of clamping needles	4.199	2	2.100	248.476	0.000	**
F_{Jmax}	Seedling plug specification	2069.470	2	1034.735	24,272.779	0.000	**
	The number of clamping needles	862.124	2	431.062	10,111.837	0.000	**

Note: ** means significant level at $p < 0.01$.

Taking the 50-hole plug seedlings as an example, the range of the F_{Nmax} of the plug seedlings was 3.77~4.09 N when the two clamping needles were used. The range of the F_{Nmax} of the plug seedlings was 3.62~3.94 N when three clamping needles were used. The range of the F_{Nmax} of the plug seedlings was 3.39~3.71 N when four clamping needles were used. As shown in Table 5, the number of clamping needles also has a significant impact on F_{Nmax} ($p < 0.01$).

For plug seedlings of the same specification, the F_{Nmax} gradually decreased with an increase in the number of clamping needles. Due to the inclined clamping of the clamping needles, the plug seedling pot was forced to deform upward and loosen, which is equivalent to applying the prying action from the inside of the plug seedling pot [36]. Therefore, with the increase in the number of clamping needles, a stronger encapsulation of the plug seedling pot can be induced, so that the clamping forces of the clamping needles are more uniform. At the same time, the internal gap caused by the clamping needles' insertion into the plug seedling pot increases, forcing the internal matrix of the plug seedling pot to loosen, and weakening the adhesion between the plug seedling pot and the hole to a certain extent.

The peak value of the clamping force (F_{Jmax}) of the plug seedlings in the mechanical experiment were analyzed (Figure 12b). Taking four clamping needles as an example, the range of the F_{Jmax} of a single clamping needle in the 50-hole plug seedling pots was 6.28~7.05 N; the range of the F_{Jmax} of the single clamping needle in the 72-hole plug seedling pots was 3.30~3.98 N; the range of the F_{Jmax} of the single clamping needle in the 128-hole plug seedling pots was 1.76~2.35 N. As shown in Table 5, the effect of the seedling plug specifications on F_{Jmax} is extremely significant ($p < 0.01$).

When the number of clamping needles is the same, as the size of the plug seedling pot decreases, the peak value of the clamping force (F_{Jmax}) applied to the seedling pot by the single clamping needle decreases, and there is a certain rule affecting the change of the F_{Nmax}. From the above analysis, it can be seen that with the decrease in the size of the plug seedling pot, the adhesion force between the plug seedling pot and the seedling plug that the plug seedling pot needs to overcome is reduced, and the clamping force (F_J) of the plug seedling pot is mainly used to overcome the adhesion force between the plug seedling pot and the seedling plug.

Taking 50-hole plug seedlings as an example, the range of the F_{Jmax} of a single clamping needle in the plug seedling pot was 12.99~13.97 N when the two clamping needles were

used; the range of the F_{Jmax} for a single clamping needle in the plug seedling pot was 8.54~9.41 N when the three clamping needles were used; the range of the F_{Jmax} of the single clamping needle in the plug seedling pot was 6.28~7.05 N when the four clamping needles were clamped. As shown in Table 5, the number of clamping needles also has a significant impact on F_{Jmax} ($p < 0.01$).

For plug seedlings with the same specification, with the increase in the number of clamping needles, the peak value of the clamping force (F_{Jmax}) applied to the plug seedling pot by a single clamping needle gradually increases linearly, and the proportional relationship is close to the proportional relationship of the number of clamping needles. Therefore, it can be concluded that for the plug seedlings of the same specification, the number of different clamping needles causes little difference in the resultant force of the clamping force applied to the plug seedling pot, and it is synchronized with the F_{Jmax} of the plug seedling pot in Figure 12a. The clamping force of the clamping needle on the plug seedling pot can be changed by adjusting the number of clamping needles. Excessive clamping force will break the plug seedling pot. Therefore, in order to ensure a better seedling-picking effect, the resultant force of the clamping force applied to the plug seedling pot should be within a reasonable range.

We analyzed the integrity of the plug seedling pot with different specifications of plug seedlings and different numbers of clamping needles, as shown in Table 6. The success rate of using the force-measuring device to remove the plug seedlings from the seedling plug clamp during the experiment was 100%, and the integrity of the plug seedling pot (I_R) was above 96% under the experimental conditions. This proves that the force-measuring device designed in this study can complete the automatic seedling-picking force-measuring experiment while ensuring a low rate of damage to the plug seedling pot.

Table 6. Integrity analysis of plug seedling pot.

Seedling Plug Specification	The Number of Clamping Needles	M_1/g	M_2/g	I_R/%
50-hole	2	34.25	33.28	97.17
	3	33.93	32.86	96.85
	4	35.62	34.34	96.41
72-hole	2	20.97	20.47	97.62
	3	22.43	21.77	97.06
	4	21.62	20.91	96.72
128-hole	2	13.25	13.06	98.56
	3	13.12	12.88	98.17
	4	12.47	12.16	97.51

4. Discussion

A force-measuring device was proposed in this study that enables the quantitative investigation of the dynamic interaction mechanisms between the seedling-picking device and plug seedlings during automated transplantation processes. The novel force-measuring device can carry out automatic seedling-picking force-measuring experimental research for different specifications of plug seedlings and different numbers of clamping needles. By providing precise force measurement capabilities to verify its functionality, applicability and versatility, the device can become a standardized experimental platform, thereby contributing to the optimization of transplanting machine performance.

Regarding the functionality of the force-measuring device, this study successfully developed a force-measuring device founded on the centrally symmetrical clamping needle layout and a simultaneous insertion and clamping mechanism. Through modular design

(supporting 2/3/4 needles switching) and parameter stepless adjustment (adapting to 50-hole/72-hole/128-hole), the dynamic response curves of the clamping force and the disengaging force of the plug seedlings during the automatic seedling picking process were accurately obtained. Compared with the built-in pot seedling clamping force sensor of Jin et al. [19], the influence of the sensor structure and installation method on the interference of the standard pick-and-throw action of the seedling-picking end-effector is effectively solved. However, the required clamping needle size is larger, which increases the likelihood of causing damage to the plug seedling pot matrix during the actual seedling picking process. Their study only detected the clamping force of the plug seedling pot. In this study, the time series coupling relationship between the clamping force F_J and the disengaging force F_N of the plug seedling pot during the seedling-picking operation was detected synchronously by the dual sensor system. In the experiment, a specific relationship was identified between the change in clamping force and the disengaging force of the plug seedling pot during the automatic seedling-picking process, consistent with the conclusion drawn by Han et al. [21] using a designed force-measuring device.

To verify the applicability of the force-measuring device, water spinach plug seedlings were used as the experimental object in this research. Through the combination of EDEM-RecurDyn coupling simulation experiment and mechanical verification experiment, the coupling simulation experiment can obtain the dynamic coupling relationship between the disengaging force (F_{Nt}) and the clamping force (F_{Jt}) of the seedling pot of the plug seedling pot particle model during the seedling-picking process. The experimental signal fluctuation resulting from the cylinder piston rod's impact is reasonably predicted in the mechanical verification experiment's results. The experimental results show that the disengaging force F_N curve and the clamping force (F_J) curve measured by the force-measuring device in Figure 10 are highly consistent with the disengaging force (F_{Nt}) curve and the clamping force (F_{Jt}) curve of the plug seedling pot particle model obtained by the coupling simulation experiment in Figure 11. The force-measuring device designed in this study can explore the dynamic coupling process between the seedling-picking device and the plug seedling. Jiang et al. [17] tested the interaction force between the designed four-needle seedling-picking end-effector and the plug seedling only by arranging the pull-pressure sensor. Tian et al. [21] qualitatively described this phenomenon only through EDEM simulation, and both lacked a comparative analysis of theoretical data and actual data.

Following the verification of the designed force-measuring device's functionality and applicability, this study conducted a universal verification experiment on the device using plug seedlings of different specifications and varying numbers of clamping needles, and analyzed the experimental results. For the same number of clamping needles, with the decrease in the size of the plug seedling pot, the peak value of the disengaging force (F_{Nmax}) required for the plug seedling pot to separate from the seeding plug due to the change of the quality of the plug seedling pot and the contact area with the seeding plug was also correspondingly reduced, which was mainly due to the decrease in the size of the plug seedling pot, which led to a decrease in the contact area with the inner wall of the seeding plug hole and the overall quality of the plug seedling, thus weakening the adhesion between the substrate and the seeding plug wall. The peak value of the clamping force (F_{Jmax}) applied to the plug seedling pot by a single clamping needle also decreased exponentially. This phenomenon is closely related to the change trend of the disengaging force, indicating that in the process of automatic seedling picking, the clamping force is mainly used to overcome the adhesion resistance between the plug seedling pot and the seeding plug. There is a significant synchronous variation between the disengaging force and the clamping force, which reflects the intrinsic correlation between the two in the mechanical mechanism. For plug seedlings of the same specifications, increasing the

number of clamping needles results in a decreasing trend in the peak disengaging force (F_{Nmax}) required to clamp the plug seedling away from the seeding plug. The main reason is that the simultaneous insertion and clamping of the clamping needles causes the pre-split zone inside the plug seedling pot to loosen during the seedling-picking process. The more clamping needles used, the more obvious the effect; at the same time, the peak value of the clamping force (F_{Jmax}) applied by a single clamping needle for the plug seedling pot is also approximately proportionally reduced. The above is due to the increase in the number of clamping needles, which leads to an increase in the number of force points and a more uniform distribution of the plug seedling pot. Under the premise that the total clamping force remains relatively stable in order to meet the needs of seedling picking, the load dispersed to each clamping needle is reduced accordingly. This decrease is basically consistent with the proportion of the increase in the number of clamping needles. Based on the content above, it can be concluded that the force-measuring device designed in this study can conduct automatic seedling-picking force-measuring experiments for various plug seedlings specifications and different numbers of clamping needles, thereby meeting general requirements.

A force-measuring device was proposed and validated in its functionality, applicability, and universality. However, several limitations still persisted, as follows: the verification process for crops was relatively simplistic, the test parameters were somewhat fixed, and the number of coupled verification was limited. These factors constrain the device's overall functionality, applicability, and universality to some extent, indicating areas for future testing and enhancement.

5. Conclusions

In this research, a universal automatic seedling-picking force-measuring device was successfully developed, which is based on the central symmetric clamp needle layout and the simultaneous insertion and clamping mechanism. The modular design enables the flexible adjustment of the number of clamping needles (2/3/4 needles), which can be adapted to the insertion depths (42.5 mm, 36 mm, 38 mm) and clamping angles (12°, 12.5°, 15.5°) of 50-hole, 72-hole, and 128-hole plug seedlings. Its functionality, applicability, and universality were verified through simulation and experimentation. The main conclusions are presented as follows:

1. A real-time monitoring system with dual pull-pressure sensors was integrated to precisely acquire the relevant mechanical curves during the automatic seedling-picking process. Through formula transformation, the dynamic response curves of the disengaging force (F_N) and the clamping force (F_J) were accurately obtained, thereby validating the functionality of the force-measuring device;

2. The results of the EDEM-RecurDyn coupling simulation experiment were highly consistent with those of the mechanical experiment. Specifically, the errors between the peak value of the disengaging force (F_{Nmax}) and the peak value of the clamping force (F_{Jmax}) were minor, and the dynamic response curves of the disengaging force (F_N) and the clamping force (F_J) were approximately identical. The above proves that the device can effectively explore the dynamic coupling process between the seedling-picking device and the plug seedling, and verifies the applicability of the force-measuring device;

3. A systematic force-measuring experiment for seedling-picking was conducted on plug seedlings of different specifications (50-hole, 72-hole, 128-hole) and with different numbers of clamping needles (2/3/4 needles). The results indicate that, regarding the characteristics of the disengaging force, the peak value of the disengaging force (F_{Nmax}) increased significantly as the hole size increased, and an increase in the number of clamping needles contributed to a reduction in F_{Nmax}; regarding the characteristics of the clamping

force, the peak value of the clamping force (F_{Jmax}) applied to the plug seedling pot by a single clamping needle was approximately inversely proportional to the number of clamping needles, and the distribution of the clamping force on the plug seedling pot under the four-needle layout was the most uniform. These results verify the general requirements of the designed force-measuring device for conducting the automatic seedling-picking force-measuring experiment.

Author Contributions: Conceptualization, T.H. and X.C.; methodology, T.H., X.C. and J.H.; software, T.H., W.L. and J.L.; validation, T.H., J.H. and W.L.; formal analysis, T.H. and Y.T.; investigation, T.H. and X.C.; resources, X.C. and J.H.; data curation, T.H. and J.L.; writing—original draft preparation, T.H.; writing—review and editing, X.C., J.H., W.L. and F.L. All authors have read and agreed to the published version of the manuscript.

Funding: This research was funded by the Research and Application of Key Technology and Equipment for Efficient Automatic Transplanting of Open field Cabbage (No. NJ2024-04); Jiangsu Modern Agricultural Machinery Equipment and Technology Demonstration Project (No. NJ2021-08); the Priority Academic Program Development of Jiangsu Higher Education institutions (No. PAPD-2023-87); China Postdoctoral Science Foundation (2024MM751185).

Institutional Review Board Statement: Not applicable.

Data Availability Statement: The original contributions presented in the study are included in the article; further inquiries can be directed to the corresponding author.

Conflicts of Interest: Author Fengpeng Li was employed by the company Qingshan Environmental Protection Technology Co., Ltd. The remaining authors declare that the research was conducted in the absence of any commercial or financial relationships that could be construed as a potential conflict of interest.

References

1. Jin, X.; Yuan, Y.; Ji, J.; Zhao, K.; Li, M.; Chen, K. Design and implementation of anti-leakage planting system for transplanting machine based on fuzzy information. *Comput. Electron. Agric.* **2020**, *169*, 105204. [CrossRef]
2. Zhou, M.; Shan, Y.; Xue, X.; Yin, D. Theoretical analysis and development of a mechanism with punching device for transplanting potted vegetable seedlings. *Int. J. Agric. Biol. Eng.* **2020**, *13*, 85–92. [CrossRef]
3. Ma, G.; Mao, H.; Bu, Q.; Han, L.; Shabbir, A.; Gao, F. Effect of compound biochar substrate on the root growth of cucumber plug seedlings. *Agronomy* **2020**, *10*, 1080. [CrossRef]
4. Liu, J.; Zhao, S.; Li, N.; Faheem, M.; Zhou, T.; Cai, W.; Zhao, M.; Zhu, X.; Li, P. Development and field test of an autonomous strawberry plug seeding transplanter for use in elevated cultivation. *Appl. Eng. Agric.* **2019**, *35*, 1067–1078. [CrossRef]
5. Zhou, M.; Xu, T.; Wang, G.; Dong, H.; Yang, S.; Wang, Z. Design of a 2R Open-Chain Plug Seedling-Picking Mechanism and Control System Constrained by a Differential Non-Circular Planetary Gear Train. *Agriculture* **2024**, *14*, 1576. [CrossRef]
6. Khadatkar, A.; Sawant, C.P.; Magar, A.P. Agricultural robots and automated machinery for handling of nursery seedlings with special reference to the transplanting devices. *Discov. Appl. Sci.* **2025**, *7*, 916.
7. Magar, A.P.; Nandede, B.M.; Khadatkar, A.; Sawant, C.P.; Pandirwar, A.P.; Chaudhary, V.P. Optimization, development and evaluation of vegetable seedlings transplanter using inclined magazine-type metering device for cylindrical paper pot seedlings. *Agric. Res.* **2024**. [CrossRef]
8. Ma, G.; Mao, H.; Han, L.; Liu, Y.; Gao, F. Reciprocating mechanism for whole row automatic seedling picking and dropping on a transplanter. *Appl. Eng. Agric.* **2020**, *36*, 751–766. [CrossRef]
9. Khadatkar, A.; Mathur, S.M.; Gaikwad, B.B. Automation in transplanting: A smart way of vegetable cultivation. *Curr. Sci.* **2018**, *115*, 1884–1892. [CrossRef]
10. Zhou, B.; Miao, H.; Guan, C.S.; Ji, X.; Wang, X.C. Design and Test of Seedling-Picking Mechanism of Fully Automatic Transplanting Machine. *Appl. Sci.* **2024**, *14*, 9235. [CrossRef]
11. Yin, J.; Wang, Z.; Zhou, M.; Wu, L.; Zhang, Y. Optimized design and experiment of the three-arm transplanting mechanism for rice potted seedlings. *Int. J. Agric. Biol. Eng.* **2021**, *14*, 56–62. [CrossRef]
12. Ye, B.; Zeng, G.J.; Deng, B.; Yang, C.L.; Liu, J.K.; Yu, G.H. Design and tests of a rotary plug seedling pick-up mechanism for vegetable automatic transplanter. *J. Int. J. Agric. Biol. Eng.* **2020**, *13*, 70–78. [CrossRef]

13. Ji, D.; Tian, S.; Wu, H.; Zhao, B.; Gong, Y.; Ma, J.; Zhou, M.; Liu, W. Design and experimental verification of an automatic transplant device for a self-propelled flower transplanter. *J. Braz. Soc. Mech. Sci. Eng.* **2023**, *45*, 420. [CrossRef]
14. Cui, J.; Li, X.; Zeng, F.; Bai, H. Study on Contact Stress Distribution Characteristics and Damage of Plug Seedlings Based on Flexible Pressure Sensor. *Sensors* **2023**, *23*, 8175. [CrossRef]
15. Yang, Y.; Ting, K.C.; Giacomelli, G.A. Factors affecting performance of sliding-needles gripper during robotic transplanting of seedlings. *Appl. Eng. Agric.* **1991**, *7*, 493–498. [CrossRef]
16. Tong, J.; Jiang, H.; Jiang, Z.; Cui, D. Experiment on Parameter Optimization of Gripper Needles Clamping Seedling Plug for Automatic Transplanter. *Trans. Chin. Soc. Agric. Eng.* **2014**, *30*, 8–16.
17. Jiang, Z.; Hu, Y.; Jiang, H.; Tong, J. Design and force analysis of end-effector for plug seedling transplanter. *PLoS ONE* **2017**, *12*, e0180229.
18. Kang, T.G.; Kim, Y.K.; Jun, H.J.; Choi, L.S. Analysis of pick-up mechanism for automatic transplanter (I). *J. Agric. Life Sci.* **2017**, *51*, 187–192. [CrossRef]
19. Jin, X.; Suo, H.; Zhang, H.; Ji, J.; Zhang, B.; Lin, C. Development and Experiment of Integrated Vegetable Pot Seedling Picking Jaw Clamping Force Detection Sensor. *Trans. Chin. Soc. Agric. Mach.* **2023**, *54*, 175–183.
20. Tian, Z.; Ma, W.; Yang, Q.; Yao, S.; Guo, X.; Duan, F. Design and experiment of gripper for greenhouse plug seedling transplanting based on EDM. *Agronomy* **2022**, *12*, 1487. [CrossRef]
21. Han, L.; Wang, Y.; Du, X.; Xu, Q.; Ma, G. Design and test analysis of the seedling pick-up mechanical equipment for automatic transplanting. *Trans. Chin. Soc. Agric. Eng.* **2025**, *41*, 47–55.
22. Magar, A.P.; Nalawade, S.M.; Walunj, A.A. Development and optimization of an automatic transplanting device for plug tray vegetable seedlings using embedded system. *Sci. Rep.* **2025**, *15*, 22483. [CrossRef]
23. Zhang, N.; Zhang, G.; Liu, H.; Liu, W.; Wei, J.; Tang, N. Design of and Experiment on Open-and-Close Seedling Pick-Up Manipulator with Four Fingers. *Agriculture* **2022**, *12*, 1776. [CrossRef]
24. Hu, J.; Pan, J.; Chen, F. Simulation and Optimization Design of Finger-clamping Seedling Picking Claw Based on EDEM-RecurDyn. *Trans. Chin. Soc. Agric. Mach.* **2022**, *53*, 75–85+301.
25. Han, L.; Xiang, D.; Xu, Q.; Du, X.; Ma, G.; Mao, H. Development of Simplified Seedling Transplanting Device for Supporting Efficient Production of Vegetable Raw Materials. *Appl. Sci.* **2023**, *13*, 10022. [CrossRef]
26. Jin, X.; Li, D.; Ma, H.; Ji, J.; Zhao, K.; Pang, J. Development of single row automatic transplanting device for potted vegetable seedlings. *Int. J. Agric. Biol. Eng.* **2018**, *11*, 67–75. [CrossRef]
27. Mao, H.; Ma, G.; Han, L.; Hu, J.; Gao, F.; Liu, Y. A whole row automatic pick-up device using air force to blow out vegetable plug seedlings. *Span. J. Agric. Res.* **2021**, *18*, e0211. [CrossRef]
28. Choi, W.C.; Kim, D.C.; Ryu, I.H.; Kim, K.U. Development of a seedling pick-up device for vegetable transplanters. *Trans. Am. Soc. Agric. Eng.* **2002**, *45*, 13–19.
29. Mao, H.; Liu, Y.; Han, L.; Sheng, B.; Ma, G.; Li, Y. X-ray Computerized Tomography for Characterization of Pick-up Destruction and Pick-up Parameter Optimization of Tomato Root Lumps. *Span. J. Agric. Res.* **2019**, *17*, e0202. [CrossRef]
30. Yue, R.; Hu, J.; Liu, Y.; Yao, M.; Zhang, T.; Shi, J. Design and Working Parameter Optimization of Pneumatic Reciprocating Seedling-Picking Device of Automatic Transplanter. *Agriculture* **2022**, *12*, 1989. [CrossRef]
31. Liu, W.; Jiang, W.; Zhang, H.; Liu, X.; Liu, H.; Zheng, W. DEM simulations of spherical particle–particle collisions. *Can. J. Chem. Eng.* **2023**, *101*, 984–995. [CrossRef]
32. Liu, W.; Wang, Q.; Jiang, H. Design and optimisation of end effector for loose substrate grasping based on discrete element method. *Biosyst. Eng.* **2024**, *241*, 43–55. [CrossRef]
33. Cui, J.; Li, X.; Zeng, F.; Bai, H.; Zhang, Y. Parameter Calibration and Optimization of a Discrete Element Model of Plug Seedling Pots Based on a Collision Impact Force. *Appl. Sci.* **2023**, *13*, 6278. [CrossRef]
34. Zhao, X.; Yan, H.; Bie, Q.; An, H.; Wang, Y.; Xie, G. Calibration of Seedling Pot Particle Parameters and Simulation and Experimentation of Seedling Picking Claw Based on EDEM-RecurDyn. *Trans. Chin. Soc. Agric. Mach.* **2024**, *55*, 197–206.
35. Mao, H.; Han, L.; Hu, J.; Kumi, F. Development of a pincette-type pick-up device for automatic transplanting of greenhouse seedlings. *Appl. Eng. Agric.* **2014**, *30*, 547–556.
36. Han, L.; Francis, K.; Mao, H.; Hu, J. Design and Tests of a Multi-pin Flexible Seedling Pick-up Gripper for Automatic. *Appl. Eng. Agric.* **2019**, *6*, 949–957. [CrossRef]

Disclaimer/Publisher's Note: The statements, opinions and data contained in all publications are solely those of the individual author(s) and contributor(s) and not of MDPI and/or the editor(s). MDPI and/or the editor(s) disclaim responsibility for any injury to people or property resulting from any ideas, methods, instructions or products referred to in the content.

agriculture

MDPI

Article

Multi-Trait Phenotypic Extraction and Fresh Weight Estimation of Greenhouse Lettuce Based on Inspection Robot

Xiaodong Zhang [1,2,*], Xiangyu Han [1], Yixue Zhang [3,*], Lian Hu [4] and Tiezhu Li [1]

[1] School of Agricultural Engineering, Jiangsu University, Zhenjiang 212013, China; 2212416036@stmail.ujs.edu.cn (X.H.); 2212316059@stmail.ujs.edu.cn (T.L.)
[2] Department of Agricultural Engineering, Jiangsu University, Zhenjiang 212013, China
[3] Basic Engineering Training Center, Jiangsu University, Zhenjiang 212013, China
[4] Key Laboratory of Key Technology on Agricultural Machine and Equipment, Ministry of Education, South China Agricultural University, Guangzhou 510640, China; lianhu@scau.edu.cn
* Correspondence: zxd700227@ujs.edu.cn (X.Z.); 1000005803@ujs.edu.cn (Y.Z.)

Abstract

In situ detection of growth information in greenhouse crops is crucial for germplasm resource optimization and intelligent greenhouse management. To address the limitations of poor flexibility and low automation in traditional phenotyping platforms, this study developed a controlled environment inspection robot. By means of a SCARA robotic arm equipped with an information acquisition device consisting of an RGB camera, a depth camera, and an infrared thermal imager, high-throughput and in situ acquisition of lettuce phenotypic information can be achieved. Through semantic segmentation and point cloud reconstruction, 12 phenotypic parameters, such as lettuce plant height and crown width, were extracted from the acquired images as inputs for three machine learning models to predict fresh weight. By analyzing the training results, a Backpropagation Neural Network (BPNN) with an added feature dimension-increasing module (DE-BP) was proposed, achieving improved prediction accuracy. The R^2 values for plant height, crown width, and fresh weight predictions were 0.85, 0.93, and 0.84, respectively, with RMSE values of 7 mm, 6 mm, and 8 g, respectively. This study achieved in situ, high-throughput acquisition of lettuce phenotypic information under controlled environmental conditions, providing a lightweight solution for crop phenotypic information analysis algorithms tailored for inspection tasks.

Keywords: in-situ detection; inspection robot; phenotypic information; computer vision; machine learning; lettuce fresh weight

1. Introduction

Lettuce phenotypic information refers to all externally observable traits of lettuce during its growth, including shape, structure, texture, and color [1]. By obtaining lettuce phenotypic information, one can fully understand the plant architecture, growth status, physiological characteristics, and yield of lettuce [2,3]. Therefore, monitoring lettuce phenotypic information is crucial for agronomists and breeders to assess lettuce growth and adjust management strategies [4]. However, traditional methods of obtaining phenotypic information rely on manual measurement, which has drawbacks such as small scale, low efficiency, and strong subjectivity, severely limiting the efficiency of agricultural breeding and production [5]. There is an urgent need to utilize advanced phenotypic analysis

technologies and equipment to achieve automated acquisition and intelligent analysis of lettuce phenotypic information [6].

Existing gantry-type [7], track-type [8], and imaging chamber-type [9] phenotyping platforms offer advantages such as high stability and detection accuracy. However, gantry-type and track-type phenotyping platforms are limited to collecting phenotypic information from crops in fixed areas, and their installation costs are generally high; imaging-type phenotyping platforms require moving crops to designated locations for information collection, resulting in low efficiency. In comparison, inspection robots capable of autonomous navigation and crop information acquisition can overcome the limitations of traditional phenotyping platforms. Inspection robots can also achieve in situ, non-destructive detection of crops through automated, high-throughput data collection and analysis [10]. For example, Miao et al. [11] designed a phenotyping inspection robot with adjustable wheel tracks, inspired by the structure of gantry-style platforms, and achieved high-throughput image collection through pixel-level algorithm registration, overcoming the fixed working area issue of traditional gantry-style platforms.

In facility agriculture production, yield is a key indicator of lettuce economic efficiency, and lettuce fresh weight directly determines yield [12]. Lettuce fresh weight refers to the total mass of the plant excluding the root system in its fresh state. Direct measurement of lettuce fresh weight requires destructive sampling methods to remove the root system. Therefore, many researchers have employed imaging devices combined with deep learning methods to predict lettuce fresh weight based on collected images. In lettuce fresh weight prediction models, using multi-view images to perform three-dimensional reconstruction of lettuce can fully capture its complex three-dimensional structural information, which offers significant advantages for fresh weight prediction tasks [13]. With the improvement of computer processing capabilities and the reduction in the size of three-dimensional data measurement devices, three-dimensional plant canopy structure measurement and reconstruction have been deployed on miniaturized platforms [14]. Victor Bloch et al. [15] used four 3D cameras to collect point clouds of lettuce plants, extracted morphological parameters such as plant volume and plant height through point cloud reconstruction, and used these parameters as inputs for linear regression to predict the fresh weight of lettuce, with the model R^2 reaching 0.85. However, facility-based phenotyping platforms must maintain a certain level of operational efficiency. Collecting multi-angle information for individual crops consumes excessive time, impairing detection efficiency. Additionally, the complex structural layout of facility environments and the compact planting arrangement of lettuce make idealized multi-angle information collection schemes unsuitable for the high-throughput in situ acquisition of facility crop phenotyping parameters. Therefore, the single-angle, multi-modal imaging approach based on mobile phenotyping platforms is more suitable for in situ monitoring of crop growth in facility environments [16].

Compared to multi-angle imaging, single-angle imaging struggles to comprehensively capture the three-dimensional morphological information of lettuce and also loses a significant amount of color and texture information, which has a substantial impact on the accuracy of fresh weight estimation [17,18]. Currently, many scholars have been exploring the prediction of lettuce fresh weight from single-view images. Tan et al. [19] combined the Mask R-CNN and PoseNet deep learning models to predict fresh weight information from tilted images of lettuce in a controlled environment; Tang et al. [20] combined the Mask3D and PointNet deep learning models to predict actual fresh weight using the three-dimensional point cloud of lettuce.

Using deep learning methods, complex feature mapping relationships can be directly learned from RGB images, depth images, or point clouds through models such as CNN and PointNet to predict the fresh weight of lettuce. Although varying degrees of accuracy

have been achieved in prediction, running complex deep learning models on small mobile devices such as inspection robots means more computing time and higher computing power consumption [21]. Therefore, the phenotypic information processing algorithms carried by inspection robots need to develop in the direction of lightweighting [22].

Extracting more phenotypic parameters with higher relevance to fresh weight from single-view, multi-modal information, deeply exploring the potential relationships between phenotypic parameters and fresh weight, and using machine learning algorithms to predict fresh weight based on phenotypic parameters may overcome the high computational demands of directly processing raw images with deep learning models, providing a lightweight solution for crop phenotypic information analysis algorithms tailored to inspection tasks [23–25]. However, most current research pursues higher prediction accuracy by using deep learning networks to directly process complex relationships within images, while neglecting the model's size. Furthermore, few platforms can achieve non-destructive, in situ, high-throughput monitoring of crops in facility environments while simultaneously ensuring automation and simple deployment.

This study aims to develop a facility-based crop information inspection robot, with the following specific research objectives. (1) Develop a robot capable of autonomous navigation and completing image acquisition and analysis tasks in a facility environment. (2) Design single-plant lettuce segmentation algorithms and point cloud reconstruction algorithms to automatically identify and segment individual lettuce plants from raw RGB and depth images and reconstruct their three-dimensional point cloud models. (3) Extract morphological parameters such as lettuce plant height and canopy width, as well as vegetation indices such as ultra-green index and normalized vegetation index and analyze the correlation between various parameters and fresh weight. (4) Construct different fresh weight prediction models based on multiple machine learning algorithms and investigate the contribution of different phenotypic parameters to fresh weight prediction.

2. Materials and Methods

2.1. Overview of the Platform

The controlled environment crop information inspection robot designed by this research institute mainly consists of a four-wheel omnidirectional chassis, a SCARA robotic arm, and information sensing devices. The specific structure is shown in Figure 1.

The robot chassis uses a programmable omnidirectional unmanned ground vehicle (UGV), which completes continuous and accurate positioning and navigation inside and outside the facility through the SLAM architecture. The UGV communicates with the board NVIDIA Jetson Orin Nano (NVIDIA Corp., Santa Clara, CA, USA) via a CAN bus interface, continuously sending odometer information and receiving driving control signals in real time. An RGB-D camera Gemini335 (Orbbec, Shenzhen, China) and a single-line laser radar LSLIDAR N10P (Leishen Intelligent System Co., Ltd., Shenzhen, China) are selected to provide visual information and 3D point clouds for the navigation system, which are used to construct a 2D grid map. The NAV2 navigation architecture under the ROS2 system is adopted. After setting navigation target points via RVIZ, the UGV can achieve continuous and precise autonomous navigation after establishing a cost map through loopback. This enables the inspection robot to stably achieve the "localization-planning-control" closed-loop in controlled environments, while ensuring navigation accuracy, obstacle avoidance safety, and task continuity.

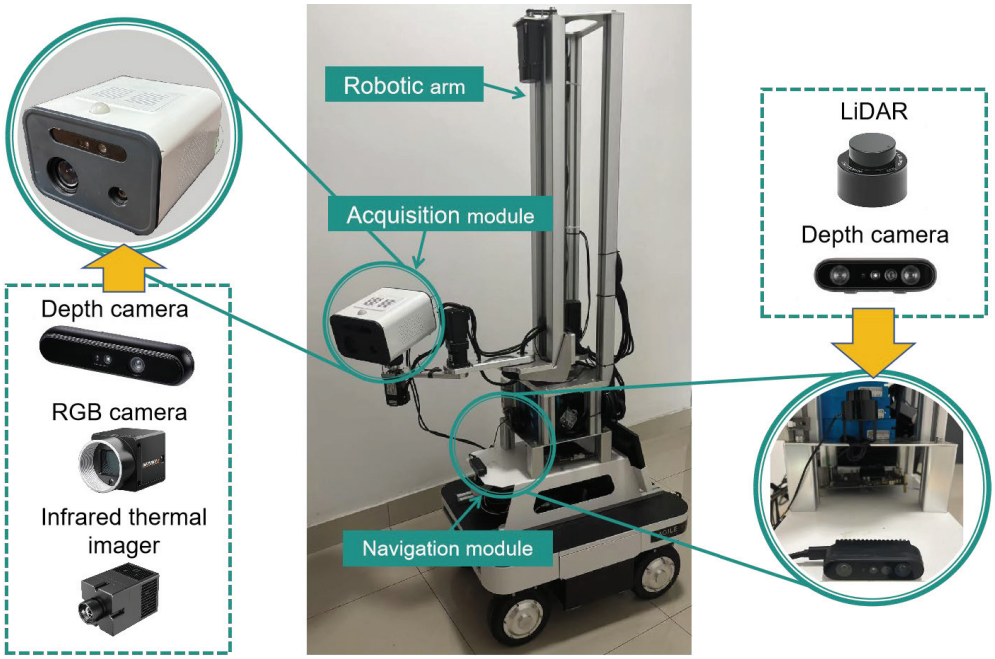

Figure 1. Hardware structure of inspection robot.

To meet the on-site data collection needs for crops of different types, growth stages, and planting methods within the facility, this study designed a five-degree-of-freedom SCARA robotic arm with a vertical lifting range of 0.9 m to 1.8 m relative to the ground and a horizontal reach of 0.7 m. Equipped with a multi-modal imaging device mounted on its end-effector, the arm can achieve 360° horizontal rotation and ±90° vertical tilt.

To achieve precise acquisition of crop information, a pre-trained lightweight semantic segmentation model, YOLOv8n-seg, is used to identify lettuce based on the RGB video stream obtained from an RGB-D camera. The identified lettuce is then mapped to the depth video stream in the form of a mask, thereby obtaining the coordinate position information of the lettuce center point relative to the depth camera. A depth threshold is then set for the lettuce center point. When the lettuce center point exceeds the depth threshold range, the robotic arm targets the lettuce center point and, through inverse kinematics calculation, controls its end effector to move to a position 1 m away from the lettuce center point; The center point of the RGB image is set as the crosshair. Through forward kinematics control of the robotic arm, the center point of the RGB-D camera at the end of the robotic arm moves toward and aligns with the center point of the lettuce, ensuring that the imaging device always faces the target lettuce at a distance of 1 m.

The information sensing device mounted on the end of the robotic arm consists of an Orbbec Gemini336L (Orbbec, Shenzhen, China), a Hikvision industrial camera MV-CS200-10GC (Hikvision, Hangzhou, China), a Gode IPM630 infrared thermal imager (Guide, Wuhan, China), a humidity sensor, and a light sensor, enabling high-throughput acquisition of crop information. The specific models are as follows:

In Table 1, resolution is the most important consideration. The high resolution of 5472 × 3648 of the RGB camera ensures high-quality RGB images; the RGB channel and depth channel resolutions of the depth camera are both 1280 × 800, which facilitates image fusion; and the 640 × 512 pixels of the infrared thermal imager are sufficient for the application of lettuce temperature measurement. The operating range only needs to cover an effective range of 0.5 m to 2 m to meet the imaging requirements of inspection robots; in most cases, the surface temperature of crops will not exceed the temperature measurement range of the infrared thermal imager.

Table 1. Image sensor model of the acquisition device.

Device Name	Device Model	Resolution	Operating Range	Depth Technology	Temperature Range	Temperature Accuracy
RGB Camera	Hikvision MV-CS200-10GC	5472 × 3648	0.5 m–30 m	-	-	-
Depth Camera	Orbbec 336L	1280 × 800	0.17 m–20 m	Stereo Vision	-	-
Infrared Thermal Imager	Gode IPM630	640 × 512	0.5 m–3.5 m	-	20 °C–50 °C	±0.3 °C

Before performing area inspection tasks, the inspection robot is manually controlled to navigate within the facility to obtain a two-dimensional grid map model of the facility environment. Each location requiring information acquisition is marked as a navigation point. The inspection robot will pause at each navigation point and initiate a vision-based robotic arm control program. Once the robotic arm is aligned with the target lettuce, the image acquisition program is activated to capture RGB images, depth images, and near-infrared images of the target lettuce from a side view perspective. After completion, the inspection robot will proceed to the next navigation point and perform the next image acquisition task.

2.2. Experimental Materials

The experimental site is located at the Zijing Farm, Ganghua, Jiangsu Province, China (119°8′21.725″ E, 32°8′27.481″ N). Italian lettuce grown by hydroponics was selected as the experimental subject. Each lettuce plant was spaced 200 mm apart, and the hydroponic rack was 1000 mm above the ground. Other management measures were consistent with local facility management practices.

The experiment was conducted on 11 April 2025, with the lettuce having already been growing in the area for 30 days prior to the experiment. The inspection robot navigated autonomously through the aisles between the hydroponic racks to complete patrols and data collection, with a maximum travel speed of 0.5 m/s. To ensure the imaging quality of all sensors, the distance between the information sensing devices and the target crops was maintained at 1000 mm. A total of 132 RGB images, depth images, and thermal infrared images of Italian lettuce were obtained.

Within 2 h of image acquisition, manually measure the lettuce using a height measurement device (Figure 2c) to determine the distance from the highest point of the lettuce to the bottom surface of the hydroponic foam board, which is used as the plant height. The maximum distance from the farthest left to the farthest right end of the lettuce parallel to the aisle direction is used as the crown width. Finally, remove the lettuce from the hydroponic rack, remove the roots, and use a balance (accuracy 0.01 g) to measure the mass of the lettuce after removing the roots as the fresh weight.

2.3. Image Processing Methods

RGB images and depth images of lettuce captured using the Orbbec Gemini336L camera were used as input for the phenotyping estimation algorithm. First, to enable the image processing algorithm to automatically identify lettuce while accounting for the processor's limited computational capacity, this study selected the lightweight model YOLOv8n-seg for embedded deployment. Compared to other YOLO variants, it offers more extreme lightweight optimization and more mature architecture. This study employed YOLOv8n-seg to train a lightweight semantic segmentation model for processing raw RGB images. This model identifies lettuce within images and generates preliminary masks, as shown in Figure 3b.



(**a**) (**b**) (**c**)

Figure 2. The scenario of the experiment. (**a**) Lettuce growing environment; (**b**) inspection robots perform inspection tasks in the greenhouses; (**c**) height measuring device with an accuracy of 0.5 mm.

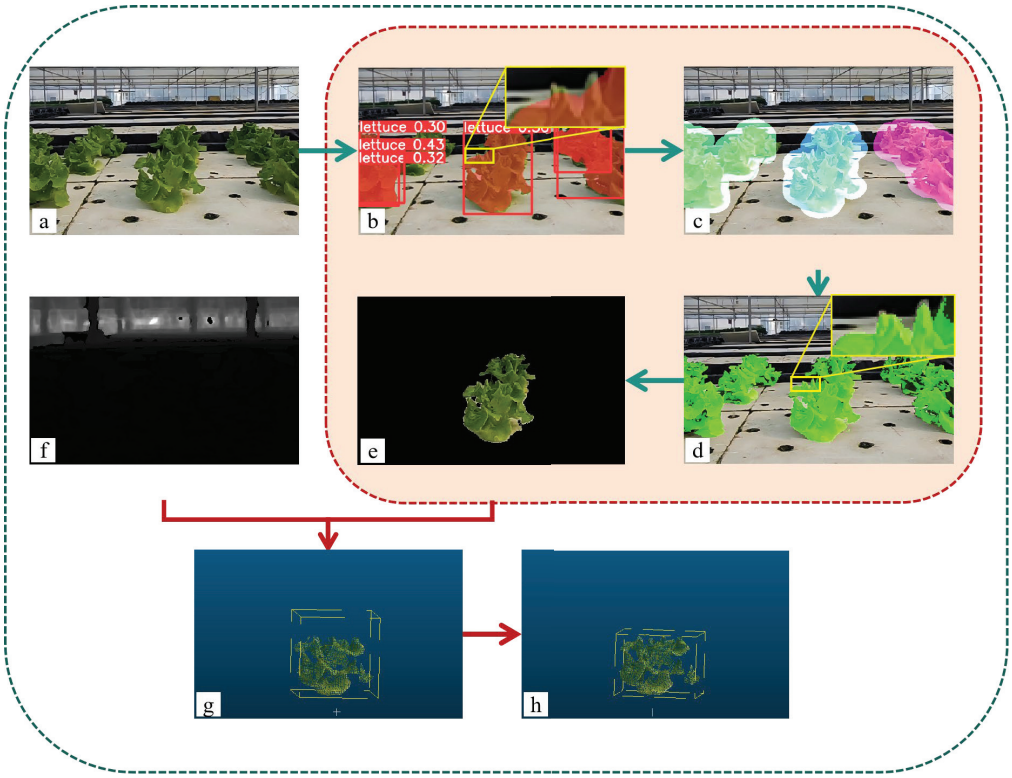

Figure 3. Flowchart of image processing algorithms. (**a**) RGB images obtained from the Gemini336L camera; (**b**) RGB images processed by YOLOv8n-seg, the mask obtained at this point has a low coverage rate for the edges of the lettuce leaves; (**c**) Expand the mask outward by 5%; (**d**) Use an algorithm based on Excess Green Feature to process the mask and obtain a more accurate mask; (**e**) Obtain the RGB image under the center position mask. At this point, the image contains the target lettuce and the lettuce in the background that cannot be segmented; (**f**) Depth images obtained from the Gemini336L camera; (**g**) Reconstruct the 3D point cloud of the mask area using RGB images and depth images, and segment the background lettuce by depth threshold; (**h**) Remove noise point clouds based on the DBSCAN clustering algorithm to obtain point clouds of individual lettuce plants.

Due to limitations in model accuracy, the mask generated by YOLOv8n-seg does not precisely cover the leaf edges. Therefore, the mask is expanded outward by 5% to ensure it fully covers the lettuce instances (Figure 3c). Then, the super-green algorithm is used to reassign values to each pixel within the mask to enhance the contrast of the G channel relative to the R and B channels, thereby avoiding situations where the G channel index of lettuce pixels is too low due to shadows or other factors, making them difficult to distinguish. Next, we set thresholds for the G channel and the supergreen index. We then

determine whether the G channel of the original RGB image and the supergreen index after processing by the supergreen algorithm exceed the thresholds. The results are combined using a logical OR operation to obtain a lettuce mask with clear boundaries (Figure 3d).

YOLOv8n-seg has already distinguished each instance of the mask during semantic segmentation. Combined with the clearly defined lettuce mask obtained, a single lettuce instance located at the center of the image can be directly extracted. Combined with the original depth image, the RGB image and depth image are aligned to the same spatial coordinate system through the intrinsic matrix, thereby reconstructing a 3D point cloud with RGB information.

Using the Orbbec SDK to obtain the camera intrinsic matrix K, coordinate transformation is applied to convert two-dimensional pixel coordinates combined with depth information into three-dimensional spatial coordinates, thereby reconstructing the three-dimensional colored point cloud of the target lettuce. The coordinate transformation formula is shown in Equation (1), as follows.

$$\left(\frac{d_z}{s}\right)\cdot\begin{bmatrix}u\\v\\1\end{bmatrix}=\begin{bmatrix}645.193 & 0 & 643.682\\0 & 645.193 & 347.782\\0 & 0 & 1\end{bmatrix}\cdot\begin{bmatrix}X\\Y\\Z\end{bmatrix} \quad (1)$$

where (u, v) represents the pixel coordinates, d_z denotes the depth value corresponding to these coordinates in the depth map, the depth scaling factor $s = 1000$, $\begin{bmatrix}645.193 & 0 & 643.682\\0 & 645.193 & 347.782\\0 & 0 & 1\end{bmatrix}$ is the internal parameter matrix, and (X, Y, Z) represents the world coordinate system coordinates corresponding to the pixel coordinates (u, v).

During the image acquisition phase, the distance between the target lettuce and the camera is controlled to be 1 m. By setting a depth threshold (0.8 m–1.2 m), point clouds outside the segmentation threshold can effectively remove depth-failed points, noise point clouds, and background lettuce (Figure 3g). The point cloud within the depth threshold is further processed using the DBSCAN clustering method to remove noise point clouds within the depth threshold, thereby obtaining a complete three-dimensional point cloud of a single lettuce plant, as shown in Figure 3h.

2.4. Phenotypic Parameter Extraction Method

2.4.1. Morphological Parameter Extraction

Extract morphological parameters from the 3D point cloud model of a single lettuce plant. The number of points in the 3D point cloud of the clustered single lettuce plant is denoted as (Np). Project this point cloud onto the X-Y plane to obtain a discrete set of projection points. Use Delaunay triangulation to divide the projection point set into multiple triangles and calculate the sum of the areas of all triangles to obtain the projected area (Ap) of the target lettuce plant. The difference between the highest and lowest vertical coordinates of the projection is the plant height (Hm), and the difference between the rightmost and leftmost horizontal coordinates is the crown width (Wm).

Using the equidistant segmentation method, the projection is divided into 10 equal intervals along the *Z*-axis, and the arithmetic mean of the *X*-axis spans corresponding to the intercepts is calculated as the average crown width (Wa), as shown in Figure 4a. Similarly, divide the projection along the *X*-axis into 10 equal intervals, and calculate the arithmetic mean of the *Z*-axis spans corresponding to the intercept lines as the average plant height (Ha), as shown in Figure 4b.

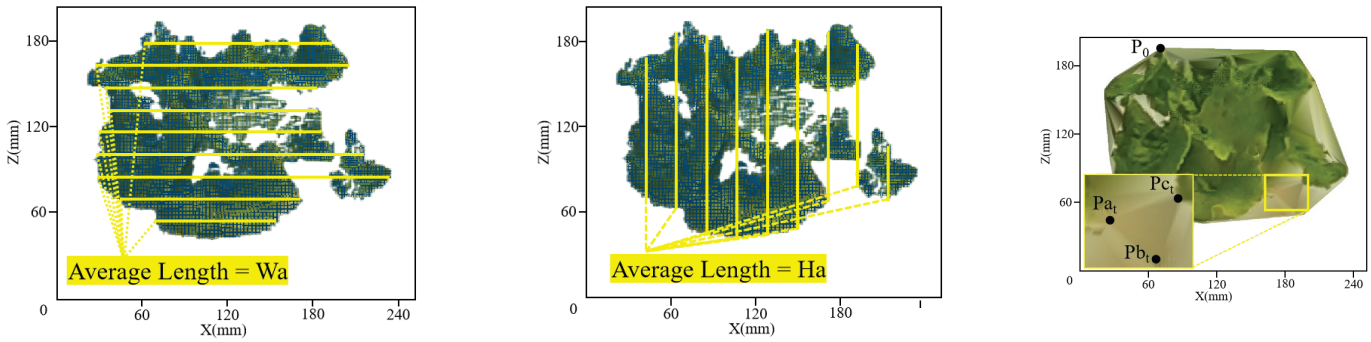

Figure 4. Methods for Extracting Morphological Parameters. (**a**) Schematic of average crown width extraction; (**b**) schematic of average plant height extraction; (**c**) the minimum convex polyhedron constructed by the 3D convex hull algorithm that encloses the point cloud of a single lettuce plant.

Using the 3D convex hull algorithm, construct the minimum convex polyhedron enclosing the point cloud of a single lettuce plant, as shown in Figure 4c. Each face of this polyhedron is a triangle formed by three vertices from the original point cloud. The volume of the convex polyhedron (Vh) can be expressed using the tetrahedral decomposition method which shown in Equation (2), as follows.

$$\mathrm{Vh} = \sum_{t=1}^{m} \frac{1}{6} \left| (\mathbf{P}_{a_t} - \mathbf{P}_0) \cdot [(\mathbf{P}_{b_t} - \mathbf{P}_0) \times (\mathbf{P}_{c_t} - \mathbf{P}_0)] \right| \tag{2}$$

where (Vh) is the volume of the convex polyhedron, m is the total number of faces of the convex hull polyhedron, $\mathbf{P}_{a_t}$, $\mathbf{P}_{b_t}$, and $\mathbf{P}_{c_t}$ are the coordinates of the three vertices of the tth face of the convex polyhedron, and $\mathbf{P}_0$ is the coordinate of the highest point of the convex polyhedron.

The abbreviations for the morphological parameters are shown in Table 2:

Table 2. Abbreviations corresponding to morphological parameters.

Morphological Parameters	Abbreviation
number of points in the 3D point cloud	Np
projected area	Ap
plant height	Hm
crown width	Wm
average plant height	Ha
average crown width	Wa
volume of the convex polyhedron	Vh

2.4.2. Vegetation Index Extraction

The amount of radiation available for crop photosynthesis exhibits a positive linear relationship with biomass. Vegetation indices, by reflecting the spectral characteristics of crops, directly relate to crop growth status and are therefore widely used in estimating crop fresh weight [26]. This study selected 10 vegetation indices that may be correlated with the fresh weight of lettuce. The specific calculation formulas are shown in Table 3:

Table 3. List of vegetation index calculation formulas.

Vegetation Index	Formula *	References
Excess red index, ExR	$\mathrm{ExR} = 1.4\mathrm{r} - \mathrm{g}$	[27]
Excess blue index, ExB	$\mathrm{ExB} = 1.4\mathrm{b} - \mathrm{g}$	[27]
Excess green index, ExG	$\mathrm{ExG} = 2\mathrm{g} - \mathrm{r} - \mathrm{b}$	[27]
Modified excess green index, MExG	$\mathrm{MExG} = 1.262\mathrm{g} - 0.884\mathrm{r} - 0.311\mathrm{b}$	[28]
Excess green minus excess red index, ExGR	$\mathrm{ExGR} = (2g - r - b) - (1.4r - g)$	[29]
Vegetation index, VEG	$\mathrm{VEG} = \frac{g}{r^{0.667} b^{0.333}}$	[30]
Visible-band difference vegetation index, VDVI	$\mathrm{VDVI} = \frac{2g - r - b}{2g + r + b}$	[31]
Red green ratio index, RGRI	$\mathrm{RGRI} = \frac{r}{g}$	[31]
Normalized green-red difference index, NGRDI	$\mathrm{NGRDI} = \frac{g - r}{g + r}$	[32]
Color index of vegetation extraction, CIVE	$\mathrm{CIVE} = 0.441\mathrm{r} - 0.811\mathrm{g} + 0.385\mathrm{b} + 18.787$	[27]

* R, G, and B represent the values of the red, green, and blue channels for each pixel, while r, g, and b represent the normalized values of the three channels. The calculation formula is as follows: $r = \frac{R}{R+G+B}$, $g = \frac{G}{R+G+B}$, $b = \frac{B}{R+G+B}$.

2.5. Fresh Weight Prediction Model

This study considered the small size of the lettuce sample dataset and the high correlation between input variables and fresh weight, selecting four algorithms—Multiple Linear Regression (MLR), Random Forest Regression (RFR), Backpropagation Neural Network (BPNN), and Dimensionality-Enhanced BPNN (DE-BP).

Among these, MLR has a simple structure, strong interpretability, and excellent ability to fit linear relationships, allowing for an intuitive assessment of the contribution of each variable to fresh weight estimation. RFR, through decision tree ensemble and random sampling strategies, exhibits strong resistance to overfitting. BPNN learns complex relationships between inputs and outputs through gradient descent by propagating error signals backward. DE-BP incorporates a feature dimensionality enhancement module consisting of two fully connected layers at the front end of the original BPNN, enhancing the richness of feature interaction information by dimensionality enhancement of lettuce phenotypic parameters, followed by feature dimensionality reduction and regression via the BP neural network, as shown in Figure 5.

The models were trained using the Adam optimizer with an initial learning rate of 0.01 and a batch size of 32. The number of epochs was determined by monitoring the Mean Absolute Error (MAE) over iterations. Ultimately, the BPNN was set to 500 epochs, while the DE-BP was set to 600 epochs. This study employed a five-fold cross-validation method for model training and evaluation, using the average coefficient of determination (R^2), average root mean square error (RMSE), and average absolute percentage error (MAPE) of the training set as evaluation metrics to compare the training performance of the four models.

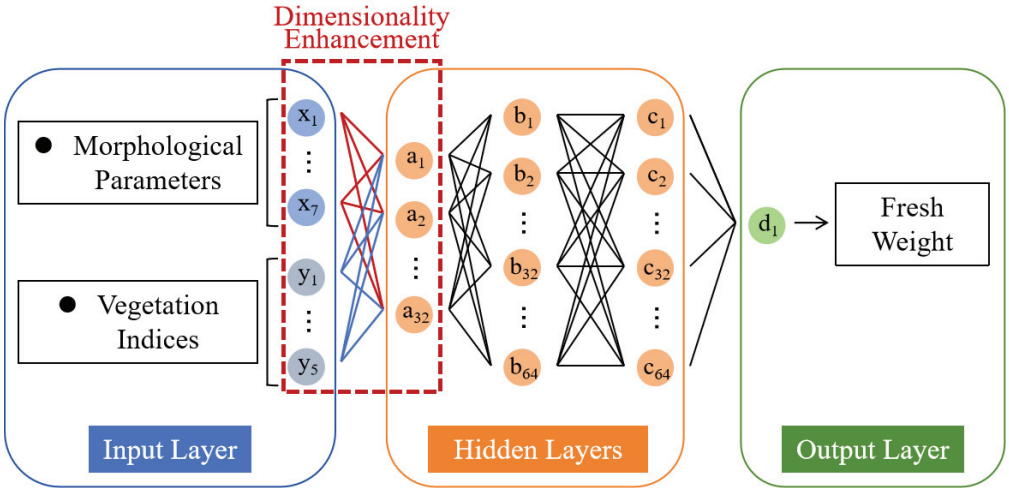

Figure 5. DE-BP Network Architecture Diagram. Building upon the BPNN structure, a feature dimensionality enhancement module has been incorporated. This module employs a branch architecture for independent dimensionality expansion, where morphological parameters undergo separate normalization before being mapped to vegetation indices. This approach enhances the complex mapping relationships of morphological parameters while preserving the original correlations of vegetation indices.

3. Results

3.1. Accuracy of Extracting Plant Height and Crown Width

Using the 132 side-view RGB images and depth maps of lettuce collected by the RGB-D camera, the single-plant lettuce 3D point cloud reconstruction and morphological parameter extraction algorithm proposed in this study was used to obtain the plant height and crown width. R^2 was used to evaluate the degree of fit between the estimated values and the actual values; RMSE, MAPE, and mean absolute error (MAE) were used to evaluate the deviation between the estimated values and the actual values. The evaluation results are as follows:

As shown in Table 4, the three-dimensional point cloud reconstruction algorithm for single lettuce plants proposed in this study has high accuracy in estimating the plant height and crown width of lettuce plants, with an average absolute error of less than 5 mm, demonstrating a certain degree of reliability.

Table 4. Prediction accuracy of plant height and crown width.

Morphological Parameters	R^2	RMSE (mm)	MAE (mm)	MAPE (%)
plant height	0.85	7	5	3.29
crown width	0.93	6	4	1.69

3.2. Correlation Analysis Between Phenotypic Parameters and Fresh Weight

In order to screen parameters with significant correlation with fresh weight as inputs for subsequent fresh weight prediction models, this study normalized the seven morphological parameters and 15 vegetation indices extracted and performed Pearson correlation analysis with lettuce fresh weight. The analysis results are shown in Figure 4.

As shown in Figure 6, there are seven morphological parameters (Hm, Wm, Ha, Wa, Ap, Np, Vh) and five vegetation indices (ExG, ExGR, MExG, VDVI, NGRDI) that are positively correlated with fresh weight and exhibit significant correlations. Among these, all morphological parameters exhibit high correlation coefficients ($r > 0.48$), with Hw and Wm showing the best performance, reaching 0.72 and 0.74, respectively, indicating that

the 7 morphological parameters extracted in this study are strongly correlated with fresh weight; Among the vegetation indices, ExG, ExGR, MExG, VDVI, and NGRDI had correlation coefficients ranging from 0.35 to 0.43, also showing a certain degree of correlation; the remaining vegetation indices were negatively correlated or weakly correlated with fresh weight.

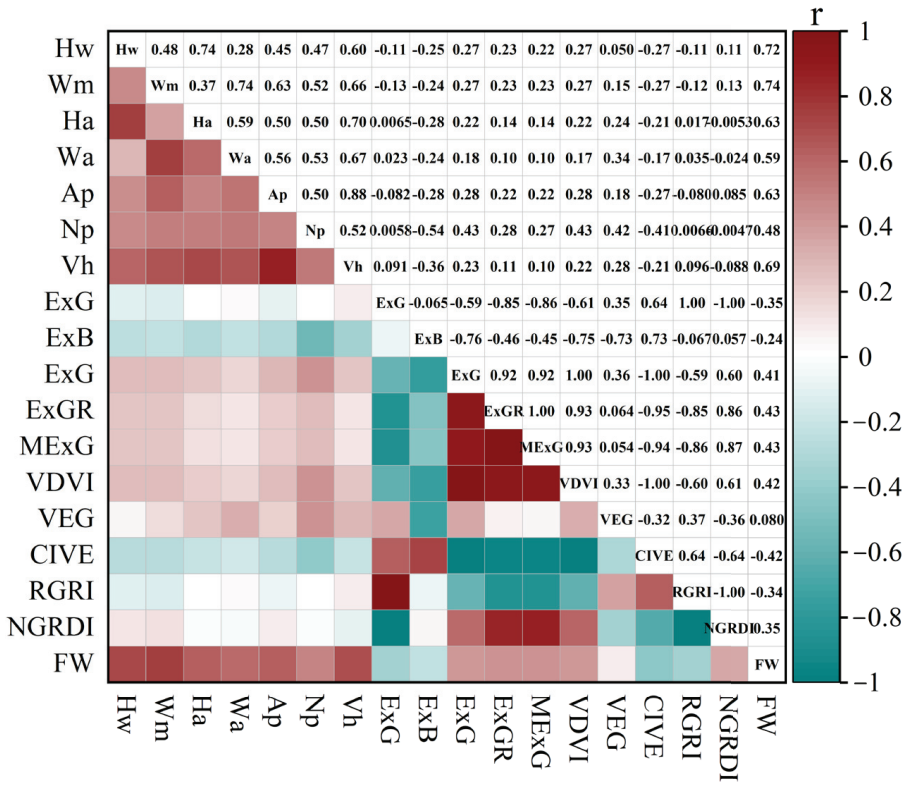

Figure 6. Pearson correlation coefficient between fresh weight and phenotypic parameters. From green to red indicates the Pearson correlation coefficient ranging from −1 to 1; the darker the color, the stronger the correlation between the two parameters. Each cell value represents the Pearson correlation coefficient between the two parameters, where (0, 1) indicates a positive correlation and (−1, 0) indicates a negative correlation.

Based on the above correlation analysis results, seven morphological parameters (Hm, Wm, Ha, Wa, Ap, Np, Vh) and five vegetation indices (ExG, ExGR, MExG, VDVI, NGRDI) were selected as inputs for the subsequent fresh weight prediction model.

3.3. Training Results of the Fresh Weight Prediction Model

Four machine learning models, MLR, RFR, BPNN, and DE-BP, were used to predict the fresh weight based on 12 phenotypic parameters extracted from 132 lettuce samples. The average R^2, RMSE, and MAPE of the training set in five-fold cross-validation were used as evaluation indicators. The training results are shown in Table 5.

In the MLR model, when MP is used as the sole input, the model exhibits a high R^2 value, indicating a certain linear relationship between MP and fresh weight. However, VI shows poor linear correlation with fresh weight. Therefore, the selection of subsequent models should focus on their ability to learn nonlinear relationships.

Compared to the MLR model, the RFR model can capture nonlinear relationships between data. Therefore, in the analysis of the training results of the RFR model, it can be observed that whether MP and VI are used as inputs individually or together, there is a certain improvement compared to the MLR model, indicating that there is a nonlinear correlation between MP, VI, and fresh weight. The model captures some

nonlinear relationships on top of the linear relationship, but the improvement in training performance is limited.

Table 5. Training results of the fresh weight prediction model.

ML Model	Features *	R^2	RMSE (g)	MAPE (%)
MLR	MP	0.61	13	11.35
	VI	−0.19	23	22.55
	MP + VI	0.62	13	10.84
RFR	MP	0.71	11	10.11
	VI	0.01	21	19.97
	MP + VI	0.74	11	9.77
BPNN	MP	0.75	10	9.49
	VI	0.22	18	18.12
	MP + VI	0.81	9	7.99
DE-BP	MP	0.77	10	8.65
	VI	0.18	19	18.21
	MP + VI	0.84	8	7.52

* MP refers to five morphological parameters, and VI refers to seven vegetation indices.

The error backpropagation characteristic of the BPNN model further enhances the model's ability to capture cross-relationships among multidimensional data. The training results show that the model's performance has been significantly improved. When VI is used as a single input, the model's R^2 no longer approaches 0 but increases to 0.22, indicating that VI has certain potential for fresh weight prediction. Additionally, from the training results of these three models, it can be observed that regardless of the training results when VI is the sole input, the training performance of the model improves when MP and VI are used as dual inputs. This indicates that MP and VI have a certain intrinsic association in the fresh weight prediction task, but a deeper and more complex feature mapping network is needed to explore this relationship.

Therefore, this study designed a feature dimension-increasing module consisting of two fully connected layers. By adjusting the number of input neurons, 5-dimensional, 7-dimensional, or 12-dimensional feature parameters can be mapped to 64 dimensions, thereby enhancing the ability to express the cross-relationships between multi-dimensional data. The BPNN model (DE-BP) with the added feature dimension-increasing module showed a certain improvement compared to other models when MP was used as the sole input. Under the MP and VI co-input conditions, the DE-BP training results achieved an R^2 of 0.84, an RMSE of 8 g, and a MAPE of 7.52% on the test set, significantly outperforming the training effects of other models.

It is worth noting that the DE-BP model performs worse than the BPNN model without the feature dimension-increasing module under single VI input conditions. This indicates that the cross-mapping of the five parameters of VI has limited effect on improving freshness weight prediction, and may even cause redundancy in input feature parameters, affecting the model's fitting ability. This warrants further verification and exploration in subsequent studies with expanded sample sizes.

4. Discussion

This study proposes a facility-based crop information inspection robot equipped with SLAM technology, enabling autonomous navigation in facility environments. Based on this, a five-degree-of-freedom SCARA robotic arm was designed. Through forward and inverse kinematic control of the robotic arm combined with machine vision technology, the system can accurately identify lettuce and actively control the end effector to align with the

lettuce. The end-effector of the robotic arm is equipped with a multi-source information sensing device designed in this study, which can simultaneously acquire RGB images, depth images, and near-infrared images of the crops. Based on this device, the inspection robot can achieve autonomous navigation in a facility environment and in situ collection of lettuce phenotypic information.

In terms of lettuce phenotypic information analysis, this study designed an automatic extraction algorithm for lettuce phenotypic information. Using the lightweight YOLOv8n-seg, ultra-green segmentation, and point cloud clustering, it extracts the point cloud model of a single lettuce plant while calculating seven morphological parameters and ten vegetation indices of the lettuce.

Considering that the complexity of the fresh weight prediction model directly affects the computational load on the robot processor and inspection efficiency, complex deep learning models with high computational power and time requirements are not suitable for deployment on mobile devices like facility inspection robots. This study selected 17 phenotypic parameters extracted directly from lettuce to analyze their relationship with fresh weight. Notably, to further enhance the description of lettuce morphology, after selecting plant height and crown width, this study proposed dividing the lettuce into equal parts to obtain the average plant height and average crown width. By analyzing the Pearson correlation coefficients between extracted phenotypic parameters and fresh weight, the coefficients for average plant height and fresh weight reached 0.63, while that for average crown width and fresh weight reached 0.59. This demonstrates that further numerical characterization of lettuce morphology is beneficial for fresh weight prediction tasks. This study identified 12 parameters for fresh weight prediction. Three lightweight machine learning models—MLR, RFR, and BPNN—were selected for lettuce fresh weight prediction. Training was conducted using five-fold cross-validation. Analysis of the average R^2, RMSE, and MAPE of the training set demonstrated that the cross-relationship between morphological parameters and vegetation indices significantly influences fresh weight prediction. A BPNN model with an added feature dimension-increasing module (DE-BP) was proposed. The training results showed that the model achieved R^2, RMSE, and MAPE values of 0.84, 8 g, and 7.52%, respectively, accurately reflecting the growth status of lettuce. Compared with recent literature predicting lettuce fresh weight using morphological parameters and vegetation indices, this study demonstrates improved prediction accuracy [33]. Additionally, the dataset established by this research institute has certain limitations. To address the issue of insufficient sample size, we selected models such as BPNN that perform well with small training datasets and employed Adam optimizer and five-fold cross-validation to prevent overfitting. Although environmental factors in lettuce-growing greenhouses are generally similar, incorporating samples from different greenhouse conditions could further enhance the model's generalization capability. Additionally, expanding the dataset to include more lettuce varieties would be an effective means of improving its quality.

This study aims to explore the relationship between easily extractable phenotypic information parameters of lettuce and fresh weight and strives to construct a lettuce fresh weight prediction model using lightweight machine learning algorithms. This addresses the issues of insufficient computing power and excessive computation time encountered when deploying existing deep learning prediction models such as CNN and Pointnet on mobile devices, thereby reducing hardware costs for inspection robot processors while improving inspection efficiency. Through the deployment of lightweight models and optimization of model structures, this study provides a method for acquiring crop phenotypic information that reduces hardware costs and improves inspection efficiency for agricultural inspection robots.

5. Conclusions

The current facility environment lacks a platform capable of non-destructive, in situ, high-throughput crop monitoring that is also automated and simple to deploy. This study designed an inspection robot capable of autonomous navigation within facilities to complete inspection tasks. Furthermore, addressing the issue of overly large models caused by deep learning networks directly learning complex linear relationships in images for lettuce fresh weight prediction, this study explores the possibility of directly predicting lettuce fresh weight using morphological parameters and vegetation indices. It successfully achieves fresh weight prediction through a structurally simple machine learning model, enabling lightweight model development for mobile devices such as inspection robots.

The inspection robot uses autonomous navigation to move to pre-set navigation points, where it uses a robotic arm to control its end-effector information collection device to align with the lettuce and maintain an optimal imaging distance of 1 m, thereby completing the collection of RGB images, depth images, and near-infrared images. Seven morphological parameters and 10 vegetation indices were extracted from the collected images, and 12 parameters with high correlation to fresh weight were selected through Pearson correlation analysis. Then, three machine learning methods (MLR, RFR, BPNN) were used to predict fresh weight based on the selected parameters. By analyzing the training results of different models and feature parameters, it was found that more complex feature mapping was needed between the 12 lettuce phenotypic parameters to enhance the expression of the intrinsic relationships between the data. Subsequently, a two-layer feature dimension-increasing module (DE-BP) based on the BPNN model was designed to improve model accuracy. The results showed that the R^2 values for predicting lettuce plant height, maximum crown width, and fresh weight were 0.85, 0.93, and 0.84, respectively, with RMSE values of 7 mm, 6 mm, and 8 g, respectively. These results accurately reflect the growth status of lettuce, providing a scientific basis for growth analysis and facility environmental control.

Author Contributions: Conceptualization, X.H. and X.Z.; methodology, X.H.; software, X.H. and Y.Z.; validation, X.Z. and L.H.; formal analysis, X.H. and T.L.; investigation, X.H.; resources, X.H. and L.H.; data curation, X.H. and T.L.; writing—original draft preparation, X.H.; writing—review and editing, X.H. and X.Z.; funding acquisition, X.Z. and Y.Z. All authors have read and agreed to the published version of the manuscript.

Funding: This research was funded by the project of the National Key Research and Development Program of China (Grant Nos.2022YFD2002302); National Key Research and Development Pro- gram for Young Scientists (Grant Nos.2022YFD2000200); Agricultural Equipment Department of Jiangsu University (Grant Nos. NZXB20210106); and Jiangsu Province Industry Forward-looking Program Project (Grant Nos. BE2023017).

Institutional Review Board Statement: Not applicable.

Data Availability Statement: The raw data supporting the conclusions of this article will be made available by the authors on request.

Acknowledgments: The authors express their gratitude to the School of Agricultural Engineering, Jiangsu University, for providing the essential instruments without which this work would not have been possible. The authors also thank the reviewers for their important feedback.

Conflicts of Interest: The authors declare no conflicts of interest.

References

1. Yuan, H.; Song, M.; Liu, Y.; Xie, Q.; Cao, W.; Zhu, Y.; Ni, J. Field Phenotyping Monitoring Systems for High-Throughput: A Survey of Enabling Technologies, Equipment, and Research Challenges. *Agronomy* **2023**, *13*, 2832. [CrossRef]
2. Rahaman, M.M.; Chen, D.; Gillani, Z.; Klukas, C.; Chen, M. Advanced Phenotyping and Phenotype Data Analysis for the Study of Plant Growth and Development. *Front. Plant Sci.* **2015**, *6*, 619. [CrossRef]
3. Taha, M.F.; Mao, H.; Mousa, S.; Zhou, L.; Wang, Y.; Elmasry, G.; Al-Rejaie, S.; Elwakeel, A.E.; Wei, Y.; Qiu, Z. Deep Learning-Enabled Dynamic Model for Nutrient Status Detection of Aquaponically Grown Plants. *Agronomy* **2024**, *14*, 2290. [CrossRef]
4. Zhao, Y.; Zhang, X.; Sun, J.; Yu, T.; Cai, Z.; Zhang, Z.; Mao, H. Low-Cost Lettuce Height Measurement Based on Depth Vision and Lightweight Instance Segmentation Model. *Agriculture* **2024**, *14*, 1596. [CrossRef]
5. Liu, T.; Zhu, S.; Yang, T.; Zhang, W.; Xu, Y.; Zhou, K.; Wu, W.; Zhao, Y.; Yao, Z.; Yang, G.; et al. Maize Height Estimation Using Combined Unmanned Aerial Vehicle Oblique Photography and LIDAR Canopy Dynamic Characteristics. *Comput. Electron. Agric.* **2024**, *218*, 108685. [CrossRef]
6. Ge, X.; Wu, S.; Wen, W.; Shen, F.; Xiao, P.; Lu, X.; Liu, H.; Zhang, M.; Guo, X. LettuceP3D: A Tool for Analysing 3D Phenotypes of Individual Lettuce Plants. *Biosyst. Eng.* **2025**, *251*, 73–88.
7. Vadez, V.; Kholová, J.; Hummel, G.; Zhokhavets, U.; Gupta, S.K.; Hash, C.T. LeasyScan: A Novel Concept Combining 3D Imaging and Lysimetry for High-Throughput Phenotyping of Traits Controlling Plant Water Budget. *J. Exp. Bot.* **2015**, *66*, 5581–5593. [PubMed]
8. Hassan, M.A.; Chang, C.Y.Y. PhenoGazer: A High-Throughput Phenotyping System to Track Plant Stress Responses Using Hyperspectral Reflectance, Nighttime Chlorophyll Fluorescence and RGB Imaging in Controlled Environments. *Plant Phenomics* **2025**, *7*, 100047.
9. Yu, H.; Dong, M.; Zhao, R.; Zhang, L.; Sui, Y. Research on Precise Phenotype Identification and Growth Prediction of Lettuce Based on Deep Learning. *Environ. Res.* **2024**, *252*, 118845. [CrossRef]
10. Jin, Y.; Liu, J.; Xu, Z.; Yuan, S.; Li, P.; Wang, J. Development Status and Trend of Agricultural Robot Technology. *Int. J. Agric. Biol. Eng.* **2021**, *14*, 1–19. [CrossRef]
11. Su, M.; Zhou, D.; Yun, Y.; Ding, B.; Xia, P.; Yao, X.; Ni, J.; Zhu, Y.; Cao, W. Design and Implementation of a High-Throughput Field Phenotyping Robot for Acquiring Multisensor Data in Wheat. *Plant Phenomics* **2025**, *7*, 100014. [CrossRef]
12. Hosoda, Y.; Tada, T.; Goto, H. Lettuce Fresh Weight Prediction in a Plant Factory Using Plant Growth Models. *IEEE Access* **2024**, *12*, 97226–97234. [CrossRef]
13. Ma, H.; Wen, W.; Gou, W.; Lu, X.; Fan, J.; Zhang, M.; Liang, Y.; Gu, S.; Guo, X. 3D Time-Series Phenotyping of Lettuce in Greenhouses. *Biosyst. Eng.* **2025**, *250*, 250–269. [CrossRef]
14. Wang, J.; Zhang, Y.; Gu, R. Research Status and Prospects on Plant Canopy Structure Measurement Using Visual Sensors Based on Three-Dimensional Reconstruction. *Agriculture* **2020**, *10*, 462. [CrossRef]
15. Bloch, V.; Shapiguzov, A.; Kotilainen, T.; Pastell, M. A Method for Phenotyping Lettuce Volume and Structure from 3D Images. *Plant Methods* **2025**, *21*, 27. [CrossRef]
16. Wang, Z.; Li, T.; Du, R.; Yang, N.; Ping, J. A High-Efficiency Lettuce Quality Detection System Based on FPGA. *Comput. Electron. Agric.* **2025**, *231*, 109978. [CrossRef]
17. Li, J.; Wang, Y.; Zheng, L.; Zhang, M.; Wang, M. Towards End-to-End Deep RNN Based Networks to Precisely Regress of the Lettuce Plant Height by Single Perspective Sparse 3D Point Cloud. *Expert Syst. Appl.* **2023**, *229*, 120497. [CrossRef]
18. Gu, W.; Wen, W.; Wu, S.; Zheng, C.; Lu, X.; Chang, W.; Xiao, P.; Guo, X. 3D Reconstruction of Wheat Plants by Integrating Point Cloud Data and Virtual Design Optimization. *Agriculture* **2024**, *14*, 391. [CrossRef]
19. Tan, J.; Hou, J.; Xu, W.; Zheng, H.; Gu, S.; Zhou, Y.; Qi, L.; Ma, R. PosNet: Estimating Lettuce Fresh Weight in Plant Factory Based on Oblique Image. *Comput. Electron. Agric.* **2023**, *213*, 108263. [CrossRef]
20. Yi, Y.A.; Shutao, M.A.; Wending, Z.H.; Houcheng, L.I.; Song, G.U. Segmenting Collective Lettuce to Predict Fresh Weight Using Three-Dimensional Point Cloud. *Trans. Chin. Soc. Agric. Eng.* **2025**, *41*, 192–199.
21. Wang, Y.; Wang, J.; Zhang, W.; Zhan, Y.; Guo, S.; Zheng, Q.; Wang, X. A Survey on Deploying Mobile Deep Learning Applications: A Systemic and Technical Perspective. *Digit. Commun. Netw.* **2022**, *8*, 1–17. [CrossRef]
22. Chen, Y.; Zheng, B.; Zhang, Z.; Wang, Q.; Shen, C.; Zhang, Q. Deep Learning on Mobile and Embedded Devices: State-of-the-Art, Challenges, and Future Directions. *ACM Comput. Surv.* **2021**, *53*, 84. [CrossRef]
23. Li, Q.; Gao, H.; Zhang, X.; Ni, J.; Mao, H. Describing Lettuce Growth Using Morphological Features Combined with Nonlinear Models. *Agronomy* **2022**, *12*, 860. [CrossRef]
24. Niu, Y.; Han, W.; Zhang, H.; Zhang, L.; Chen, H. Estimating Maize Plant Height Using a Crop Surface Model Constructed from UAV RGB Images. *Biosyst. Eng.* **2024**, *241*, 56–67. [CrossRef]
25. Zhang, L.; Song, X.; Niu, Y.; Zhang, H.; Wang, A.; Zhu, Y.; Zhu, X.; Chen, L.; Zhu, Q. Estimating Winter Wheat Plant Nitrogen Content by Combining Spectral and Texture Features Based on a Low-Cost UAV RGB System throughout the Growing Season. *Agriculture* **2024**, *14*, 456. [CrossRef]

26. Barboza, T.O.C.; Ardigueri, M.; Souza, G.F.C.; Ferraz, M.A.J.; Gaudencio, J.R.F.; Santos, A.F.d. Performance of Vegetation Indices to Estimate Green Biomass Accumulation in Common Bean. *AgriEngineering* **2023**, *5*, 840–854. [CrossRef]
27. Guijarro, M.; Pajares, G.; Riomoros, I.; Herrera, P.J.; Burgos-Artizzu, X.P.; Ribeiro, A. Automatic Segmentation of Relevant Textures in Agricultural Images. *Comput. Electron. Agric.* **2011**, *75*, 75–83. [CrossRef]
28. Burgos-Artizzu, X.P.; Ribeiro, A.; Guijarro, M.; Pajares, G. Real-Time Image Processing for Crop/Weed Discrimination in Maize Fields. *Comput. Electron. Agric.* **2011**, *75*, 337–346.
29. Meyer, G.E.; Neto, J.C. Verification of Color Vegetation Indices for Automated Crop Imaging Applications. *Comput. Electron. Agric.* **2008**, *63*, 282–293. [CrossRef]
30. Hague, T.; Tillett, N.D.; Wheeler, H. Automated Crop and Weed Monitoring in Widely Spaced Cereals. *Precis. Agric.* **2006**, *7*, 21–32. [CrossRef]
31. Gamon, J.A.; Surfus, J.S. Assessing Leaf Pigment Content and Activity with a Reflectometer. *New Phytol.* **1999**, *143*, 105–117. [CrossRef]
32. Iyoob, A.L.; Norbert, S.A.; Ameer, M.L.F.; Nasar-u-Minallah, M.; Zahir, I.L.M.; Nuskiya, M.H.F. Using UAV RGB Image for Object-based Feature Detection. *Procedia Comput. Sci.* **2025**, *260*, 1052–1059. [CrossRef]
33. Lee, D.-H.; Park, J.-H. Development of a UAS-Based Multi-Sensor Deep Learning Model for Predicting Napa Cabbage Fresh Weight and Determining Optimal Harvest Time. *Remote Sens.* **2024**, *16*, 3455. [CrossRef]

Disclaimer/Publisher's Note: The statements, opinions and data contained in all publications are solely those of the individual author(s) and contributor(s) and not of MDPI and/or the editor(s). MDPI and/or the editor(s) disclaim responsibility for any injury to people or property resulting from any ideas, methods, instructions or products referred to in the content.

agriculture

MDPI

Article

Design and Test of a Bionic Auxiliary Soil-Crushing Device for Strip-Tillage Machines

Kui Zhang †, Yong-Ying Zhang †, Xinliang Zhao, Yun Zhao, Xin Feng, Qi Wang * and Jinwu Wang *

College of Engineering, Northeast Agricultural University, Harbin 150030, China; s230701023@neau.edu.cn (K.Z.); s220701003@neau.edu.cn (Y.-Y.Z.); s220701005@neau.edu.cn (X.Z.); s210702014@neau.edu.cn (Y.Z.); fx2020fx@163.com (X.F.)

* Correspondence: wangqi@neau.edu.cn (Q.W.); jinwuw@neau.edu.cn (J.W.)

† These authors contributed equally to this work.

Abstract: Suitable strip-tillage effectively enhances crop productivity and soil quality in Northeast China, yet conventional strip-tillage machines suffer from inadequate soil fragmentation. To address this issue, this study developed a bionic auxiliary soil-crushing device for the equipment. Specifically, we conducted a theoretical analysis of the soil-crushing blade to identify the key structural parameters affecting operational performance, along with their optimal value ranges. The blade tooth structure was designed following the claw-toe contour of the Oriental mole cricket (*Gryllotalpa orientalis*) for enhanced efficiency. A two-factor (working width and working depth), three-level central composite design (CCD) experiment was carried out using EDEM 2021 discrete element simulation software, taking the soil fragmentation rate and operational resistance as response variables. The results suggested that optimal performance was achieved at a working width of 40.66 mm and a working depth of 50 mm. Field experiments demonstrate that the soil fragmentation rate increased as the operational speed rose. The addition of the auxiliary device contributed to a soil fragmentation rate of 94.54%, bringing about an 11.54% improvement compared to the non-equipped machine. This outcome also validated the accuracy of the simulation experiments. This research provides technical and equipment support for the further development of conservation tillage practices.

Keywords: passive strip-tillage machines; biomimicry; auxiliary soil-crushing device; discrete element method; structural optimization

1. Introduction

Strip-tillage is an emerging conservation tillage technique that relocates crop residue between planting rows to protect the soil and generate residue-free strips for seeding operations. This method facilitates crop growth and enhances ecological benefits [1–3]. However, low soil fragmentation rates lead to poor soil aeration and hence restrict crop growth [4,5]. Strip-tillage machines play a crucial role in implementing strip-tillage operations, and their soil-crushing components are fundamental to ensuring optimal conditions for seedbed preparation [6]. Typically, an increase in the soil fragmentation rate induces higher soil disturbance, greater operational resistance [7], and increased energy consumption. Therefore, research on developing soil-crushing devices for strip-tillage machines should primarily focus on enhancing soil fragmentation and disturbance while minimizing operational resistance.

Currently, passive strip-tillage machines are widely adopted due to their superior adaptability and contour-following capabilities [8,9]. Their primary soil-crushing compo-

nents include disc plows and press wheels [10,11]. The press wheel, mounted at the rear of the tillage implement, assists in soil fragmentation and the fulfillment of its compaction function [12,13]. The disc plow, as the primary soil-crushing device, is favored for its simple structure, strong cutting ability, and effective soil fragmentation performance [14,15]. Researchers have made various modifications to disc plows to improve their operational efficiency. For example, Zhong et al. [16] developed a disc plow with a supporting device, achieving a straw-cutting rate of 71.7%. Zeng et al. [17] investigated the effect of disc plow diameter on soil disturbance, unveiling that increasing the diameter from 457 mm to 559 mm expanded the soil disturbance area by 127%, albeit at the cost of a 26% increase in vertical force. Nonetheless, current research on disc plows has focused on soil disturbance and cutting performance while overlooking post-disturbance soil fragmentation and the corresponding effect on operational resistance.

In recent years, bionics has emerged as an innovative design concept, providing new perspectives and solutions for mechanical structure optimization [18–20]. Wang et al. [21] utilized the bionic design method and developed a bionic elastic row cleaner inspired by the motion behavior of mole excavation, which improved the straw cleaning rate by 13.04% and reduced the working resistance by 39.24% compared with the conventional straw clearing wheel. Based on the excellent soil excavation ability of the hare, Zhao et al. [22] designed a bionic energy storage–profiling device, which improved the ability of flexible profiling, tillage depth control, and elastic energy storage while reducing the resistance of deep loosening, and ultimately reduced the energy consumption of deep loosening by 16.1%. Tan et al. [23] proposed a bionic furrowing blade using the contour curve of a dog's paw, which reduced the vertical tillage resistance, thus reducing the energy consumption by 4.88% compared to conventional blades. The forelegs of the Oriental mole cricket (*Gryllotalpa orientalis*) feature tooth-like structures, with claw tips curved outward, allowing for efficient soil excavation [24]. Xiao et al. [25] designed a bionic rotary tillage blade based on the claw-toe contour of the Oriental mole cricket, achieving a 9.91% and 9.09% reduction in horizontal and vertical resistance, respectively, at a blade shaft speed of 150 r/min. Liu et al. [26] optimized the structure of an excavation shovel by employing the extracted claw-toe contours of the Oriental mole cricket, so as to significantly improve mechanical performance and harvest efficiency. Although extensive research has been conducted on the Oriental mole cricket (*Gryllotalpa orientalis*), existing studies primarily focus on their geometric morphology and the mechanisms of viscosity reduction and resistance reduction. No studies have yet investigated the structural optimization of tillage implements through biomimetic design inspired by the claw-toe morphology of *Gryllotalpa orientalis* to enhance soil fragmentation performance under heavy clay conditions.

Although the strip-tillage system and its supporting equipment hold substantial market potential and development prospects in China, enhancing soil-crushing efficiency and operational quality in heavy clay soils remains an urgent challenge. To address this, the objectives of this study were to: (1) establish a high-efficiency bionic auxiliary soil-crushing device for integration with disc plows, tailored to the agronomic requirements of conservation tillage in northeastern China; (2) develop a discrete element simulation model of the soil-crushing blade interacting with the soil; (3) obtain the effects of blade geometry and forward speed on tillage performance metrics; and (4) validate the simulation accuracy through field experiments assessing the device's operational performance.

2. Materials and Methods

2.1. Structure and Working Principle of Auxiliary Soil-Crushing Device

An auxiliary soil-crushing device was integrated into the disc plow system to enhance the soil fragmentation rate and soil disturbance of existing strip-tillage machines

(Figure 1) [8]. The strip-till unit consisted of a profiling mechanism, a pressure spring, a straw-cutting coulter, an automatic-width-control row cleaner, two soil-loosening disc plows, and a V-shaped soil-crushing wheel. A good-quality seedbed, free of straw residue and with a uniform soil structure, can be established prior to sowing. The main technical parameters are set out in Table 1.

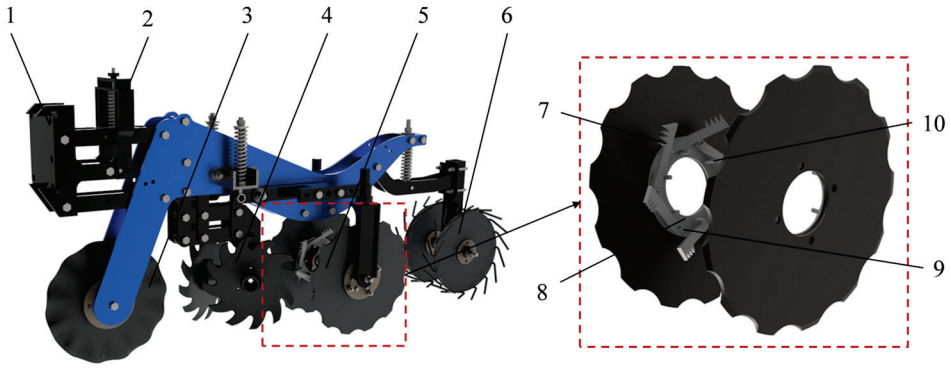

Figure 1. Schematic of strip-tillage machine and auxiliary soil-crushing device structure. 1. profiling mechanism. 2. tillage-depth-stabilization control system. 3. Straw-cutting coulter. 4. automatic-width-control row cleaner. 5. soil-loosening disc plow. 6. V-shaped soil-crushing wheel. 7. soil-crushing blade. 8. soil-crushing blade disk. 9. soil-crushing blade shaft. 10. positioning lugs.

Table 1. Main technical parameters.

Parameter	Values
Structure type	Three-point suspension
Dimension (length × width × height)/mm	1800 × 920 × 300
Machine quality (kg)	300
Row spacing (mm)	450–950
Working width (mm)	180–240
Tillage depth (mm)	60–120

The auxiliary soil-crushing device comprises two primary components: the soil-crushing blade disk and the soil-crushing blades. The soil-crushing blade shaft was concentrically mounted to the disc at a constant diameter, with positioning lugs welded radially inward. The soil-crushing blades were mounted on the soil-crushing blade shaft, positioned by positioning lugs, and welded to the soil-crushing blade disk after angle adjustment, facilitating precise soil-cutting and fragmentation performance.

During operation, the tractor provides power to drive the implement forward. The pressure spring applies force to the profiling mechanism, maintaining consistent downforce on the monobloc to ensure stable tillage depth. The coulters cut off the residual straw between rows, and the automatic-width row cleaner pushes the residual straws into the working row and throws them to the two sides of the working width. The soil-loosening disc plow loosens and breaks the soil under the preset width in a clean row. Following that, the V-shaped soil-crushing device impacts and breaks the loosened soil, forming clean and consistent strips.

The combined effect of the traction force of the implement and the reaction force of the soil yields a force couple. As a result, the disc plow passively rotates around a fixed axis, exerting compression and overturning forces on the soil within the strip. As the disc plow rotates, the auxiliary soil-crushing device engages with displaced soil particles and the surface soil within the strip, performing cutting and dispersing actions to further fragment the disturbed soil. Subsequently, the crushed soil is redirected by the disc plow, ensuring a level and uniform soil surface within the tilled strip.

2.2. Design and Analysis of Key Components

2.2.1. Design and Analysis of the Soil-Crushing Blade Structure

During operation, the working principle of the soil-crushing blade in the auxiliary soil-crushing device is similar to that of a reverse rotary tillage blade [27,28]. In this study, the IT245 rotary tillage curved blade was used as a reference for the design of the soil-crushing blade, with a selected blade rotation angle β of 37° [29,30]. Figure 2 illustrates the front view and side view of the soil-crushing blade. As revealed from the analysis, the structural parameters of the soil-crushing blade satisfy:

$$l_1^2 = a^2 + r^2 - 2arc\cos(\beta) \tag{1}$$

$$l = \frac{s}{\sin(\alpha)} + 0.012 \tag{2}$$

$$l_1 = \frac{l - 0.012}{\cos(\alpha)} \tag{3}$$

where l_1 denotes the projection length of the soil-crushing blade on the disc plow (m); a represents the eccentric distance of the soil-crushing blade (m); r indicates the projected rotational radius of the auxiliary soil-crushing device on the disc plow (m); s embodies the working width of the soil-crushing blade (m); β refers to the rotation angle of the soil-crushing blade (rad); l describes the length of the soil-crushing blade (m); α expresses the offset angle of the soil-crushing blade (rad).

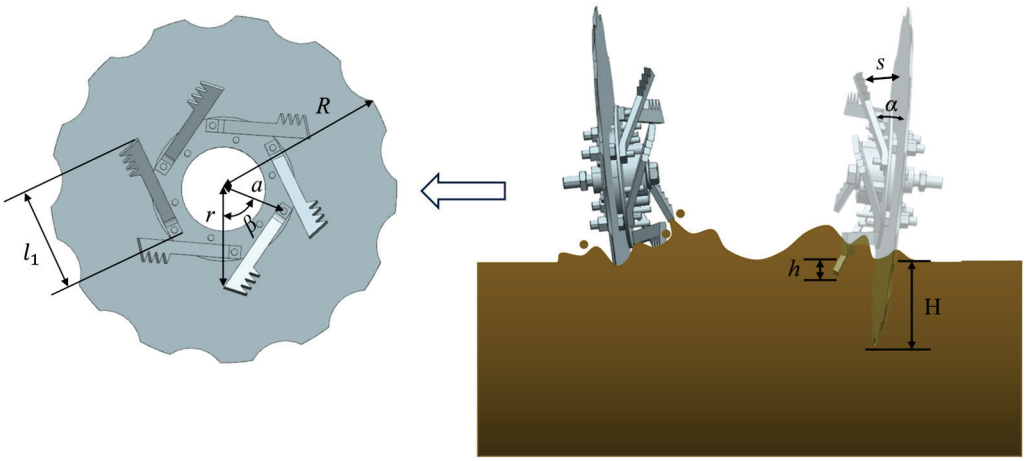

Figure 2. Structural parameters of soil-crushing blade.

When the soil-crushing blade reaches its maximum working depth, the following parameters satisfy the given relationship:

$$r = R - \frac{H + h}{\cos(\theta)} \tag{4}$$

where R represents the radius of the opposing disc plow (m); H denotes the working depth of the opposing disc plow (m); h embodies the working depth of the soil-crushing blade (m).

The l, α, β and a significantly impact the operational performance of the auxiliary soil-crushing device. In Equations (1)–(4), the working width s and the working depth h of the soil-crushing blade are the primary structural parameters affecting its operational efficiency.

2.2.2. Determination of Soil-Crushing Blade Parameter Ranges

The tilt angle and inclination angle of the disc plow trigger variations in its internal spatial configuration, which directly affect the working width of the soil-crushing blade [14,31,32]. In

this study, we established a spatial coordinate system ($OXYZ$) with the center of the disc plow as the origin to analyze the relationship between blade working width and disc plow rotation angle. Specifically, the X-axis represents the forward direction of the auxiliary soil-crushing device, the Y-axis lies in the horizontal plane perpendicular to the X-axis, and the Z-axis is in the vertical direction. The tip of the soil-crushing blade projects onto the disc plow at point A with coordinates $(x, 0, z)$ when the disc plow is not tilted. However, the new coordinates of point A shift to (x_1, y, z_1) after the disc plow undergoes tilting and inclination. The maximum Y-axis value of point A was determined through a spatial coordinate rotation matrix and conditional extremum calculations. In this way, the working width range of the soil-crushing blade was optimized to enhance soil fragmentation and simultaneously minimize operational resistance:

$$\begin{pmatrix} 1 & 0 & 0 \\ 0 & \cos(\theta) & -\sin(\theta) \\ 0 & \sin(\theta) & \cos(\theta) \end{pmatrix} \cdot \begin{pmatrix} x \\ 0 \\ z \end{pmatrix} = \begin{pmatrix} x_0 \\ y_0 \\ z_0 \end{pmatrix} \tag{5}$$

$$\begin{pmatrix} \cos(\gamma) & -\sin(\gamma) & 0 \\ \sin(\gamma) & \cos(\gamma) & 0 \\ 0 & 0 & 1 \end{pmatrix} \cdot \begin{pmatrix} x_0 \\ y_0 \\ z_0 \end{pmatrix} = \begin{pmatrix} x_1 \\ y \\ z_1 \end{pmatrix} \tag{6}$$

$$y = x\sin(\gamma) - z\sin(\theta)\cos(\gamma) \tag{7}$$

$$x^2 + z^2 = r^2 \tag{8}$$

$$r = h + R - \frac{H}{\cos(\theta)} \tag{9}$$

$$s_m = \frac{S_0 - 2|y|}{2} \tag{10}$$

where θ denotes the rotation angle of the opposing disc plow around the forward direction (X-axis) (rad); γ represents the rotation angle of the opposing disc plow around the vertical direction (Z-axis) (rad); S_0 indicates the center distance between the two opposing disc plows (m); s_m embodies the maximum working width of the soil-crushing blade (m) (Figure 3).

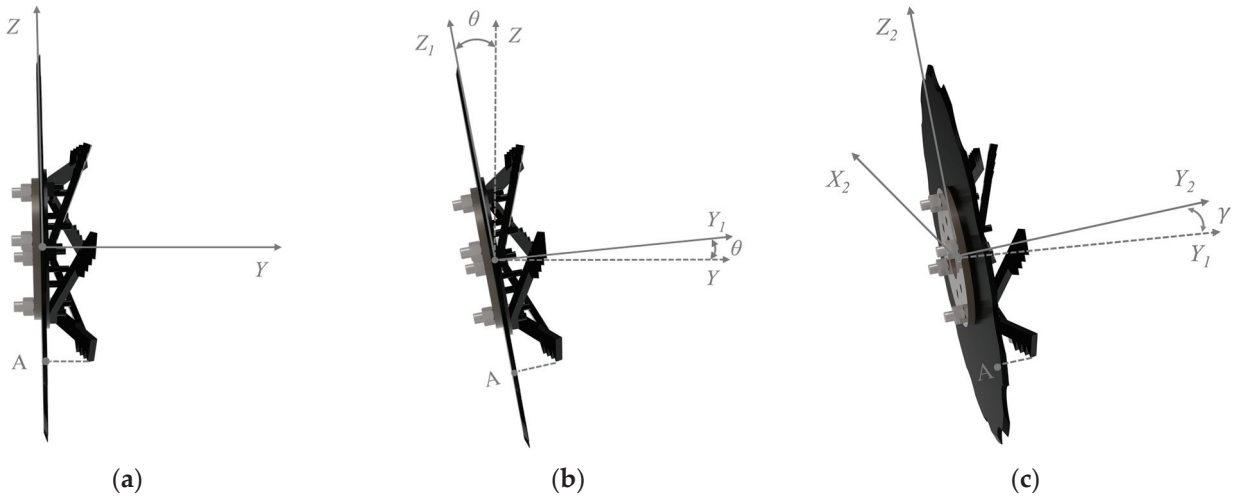

(**a**) (**b**) (**c**)

Figure 3. Schematic of disc plow tilting process. (**a**) Without tilting or inclination; (**b**) Tilting around X-axis; (**c**) Tilting around the Z-axis after the X-axis rotation.

The working width (s) of the soil-crushing blade is defined as the vertical distance between the blade tip and the disc plow, satisfying the following relationship:

$$s = l\sin(\alpha) \leq s_m \tag{11}$$

Following the above analysis and the field conditions of low-tillage seeding operations in Northeast China, the tilt angle and inclination angle of the disc plow were set at 5° and 4°, respectively [33]. According to the technical requirements of low-tillage seeding operations, the soil-crushing blade primarily acts on displaced soil clods and compacted surface soil disturbed by the disc plow. Therefore, the penetration depth h of the blade tip should be consistent with the seeding depth. It has been calculated based on these design requirements that the parameter ranges for optimal performance are 35 mm $\leq s \leq$ 95 mm and 30 mm $\leq h \leq$ 50 mm.

2.2.3. Determination the Number of Soil-Crushing Blades to Be Installed

During operation, the cutting interval of the soil-crushing blade significantly impacts the degree of soil fragmentation [34]. The cutting interval can be calculated by:

$$S = v_m t = \frac{2\pi R}{Z\lambda} \tag{12}$$

$$t = \frac{2\pi}{Z\omega} \tag{13}$$

where S denotes the cutting interval (mm); v_m indicates the forward speed of the implement (m/s); t refers to the time interval between two consecutive blade cuts (s); Z represents the number of blades; λ stands for the ratio of the blade tip's circumferential velocity to the implement's forward velocity; ω describes the angular velocity of the blade tip's circular motion.

Finely crushed soil particles can fill voids between each other, forming a stable soil aggregate structure and thus promoting crop growth [35]. As suggested by setting the cutting interval S at 60 mm, an optimal blade count of six meets agronomic requirements for effective soil fragmentation [36].

2.3. Bionic Design of Soil-Crushing Blade

In this study, the Oriental mole cricket was selected as the bionic prototype because the strong digging capabilities of its rake-shaped forelegs enable it to be highly effective in soil fragmentation [24,37]. With the purpose of achieving optimal soil-crushing performance, the study primarily focuses on extracting and applying parameters from its more robust claw toes. Specifically, the claw toe length is 1.9 mm, the toe tip angle is 35°, and the distance between adjacent toe tips is 2.5 mm. Regarding practical engineering applications, the rounded shape of the toe tips was simplified in the study by considering only the frontal contour of the claw toes [38]. Based on the earlier analysis of the working width and depth of the soil-crushing blade, the claw toe length and toe tip spacing were scaled proportionally to determine the final structural dimensions of the soil-crushing blade: blade tooth length = 13 mm, tooth spacing = 10 mm, and tooth angle = 35°. The design process is depicted in Figure 4.

2.4. Simulation Test Based on DEM

2.4.1. Establishment of EDEM Discrete Element Model

The auxiliary soil-crushing device model was simplified by removing irrelevant components that do not affect its operational performance, to ensure rational and effective simulation and computation. The 3D model of the device was created in CATIA P3

V5-6R2020 software (Dassault System, Paris, France) at scale 1:1 and imported into the Geometry module of engineering discrete element method (EDEM) software in .igs format. The material properties of the simulation model were set as follows: 65 Mn steel, a Poisson's ratio of 0.3, shear modulus of 7.9×10^{10} Pa, and density of 7865 kg/m^3 [39,40]. Considering the structural characteristics of Northeast China's soil, the Hertz–Mindlin with Bonding model was selected to define the mechanical interactions between soil particles, with a shear modulus of 1.21×10^6 Pa, density of 2130 kg/m^3, and Poisson's ratio of 0.4. Furthermore, a single spherical particle with a radius of 3 mm was adopted as the soil particle model for accurate simulation. The specific contact parameters for the simulation materials are listed in Table 2 [21,41].

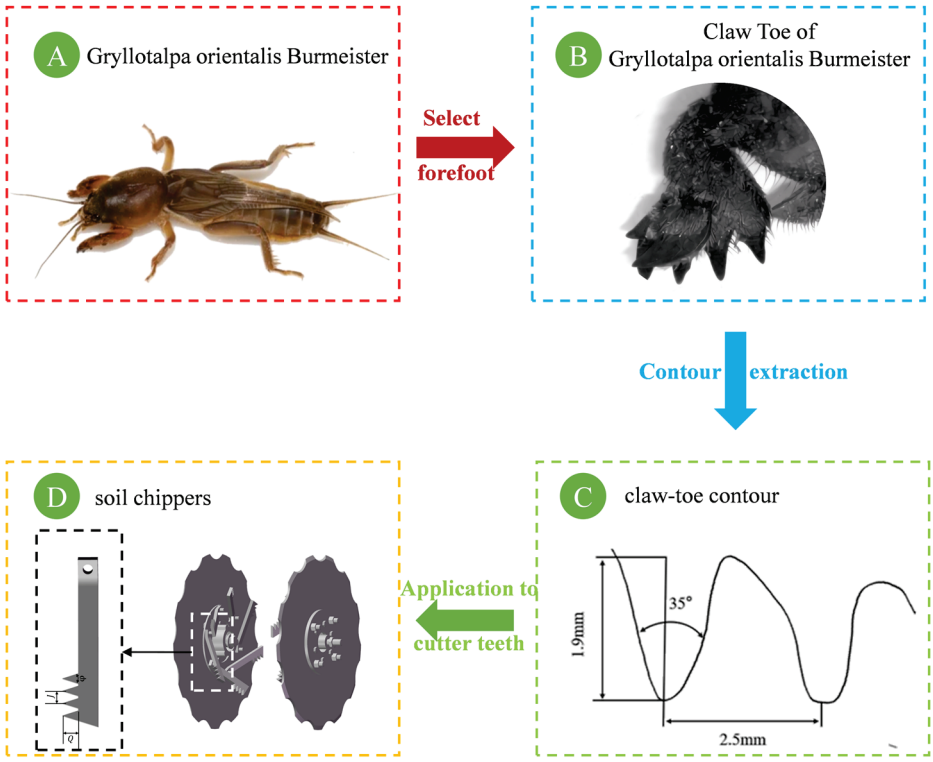

Figure 4. The bionic design process of the auxiliary soil-crushing blade.

Table 2. Contact parameters of simulation materials.

Material	Parameter	Value
Soil particle—soil particle	Coefficient of restitution	0.5
	Static friction coefficient	0.3
	Rolling friction coefficient	0.2
Soil particle—65 Mn steel	Coefficient of restitution	0.6
	Static friction coefficient	0.6
	Rolling friction coefficient	0.05

A virtual soil bin was constructed in EDEM 2021 software (Altair, Troy, MI, USA) to simulate the actual soil-crushing conditions in the field. The dimensions of the soil bin were set to 2200 mm × 500 mm × 300 mm (length × width × height) and designated as a virtual particle factory, ensuring a sufficient quantity of soil particles for simulation (Figure 5). During the generation of soil particles, they could freely settle under gravity. After the formation of the entire particle group, a vertical load was applied on the top layer

to calibrate soil density and compact the soil model. This guarantees that the simulation closely matched actual field soil conditions.

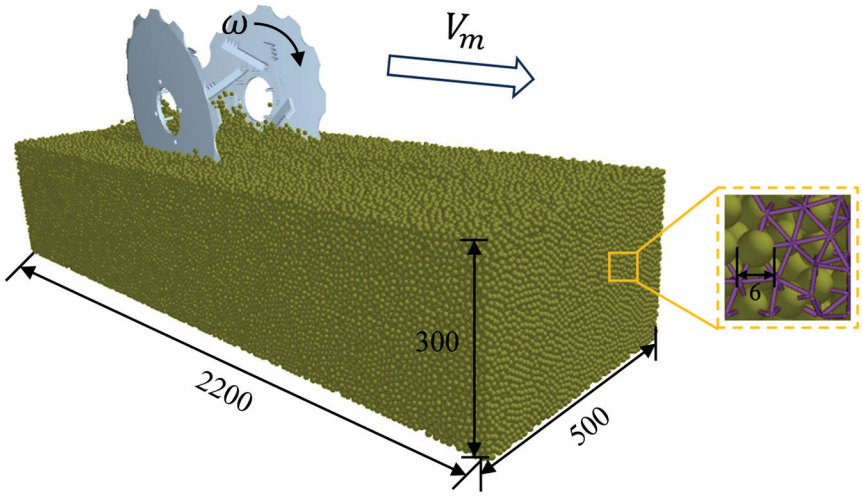

Figure 5. Soil-crushing operation simulation process.

The simulation process is illustrated in Figure 5.

2.4.2. Simulation Test Measurement Methods

(1) Soil Fragmentation Rate

The number of Bonding connections between soil particles was extracted by the Export function in the Analyst module of EDEM software. As shown in Figure 6, the orange dashed indicates the stable value of the number of broken bonds. Afterward, the soil fragmentation rate was determined by calculating the ratio of the number of broken Bonding connections to the total number of Bonding connections within the tilled strip.

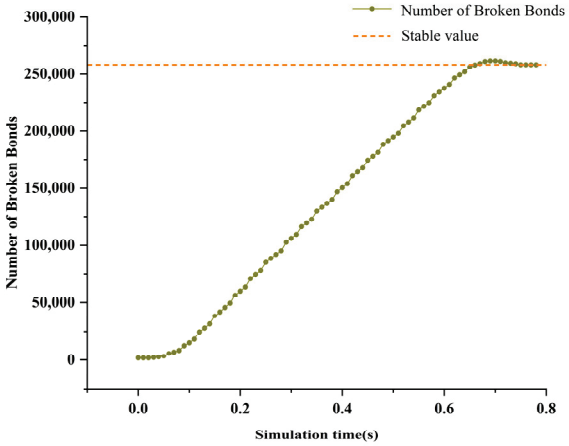

Figure 6. Number of broken soil particle bonding bonds.

(2) Operational Resistance

The Graph module in the Analyst section of EDEM software was utilized to collect the real-time force data acting on the soil-crushing device during the simulation. The red dashed line in Figure 7 is within the data collection area, and the blue dashed line is the average of the determination of operational resistance in the data collection area as determination of operational resistance.

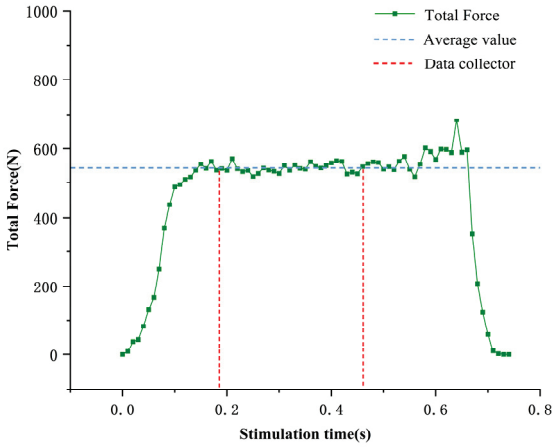

Figure 7. Determination of operational resistance.

2.4.3. Simulation Test Design

(1) CCD Experiment

The soil-crushing blade parameters were optimized through a two-factor, three-level central composite design (CCD) experiment. Following theoretical analysis, the experimental factors were the blade's working width and working depth, and the response variables were soil fragmentation rate and operational resistance. The multi-factor experimental variables and their corresponding codes are presented in Table 3.

Table 3. Experimental factors and levels.

Code	Factor	
	X_1 Working Width s (mm)	X_2 Working Depth *h* (mm)
−1	35	30
0	55	40
1	75	50

(2) Blade Tooth Structure Comparison Test

The objectives of this test were to investigate the effects of forward speed and different types of blade tooth structures on soil fragmentation rate and operational resistance. While the disc plow parameters and the optimized soil-crushing blade structure remained unchanged, a comparative simulation test was conducted between bionic and non-bionic blade tooth structures at different operating speeds to analyze the effects of bionic design and forward speed on operational performance.

2.5. Field Experiment

2.5.1. Field Experiment Method

The bionic auxiliary soil-crushing device was designed to reinforce soil fragmentation efficiency. Therefore, our team conducted the field experiment at the Xiangyang Farm Research Base in Harbin, Heilongjiang Province, from 15 to 22 October 2023. Different forward speeds were set in combination with the agronomic standards of Heilongjiang Province to further evaluate the effect of forward speed on soil fragmentation rate. The experimental field featured Northeast black clay soil with maize as the previous crop. The straw cover in the experimental area was quantified as 1.8 kg/m^2 using a standardized five-point sampling protocol. The moisture content of the straw was determined to be 50% by oven-drying at 105 °C until constant weight was achieved. This experiment was exclusively designed to assess the soil fragmentation rate without investigating force conditions. The

disc plow was attached to a Dituo 704 tractor (Shandong Dituo Agricultural Equipment Co., Ltd., Weifang, China) with a three-point hitch system. To ensure experimental accuracy, we divided each test run into sections, with a working length of 70 m and a working width of 3 m, while designating the middle 50 m as the data collection zone.

During the field experiment, the disc plow working depth was set to 120 mm, and the operating width was set to 260 mm. Besides, the forward speeds of the tractor were set at 6 km/h, 8 km/h, and 10 km/h. The field experiment setup is displayed in Figure 8.



(**a**) (**b**)

Figure 8. Field experiment. (**a**) Field operation of the bionic auxiliary soil-crushing device; (**b**) Field operation effect.

2.5.2. Bionic Auxiliary Soil-Crushing Device Field Operation

The soil fragmentation performance was evaluated by calculating the percentage of soil clods of different sizes relative to the total soil mass [9]. After each test, soil samples were collected from three evenly spaced measurement points within the data collection zone. Each measurement point had dimensions of 0.5 m (length) × 0.26 m (width) × 0.12 m (height). The mass of soil clods smaller than 4 cm was weighed and compared to the total soil mass in the sample area. Subsequently, the soil fragmentation rate was calculated as the ratio of small clod mass to total soil mass, allowing for a quantitative assessment of the soil-crushing efficiency. The measurement process is provided in Figure 9.



(**a**) (**b**)

Figure 9. Operational effect and measurement indicators. (**a**) Selection of soil fragmentation rate measurement points; (**b**) Soil fragmentation rate measurement process.

2.6. Statistical Methods

In this study, we conducted parameter optimization, simulation experiments, and field trials using Design-Expert 13 (Stat-Ease, Minneapolis, MN, USA), Excel 2019(Microsoft, Washington, DC, USA), and SPSS 26 software (IBM, Chicago, IL, USA). The collected data were analyzed through least significant difference (LSD) analysis, analysis of variance (ANOVA), regression analysis, and response surface analysis. LSD analysis was performed to evaluate whether significant differences existed between different levels of the same experimental factor. ANOVA and regression analysis were employed to establish the regression equations for the relationship between soil-crushing blade working width, working depth, soil fragmentation rate, and operational resistance. The F-test and *p*-value were applied to select the most suitable model. Additionally, the response surface analysis was performed to visualize the interaction effects of soil-crushing blade parameters on the response indicators. LSD analyses and Tukey's test were used to assess whether there were significant differences between different levels of cutter tooth type and forward speed. This was used to determine whether the bionic knife teeth had a significant advantage in terms of work resistance and soil fragmentation rate, and to identify the pattern of the effect of different levels of operating speed on these two indicators. Furthermore, the LSD analysis was implemented to investigate whether significant differences existed between the field test results of machines with and without the bionic auxiliary soil-crushing device.

3. Results and Discussion

3.1. Optimization and Analysis of CCD Experiment

The experimental results are presented in Table 4.

Table 4. Experimental design and results.

Trial No.	Experimental Factors		Evaluation Indicators	
	Working Width X_1	Working Depth X_2	Soil Fragmentation Rate Y_1 (%)	Operational Resistance Y_2 (N)
1	35	30	83.53	544.67
2	75	30	85.73	598.68
3	35	50	85.98	583.15
4	75	50	87.06	654.68
5	26.7157	40	83.88	539.27
6	83.2843	40	85.83	640.48
7	55	25.8579	84.70	565.88
8	55	54.1421	88.24	627.90
9	55	40	86.03	590.97
10	55	40	86.31	594.66
11	55	40	86.30	593.56
12	55	40	86.5	599.39
13	55	40	86.29	594.63

3.1.1. ANOVA

A multiple regression fitting was performed on the data in Table 4, to establish regression equations for soil fragmentation rate Y_1 and operational resistance Y_2 as functions of working width X_1 and working depth X_2, expressed as:

$$Y_1 = 86.29 + 0.7547X_1 + 1.1X_2 - 0.28X_1X_2 - 0.7374X_1^2 + 0.0701X_2^2 \quad (14)$$

$$Y_2 = 594.64 + 33.58X_1 + 22.77X_2 + 4.38X_1X_2 - 1.91X_1^2 + 1.6X_2^2 \quad (15)$$

The ANOVA for the response values Y_1 and Y_2 is summarized in Table 5. The lack-of-fit terms for both models were greater than 0.05, implying that the lack of fit was insignificant. In other words, the regression models fit well. The *p*-values for the regression models were both less than 0.01, reflecting that they are highly significant and that the regression results are reliable.

Table 5. ANOVA results.

Source of Variation	Y_1					Y_2				
	Sum of Squares	**Degree of Squares**	**Mean square**	***F***	***p***	**Sum of Squares**	**Degree of Squares**	**Mean Square**	***F***	***p***
Model	18.50	5	3.70	74.10	<0.0001 **	13,298.48	5	2659.70	209.35	<0.0001 **
x_1	4.56	1	4.56	91.26	<0.0001 **	9023.12	1	9023.12	710.24	<0.0001 **
x_2	9.65	1	9.65	193.27	<0.0001 **	4149.13	1	4149.13	326.59	<0.0001 **
$x_1\ x_2$	0.3136	1	0.3136	6.28	0.0406 *	76.74	1	76.74	6.04	0.0436 *
${x_1}^2$	3.78	1	3.78	75.75	<0.0001 **	25.26	1	25.26	1.99	0.2014
${x_2}^2$	0.0342	1	0.0342	0.6851	0.4351	17.86	1	17.86	1.41	0.2745
Residual	0.3495	7	0.0499			88.93	7	12.70		
Lack of Fit	0.2374	3	0.0791	2.82	0.1709	51.73	3	17.24	1.85	0.2779
Corrected Total	18.85	12				13,387.41	12			
R^2	0.9815					0.9934				

Note: "**" indicates highly significant ($p < 0.01$) and "*" indicates significant ($0.01 < p < 0.05$).

The analysis of soil fragmentation rate reveals that x_1, x_2, and ${x_1}^2$ have a highly significant impact ($p < 0.01$); ${x_2}^2$ has a significant impact ($0.01 < p < 0.05$); and the interaction terms x_1 and x_2 do not exhibit a significant impact. The factor weight ranking for soil fragmentation rate is: working depth > working width, suggesting that working depth exerts a greater impact on soil fragmentation compared to working width. Similarly, the analysis of operational resistance demonstrates that x_1 and x_2 have a highly significant impact ($p < 0.01$), and the interaction terms x_1 and x_2 have a significant impact ($0.01 < p < 0.05$), but ${x_1}^2$ and ${x_2}^2$ do not have a significant impact. The factor weight ranking for operational resistance is: working width > working depth.

3.1.2. Response Surface Analysis

Figure 10a illustrates the effect of the working width and working depth of the soil-crushing blade on the soil fragmentation rate. When the working depth remains constant, the soil fragmentation rate initially increases and then decreases with the working width. When the working width remains constant, the soil fragmentation rate increases as the working depth increases. The primary reason for this trend is that as working width increases, maintaining the same working depth necessitates a longer blade, contributing to greater soil penetration, an expanded working range, and thereby reinforced soil fragmentation. However, the angle between the soil-crushing blade and the disc plow also increases when the working width continues to increase, potentially triggering soil accumulation. This accumulation can obstruct the interaction between soil particles and the disc plow, lowering the degree of soil fragmentation. In contrast, increasing the working depth results in the blade engaging with a larger volume of soil particles, and, hence, fragmentation efficiency is enhanced through additional effects and cutting actions.

Figure 10b illustrates the effect of working width and working depth on operational resistance. When the working depth remains constant, operational resistance increases as the working width increases. When the working width remains constant, operational resistance also increases with increasing working depth. This trend can be explained as follows: a wider working width enlarges the cutting area, requiring the blade to break and displace more soil. As a result, operational resistance is strengthened. Similarly, a greater working depth brings about deeper soil penetration, an expanded contact area between the blade and soil particles, and subsequently higher operational resistance. This finding aligns

with the research conducted by Hasimu [42], which suggests that operational resistance increases with the depth of operation and width of operation of the implement.

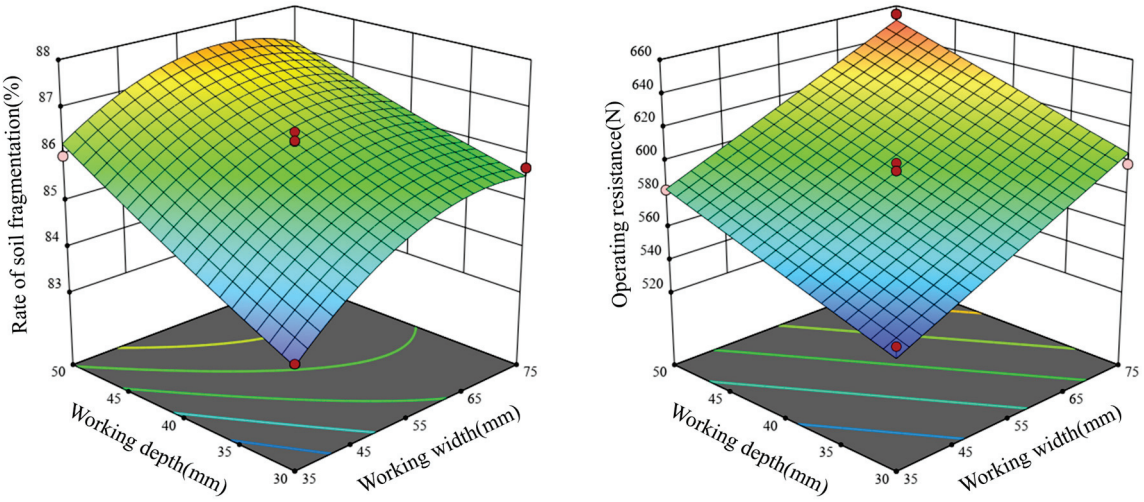

(**a**) (**b**)

Figure 10. Interaction effects on experimental indicators. (**a**) Interaction effect on soil fragmentation rate; (**b**) Interaction effect on operational resistance.

An optimization design was conducted based on the principles of maximizing soil fragmentation rate and minimizing operational resistance to determine the optimal structural parameter combination for the soil-crushing blade. A multi-objective variable optimization method was employed under the integration with the boundary conditions of the experimental factors. A nonlinear programming parameter model was established as:

$$\begin{cases} \max Y_1(X_1, X_2) \\ \min Y_2(X_1, X_2) \\ \text{s.t.} \begin{cases} 26.7157 \leq X_1 \leq 83.2843 \\ 25.8579 \leq X_1 \leq 54.1421 \end{cases} \end{cases} \tag{16}$$

We analyzed and solved the mathematical model through the optimization module in Design-Expert 13 software to determine the optimal parameter combination. A reasonable set of structural parameters was selected based on the optimization results. Specifically, when the working width of the soil-crushing blade was 40.66 mm and the working depth was 50 mm, the operational performance was ideal, with a soil fragmentation rate of 86.74% and an operational resistance of 590.81 N. Furthermore, we performed a virtual simulation using the optimized parameters to validate these results. The simulation yielded a soil fragmentation rate of 86.90% and an operational resistance of 589.43 N, consistent with the optimization results. Thus, it was confirmed that the model possesses favorable accuracy and reliability of predictions.

3.2. Blade Tooth Structure Comparison Test

The comparative test results of different blade tooth structures are shown in Table 6.

In Figure 11, the type of blade tooth structure exerted a highly significant impact on operational resistance ($p < 0.01$). The bionic blade tooth structure (Bs) exhibited an average operational resistance of 604.68 N, which was 7.682% lower than that of the original blade tooth structure (Os). This finding aligns with the research conducted by Jia [43], which suggests that the special sawtooth shape cuts more effectively and requires less force to

complete the job than the original saw blade. Further analysis also unveils that operating speed posed a highly significant impact on operational resistance ($p < 0.01$). As the forward speed increased from 6 km/h to 10 km/h, the average operational resistance rose from 613.61 N to 643.44 N, a 4.86% increase. This can be attributed to the fact that a higher forward speed resulted in a higher rotational speed of the soil-crushing blade, an increased amount of soil engaged per unit time, a greater force required to overcome soil shear strength, and thus higher operational resistance—similar to the findings of Kheiralla [44].

Table 6. Comparison of test results with different types of blade tooth structure.

Type of Blade Tooth Structure	Operational Resistance (N)	Soil Fragmentation Rate (%)
Bs	604.68	86.59
Os	652.87	85.49
Comparison	Reduced by 48.19	Upgraded by 1.1

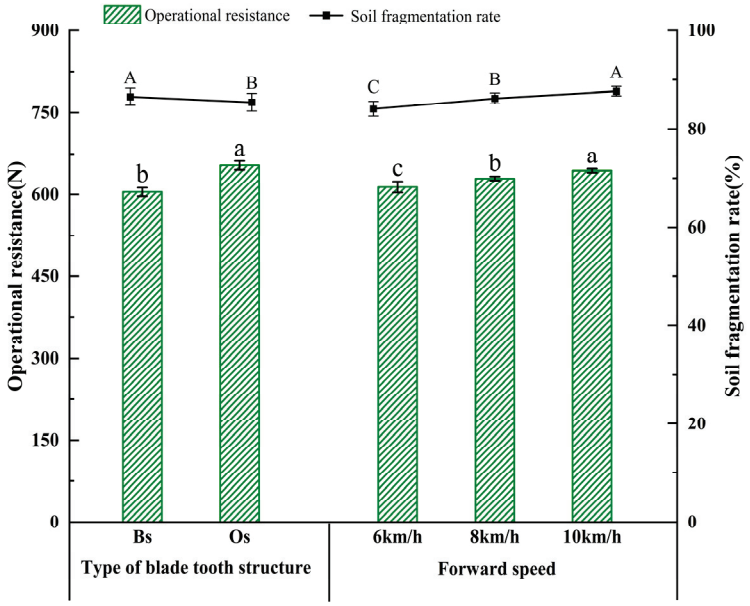

Figure 11. Effects of different blade tooth structures and forward speed on experimental indicators: means followed by different lowercase or uppercase letters are significantly different according to Tukey's test and LSD multiple range test at the significance level of 0.05; error bars are standard deviations.

Figure 11 exhibits the variation in soil fragmentation rate as a function of blade tooth structure and forward speed. The Bs demonstrated a higher average soil fragmentation rate of 86.59%, which was 1.45% higher than that of the Os. This finding aligns with the research conducted by Zhu [37], where a soil-crushing blade with bionic tooth profiles improved crushing performance compared to conventional blades. Further analysis specifies that the soil fragmentation rate increased with increasing forward speed. When the forward speed increased from 6 km/h to 10 km/h, the average soil fragmentation rate rose from 84.15% to 87.70%, a 4.22% improvement. This can be explained by the fact that higher forward speeds contributed to a higher blade rotational speed, which in turn increased the number of effects per unit time and therefore reinforced soil fragmentation efficiency—similar to the findings of Matin [45].

3.3. Field Experiment Results

In Figure 12, the presence of the bionic auxiliary soil-crushing device exerted a highly significant impact on the soil fragmentation rate ($p < 0.01$). When the bionic auxiliary soil-crushing device was installed, the average soil fragmentation rate reached 94.54%, which was 11.54% higher than that obtained when the device was not installed. This improvement was achieved due to the ability of the bionic auxiliary soil-crushing device to effectively crush displaced soil clods and compacted surface soil disrupted by the disc plow, thereby enhancing the overall soil fragmentation rate. Additionally, operating speed also posed a highly significant impact on the soil fragmentation rate ($p < 0.01$). An increase in the forward speed from 6 km/h to 10 km/h led to a growth of the average soil fragmentation rate from 87.67% to 91.60%, a 4.48% improvement.

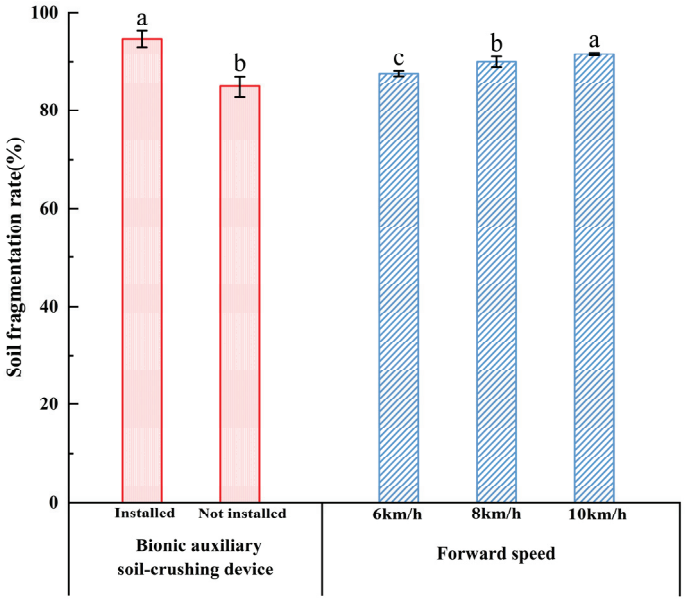

Figure 12. Field experiment results: means followed by different lower case letters are significantly different according to Tukey's test and LSD multiple range test at the significance level of 0.05; error bars are standard deviations.

Although certain discrepancies appeared between the field experiment results and the simulation results, their trends remained consistent. The measured soil fragmentation rate in the simulation was lower than that in the field experiment owing to differences in data collection methods. The field experiment excluded soil clods smaller than 4 cm, whereas soil aggregates under 4 cm may still have contained unbroken bonding connections in the simulation, leading to an underestimation of the fragmentation rate in the simulation.

4. Conclusions

In this study, we designed and analyzed a bionic auxiliary soil-crushing device. Specifically, the optimal parameter range was determined by theoretical analysis, and biomimetic tooth structures were designed following the claw-toe morphology of the Oriental mole cricket. Additionally, we optimized the structural parameters of the soil-crushing blade and compared the performance of different blade tooth structures by employing a discrete element simulation model. The device was further validated through field experiments. The main conclusions are outlined as follows.

Theoretical analysis and numerical calculations established that the working width (s) and working depth (h) of the soil-crushing blade were the key structural parameters affecting operational performance. The optimal parameter range was determined as

35 mm $\leq s \leq$ 95 mm and 30 mm $\leq h \leq$ 50 mm. Based on the claw-toe contour of the Oriental mole cricket, a bionic design was developed for the soil-crushing blade teeth.

We constructed a discrete element simulation model suitable for Northeast China's soil conditions. A CCD experiment was conducted with working width and working depth as experimental factors and soil fragmentation rate and operational resistance as response variables. Furthermore, we established a mathematical model to analyze the relationship between factors and response indicators and adopted a multi-objective optimization model to determine the optimal parameter combination: working width = 40.66 mm and working depth = 50 mm. A comparative simulation of two blade tooth structures suggested that the bionic blade tooth structure significantly improved operational performance, with a soil fragmentation rate of 86.90% and an operational resistance of 589.43 N. These results demonstrated a 1.45% increase in soil fragmentation rate and a 7.68% reduction in operational resistance compared to the original blade tooth structure.

Field experiments were performed on the simulation results. The results revealed that after the bionic auxiliary soil-crushing device was installed, the soil fragmentation rate reached 94.54%, an 11.54% increase compared to the non-installed condition. The trends in the field test results were consistent with the simulation results, verifying the reliability of the design. Moreover, the superior operational performance of the machine with the bionic auxiliary soil-crushing device satisfied the agronomic and technical requirements for strip-tillage operations.

This study has several limitations. The test results were obtained in a defined plot, so the machine may need to be made adjustable when used in other plots. Additionally, we did not consider energy consumption when measuring resistance. In future research, we will conduct a farm-scale experiment and assess the energy consumption of the tillage process under different operating modes.

Author Contributions: Conceptualization, Q.W.; methodology, Y.Z. and Q.W.; software, Y.Z., K.Z., and Y.-Y.Z.; validation, K.Z., Y.-Y.Z. and X.Z.; formal analysis, Y.Z. and X.Z.; investigation, Y.Z. and Q.W.; resources, Q.W.; data curation, Y.Z. and X.Z.; writing—original draft preparation, K.Z., Y.-Y.Z., and Q.W.; writing—review and editing, Q.W. and X.F.; visualization, Q.W.; supervision, Q.W. and X.F.; project administration, Q.W. and J.W.; funding acquisition, Q.W. and J.W. All authors have read and agreed to the published version of the manuscript.

Funding: This research was financially supported by the Heilongjiang Provincial Key Research and Development Program (No. 2022ZX05B04), the National Natural Science Foundation of China (No. 52005094, No. 52205253), the Heilongjiang Provincial Natural Science Foundation of China (No. LH2022E007), and the Heilongjiang Provincial Natural Science Foundation Research Team Project (No. TD2023E001).

Institutional Review Board Statement: Not applicable.

Data Availability Statement: The original contributions presented in this study are included in the article. Further inquiries can be directed to the corresponding authors.

Acknowledgments: The authors would like to thank their schools and colleges, as well as the funding providers of the project. All support and assistance are sincerely appreciated.

Conflicts of Interest: The authors declare no conflicts of interest.

References

1. Blanco-Canqui, H.; Lal, R. Crop residue removal impacts on soil productivity and environmental quality. *Crit. Rev. Plant Sci.* **2009**, *28*, 139–163. [CrossRef]
2. Ren, Z.J.; Han, X.J.; Feng, H.X.; Wang, L.F.; Ma, G.; Li, J.H.; Lv, J.J.; Tian, W.Z.; He, X.H.; Zhao, Y.N.; et al. Long-term conservation tillage improves soil stoichiometry balance and crop productivity based on a 17-year experiment in a semi-arid area of northern china. *Sci. Total Environ.* **2024**, *908*, 168283. [CrossRef] [PubMed]

3. Nunes, M.R.; Karlen, D.L.; Veum, K.S.; Moorman, T.B.; Cambardella, C.A. Biological soil health indicators respond to tillage intensity: A us meta-analysis. *Geoderma* **2020**, *369*, 114335. [CrossRef]
4. Xu, X.Z.; Xu, Y.; Chen, S.C.; Xu, S.G.; Zhang, H.W. Soil loss and conservation in the black soil region of northeast china: A retrospective study. *Environ. Sci. Policy* **2010**, *13*, 793–800. [CrossRef]
5. Tagar, A.A.; Adamowski, J.; Memon, M.S.; Do, M.C.; Mashori, A.S.; Soomro, A.S.; Bhayo, W.A. Soil fragmentation and aggregate stability as affected by conventional tillage implements and relations with fractal dimensions. *Soil. Till Res.* **2020**, *197*, 104494. [CrossRef]
6. Guan, C.S.; Fu, J.J.; Xu, L.; Jiang, X.Z.; Wang, S.L.; Cui, Z.C. Study on the reduction of soil adhesion and tillage force of bionic cutter teeth in secondary soil crushing. *Biosyst. Eng.* **2022**, *213*, 133–147. [CrossRef]
7. Wang, J.W.; Wen, N.; Liu, Z.M.; Zhou, W.Q.; Tang, H.; Wang, Q.; Wang, J.F. Coupled bionic design of liquid fertilizer deep application type opener based on sturgeon streamline to enhance opening performance in cold soils of northeast China. *Agriculture* **2022**, *12*, 615. [CrossRef]
8. Wang, Q.; Wang, B.; Sun, M.J.; Sun, X.B.; Zhou, W.Q.; Tang, H.; Wang, J.W. Design and testing of an automatic strip-till machine for conservation tillage of corn. *Agronomy* **2023**, *13*, 2357. [CrossRef]
9. Wu, B.; Huang, T.C.; Qiu, X.X.; Zuo, T.L.; Wang, X.S.; Xie, F.P. Design and experimental study of potato-soil separation device for sticky soils condition. *Appl. Sci.* **2021**, *11*, 10959. [CrossRef]
10. Tukhtakuziyev, A.; Ishmuradov, S.U.; Abdumajidov, R. Researching the parameters of the disc plough and its smooth run throughout the tillage depth. In *IOP Conference Series: Earth and Environmental Science*; IOP Publishing: Bristol, UK, 2021; p. 012058.
11. Han, C.J.; Liu, Z.; Mao, H.P.; Ma, X.; Wang, S. Design and experiment of variable rate fertilization combined soil preparation machine. *Trans. Chin. Soc. Agric. Mach.* **2024**, *55*, 250–261, 284.
12. Li, F.; Yang, H.J.; Zheng, X.; Hu, H.Y. Development of the soil layer construction device for the cotton seedbed in sandy soil of arid areas. *Trans. Chin. Soc. Agric. Eng. (Trans. CSAE)* **2024**, *40*, 55–65.
13. Kayombo, B.; Lal, R. Effects of soil compaction by rolling on soil structure and development of maize in no-till and disc ploughing systems on a tropical alfisol. *Soil. Tillage Res.* **1986**, *7*, 117–134. [CrossRef]
14. Ucgul, M. Simulating soil–disc plough interaction using discrete element method–multi-body dynamic coupling. *Agriculture* **2023**, *13*, 305. [CrossRef]
15. Onwualu, A.; Watts, K. Draught and vertical forces obtained from dynamic soil cutting by plane tillage tools. *Soil. Tillage Res.* **1998**, *48*, 239–253. [CrossRef]
16. Zhong, G.Y.; Li, H.W.; He, J.; Wang, Q.J.; Lu, C.Y.; Wang, C.; Tong, Z.W.; Cui, D.D.; He, D. Design and test of single-disc opener for no-till planter based on support cutting. *Agriculture* **2023**, *13*, 1635. [CrossRef]
17. Zeng, Z.W.; Chen, Y. Performance evaluation of fluted coulters and rippled discs for vertical tillage. *Soil. Till Res.* **2018**, *183*, 93–99. [CrossRef]
18. Li, J.W.; Li, X.Y.; Hu, B.; Gu, T.L.; Wang, Z.J.; Wang, H.L. Analysis of the resistance reduction mechanism of potato bionic digging shovels in clay and heavy soil conditions. *Comput. Electron. Agr.* **2023**, *214*, 108315. [CrossRef]
19. Jia, H.L.; Wang, W.J.; Wang, W.P.; Zheng, J.; Wang, Q.; Zhuang, J. Application of anti-adhesion structure based on earthworm motion characteristics. *Soil. Till Res.* **2018**, *178*, 159–166. [CrossRef]
20. Sun, J.Y.; Wang, Y.M.; Ma, Y.H.; Tong, J.; Zhang, Z.J. Dem simulation of bionic subsoilers (tillage depth >40 cm) with drag reduction and lower soil disturbance characteristics. *Adv. Eng. Softw.* **2018**, *119*, 30–37. [CrossRef]
21. Wang, Q.; Wang, Z.M.; Zhang, Z.H.; Zhang, K.; Yao, S.; Zhou, W.Q.; Sun, X.B.; Wang, J.W. Design and test of bionic elastic row cleaner with improved straw cleaning performance. *Agriculture* **2024**, *14*, 186. [CrossRef]
22. Zhao, J.L.; Lu, Y.; Wang, X.G.; Zhuang, J.; Han, Z.W. A bionic profiling-energy storage device based on mbd-dem coupled simulation optimization reducing the energy consumption of deep loosening. *Soil. Till Res.* **2023**, *234*, 105824. [CrossRef]
23. Tan, H.C.; Shen, C.C.; Ma, J.L.; Wu, C.L.; Xu, L.M.; Ma, S. The reduction of energy consumption and soil disturbance mechanisms in trenching using biomimetic blades. *Comput. Electron. Agr.* **2025**, *230*, 109887. [CrossRef]
24. Zhang, Z.J.; Jia, H.L.; Sun, J.Y. Review of application of biomimetics for designing soil-engaging tillage implements in northeast china. *Int. J. Agric. Biol. Eng.* **2016**, *9*, 12–21.
25. Xiao, M.; Wang, K.; Yang, W.; Wang, W.; Jinag, F. Design and experiment of bionic rotary blade based on claw toe of *Gryllotalpa orientalis* burmeister. *Nongye Jixie Xuebao/Trans. Chin. Soc. Agric. Mach.* **2021**, *52*, 55–63.
26. Liu, S.H.; Weng, S.J.; Liao, Y.L.; Zhu, D.Y. Structural bionic design for digging shovel of cassava harvester considering soil mechanics. *Appl. Bionics Biomech.* **2014**, *11*, 1–11. [CrossRef]
27. Shibusawa, S. Reverse-rotational rotary tiller for reduced power requirement in deep tillage. *J. Terramechanics* **1993**, *30*, 205–217. [CrossRef]
28. Salokhe, V.; Ramalingam, N. Effects of direction of rotation of a rotary tiller on properties of bangkok clay soil. *Soil. Tillage Res.* **2001**, *63*, 65–74. [CrossRef]

29. Wang, J.; Yang, D.; Wang, Z.; Fu, Z.; Wang, J.; Weng, W. Design and experiment of rice straw biaxial deep-buried returning machine. *Nongye Jixie Xuebao/Trans. Chin. Soc. Agric. Mach.* **2023**, *54*, 21–30.
30. Zhang, X.Y.; Yu, S.Y.; Hu, X.; Zhang, L.X. Study on rotary tillage cutting simulations and energy consumption predictions of sandy ground soil in a xinjiang cotton field. *Comput. Electron. Agr.* **2024**, *217*, 108646. [CrossRef]
31. O'Dogherty, M.; Godwin, R.; Hann, M.; Al-Ghazal, A. A geometrical analysis of inclined and tilted spherical plough discs. *J. Agric. Eng. Res.* **1996**, *63*, 205–217. [CrossRef]
32. Kogut, Z.; Sergiel, L.; Żurek, G. The effect of the disc setup angles and working depth on disc harrow working resistance. *Biosyst. Eng.* **2016**, *151*, 328–337. [CrossRef]
33. Cheng, Y.; Yan, X.; Zhu, R.; Li, C.; Liu, Y.; Liu, Z.; Lu, Q. Design and experiment of testing device for passive disc. *J. Northwest Univ. Nat. Sci. Ed.* **2016**, *44*, 228–234.
34. Yang, Z.; Zhang, K.; Zhang, Y.; An, J. Discrete element method–multibody dynamics coupling simulation and experiment of rotary tillage and ridging process for chili pepper cultivation. *Agronomy* **2024**, *14*, 446. [CrossRef]
35. Tisdall, J.M.; Oades, J.M. Organic matter and water-stable aggregates in soils. *J. Soil Sci.* **1982**, *33*, 141–163. [CrossRef]
36. Bao, P.; Wu, M.; Guan, C.; Luo, H.; He, Y.; Xiang, W. Design of plow-rotary style ditching and ridging device for rapeseed seeding. *Trans. Chin. Soc. Agric. Eng.* **2017**, *33*, 23–31.
37. Zhu, H.; Wang, D.; He, X.; Shang, S.; Zhao, Z.; Wang, H.; Tan, Y.; Shi, Y. Study on plant crushing and soil throwing performance of bionic rotary blades in cyperus esculentus harvesting. *Machines* **2022**, *10*, 562. [CrossRef]
38. Zhang, Z.; Sun, X.; Jin, Z.; Bing, Z.; Sun, J.; Tong, J. Design and test of crushing bionic soil covering device of soybean seeder. *Nongye Jixie Xuebao/Trans. Chin. Soc. Agric. Mach.* **2018**, *49*, 34–40.
39. Zhu, A.W.; Xu, C.T.; Liu, Y.F.; Wang, J.S.; Tan, X.D. Design and experiment of oblique stubble-cutting side-throwing anti-blocking device for no-tillage seeder. *Agriculture* **2024**, *14*, 2250. [CrossRef]
40. Zhang, L.; Wang, X.W.; Chen, J.N.; Wang, H.Y.; Cao, Y.G. Analysis and optimization of low-resistance animal bionic subsoiling shovel based on edem. *Agriculture* **2024**, *14*, 2046. [CrossRef]
41. Zhao, S.; Gao, L.; Yuan, Y.; Hou, L.; Zhang, X.; Yang, Y. Maize straw motion law in subsoiling operation using discrete element method. *Trans. Chin. Soc. Agric. Eng.* **2021**, *37*, 53–62.
42. Hasimu, A.; Chen, Y. Soil disturbance and draft force of selected seed openers. *Soil. Till Res.* **2014**, *140*, 48–54. [CrossRef]
43. Jia, H.L.; Li, C.Y.; Zhang, Z.H.; Wang, G. Design of bionic saw blade for corn stalk cutting. *J. Bionic Eng.* **2013**, *10*, 497–505. [CrossRef]
44. Kheiralla, A.F.; Yahya, A.; Zohadie, M.; Ishak, W. Modelling of power and energy requirements for tillage implements operating in serdang sandy clay loam, malaysia. *Soil. Till Res.* **2004**, *78*, 21–34. [CrossRef]
45. Matin, M.A.; Fielke, J.M.; Desbiolles, J.M.A. Torque and energy characteristics for strip-tillage cultivation when cutting furrows using three designs of rotary blade. *Biosyst. Eng.* **2015**, *129*, 329–340. [CrossRef]

Disclaimer/Publisher's Note: The statements, opinions and data contained in all publications are solely those of the individual author(s) and contributor(s) and not of MDPI and/or the editor(s). MDPI and/or the editor(s) disclaim responsibility for any injury to people or property resulting from any ideas, methods, instructions or products referred to in the content.

MDPI AG
Grosspeteranlage 5
4052 Basel
Switzerland
Tel.: +41 61 683 77 34

Agriculture Editorial Office
E-mail: agriculture@mdpi.com
www.mdpi.com/journal/agriculture



Disclaimer/Publisher's Note: The title and front matter of this reprint are at the discretion of the Guest Editors. The publisher is not responsible for their content or any associated concerns. The statements, opinions and data contained in all individual articles are solely those of the individual Editors and contributors and not of MDPI. MDPI disclaims responsibility for any injury to people or property resulting from any ideas, methods, instructions or products referred to in the content.





Academic Open
Access Publishing

mdpi.com

ISBN 978-3-7258-8988-4